Development and Experimental Validation of Direct Controller Tuning for Spaceborne Telescopes

by

Gregory J. W. Mallory

B.Sc.Eng., Electrical Engineering, University of New Brunswick, 1994
M.Sc., Physics, University of New Brunswick, 1996

SUBMITTED TO THE DEPARTMENT OF AERONAUTICS AND ASTRONAUTICS
IN PARTIAL FULFILLMENT OF THE DEGREE OF

DOCTORATE OF PHILOSOPHY

at the

MASSACHUSETTS INSTITUTE OF TECHNOLOGY

June 2000

Signature of Author . . . .
Department of Aeronautics and Astronautics
April 21, 2000

Certified by . . . .
Professor David W. Miller, Committee Chair
Department of Aeronautics and Astronautics

Certified by . . . .
Professor Eric Feron
Department of Aeronautics and Astronautics

Certified by . . . .
Dr. Brent D. Appleby
Charles Stark Draper Laboratory

Certified by . . . .
Professor David H. Staelin
Department of Electrical Engineering

Accepted by . . . .
Professor Nesbitt W. Hagood IV
Chairman, Department Graduate Committee

Development and Experimental Validation of Direct Controller Tuning for Spaceborne Telescopes

by

GREGORY J. W. MALLORY

Submitted to the Department of Aeronautics and Astronautics
on April 21, 2000 in Partial Fulfillment of the
Requirements for the Degree of Doctorate of Philosophy
at the Massachusetts Institute of Technology

ABSTRACT

Strict requirements in the performance of future space-based observatories such as the Space Interferometry Mission (SIM) and the Next Generation Space Telescope (NGST), will extend the state-of-the-art of critical mission spaceflight-proven active control design. A control design strategy, which combines the high performance and stability robustness guarantees of modern, robust-control design with the spaceflight heritage of conventional control design, is proposed which will meet the strict requirements and maintain traceability to the successful controllers from predecessor spacecraft. Two principal tools are developed: an analysis algorithm that quantifies each sensor/actuator combination's effectiveness for control, and a design engine which tunes a baseline controller to improve performance and/or stability robustness.

The sensor/actuator effectiveness indexing tool requires a reduced-order state-space model of the plant. A modification of the balanced reduction method is introduced which improves numerical conditioning so that the order of large models of flexible spacecraft may be decreased. For each sensor and actuator an index is computed using the modal controllability from an actuator weighted by the modal cost in the performance, and the model observability of a sensor weighted by the modal cost of the disturbance. The special case of actuators that are used for active output isolation is handled separately. The designer makes use of the sensor/actuator indexing tool to select which control channels to emphasize in the tuning.

The tuning tool is based on forming an augmented cost from weighting performance, stability robustness, deviation from the baseline controller, and controller gain. The tuning algorithm can operate with the plant's state-space design model or directly with the plant's measured frequency-response data. Two differentiable multivariable stability robustness metrics are formed, one based on the maximum singular value of the Sensitivity transfer matrix and one based on the multivariable Nyquist locus. The controller is parameterized with a general tridiagonal parameterization based on the real-modal state-space form. The augmented cost is chosen to be differentiable and a closed-loop stability-preserving unconstrained nonlinear descent program is used to directly compute controller parameters that decrease the augmented cost. To automate the closed-loop stability determination in the measured-data-based designs, a rule-based algorithm is created to invoke the multivariable Nyquist stability criteria.

The use of the tuning technique is placed in context with a high-level control design methodology. The tuning technique is evaluated on a sample problem and then experimentally demonstrated on a laboratory test article with dynamics, sensor suite, and actuator suite all similar to future spaceborne observatories. The developed test article is the first space-telescope-like experimental facility to combine large-angle slewing with nanometer optical phasing and sub-arcsecond pointing in the presence of spacecraft-like disturbances. The technique is applied to generate an improved controller for a model of the SIM spacecraft.

Thesis Supervisor:
Prof. David W. Miller
Dept. of Aeronautics and Astronautics

ACKNOWLEDGMENTS

I would like to thank my advisor, Prof. David W. Miller for his support over the course of my time at MIT. He has provided me with the opportunity to work theoretically and practically on multiple projects, to work with many of the agencies that guide U.S. aerospace research, to travel internationally to present our work, and to appreciate systems-level engineering.

I would also like to acknowledge the contributions of my other thesis committee members who guided me towards practical research while ensuring a solid theoretical footing. I benefitted greatly from Prof. Feron's wide knowledge of the Literature and of control theory, from Dr. Appleby's appreciation of what is useful for the control of real-world spacecraft, and Prof. Staelin's knowledge of interferometry and optical systems, and suggestions for expanding the audience of the thesis beyond the control community. I benefitted greatly from several discussions with Prof. Wallace Vander Velde regarding sensor/actuator placement. I appreciate his suggestions for communicating mathematical expressions in physical terms. I would like to thank Prof. Jon How for reading the thesis and for providing insightful comments near the end of the work. The sensor/actuator selection work benefitted from discussions with Prof. Arthur Mutambara.

The theoretical work has benefitted greatly from conversations with many current and former graduate students of the Space Systems Laboratory: Frederic Bourgault, Olivier deWeck, Dr. Homero Guiterrez, Sean Kenny, Dr. Brett Masters, and Jeremy Yung. Particular thanks goes to Dr. Carl Blaurock for several critical suggestions relating to the tuning methodology, and to my office-mate Brett deBlonk for suggestions that influenced the development of the work and for the FEM model of the sensor/actuator test grid structure.

I would like to acknowledge the other members of the Origins Testbed team for helping to conceptually design and assemble the test article under Prof. Miller's guidance: Brett deBlonk, Dr. Homero Guiterrez, Mitch Ingham, Sean Kenny and Dr. Yool Kim. Alvar Saenz-Otero, Abby Spinak and Johnathan Wong contributed greatly to the development of the Origins Testbed as Undergraduate Research Opportunities Program students. Alvar's 20 month contribution deserves special mention, including: design and construction of much of the fine pointing system and the development of an auto-alignment capability.

I would like to thank all of my friends in the Space System Lab and the Active Materials and Structures Lab. The students make these labs special places to work. Thank you to Kräzy Haus™ for hours of free entertainment and to Tom, my friend-from-home-in-Boston, for taking me away from MIT once in a while. I especially appreciate the support, encouragement, wisdom, dry goods, and food that my wonderful friend Yool has provided for me as I finished this work. I am spoiled.

I have valued and benefited from my family's support through all stages of my education; for that I am thankful.

The thesis has been supported by the MIT Space Systems Laboratory, administrated by Ms. SharonLeah Brown acting as MIT Fiscal Officer. SIM technical support was provided by the Jet Propulsion Laboratory, and NGST technical support was provided by NASA Goddard Spaceflight Center. The SIM Classic model was provided to the MIT Space Systems Laboratory by the Jet Propulsion Laboratory for contract SIM: 961-123, with technical monitor, Dr. Sanjay Joshi. Further financial support was provided in the form of a National Science and Engineering Research Council of Canada fellowship and a Canadian Space Agency fellowship.

TABLE OF CONTENTS

LIST OF FIGURES

LIST OF TABLES

NOMENCLATURE

Abbreviations

BC	baseline controller
CCD	charge coupled device
dof	degree of freedom
DPL	differential pathlength
ENC	encoder
FEM	finite element method or finite element model
FSM	fast-steering mirror
i/o	input/output
JPL	Jet Propulsion Laboratory
LQG	linear quadratic Gaussian
LQR	linear quadratic regulator
LTI	linear time-invariant
MIMO	multiple-input, multiple-output
MIT	Massachusetts Institute of Technology
NGST	Next Generation Space Telescope
ODL	optical delay line
OT	Origins Testbed
PZT	mirror on piezo stack actuator
QC	quad-cell photodiode
RB	rigid body
RG	rate gyroscope
RMS	root mean square
RWA	reaction wheel assembly
S/A	sensor/actuator
SERC	Space Engineering Research Center
SIM	Space Interferometry Mission
SISO	single-input single-output
ST	star tracker
s.v.	singular value
SVD	singular value decomposition
SWLQG	Sensitivity-Weighted Linear Quadratic Gaussian
VC	Voice coil

Symbols

z	performance variable
y	sensor measurement
w	exogenous disturbances, including process and sensor noises
x	plant state vector
u	actuator inputs
A	plant dynamics matrix
B_w	plant disturbance input matrix
B_u	plant actuation input matrix
C_z	plant performance measurement matrix
C_y	plant sensor measurement matrix
D_{zw}	plant disturbance to performance feedthrough matrix
D_{zu}	plant actuation to performance feedthrough matrix
D_{yw}	plant disturbance to sensor feedthrough matrix
D_{yu}	plant actuation to sensor feedthrough matrix
$G(s)$	plant transfer matrix
$G_{zw}(s)$	plant disturbance to performance transfer matrix
$G_{zu}(s)$	plant actuator to performance transfer matrix
$G_{yw}(s)$	plant disturbance to sensor transfer matrix
$G_{yu}(s)$	plant actuator to sensor transfer matrix
x_c	controller state variable
A_c	controller dynamics matrix
B_c	controller input matrix
C_c	controller output matrix
$K(s)$	controller transfer matrix
ω	frequency (radian/second)
$S(s)$	Sensitivity transfer matrix
A_s	Sensitivity dynamics matrix
B_s	Sensitivity input matrix
C_s	Sensitivity output matrix
D_s	Sensitivity feedthrough matrix
$\sigma_{\max}(\cdot)$	maximum singular value operator
$\underline{\sigma}_{\min}(\cdot)$	minimum singular value operator
$\bar{\sigma}$	maximum singular value over all frequency (H_∞ norm)
$J(\cdot)$	cost function
$K_b(s)$	baseline controller transfer matrix
$d(\cdot)$	distance function for comparing controllers
R_y	resolution-based scale factor for the sensors
R_z	performance-requirement-based scale factor for the performance variables
R_u	resolution-based scale factor for the actuators
R_w	intensity-based scale factor for the disturbances
q	left eigenvector of A
p	controller parameter vector or right eigenvector of A

f	controllability measure
h	observability measure
J	cost or modal control cost
V	modal output state cost
α	performance-weighted controllability measure
β	disturbance-weighted observability measure
B_e	output-isolation effective actuator input matrix
J_A	augmented tuning cost
M	penalty term for control use
S_R	penalty term for stability non-robustness
S_S	penalty term for deviations of max s.v. of Sensitivity greater than threshold
S_{cr}	penalty term for distance of Nyquist locus to the critical point
γ_{cr}	stability non-robustness term mixing parameter
μ	stepsize
H	estimate of the inverse of the Hessian matrix

Chapter 1

INTRODUCTION

Strict requirements on the performance of future space-based observatories such as the Space Interferometry Mission (SIM) and the Next Generation Space Telescope (NGST), will extend the state-of-the-art of mission-critical spaceflight-proven active control design. A control design strategy which combines the high performance and stability robustness guarantees of modern, robust-control design with the spaceflight heritage of conventional control design is proposed which will meet the strict requirements, while maintaining traceability to the successful controllers from predecessor spacecraft.

The thesis outlines a technique for tuning baseline controllers to meet strict requirements while maintaining the heritage to previous missions. Two principal tools are developed: an analysis algorithm that quantifies each sensor/actuator combination's effectiveness for control, and a design engine which tunes a baseline controller to improve performance and/or stability robustness. The designer makes use of the sensor/actuator indexing tool to select which control channels to emphasize in the tuning. The tuning tool is flexible and allows the alteration of the controller topology, trades of performance and stability robustness, and limits of the deviation of the tuned controller from the heritage-rich baseline controller. Further, the tuning algorithm can operate with the plant's design model or directly with the plant's measured frequency response data.

The use of the tuning technique will be placed in context with a high-level control design methodology. The sensor / actuator indexing tool and the tuning technique will be evaluated on a sample problem, and then demonstrated on a laboratory test article with similar dynamics, a similar sensor suite, and a similar actuator suite to future space-based observatories. The development of the test article, the first to combine large-angle slewing with nanometer optical phasing in the presence of spacecraft-like disturbances, is a contribution of the thesis and will be presented in suitable detail. Lastly the tools will be applied to a model of the SIM spacecraft.

The introduction is divided into a summary of the research objectives, a placement of the work in the context of other dynamics and control research for space-borne telescopes, a review of relevant previous work, and a roadmap of the thesis.

1.1 Research Objectives

The fundamental goal of the research is to improve the control technology readiness for spaceborne telescopes. The work is motivated by three characteristics of future space-based telescopes:

1. *No 1-g deployment*: Future spaceborne telescopes are large in dimension and lightweight and will not be able to support their own weight in a gravity field. No ground testing or model updating will be possible. The initial controller must be designed with sufficient stability robustness using a non-updated finite element method (FEM) model. Further, the controller may require updating to handle inevitable on-orbit model/plant mismatches.
2. *Tight performance requirement*: The pointing and phasing requirements are beyond the current state-of-the-art. To improve performance, the controller should take advantage of all relevant sensor / actuator control channels and of knowledge of disturbance statistics.
3. *Mission profile*: Future spaceborne telescopes are expensive and have a high public profile. Instability and failure are not acceptable. A control strategy with spaceflight and experimental heritage should be employed.

We wish to begin to bridge the gap between classical design with spaceflight heritage and modern optimization-based design, with the hope to improve the achievable control performance so that the tight imaging requirements can be met while maintaining the required stability robustness. The theory/practice gap is addressed in [Bernstein, 1999] for general control theory. The work in this thesis attempts to link theory and practice for flexible spacecraft control.

Particular objectives of this research can be summarized as:

- Outline a framework for the design of controllers for lightweight flexible spacecraft.
- Develop a technique to quantify the suitability of a plant for local control, and to quantify the advantages of global control. In particular we wish to
  - Quantify the effectiveness of sensors and actuators for control,
  - Determine the incremental effect of adding sensors and actuators.
- Develop a control design technique which takes advantage of modern optimal control theory while preserving the critical mission heritage of conventional, classical control designs. We adopt a strategy of tuning a baseline controller (with mission critical heritage). The desirable features of the methodology include:
  - improvements in performance and/or stability robustness over the baseline controller,
  - an ability to control the deviation of the tuned controller from the baseline controller,
  - an ability to tune control designs using design models *and* experimentally determined measurement models,
  - an ability to quantify and take advantage of the addition of extra states to the baseline controller,
  - an ability to quantify and take advantage of the enhancement of coupling in the baseline controller.
- Develop a laboratory test article which captures the relevant dynamics and control issues anticipated for future space-based lightweight, flexible spacecraft.
- Experimentally validate the control design methodology on the laboratory test article. We follow a procedure anticipated for the control design of the Space Interferometry Mission: first, design and implement a baseline controller with conventional, classical techniques, and then apply the developed methodology to arrive at a tuned, final design.
- Demonstrate the application of the control design methodology to an existing integrated model of the Space Interferometry Mission. We begin with the JPL/MIT-designed baseline controller, synthesized with conventional, classi-

cal techniques, and then apply the developed methodology to arrive at a tuned, final design.

1.2 Research Context

The control design for complex space structures must be placed within the context of the entire system design [Joshi, 1999]. The MIT Space Systems Laboratory has developed a framework for the analysis and design of the structure, dynamics and control for future spaceborne telescopes. The framework provides a structured environment for the modeling, model assembly and conditioning, analysis, evaluation against requirements, and if necessary, redesign for flexible space structures. Application of the framework to NGST is presented in [de Weck et al., 2000]. Figure 1.1 is a framework block diagram.

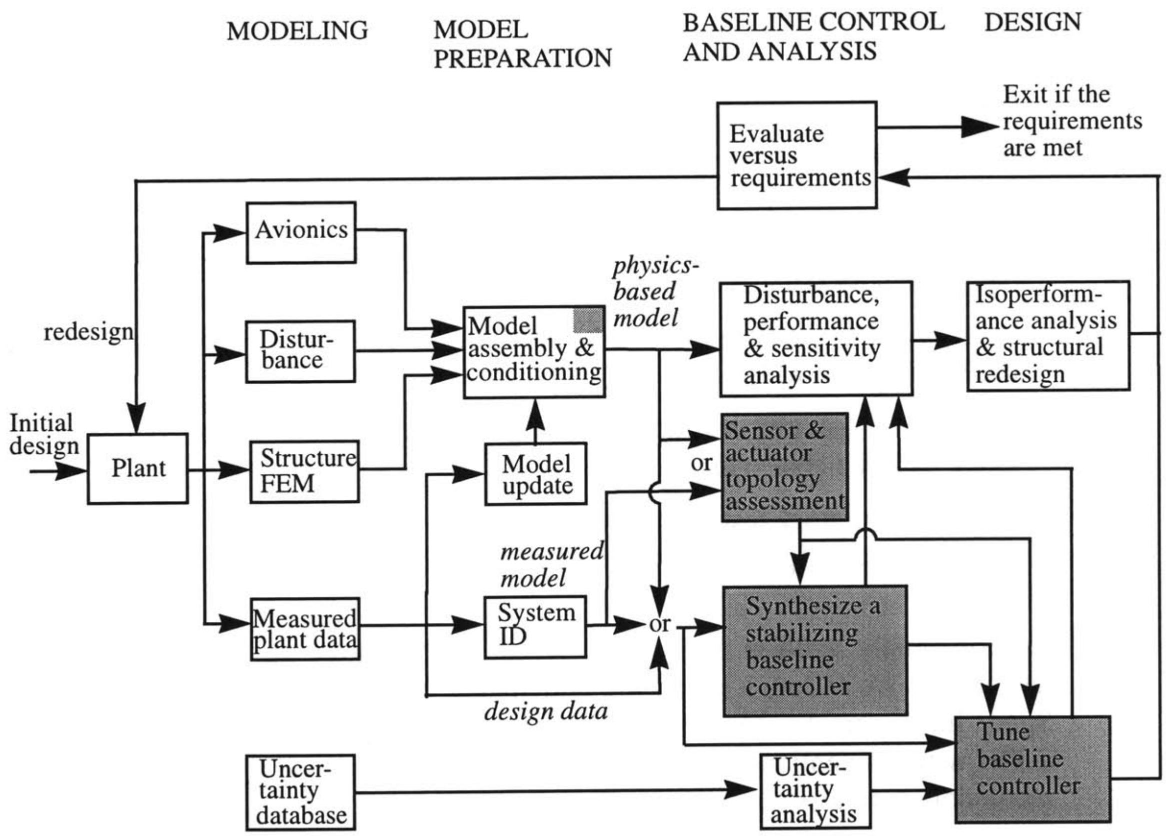

Figure 1.1 Dynamics, structures and control framework for analysis and design of flexible space structures. The thesis contributions to the framework are shaded. Models (and design data) are shown in italics.

The four column headings in the framework correspond to integrated modeling steps, while the individual blocks correspond to step components (tools where applicable). The framework is entered with an initial design. The design is modeled, and the FEM state-space *physics-based model* is assembled from the avionics, disturbance, and structural models. The model is conditioned and if a prototype is available measured data is used for model updating. Alternately system identification can be used to estimate a state-space *measurement model* from the measured data. With a state-space model a tool developed in Chapter 3 can be used to assess the effectiveness of particular sensors and actuators for control. The sensor/actuator effectiveness assessment along with a state-space plant model (or measured *design data*) are used to design a baseline controller. The baseline controller, sensor/actuator assessment, plant model (physics-based, measurement, *or* direct data), and the result of an uncertainty analysis (to set stability margins requirements) feed the controller tuning methodology of Chapter 4. The resulting controller improves the performance and/or stability robustness of the baseline controller without losing the spaceflight heritage of the baseline controller. By appending the controller to the physics-based model we can assess the effect of disturbances, performance and sensitivity of the system. The sensitivity analysis allows an isoperformance trade of the subsystem requirements, leading to a (if necessary) plant redesign. Table 1.1 references the MIT research contributions that make up the framework.

The tools developed in this thesis provide critical contributions to the dynamics, structures and control framework for analysis and design future spaceborne telescopes.

1.3 Literature Review

Control design for lightweight flexible space structures and the control-structure interaction is an area which has received much attention in the literature. [Crawley et al., 2001] provides an overview of the dynamics and control of lightly damped structures. The application and implementation of lightweight flexible space structure control was demonstrated on-orbit with success during the Middeck Active Control Experiment (MACE)

TABLE 1.1 Research references for the dynamics, structures and controls framework

Step	Component Tool	Reference[a]
MODELING	Avionics modeling	Includes sensor dynamics, actuator dynamics and delay [Glaese, 1994], **Section 2.2.7**
	Disturbance modeling	[Gutierrez, 1999] and [Masterson, 1999]
	Structural modeling	[Glaese, 1994]
	Measuring plant data	As an example see **Chapter 6**
	Uncertainty database	[Bourgault, 2000]
MODEL PREPARATION	Model assembly and conditioning	[Glaese, 1994], [Gutierrez, 1999], see **Section 3.1.2**
	Model updating	[Glaese, 1994]
	System identification	[Jacques, 1995]
BASELINE CONTROL & ANALYSIS	Disturbance, performance and sensitivity analysis	[Gutierrez, 1999]
	Sensor / actuator topology assessment	**Chapter 3**
	Synthesize a baseline compensator	Standard control design, see **Chapter 2**. As an example, see **Section 6.4**
	Uncertainty analysis	[Bourgault, 2000]
DESIGN	Isoperformance analysis and structural redesign	[Gutierrez, 1999] and [de Weck et al., 2000]
	Controller tuning	**Chapter 4**

a. References in bold are sections of this thesis which contribute to the framework. Listed references are representative and are not meant to be exhaustive. References are principally current and legacy research from the MIT Space Systems Laboratory which led to the development of the framework.

program [Miller et al., 1996]. However, the techniques with the greatest performance were modern model-based control designs which have little on-orbit heritage in non-experimental applications. A tuning strategy is adopted to link modern robust optimization techniques to conventional spacecraft control techniques.

An important component of the work is an algorithm to assess the suitability of sensor and actuator combinations for control. Based on the sensor/actuator assessment, the designer can select control channels to emphasize when applying the tuning methodology. We review techniques to determine the suitability of actuators and sensors for control design and find that a technique which incorporates knowledge of the disturbance and performance to index sensors/actuator combinations for control is needed.

We review controller tuning and find that an optimization-based frequency-domain strategy is lacking with the following critical characteristics: (1) tunes a *general* baseline controller, (2) allows specification of the topology (order and sensor / actuator connectivity) of the tuned controller parameters (3) designs with an explicit metric of stability robustness, (4) allows specification of the tuned controller's deviation from the baseline controller, and (5) tunes with a design-model and/or measured-data.

Further, we review spacecraft-like controlled structure laboratory testbeds and demonstrate that a testbed which captures all elements of the operation of a space-based observatory: slewing, phasing, pointing, and optical capture in the presence of realistic disturbances, has not been previously developed.

1.3.1 Sensor / Actuator Assessment for Control Effectiveness

Most relevant research in the literature for assessing sensor/actuator control effectiveness is in the area of actuator and sensor placement for the control problem. [Anderson, 1993] includes a detailed literature survey on the actuator placement problem for structural systems.

Closed-loop sensor / actuator assessment

Closed-loop techniques, whereby a constrained topology controller is synthesized and evaluated, are expected to provide the most direct and accurate comparisons of sensor/actuator topologies. [Mercadal, 1991] provides H_2 optimal first-order necessary conditions for block diagonal controller topologies. In practice though, the constrained topology H_2 optimal controllers prove difficult to synthesize. Recently [Hassibi et al., 1999] developed a structural controller design technique which can be used to derive a sparse low-authority controller based on a relaxed linear programming constraint. The sensor/actuator topology is not pre-specified but determined simultaneous with the control design. The technique is extended to linear perturbations of the high-authority (performance improving) control, but does not rank the effectiveness of the sensors and actuators. The closed-loop sensor evaluation problem is examined in [Mallory and Miller, 2000] where the ability of each sensor to H_2 optimally estimate each of the system states is determined by a solution of a Ricatti Equation. The technique can be extended to the dual, actuator problem, but combining the sensor and actuator problems is difficult.

Open-loop sensor/actuator assessment

In open-loop techniques, the design model is analyzed without explicitly solving for the controller. One set of strategies for the actuator/sensor placement problem involve defining a measure of controllability and observability and selecting sensor/actuator combinations with the highest combined observability/controllability [Gawronski and Lim, 1996], [Lim, 1992]. [McCasland, 1989] is similar but includes weightings by fault probabilities. To eliminate the difficulty of discrete locations, [Maghami and Joshi, 1993] approximate sensor measurements and actuator forces with spatially continuous functions to arrive at a well-posed nonlinear programming problem. These approaches use the actuator-to-sensor transfer matrix and do not exploit knowledge of the disturbance and performance characteristics.

Skelton's modal cost analysis [Skelton and Hughes, 1980] breaks up the system's H_2 performance cost into a sum of modal contributions. By examining the effect of each actuator, and the measure of each sensor on modes of the open-loop cost, a subset of sensors *or* actuators can be chosen which are determined to be effective [Skelton and Chiu, 1983], [Lin, 1996]. The simultaneous selection of sensors *and* actuators is not presented. The technique is modified to account for closed-loop effects in [Skelton and DeLorenzo, 1983] whereby the LQG problem is solved, sensors and actuators with little contribution are removed and the process is repeated. What results is a subset of actuators and sensors that are suited for LQG control. The technique does not index actuators and sensors for a general control topology.

In [Kim and Junkins, 1991] controllability measures are combined with Skelton's modal cost techniques to place actuators with an open-loop strategy that accounts for disturbance and performance characteristics.

The technique developed in this thesis extends [Kim and Junkins, 1991] to the sensor problem, and then combines sensors and actuators to account for their acting together. Further, the technique captures the special case of actively decoupling of the uncontrollable modes from the performance.

1.3.2 Controller Tuning Strategies

Controller tuning and synthesis are differentiated in this thesis as visualized in Figure 1.2. Controller synthesis involves designing a compensator for the open-loop system. By tuning we describe the process whereby the closed-loop system is modified by perturbing a baseline controller. In a tuning case we may limit the deviation of the tuned controller from the baseline controller. The control synthesis of [Miotto, 1997] is based on a similar concept whereby controllers for aircraft are tuned without changes in the control architecture (*i.e.* preserve heritage).

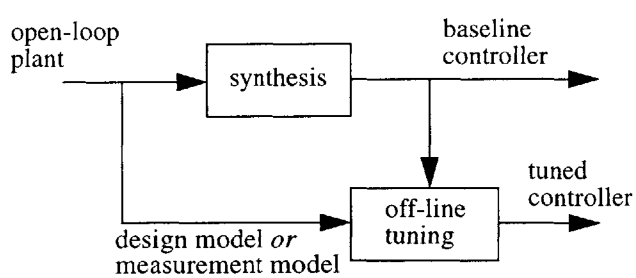

Figure 1.2 Controller synthesis and tuning

Many references exist for the synthesis of controllers. [Ogata, 1990] and [Van de Vegte, 1990] are complete references on the classical synthesis of controllers, applied to single-input, single-output (SISO) systems. [Kwakernaak and Sivan, 1972] is a classic reference on the synthesis of multiple-input, multiple-output (MIMO) H_2 controllers. [Zhou et al., 1996] is a more modern treatment, encompassing H_∞ and μ synthesis controllers. [Grocott, 1994] compares several robust control synthesis techniques.

Off-line controller tuning

A number of control synthesis techniques can be alternately considered as tuning techniques. The following section reviews a number of off-line controller tuning strategies and places the developed tuning methodology in context with the Literature.

$H_{2/\infty}$ design weight tuning

The use of design weights in the H_2/H_∞ control problem allow the designer to indirectly tune and shape the closed loop transfer matrix singular values [Gupta, 1980] and [Lublin et al., 1996]. By iterating on the frequency domain shape of the weightings the controller can be tuned. The technique guarantees a stable closed loop on the design model. The technique suffers from (1) a complicated mapping through a set of Ricatti Equations from weight adjustment to closed-loop performance, (2) the required use of a design model, and (3) a large order since weighting states are reflected in the controller order. Further details on loop shaping can be found in [Zhou et al., 1996] and the references therein.

Sensitivity-Weighted Linear Quadratic Gaussian tuning

A more direct controller tuning, with emphasis on improving stability robustness is given by Sensitivity-Weighted Linear Quadratic Gaussian (SWLQG) control design, [Okada and Skelton, 1990], [Grocott, 1994]. In this technique, the H_2 cost matrices are perturbed to account for minimizing an approximation to a set of sensitivity states. The adjusted Ricatti equations are solved to obtain the SWLQG controller and in the case of lightly damped structures considerable stability robustness improvements can be achieved with only slight performance degradation. The technique (1) requires a design model, and (2) requires a large-order model-based controller.

We note that for the implementation of H_2 and SWLQG controllers [Masters, 1997] manually tuned the controller parameters, post-synthesis, to increase robustness, with little degradation of performance. The poles of the controller were displayed on the complex plane and the designer perturbed the frequency and damping of controller poles near critical points on the Nichols plot. If perturbed properly, loops and near-critical-point encirclements can be pushed away from the critical point, increasing robustness enough to allow implementation of the controller. Robustness was particularly sensitive to the location of any unstable controller poles. Though this method can be applied to any controller, it suffers from (1) no explicit recipe for pole perturbation, and (2) an incomplete controller parameterization, and (3) a capability for only small adjustments to the controller.

Youla Parameter Tuning

[Youla et al., 1976] develops the parameterization of all stabilizing controllers for MIMO systems. The theory shows that *every* controller that stabilizes a plant is contained in a set which can be parameterized by a MIMO parameter, Q. Further, the mapping from Q to many closed-loop functions is affine, allowing the closed-loop system to be directly tuned. The implication is that by properly applying Q, we set up a well behaved affine optimization problem of tuning Q to directly minimize a cost. This Q parameterization tuning approach was directly developed by [Boyd et al., 1988] and [Polak and Salcudean, 1989]. A detailed description and development of the framework is presented in [Boyd and Barratt, 1991]. Recently, [McGovern, 1996] and [Lintereur, 1998] applied the technique to the multiple-loop SISO control design for a lightly-damped flexible laboratory structure. The Q parameterization suffers from several critical disadvantages: (1) A generalized baseline controller is not possible since Q must be connected to the system such that it provides no feedback, limiting the baseline controller to be model-based, or to include a contribution from the plant dynamics that enters the controller structure as Q becomes nonzero, and (2) Q must be parameterized using basis functions, resulting in large-order controllers and limitations from approximating an infinite basis set with a finite number of functions.

SISO Classical Controller Tuning

Two tuning methods by Ziegler and Nichols are common for SISO process control [Van de Vegte, 1990] and based upon classical control synthesis. We assume a structure for the controller: proportional (P), proportional/integral (PI), or proportional/integral/derivative (PID). The gains are tuned based on the step response of the plant to achieve a desired overshoot. The method assumes a controller structure, a low-order plant, and gains are non-optimally tuned based on heuristic rules.

Further tuning rules for low-order classical SISO controllers are present in the Literature. The importance of P, PI, and PID control design is stressed by their abundance in industrial application. [Åström et al., 1998] presents a technique for selecting the gains of a PI controller to optimize a cost function based on maximizing the load disturbance rejection while setting constraints on tracking and the sensitivity. The paper is relevant to the work in this thesis since the control design problem is reduced to a non-convex optimization. A family of papers by Åström derive methods for the optimal design and tuning of these classical low-order controllers (see for example [Åström and Hagglund, 1995]). [Johansson et al., 1998] extends the methodology to MIMO systems in a limited manner. The paper of [Ho et al., 1998] presents an extension of the Ziegler-Nichols tuning which ensures robust PID controllers by optimizing a classical performance index: integral square error (ISE), integral absolute error (IAE), or integral time absolute error (ITAE), while directly ensuring specified gain and phase margins.

[Hjalmarsson et al., 1998] details a technique for low-order SISO controller tuning similar to that developed in this thesis. The controller is parameterized and an optimization a carried out over the parameters of the controller. The gradients of the cost function with respect to controller parameters are computed (estimated) and a Newton-Gauss optimization is iteratively performed. Stability robustness is not directly handled though proper specifications by the designer will ensure suitable margins.

The preceding SISO tuning rules perform well on the low-order, heavily damped plants of process control, but suffer from three defects: (1) the plant is assumed to have a low-order and is typically without lightly-damped dynamics, (2) the controller has a low-order and is of a fixed structure (3) the SISO techniques are not easily extendable to MIMO systems.

Direct (Parameter Optimization) MIMO control

The direct synthesis of MIMO H_2 controllers differs from conventional H_2 control in that no Ricatti Equations are solved. Instead a cost function is formed, gradients with respect to controller parameters are computed, and controller parameters are computed by decreasing the cost function with a nonlinear program or with a homotopy algorithm. Necessary conditions for H_2 optimality, given a state-space design model, are derived in [Mercadal, 1991] for the full-order, reduced-order and partially constrained controller topology. Extending this synthesis technique to tuning is trivial. The optimal projection equations of [Hyland and Bernstein, 1984] are similar necessary conditions for the reduced-order H_2 control problem. Synthesizing the optimal controller by satisfying the necessary conditions is difficult but a nonlinear program to directly improve the cost of a baseline controller proves to be beneficial. Care must be taken to ensure that the resulting controller stabilizes the design model. [Collins and Sadhukhan, 1998] compare the use of homotopy algorithms with nonlinear programming techniques for the H_2 optimal reduced-order control design. [Ly et al., 1985] derive similar cost functions and gradients for a design-model but use a reduced controller parameterization. Ly's technique is made more general in [Ly, 1998] and includes a multiple-model capability similar to that of [MacMartin et al., 1991] to implicitly ensure stability robustness. The main limitations of these direct MIMO control techniques are (1) stability robustness is not captured as an explicit element of the cost, (2) no framework for a general controller parameterization (with variable controller order and sensor/actuator topology) seems apparent in the literature, and (3) all development is with design models: no capability to directly tune controllers with measured plant data is apparent. The tuning methodology developed in this thesis will extend direct (parameter optimization) tuning and surpass these limitations.

Measured Data-Based Control Design

Designing controllers directly with measured transfer matrix data (*i.e.* without a design model) is a classical control concept. Many frequency-domain based classical graphical design techniques such as Bode design, Nyquist design and Nichols design can be applied without a state-space model [Ogata, 1990]. Extending these design techniques to MIMO systems has proven to be difficult despite the existence of a MIMO Nyquist criteria [Lehtomaki et al., 1981].

More recently, the concept of unfalsified control has been introduced [Safanov and Tsao, 1997]. Controllers are falsified when experimental plant measures indicate that the controller would lead to instability or fail to meet requirements. Falsified controllers are removed from a set of available controllers. [Woodley et al., 1999] uses a linear program to select an optimal SISO controller from an unfalsified set of controllers of a fixed order. The unfalsified control concept is limited by (1) the difficulty of finding an initial set of controllers for a general MIMO case, (2) a lack of techniques for efficiently removing falsified controllers from the set, and (3) a lack of general, MIMO techniques for extracting a good controller from the unfalsified set.

During the MACE experiment [Miller et al., 1996] measured experiment data was incorporated into the control synthesis strategy as an evaluation step. If the control design did not perform well, as simulated with the measured data, then the design weights were manually tuned. The work in this thesis intends to automate this ad-hoc design strategy by directly using the measured data for control design.

Adaptive control and on-line tuning

In adaptive control, the controller is iteratively tuned on-line to ensure stability for a not-necessarily well modeled, perhaps time-varying, plant [Narendra and Annaswamy, 1989]. Extensions of adaptive control to nonlinear plants are made [Slotine and Li, 1991]. Often, stability is considered of primary importance, at the expense of considering guaranteed performance secondary. The principal drawback of adaptive control for the near-term control of future spaceborne telescopes is a lack of spaceflight heritage. Linear time-invariant control theory is more established than its adaptive counterpart for space systems. Converting some of the direct strategies discussed above to adaptive tuning is feasible with on-line monitoring of the plant. To build spaceflight heritage [Davis et al., 1999] intend to demonstrate a frequency-based adaptive control for a lightly damped flexible space structure on the MACE reflight program.

The proposed technique of this thesis is a degenerate case of direct adaptive control whereby iterative tuning is performed off-line. The technique balances performance and stability robustness in the control design. Further by designing with measurement models, our technique comes closer to the realism of on-line tuning than standard design-model tuning techniques. Lastly, the developed tuning technique shall be extendable to on-line tuning with minimal alterations.

1.3.3 Experimental Test Articles

Multiple ground-based experimental facilities exist for the validation of control techniques on flexible systems. [Sparks and Juang, 1992] surveys the U.S. experimental facilities for control of flexible structures. In this work, experiments are categorized as control experiments, encompassing topics such as vibration suppression, slew control, system identification and deployment, or as test facilities for testing sensors, actuators and systems under on-orbit environmental conditions. No facility is available which includes all elements of space telescope operation: slew, optical capture, observation control under reaction wheel disturbance with realistic actuators and sensors.

The Jet Propulsion Laboratory (JPL), as the prime contractor for SIM spacecraft, have developed a series of interferometer test articles culminating with the Micro-Precision Interferometer (MPI) testbed. MPI is a technology demonstrator for validating nanometer-level phasing control [Neat et al., 1997], [Neat and O'Brien, 1996], sub-arcsecond pointing control [O'Brien and Neat, 1995], and integrated modeling techniques [Melody and Neat, 1999]. The disturbance source for regulation control experiments is a shaker emulating on-board disturbances. MPI proves to be an extremely high-fidelity system but is limited in that (1) it cannot perform a slew maneuver and (2) reaction wheel windup disturbances are not realistically generated by the shaker.

TABLE 1.2 Experimental test articles relevant to future spaceborne telescopes[a]

Experimental facility	Large-angle slew	Phasing control	Fine-pointing control	Spacecraft disturbance	Notes and Reference[b]
JPL Microprecision Interferometer	None	~ 10 nm	~0.4 arcsec	None (shaker)	[Melody and Neat, 1999] Adding reaction wheel disturbance
Palomar testbed interferometer	None	~ 10-20 nm	Yes, with unknown fidelity	None	[Colavita et al., 1999] Fringe-measuring ground-based testbed
Advanced space structures technology experiments	Yes	None	None	Reaction wheels, cold gas thrusters	[Vadali et al., 1995] Air force slew and structural control experiment
Space integrated controls experiment	None	None	~0.04 arcsec	None (shakers)	[Personal communication with R. Ninneman]
MIT multipoint alignment testbed	None	~ 50 nm	None	None (shakers)	[Blackwood et al., 1991]
MIT single-axis interferometer	None	~ 50 nm	None	None (shakers)	[Masters, 1997]
MIT Origins Testbed	**30 degrees**	**~ 50 nm**	**~ 1 arcsec**	**Reaction wheels**	**Detail in the thesis**

a. Other relevant test articles exist, but none except the Origins Testbed are know to have (1) large-angle slew, (2) phasing control, (3) fine-pointing control *and* (4) spacecraft-like disturbance.

b. Personal communication with M. Colavita of the Jet Propulsion Laboratory and S. Griffin and R. Ninneman both of the Air Force Research Laboratory, is acknowledged.

The MIT Space Systems Laboratory has developed a family of experimental facilities detailed in [Miller and Mallory, 1998]. A fixed closed-topology truss structure called the multipoint alignment (MPA) testbed was designed to investigate the precision control of optical elements in a lightweight structure. Control experiments involved rejecting the transmission of an induced shaker disturbance to an optical pathlength performance metric. The single-axis interferometer (SAI) testbed of [Masters, 1997] evolved from the

MPA to be more SIM-like with collectors at the end of two booms reflecting to a central combiner. An induced shaker disturbance is rejected in an optical pathlength measure with a combination of structural and optical control. The next test article in this family can be made more space-telescope like by including: (1) an ability to combine a regulating observation mode with an ability to slew over large angles, (2) a realistic on-board reaction-wheel induced disturbance, (3) a combination of optical pathlength control and a fine-pointing control system.

Table 1.2 compares an non-exhaustive list of relevant test articles in terms of there capability for large angle slew with fine phasing and pointing control in the presence of a physical spacecraft-like disturbance. The Origins Testbed is believed to be the first spacecraft-like testbed to combine large-angle slew control with fine phasing and pointing control in the presence of realistic disturbances.

1.4 Research Contributions

The following unique contributions were made by meeting the thesis research objectives. The contributions are developed in the thesis and summarized in the concluding chapter of the document

- A framework for the design of controllers for spaceborne telescopes is developed.
- An improvement to the numerical robustness of the common balanced reduction method is developed.
- An algorithm is developed for determining the effectiveness of particular actuators and sensors for the regulator control problem.
- A methodology is developed for tuning baseline controllers to allow trades of four control features: (1) performance, (2) stability robustness, (3) deviation of the tuned controller from the baseline controller, and (4) control channel magnitudes.
- An automated algorithm for determining closed-loop system stability directly on model data is developed.

- The sensor/actuator effectiveness matrix is validated as a guideline for determining effective channels for control, and linked with the tuning methodology on a one-dimensional interferometer sample problem.
- The Origins Testbed, the first spacecraft-like test article with a large-angle slew capability, a 50 nm phasing metrology system, and arcsecond pointing optics in the presence of reaction-wheel induced disturbances is designed, developed and experimental tested.
- The tuning methodology is experimentally validated on the Origins Testbed.
- The tuning methodology is applied to a large-order model of the SIM spacecraft.
- An optimal decentralized state estimation framework was developed.
- Necessary conditions are derived for arbitrary-topology H_2 optimal controllers.

1.5 Thesis Overview

The flowchart of Figure 1.3 provides a sequential outline for the thesis. The work is divided into two principal areas: development and validation.

The development flowchart provides the reader with a chronological sequence of how the developed tools should be applied. Given a model of the plant the designer can assess the level of coupling in the plant by applying the sensor/actuator indexing algorithm to quantify the natural plant couplings. The algorithm is developed in Chapter 3. By selecting sensor and actuator sets the designer breaks the system up into a set of control problems and designs a baseline controller using a synthesis technique from Chapter 2. The designer then checks if the system meets the requirements. If so then the control design is complete. If not then the designer can apply the tuning methodology of Chapter 4. The sensor/actuator indexing information helps the designer decide which control channels should be emphasized in the tuning. Again the closed-loop system is checked against the design requirements. If the requirements are still not met then the tuning process continues. States can be added and control sensor/actuator channels can be opened. Should the designer eventually decide that a tuned controller will never satisfy the requirements then the plant must be redesigned following the framework of Figure 1.1.

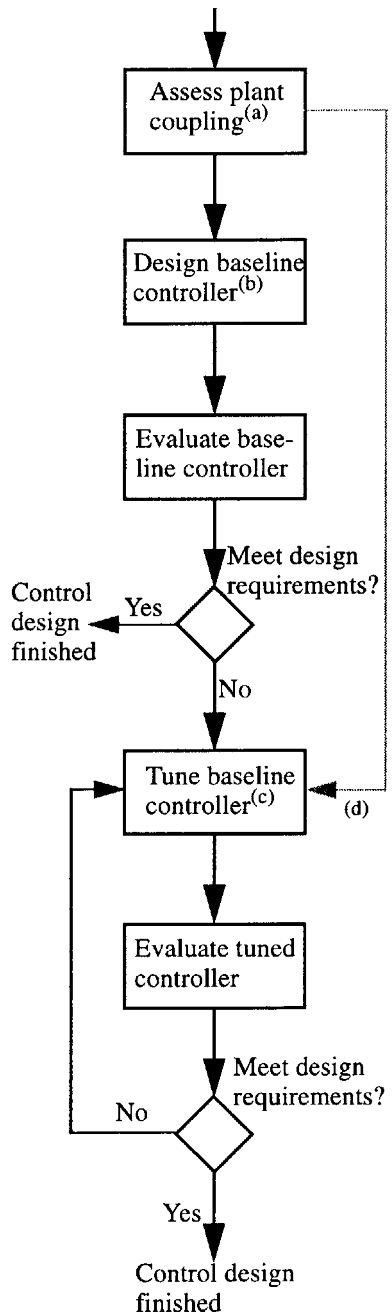

Comments

(a)Determine the plant's natural level of dynamic coupling to (1) choose baseline control strategy, and (2) quantify non-local control advantages [Chapter 3].

(b)Synthesize the baseline controller with the required heritage. A methodology is outlined in Chapter 2. Typical designs are with local controllers.

(c)Tune the baseline controller by using a (1) design or evaluation model, *or* (2) a measurement model [Chapter 4].

(d)Use the plant's level of dynamic coupling to determine local loops to combine for tuning [Chapter 3].

(e)Demonstrate application of controller tuning to a simulation sample problem to verify function and generate intuition [Chapter 5]

(f) Design and construct a testbed to capture dynamics and control problems of space telescopes [Chapter 6].

(g)Experimentally validate developed tuning strategy on the representative testbed [Chapter 6].

(h)Design a controller for the SIM model. Confidence in design is increased by testbed experiments [Chapter 7].

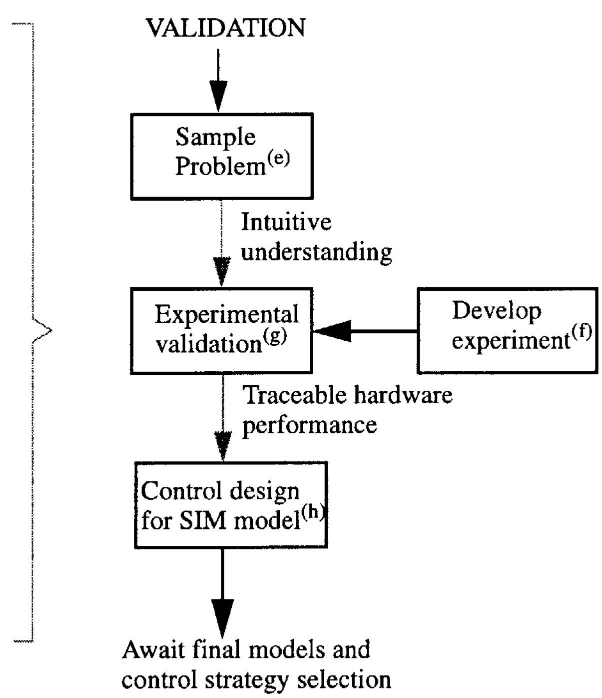

Figure 1.3 Thesis flow: the development and validation of global controller tuning for spaceborne telescopes

The developed tools must be validated. Validation is presented as a flow chart in Figure 1.3 and in tabular form in Table 1.3. From the application of the developed tools to a sample problem we develop an intuitive understanding (Chapter 5). Based on this understanding the techniques are successfully implemented on an experimental test article designed and constructed to be traceable to spaceborne telescopes (Chapter 6). Success with traceable experimental test articles increases our confidence of the applicability of the techniques to the true mission spacecraft. Lastly, the techniques are applied to a conceptual model of a spaceborne telescope in Chapter 7.

TABLE 1.3 Validation of developed techniques: test matrix

System	Assess Sensor/ Actuator Effectiveness	Design Baseline Controller	Apply Tuning Methodology	Experimental Evaluation	Thesis Chapter
Sample Problem	✓	✓	✓	–	Chapter 5
Origins Testbed	✓	✓	✓	✓	Chapter 6
SIM Model	✓	✓[a]	✓	–	Chapter 7

a. The SIM baseline controller is provided by JPL with the exception of the fine pointing optical control, introduced in [Gutierrez, 1999] and modified in this thesis.

Chapter 2

CONTROL DESIGN FRAMEWORK

In this chapter we discuss a framework for synthesizing robust controllers for high-performance flexible spacecraft. A similar methodology was employed during the Middeck Active Control Experiment (MACE) to design robust, high-performance controllers [Miller et al., 1996 and Campbell et al., 1999]. The goal of presenting a control synthesis methodology is to present a procedure for synthesizing controllers for space structures and to place the developed tuning methodology in context as a tool within a control design framework.

The chapter begins with an introduction to the notation and state-space concepts that will be used throughout the thesis. The standard control regulator problem will be introduced. Emphasis will be placed on the use and limitations of multivariable stability robustness metrics. These metrics will be essential for (1) the evaluation and pre-implementation safety testing steps in the controller synthesis framework and (2) the development of the tuning methodology that forms the focus of the thesis in subsequent chapters. A controller synthesis framework is presented which outlines the steps in control design. The framework includes: specification of the control problem, model development, control strategy selection, synthesis, evaluation and implementation. Controller tuning is also explicitly included in the framework. Lastly, we state the thesis problem, and place the contribution of the thesis in context with the controller synthesis framework.

2.1 Notation and Formulation

We begin with an introduction to the notation that will be used in the thesis. We will consider linear time-invariant (LTI) systems which can be represented with constant state-space matrices. Though classical techniques often use numerator/denominator formulations, most modern techniques are developed for state-space systems. The availability of tools (for example, MATLAB) for synthesis, analysis, and their numerical maturity (*i.e.* robustness to numerical problems) also support a state-space convention.

The section begins with a description of the standard control problem and definitions of signals that will be used in the thesis. The Sensitivity transfer matrix is introduced. Defining metrics for MIMO stability robustness is critical for the tuning methodology and subsequently the issue of MIMO stability is detailed. The use of the singular values of the Sensitivity transfer matrix as a conservative estimate of the gain and phase margins is detailed, and the use of the multivariable Nyquist locus as a metric of stability robustness is introduced.

2.1.1 Standard Control Problem

In Figure 2.1 we have a block diagram of the standard control problem. We have a plant, $G(s)$, with a set of inputs and outputs that will be represented with vectors: exogenous disturbances $w \in \Re^{n_w}$, actuator inputs $u \in \Re^{n_u}$, performance variables $z \in \Re^{n_z}$, and sensor measurements $y \in \Re^{n_y}$, where s represents the Laplace variable. $\Re$ represents the field of real numbers. A compensator, $K(s)$, receives y as an input and generates actuator signals, u. Tracking is enabled by introducing a reference, $r \in \Re^{n_r}$ at an appropriate location in the loop.

All definitions are presented for multiple-input, multiple-output (MIMO) systems unless otherwise noted. With the controller unconnected, we can write the open loop system as,

$$\begin{bmatrix} z \\ y \end{bmatrix} = G(s)\begin{bmatrix} w \\ u \end{bmatrix}, \tag{2.1}$$

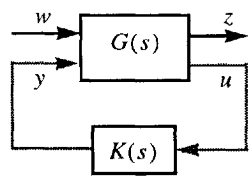

Figure 2.1 General control system interconnection

where we can parse the transfer matrix $G(s)$ as,

$$G(s) = \begin{bmatrix} G_{zw}(s) & G_{zu}(s) \\ G_{yw}(s) & G_{yu}(s) \end{bmatrix}. \tag{2.2}$$

We can write $G(s)$ in state-space form with the notation,

$$\begin{aligned} \dot{x} &= Ax + B_w w + B_u u \\ z &= C_z x + D_{zw} w + D_{zu} u \\ y &= C_y x + D_{yw} w + D_{yu} u \end{aligned} \tag{2.3}$$

where $x \in \Re^{n_x}$ is the state variable, $A \in \Re^{n_x \times n_x}$ is the plant dynamics matrix, $B_w \in \Re^{n_x \times n_w}$ is the disturbance input matrix, $B_u \in \Re^{n_x \times n_u}$ is the actuator input matrix, $C_z \in \Re^{n_z \times n_x}$ is the performance output matrix, $C_y \in \Re^{n_y \times n_x}$ is the sensor measurement matrix, and D_{zw}, D_{zu}, D_{yw}, and D_{yu} are respective feedthrough matrices of commensurate dimensions. With these definitions, $G_{yu}(s)$ can be written as,

$$G_{yu}(s) = C_y(sI - A)^{-1}B_u + D_{yu}. \tag{2.4}$$

The remaining elements of $G(s)$ can be similarly defined.

The controller, $K(s)$ can be written in state-space form as

$$\begin{aligned} \dot{x}_c &= A_c x_c + B_c y \\ u &= C_c x_c \end{aligned} \tag{2.5}$$

where $x_c \in \Re^{n_c}$ is the controller state, $A_c \in \Re^{n_c \times n_c}$ is the controller dynamics matrix, $B_c \in \Re^{n_c \times n_y}$ is the controller input matrix, and $C_c \in \Re^{n_u \times n_c}$ is the controller output matrix.

When the controller is appended to the dynamics of Equation 2.1 with positive feedback[1] we arrive at

$$\begin{aligned} z &= [G_{zw}(s) + G_{zu}(s)K(s)(I - G_{yu}(s)K(s))^{-1}G_{yw}(s)]w \\ y &= (I - G_{yu}(s)K(s))^{-1}G_{yw}(s)w \end{aligned} \tag{2.6}$$

in transfer function notation, which we write in state-space notation as,

$$\begin{aligned} \begin{bmatrix} \dot{x} \\ \dot{x}_c \end{bmatrix} &= \begin{bmatrix} A & B_u C_c \\ B_c C_y & A_c + B_c D_{yu} C_c \end{bmatrix} \begin{bmatrix} x \\ x_c \end{bmatrix} + \begin{bmatrix} B_w \\ B_c D_{yw} \end{bmatrix} w \\ z &= \begin{bmatrix} C_z & D_{zu} C_c \end{bmatrix} \begin{bmatrix} x \\ x_c \end{bmatrix} + D_{zw} w \\ y &= \begin{bmatrix} C_y & D_{yu} C_c \end{bmatrix} \begin{bmatrix} x \\ x_c \end{bmatrix} + D_{yw} w \end{aligned} \tag{2.7}$$

We will use the notation $A^{(cl)}, B_w^{(cl)}, C_z^{(cl)}, C_y^{(cl)}, D_{zw}^{(cl)}, D_{yw}^{(cl)}$ for the above state-space matrices, where the $(\cdot)^{(cl)}$ superscript refers to a closed-loop system.

2.1.2 Sensitivity Transfer Matrices

Our definitions of Sensitivity transfer matrices are derived from the standard feedback configuration of Figure 2.2. In the diagram, r is a reference, d is an exogeneous process noise, n and is an exogeneous sensor noise. Recall the positive feedback convention.

With simple block diagram manipulations we find,

1. A positive feedback convention will be used for all theoretical developments in this thesis, with the exception of graphical displays of stability where the classical negative feedback convention will be employed.

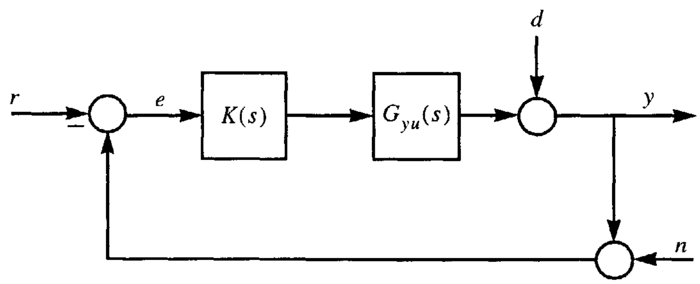

Figure 2.2 Standard feedback configuration

$$\begin{aligned} e &= (I - G_{yu}(s)K(s))^{-1}(-r + n + d) \\ y &= (I - G_{yu}(s)K(s))^{-1}d + G_{yu}(s)K(s)(I - G_{yu}(s)K(s))^{-1}(-r + n) \end{aligned} \tag{2.8}$$

The function

$$S(s) = (I - G_{yu}(s)K(s))^{-1} \tag{2.9}$$

is called the Sensitivity transfer matrix[1]. $S(s)$ relates the process noise d to the output y. We can also think of the Sensitivity transfer matrix as the sensitivity of the closed-loop response to perturbations in the open-loop [Van de Vegte, 1990]. To see this we consider a SISO case. We derive the closed-loop function from the input r to the output y and find that

$$\frac{y}{r} = C(s) = \frac{-G_{yu}(s)K(s)}{1 - G_{yu}(s)K(s)}. \tag{2.10}$$

We wish to determine the sensitivity of changes in the closed-loop tracking, ΔC, with respect to changes in the open-loop plant, ΔG_{yu},

$$S_{C/G} = \frac{\Delta C}{C} / \frac{\Delta G_{yu}}{G_{yu}}. \tag{2.11}$$

By allowing the changes to become infinitessimal we differentiate to arrive at

1. Equation 2.9 is the output Sensitivity transfer function, defined by cutting the loop at the plant output. In the thesis, *Sensitivity Transfer Matrix* refers to the *output* Sensitivity Transfer Matrix.

$$S_{C/G} = \frac{1}{1 - G_{yu}(s)K(s)} \tag{2.12}$$

which is the SISO expression for the Sensitivity transfer matrix defined above. Thus when $S_{C/G}$ is small, the closed-loop transfer function is insensitive to perturbations of the open-loop plant. The desensitization of the closed loop to perturbations in the open loop is an advantage of feedback. Alternately when $S_{C/G}$ is large, the effect of open-loop plant perturbations is amplified in the closed loop. If $G_{yu}(s)K(s)$ approaches 1 at some frequency $S_{C/G}$ blows up, which is an indication of instability. Thus we have an intuitive connection with $S_{C/G}$ and stability robustness. The connection will be quantified in the next section.

We should note that $S(s)$ itself does not provide a metric of absolute stability. When $S(s) \to \infty$ it is an indication of an ill-behaved system; one where the slightest perturbation may lead to instability. For SISO systems an absolute measure of stabililty is given by the Nyquist condition [Ogata, 1990].

The MIMO function relating y to r,

$$C(s) = -G_{yu}(s)K(s)(I - G_{yu}(s)K(s))^{-1} \tag{2.13}$$

is called the Complementary Sensitivity transfer matrix. $C(s)$ relates the sensor noise n to the output y, and also determines the tracking performance, $y = C(s)r$. Further, the identity

$$S(s) + C(s) = I \tag{2.14}$$

is easily verified to hold.

To determine state-space relations for $S(s)$ and $C(s)$ we first form a state-space system corresponding to the loop gain, $G_{yu}(s)K(s)$:

$$
\begin{aligned}
\begin{bmatrix} \dot{x} \\ \dot{x}_c \end{bmatrix} &= \begin{bmatrix} A & B_u C_c \\ 0 & A_c \end{bmatrix} \begin{bmatrix} x \\ x_c \end{bmatrix} + \begin{bmatrix} 0 \\ B_c \end{bmatrix} e \\
y &= \begin{bmatrix} C_y & D_{yu} C_c \end{bmatrix} \begin{bmatrix} x \\ x_c \end{bmatrix}
\end{aligned}
\quad . \tag{2.15}
$$

where we have $d = 0$ in Figure 2.2. By substituting $e = r + y$ we can derive a state-space model for $C(s)$, and with Equation 2.14 we can write a state-space representation of $S(s)$,

$$
\begin{aligned}
\begin{bmatrix} \dot{x} \\ \dot{x}_c \end{bmatrix} &= \begin{bmatrix} A & B_u C_c \\ B_c C_y & A_c + B_c D_{yu} C_c \end{bmatrix} \begin{bmatrix} x \\ x_c \end{bmatrix} + \begin{bmatrix} 0 \\ B_c \end{bmatrix} r \\
y &= \begin{bmatrix} C_y & D_{yu} C_c \end{bmatrix} \begin{bmatrix} x \\ x_c \end{bmatrix} + Ir
\end{aligned}
\quad . \tag{2.16}
$$

The Sensitivity state-space system of Equation 2.16 will be denoted with the matrices, $\{A_s, B_s, C_s, D_s\}$. We note that the state-space relations for the Complementary Sensitivity transfer matrix $\{A_{cs}, B_{cs}, C_{cs}, D_{cs}\}$ are related to those for $S(s)$ by

$$A_{cs} = A_s, B_{cs} = B_s, C_{cs} = C_s, D_{cs} = 0 . \tag{2.17}$$

[Zhou et al., 1996] demonstrates the use the sensitivity functions $S(s)$ and $C(s)$ for loop shaping control design.

In the SISO case, at frequencies where the loop gain $|G_{yu}(j\omega)K(j\omega)|$ is large we have $|S(j\omega)| \to \frac{1}{|G_{yu}(j\omega)K(j\omega)|}$ which will be small and $|C(j\omega)| \to 1$. Thus where we have a large loop gain, we have a small sensitivity which corresponds to good rejection of d in y and good stability robustness. At frequencies where the loop gain is small we have $|S(j\omega)| \to 1$ and $|C(j\omega)| \to |G_{yu}(j\omega)K(j\omega)|$ which will be small. When the loop gain is small we loose the benefit of feedback: the performance reduces to the open-loop case, and the closed-loop system is as sensitive to perturbations as the open-loop system.

2.1.3 Sensitivity as a Measure of Stability Robustness

The physical interpretation of $S(s)$ as the sensitivity of the closed-loop system to perturbations in the open-loop plant indicate that $S(s)$ may be used as a measure of stability robustness. In this section the use of $S(s)$ as a stability robustness measure is developed for SISO systems and then extended in a limited manner to MIMO systems.

SISO Development

At frequencies where the loop gain is near unity, (*i.e.* $G_{yu}(j\omega)K(j\omega) = \alpha + j\omega$ with $\sqrt{\alpha^2 + \omega^2} \approx 1$) we find that $|S(j\omega)|$ is very dependent on the loop gain's phase. We have

$$|S(j\omega)| \approx \frac{1}{2(1-\alpha)} \tag{2.18}$$

where α varies from $-1 \le \alpha \le 1$ implying that $\frac{1}{4} \le |S(j\omega)| \le \infty$. Clearly, near crossover, where the loop gain is near unity a proper phase is important to avoid a large Sensitivity and subsequent poor stability robustness. These SISO stability arguments are consistent with the gain and phase margins of Bode stability theory [Ogata, 1990].

To maintain good stability robustness, it seems that we should simply ensure $|S(j\omega)| \le 1$ for all frequencies. Generally, this is not possible. There are design tradeoffs when we tune the Sensitivity. For SISO linear systems the phase and magnitude are related through Bode's gain and phase relation [Zhou et al., 1996]. This relation computes $\angle G_{yu}(j\omega_0)K(j\omega_0)$ at a frequency ω_0 by integrating a function of the loop gain over all frequency and correcting for the phase contributions of non-minimum phase zeros.

A further quantitative example is provided by the Bode Sensitivity Integral [Looze and Freudenberg, 1996] which states: given a SISO loop gain, $G_{yu}(s)K(s)$ with right-half plane poles $\{p_i, i = 1, \ldots, n_p\}$, then

$$\int_0^{\infty} (\log|S(j\omega)|)d\omega = \pi \sum_{i=1}^{n_p} Re(p_i) \tag{2.19}$$

if $G_{yu}(s)K(s)$ has at least two more poles than zeros. The implication of Equation 2.19 is that the area under $\log|S(j\omega)|$ depends only on the open-loop unstable poles. Thus if $|S(j\omega)|$ is pushed down in one frequency region, it must pop up in another frequency region. Though Equation 2.19 holds exactly only for SISO systems, the Sensitivity push-pop also manifests itself in MIMO systems. Additional integral Sensitivity constraints are found in [Freudenberg and Looze, 1985].

Extension to MIMO Systems

Trivial extensions of the preceding analysis to MIMO systems are not possible. In a multivariable example the loop gain becomes a matrix quantity which implies that singular values must be used as a measure of size along a particular y direction[1]. Thus, the loop gain may be small in one y direction while it is large in another. More seriously, the loop gain may be near unity at multiple frequencies for multiple singular values corresponding to a particular y directions. The probabilistic occurrence of sensor inputs coinciding with these directions is difficult to quantify. Near-unity loop gain singular values can lead to a blow-up of Sensitivity transfer matrix singular values, indicating near-instability. To further complicate matters, the Bode integral relations are not known to be extendable to the general MIMO case. In practice, similar limitations are observed in MIMO systems but they are not quantified. In the following section the MIMO extension of the use of $S(s)$ and the multivariable Nyquist locus as metrics of stability robustness will be explored.

To quantify stability robustness, we can use the unstructured uncertainty MIMO stability margin as defined in [Lehtomaki et al., 1981]. The result is derived based on the Small Gain Theorem which will be stated using Figure 2.3. Traditionally $\Delta(s)$ is considered to be a perturbation to the plant $M(s)$, and the Small Gain Theorem sets conservative limits on the size of $\Delta(s)$ that can be withstood without destabilizing the interconnection. We assume that we have little knowledge of the form of $\Delta(s)$ so we treat it as an unstructured uncertainty.In the figure $y = M\Delta y$.

1. In a MIMO system the sensor signal y is a vector quantity with both a magnitude and a direction.

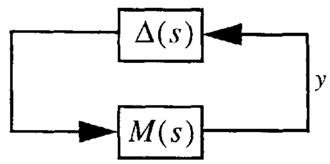

Figure 2.3 Small Gain Theorem block diagram

We state the Small Gain Theorem: given that $\Delta(s)$ and $M(s)$ are stable, and $\gamma > 0$ then the system of Figure 2.3 is stable for (a) $\|\Delta(s)\|_\infty \le 1/\gamma$ if and only if $\|M(s)\|_\infty < \gamma$ and (b) $\|\Delta(s)\|_\infty < 1/\gamma$ if and only if $\|M(s)\|_\infty \le \gamma$. A proof of the Small Gain Theorem can be found in [Zhou et al., 1996].

We will assume that we cast the uncertainty of the plant as divisive uncertainty as shown in Figure 2.4.

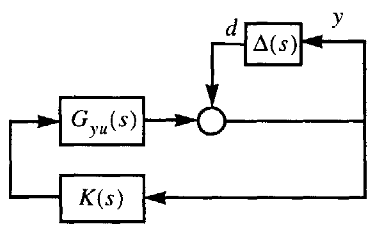

Figure 2.4 Divisive uncertainty

With a series of simple block manipulations we arrive at,

$$\begin{aligned} y &= d + G_{yu}(s)K(s)y \\ &= (\Delta(s) + G_{yu}(s)K(s))y \end{aligned}, \tag{2.20}$$

which we can rewrite as,

$$\Delta(s)y = (I - G_{yu}(s)K(s))y\,. \tag{2.21}$$

By setting $M(s) = (I - G_{yu}(s)K(s))^{-1}$ we can use the Small Gain Theorem to define a robust stability condition of

$$\left\|(I - G_{yu}(s)K(s))^{-1}\right\|_{\infty} < \frac{1}{\|\Delta(s)\|_{\infty}} \tag{2.22}$$

for guaranteed stability.

By following a procedure in [Chao and Athans, 1996] we extend this result. First we define a stable, minimum-phase, weighting scalar, $m(s)$, such that $\Delta(s) = m(s)\Delta_n(s)$ for some $\|\Delta_n(s)\|_{\infty} \leq 1$. By substituting in Relation 2.22 and using the definition of the H_{∞} norm we write a condition for stability robustness as

$$\sigma_{\text{max}}[(I - G_{yu}(j\omega)K(j\omega))^{-1}] < \frac{1}{|m(j\omega)|}, \forall\omega \geq 0 \tag{2.23}$$

where $\sigma_{\text{max}}[f(j\omega)]$ is the maximum singular value of $f(j\omega)$ at frequency ω, and the Laplace variable is evaluated as $s = j\omega$. Stability robustness requires that $S(s)$ is smaller than the uncertainty function, $1/|m(j\omega)|$ at all frequencies. We note that $|m(j\omega)|$ is small where the model is certain and approaches unity where the model is uncertain. We conclude that for good stability robustness we require that $\sigma_{\text{max}}[S(j\omega)]$ remains small where the model is uncertain.

By taking maximum singular value over all frequencies we compute the maximum singular value of the Sensitivity:

$$\bar{\sigma} = \max_{\omega}(\sigma_{\text{max}}[(I - G_{yu}(j\omega)K(j\omega))^{-1}]) \, . \tag{2.24}$$

We can define a MIMO guaranteed gain margin as,

$$\text{GM} = \frac{\bar{\sigma}}{\bar{\sigma} \pm 1} \tag{2.25}$$

and a guaranteed phase margin,

$$\text{PM} = \pm\arccos\left[1 - \frac{1}{2}\left(\frac{1}{\bar{\sigma}}\right)^2\right]. \tag{2.26}$$

We are guaranteed stable if the gains of all channels *or* phases of all channels are changed simultaneously within the margins [Lehtomaki et al., 1981].

In a similar sense, we can define

$$\underline{\sigma} = \min_{\omega}(\sigma_{\min}[I - G_{yu}(j\omega)K(j\omega)]) \tag{2.27}$$

as the minimum singular value of $S(j\omega)^{-1}$. The operator $\sigma_{\min}[f(j\omega)]$ returns the minimum singular value of $f(j\omega)$ at frequency ω. We note that $\bar{\sigma} = 1/\underline{\sigma}$.

By substituting in $\bar{\sigma}$ into Relation 2.23 we arrive at

$$\bar{\sigma} < \frac{1}{|m(j\omega)|}, \forall\omega \geq 0 \tag{2.28}$$

as a condition for stability robustness. Condition 2.28 implies that reducing $S(s)$ in regions where the model is uncertain will ensure stability robustness. Through Equation 2.14 we see that $C(s)$ can be used for alternate stability robustness relations [Chao and Athans, 1996].

We loosely interpret $\bar{\sigma}$ as a minimum distance to the critical point, such that if the channel complex deviation exceeds this minimum distance, the number of encirclements (in a Nyquist sense) of the critical points is altered and the, assumed stable, system destabilizes. Section 2.1.4 provides an analysis of the use of the MIMO Nyquist criteria as a measure of stability robustness.

A major problem with the Sensitivity singular value analysis for stability robustness is that it can be extremely conservative. The deviations (uncertainty) of the plant are assumed possible in any direction – even directions that are physically impossible. The research in [Bourgault, 2000] and the references therein model the probabilistic uncertainty for flexible space structures and future research should couple this uncertainty research with metrics for stability robustness. In practice, however, [Miller et al., 1996] found that monitoring $\bar{\sigma}$ provided a useful indication of stability robustness where emphasis is placed on (1) frequency regions where the plant is not well modeled (high uncertainty), and (2) frequency regions where the predicted Sensitivity singular values (predicted by simulating the controller on the design model) differ from the measured Sensitivity singular values.

2.1.4 Nyquist Locus as a Measure of Stability Robustness

Analysis of the Sensitivity transfer matrix provides a measure of stability robustness, but unless $S(s)$ is singular, no measure of the absolute stability. The Nyquist locus provides a graphical method to determine absolute stability. In this section the Nyquist locus is introduced for SISO systems and its extension to MIMO systems is made. The use and limitations of the MIMO Nyquist locus as a measure of stability robustness is explored.

SISO Development

The Nyquist locus and Nyquist stability criteria are hallmarks of classical control [Ogata, 1990]. The SISO Nyquist locus is a computed by evaluating the loop gain $G_{yu}(j\omega)K(j\omega)$ along a frequency contour. A sample Nyquist locus is plotted in Figure 2.5 (for simplicity only the positive frequency plot is drawn).

For closed-loop stability, the number of encirclements of the $(-1, 0)$ critical point must be equal to the number of open-loop unstable poles. Assuming the plant is stable, a change in the number of encirclements indicates a change to instability. From this logic we can use the Nyquist plot to determine stability margins. In Figure 2.5 the traditional gain margin is indicated by α and the phase margin by the angle γ. An alternate view on Nyquist locus stability robustness is provided if the uncertainty in the loop gain is known as a function of frequency. Balls of uncertainty can be drawn on the Nyquist locus [Lublin 1992] as shown in Figure 2.5. A ball represents the possible locations of the Nyquist locus at that frequency. The shape of the ball depends on the physics of the plant and needs not be circular. The research of [Bourgault, 2000] characterizes the uncertainty for flexible space structures. If the balls of uncertainty never include the critical point then the system is robustly stable.

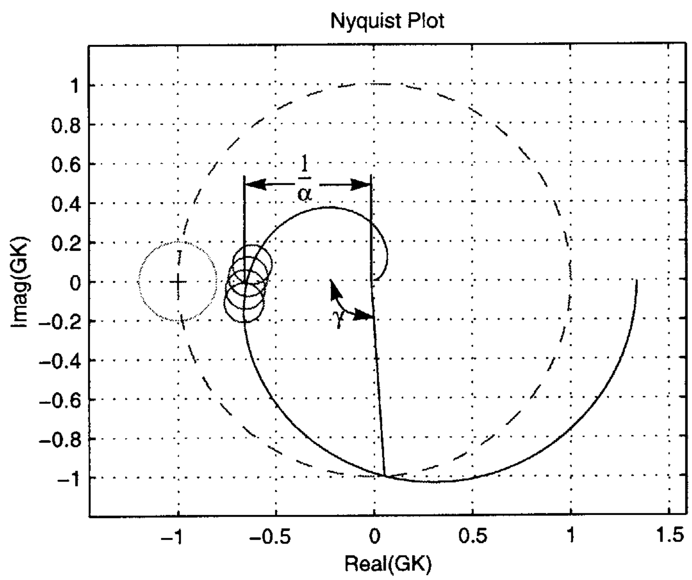

Figure 2.5 SISO Nyquist plot (positive frequency) is drawn with solid line. The unity gain circle is indicated with a dashed circle. The gain margin, α, and phase margin are, γ, are indicted on the figure. Small circles along the locus correspond to balls of uncertainty at several respective frequency points. The circle around the (−1,0) critical point indicated a guaranteed robustness region.

The detraction of the balls-of-uncertainty viewpoint is that: (1) the shapes of the balls are extremely difficult to probabilistically compute, and (2) an infinite number of balls exist (one for each frequency in the Nyquist locus). To simplify we assume that we are quantifying the robustness of an already stable system. We claim to have robust stability if the Nyquist locus never enters a ball centered at the critical point, $(-1, 0)$. The intuitive conclusion is that the closer the Nyquist locus passes by $(-1, 0)$, the closer we are to a change in the number of encirclements which indicates a change in stability. Thus the closest distances from the Nyquist curve to the critical point provide a measure of stability robustness.

Extension to MIMO Systems

The Nyquist absolute stability criterion is extendable to the MIMO case [Lehtomaki et al., 1981]. For closed-loop stability, the net number of counterclockwise encirclements of the critical point of the Nyquist function,

$$L_n(j\omega) = -1 + \det(I - G_{yu}(j\omega)K(j\omega)) \tag{2.29}$$

must equal the number of poles of the open-loop system, $G_{yu}(s)K(s)$ (assuming no unstable pole/zero cancellations).

The properties of the determinant operator ensure that extending the stability robustness results to the MIMO case proves to be problematic. Consider a loop gain evaluated at a frequency ω_o:

$$G_{yu}(j\omega_o)K(j\omega_o) = \begin{bmatrix} 0 & 0 \\ \frac{1}{\varepsilon} & 0 \end{bmatrix} \tag{2.30}$$

where ε is a small real number. The resulting point of the MIMO Nyquist is $L_n(j\omega_o) = 0$, well away from the critical point. With an ε perturbation of one entry, we have

$$G_{yu}(j\omega_o)K(j\omega_o) = \begin{bmatrix} 0 & \varepsilon \\ \frac{1}{\varepsilon} & 0 \end{bmatrix} \tag{2.31}$$

and the resulting MIMO Nyquist point is $L_n(j\omega_o) = -1$ indicating instability. This example demonstrates that in a MIMO system, maintaining a safe distance from the Nyquist locus to the critical point is a necessary but not sufficient condition for good stability robustness. The minimal distance from the critical point to the Nyquist locus is thus an under-conservative measure of stability robustness. The properties of the determinant that cause this behavior provides the impetus for the singular value analysis of Section 2.1.3.

In practice [Masters, 1997] shows the utility of such a stability robustness metric. By manually tuning compensator poles to increase the minimal distances of the Nyquist locus to the critical point [Masters, 1997] was able to implement controllers that otherwise proved to cause an unstable closed loop. By using a stability robustness measure based on this distance, the tuning algorithm of Chapter 4 automates his procedure.

2.2 Controller Design Methodology

A control design methodology must integrate the quantitative techniques for controller synthesis with a heuristic set of experience and intuition-based rules employed by the designer. Many of the capabilities that are required in the Methodology are provided in a Graphical User Interface based toolbox discussed in [Henderson et al., 1998]. Further work can include the development of an expert system based on a heuristic set of general design rules, to simplify the necessary designer input to the control design process.

A control design methodology follows the flowchart of Figure 2.6. In this flowchart, inputs to the left of the dashed line are opportunities for the designer to interface directly with the control design methodology. This is where the designer intuition, experience, and heuristic rules enter the design methodology. On the right we have the principle blocks which are directly connected quantitatively (*i.e.* by passing models, mathematical constraints, *etc.*).

2.2.1 Problem Specification

The first step in the control synthesis methodology is to properly specify the problem. The design must quantitatively set up the control problem from an abstract problem statement. We require the specification of the variables in Table 2.1 to quantify the control problem. Other requirements can be levied at this stage.

For example, stability robustness guarantees against an unknown, but bounded, plant uncertainty may be required, or a limit on the magnitude of an actuator signal. Less

TABLE 2.1 Variables to quantify a control problem

Vector	Specification
z	define performance variables
w	define exogeneous disturbance
u	select actuator suite
y	select sensor suite

explicit requirements may be placed on the structure (for example PID) or on the complexity of the controller. Controller structure requirements may be driven by implementation issues such as hardware, or by control heritage for critical applications. The anticipated implementation of the controller also drives the design. For example, digital implementation limits the maximum frequency of controller eigenvalues. Also, controller input/output hardware (for example 12 bits), limits the controller's dynamic range.

The control design problem simplifies to the statement: *Find a controller that meets the requirements, if one exits. Otherwise determine that no controller exists [*Boyd and Barratt, 1991*].*

2.2.2 Modeling for Control

The second step in the design process is to find a model of system for control design. This step is particularly important if a modern, model-based design method is to be employed. The model should have the following characteristics:

1. *Fit the plant behavior well in the bandwidth on interest.* In particular, the frequency region where the controller will be adding energy to the plant should be well modeled for stability robustness. In particular the model should describe the behavior of the plant well at the anticipated cross-over frequencies [Lintereur, 1998]. To ensure stability, particular emphasis should be placed on the phase of the channels of the transfer matrix from the sensors to actuators, $G_{yu}(s)$.
2. *Should accurately capture the physical zeros of the plant.* The zeros of the plant have a major impact on the control design, and thus should be properly modeled. Particular attention must be paid to any nonphysical nonminimum phase model zeros.

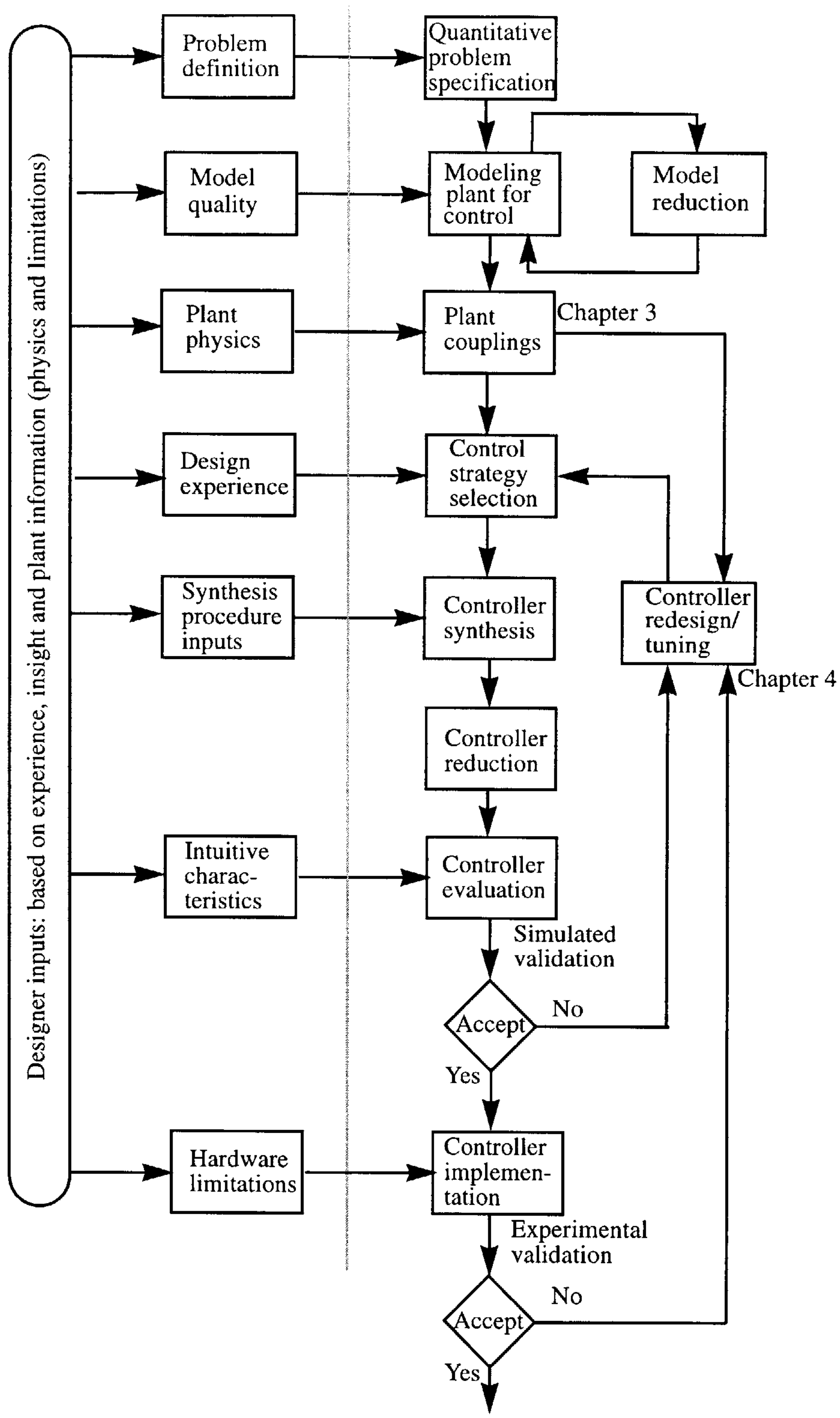

Figure 2.6 Controller design framework flowchart

3. *Have the lowest possible order.* The design model should be as low order as possible while still satisfying 1 and 2 above. The low-order design model may be reduced from a higher-order evaluation model. A low-order model eases the computational burden of the design process, and effectively reduces the order of model-based compensators.
4. *Capture the plant uncertainty.* Uncertainty in the plant (and the corresponding plant models) should be captured [Bourgault, 2000]. Plant uncertainty models can be used to evaluate the stability and performance of the closed-loop system given multiplicative and parametric uncertainty

At this stage we would ideally have three models: (1) A low-order state-space design model, (2) A high-order state-space evaluation model, and (3) a measured plant frequency response for each input and output of interest. Sometimes system identification experiments are not possible so that (3) is not available, and we must appeal to a finite element model (FEM) for models (1) and (2). This is true for SIM and NGST which will not be deployable in the Earth's gravity field.

2.2.3 Plant Coupling Analysis

Based on the physics of the plant the designer can decouple the control problem into a set of simpler problems. In this manner, a complex global control problem is cast into a set of more tractable, simpler control problems. Well designed systems can often be partially decoupled.

We can decouple a system in two principal ways:

1. *Input/output decoupling*: We select subsets of the sensor and actuator suites for control. For example in a spaceborne telescope we decouple the attitude control from the optical control. We assume that a sensor measures the local characteristics of the system and that an actuator controls locally. This is the principle behind collocated local control. A technique that provides a quantitative assessment of the sensors and actuators for local control is a contribution of the thesis and is developed in Chapter 3. Appendix A develops a technique for assessing the suitability of particular sensors for local/global state estimation.
2. *Dynamic decoupling*: We transform the A matrix to be approximately block diagonal whereby weak structural coupling is exhibited between subsystems. For example a local power plant can be controlled by assuming that it is

decoupled it from the power grid. [Mutambara, 1998] and [Hillier and Lieberman, 1995] provide techniques for dynamic decoupling.

In both cases the control designer must be careful to ensure stability by quantifying interaction of the local controllers.

2.2.4 Control Strategy Selection

The selection of a control strategy, such as H_2 or classical, is often driven by the requirements. The factors which drive the selection of a control strategy are enumerated below. The enumeration considers requirements, and represents the first stage in a requirements flow down from the problem statement to the controller synthesis.

1. *Ease of implementation.* Planned hardware may limit the structure (order and input/output topology), bandwidth or dynamic range of a controller. A quantitative trades between controller complexity and computation is an area to be researched.
2. *Inherent robustness.* Strategies with a built-in robustness (for example, linear quadratic regulator (LQR) and loop transfer recovery (LTR)) are desirable for critical applications where stability is the prime concern.
3. *Desired performance.* If performance is the prime design concern then optimal control strategies can be employed.
4. *Ease of stabilization.* Some systems, in particular those with nonminimum phase behavior prove to be difficult to stabilize. Methods which provide stability guarantees are favored in these instances.
5. *Heritage for applications.* Critical applications may require that a particular control strategy be employed (for example PID) because of a heritage of successful operation in similar systems.
6. *Ease of design tuning.* Certain control strategies are more easily tuned than others during successive iterations of the design process. For example, Sensitivity Weighted LQG (SWLQG) follows from a slight modification of the design matrices of an original LQG design [Grocott, 1994]. Another example includes the use of the Q parameterization to tune a model-based initial design [Lintereur, 1998 and Boyd and Barratt, 1991].
7. *Subsystem complexity.* The complexity of each subsystem in the decoupled system can drive compensator strategy selection. For example, simple SISO systems are easily controlled classically, but a complex MIMO subsystem, may require modern MIMO synthesis methods.

Table 2.2 is a non-exhaustive list of control strategies that have experimental *heritage* (with emphasis in the MIT SERC laboratory). We pay particular attention to *design tuning* opportunities. No detail of the strategies is provided here, though references to theoretical descriptions are provided.

2.2.5 Synthesizing Baseline Controller

When a control strategy has been selected, we now can synthesize a baseline controller. Different control strategies will require different amounts of designer interaction and input at this stage. Most strategies do not explicitly handle design constraints (with the exception of constrained optimization techniques [Boyd and Barratt, 1991]. Further, explicitly handling stability and performance robustness can also severely complicate the design, as in the D-K iteration of μ synthesis [Zhou et al., 1996]. In Table 2.2 we include a list of possible synthesis methods with the necessary designer inputs for each method.

Once the controller has been designed, we must reduce it to a size that can be implemented (most techniques do not allow a specific constraint of controller order and structure). Similar system reduction techniques were also used for modeling for control as discussed in Section 2.2.2.

2.2.6 Controller Evaluation

Now that a controller has been designed, its performance and stability robustness must be evaluated. In particular, the controller is checked to see if the design requirements are met. Evaluating the performance is difficult since w is by definition unknown. Typically, we appeal to statistical methods. For example, for a linear (stable) system we can determine the RMS performance and actuation use. Maximum noise amplification, $\|G_{zw}\|_{\infty}$, is often used as a metric. Typical simulation evaluation will include evaluating the controller on: (1) the control model, (2) the evaluation model, and (3) on measured system data (if available).

To determine the stability properties of the MIMO system a set of tools is used,

TABLE 2.2 Non-exhaustive list of control strategies with (mostly) MIT SERC experimental heritage

Control Technique	Design Inputs	Tuning Adjustments	Theoretical Description	Experiment Heritage
Classical filter design	shaped by design to meet specifications	gain, filter order, filter parameters	[Ogata, 1990]; [Van de Vegte, 1990]	[Masters, 1997]; [Mallory and Miller, 1999]
H_2 synthesis	control model, design weights	design weights	[Zhou et al., 1996]; [Kwakernaak and Sivan, 1972]	[Grocott et al., 1997]; [Lublin and Athans, 1995]
SWLQG[a]	control model, design weights, sensitivity weights	design weights, sensitivity weights. Used to tune H_2 design	[Grocott, 1994]	[Masters, 1997]; [Grocott et al., 1997]
Multiple model	set of control models, initial stabilizing controller	Tunes the initial stabilizing controller to minimize a cost over the set of models	[MacMartin et al., 1991]	[Grocott et al., 1997]
H_∞ synthesis	control model, design weights	design weights, γ[b]	[Zhou et al., 1996]	[Lublin and Athans, 1995]
μ synthesis	control model, design weights, uncertainty model	D-K iterations tunes successive H_∞ controllers	[Zhou et al., 1996]	[How, 1993] (Popov, real μ synthesis)
Constrained optimization	control model, initial stabilizing controller, expansion coefficients of Youla parameter[c]	expansion coefficients of Youla parameter	[Boyd and Barratt, 1991]; [Polak and Salcudean, 1989]	[Lintereur, 1998][d]

a. Sensitivity-Weighted Linear Quadratic Gaussian

b. as γ varies from a high value to a lower limit, the design goes from pure H_2 to pure H_∞

c. We expand the infinite dimensional Youla parameter with basis functions. The coefficients of the basis function in the expansion are termed expansion coefficients

d. Draper Laboratory experimental result

1. *Stability Determination.* (Section 2.1.4) To determine absolute stability, the MIMO Nyquist Criteria is used. For graphical purposes, we can plot, $L_n(j\omega)$ on a log-magnitude versus phase plot (called a Nichols plot) to determine absolute stability. Graphically, the closed-loop system is stable if and only if the number of number of left to right passes over critical points $(\exp(-j(1 \pm 2n)\pi)$, $n = 1, \ldots, \infty)$ is equal to the number of open-loop system unstable poles.

2. *Stability Robustness.* (Section 2.1.3) Once absolute stability has been determined, sensitivity to plant perturbations can be determined from the Sensitivity transfer matrix, $S(s)$, as detailed in Section 2.1.2. Equation 2.23 is a

condition for stability robustness, and Equations 2.25 and 2.26 provide Gain and Phase Margins based on $\bar{\sigma}$ (from Equation 2.24).

3. *Stability Robustness to parametric uncertainty.* The maximum singular values of $S(s)$ provides a conservative measure of the stability robustness to multiplicative uncertainty. To determine a less conservative measure of stability robustness to parametric uncertainty, the final controller designs should be evaluated with the structured singular value μ or with a similar analysis tool.

Both (1) and (2) are required since a system can be nearly singular without det(·) being close to zero, and the value of $\bar{\sigma}$ does not by itself determine stability. This set of stability tests has been used to evaluate stability performance of controllers [Grocott, 1994] and [Miller et al., 1996]. The third tool is required to capture the effect of parametric uncertainty in the frequency and the damping of the structural modes [Zhou et al., 1996 and How, 1993].

2.2.7 Controller Implementation

After the controller has been properly evaluated with simulation, it can be tested on a physical system. Key hardware issues and the advantages of physical control experiments are found in [Miller and Mallory, 1998] and [Bernstein, 1999]. The implementation hardware for control is found in Figure 2.7. Due to its common occurrence in modern control applications and its special hardware issues, a digital compensator is examined.

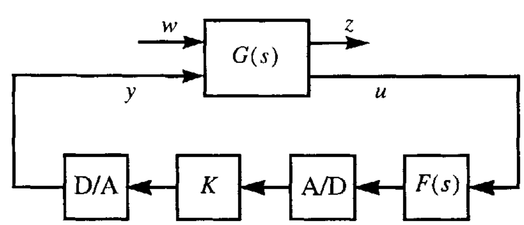

Figure 2.7 Control implementation hardware.

The system $G(s)$ is controlled by a discrete compensator K which is implemented on a computer. In this thesis, continuous compensators will be designed and then discretized for implementation. The plant is considered a continuous system with actuator inputs, u and sensor outputs, y. The computer receives analog signals through a bank of analog to digital converters (A/D) and generates analog control signals through a bank of digital to analog converters (D/A). The sampling A/D requires the use of antialiasing filters, $F(s)$

Time delay adds a unity-gain phase lag to the system, and must be accounted by the controller designer. Pade approximations allow delay to be modeled with the required fidelity. If a measurement model is to be used, then delay can be included in the model by including the A/D, control computer, and D/A in the identification loop.

The quantization of the A/D and D/A provide fundamental limits to the resolution of the system sensors and actuators. For example, a sensor with a range of ±10 V sampled with a 12 bit A/D, will be binned in 4 mV quanta. That is, if 12 bit quantization is used then it is not economic to purchase sensors with resolutions better than 4 mV. Quantization often determines the fundamental noise floor. The resolution of actuators is treated in an identical way. In an analogous fashion, quantization also provides a fundamental stroke/resolution trade. For example, if a force actuator is set up to have a 1 mN resolution then 12 bit quantization will limit the stroke to ±2 N. Improving the stroke or resolution requires higher resolution A/D and D/A converters or the use of multiple/staged actuators (sensors). For example a coarse actuator can be used for large stroke control, while a fine actuator is added to compensate for the coarse stage's quantization error. Quantization limits the dynamic range of the compensator. Quantization effects on the compensator, $K(z)$, are minimized if the full quantized range (i.e. ±10 V in the example above) is utilized. It is useful for the system, $G(s)$, to include variable gains on each of the sensor and actuator channels. Gain can then be distributed around the loop allowing the compensator to fill the quantized range. Frequency dependent sensor and actuator gains can further refine this gain distribution, showing that physical considerations can influence the selection of the gains and frequency characteristics of the sensors and actuators.

The compensator can be represented in state-space form as $\{A_c, B_c, C_c\}$. This form is non-unique and presents a trade between computational efficiency and numerical conditioning. For example, the compensator dynamics matrix A_c can be tridiagonalized, allowing sparse computation, whereas a numerically balanced realization tends to be fully populated. High gain and unstable compensators can kick the system with strong startup transients. In fact, unstable compensators can be very difficult to implement in practice.

When the controller is implemented, we can perform open-loop and closed-loop identification experiments to measure the performance and stability robustness properties. We can experimentally plot the multivariable Nichols plot and plot the maximum singular value of $S(s)$.

2.2.8 Controller Redesign and Tuning

Once the baseline controller has been designed and evaluated, if it is found to meet the design requirements then the control design is complete. More likely, certain requirements will not be met, and the controller will need to be tuned. Developing a controller tuning methodology is the focus of the remainder of the thesis. In the next section the tuning problem will be specified.

2.3 Problem Specification

Formally, now that notation had been defined, and a control design methodology has been described, we can specify the central problem that will be investigated in this thesis. We wish to provide a methodology for controller redesign should the original controller fail to meet requirements. In Figure 2.6 we consider the *controller redesign/tuning* block.

Problem 1: Given a plant, and a baseline stabilizing controller, $K_b(s)$, design a controller, $K(s)$ to,

$$\begin{aligned} \underset{K(s)}{\text{minimize}} \quad & J(K(s)) \\ \text{subject to} \quad & S_s(K(s)) < \alpha_S \\ & d(K(s) - K_b(s)) < d_{\max} \\ & |K_{ml}(j\omega)| < \alpha_{K,\,ml}(\omega) \end{aligned} \tag{2.32}$$

where $J(K(s))$ is the performance as an explicit function of the controller (dependent on the selected performance variables, z), $S_s(K(s))$ is a measure of the stability robustness of the closed loop, α_S is a requirement set on the stability robustness, $d(\cdot)$ is a distance metric relating the change of the tuned controller $K(s)$ to the baseline controller $K_b(s)$, $d_{\max}$ is the maximum allowed deviation from the baseline controller, $\|K_{ml}(j\omega)\|$ measures the gain of the ml-th control channel at frequency ω and $\alpha_{K,\,ml}(\omega)$ is a constraint on the gain magnitude of the ml-th control channel.

In words, we wish to tune the baseline controller to arrive at a tuned controller which improves the closed loop performance subject to satisfying: a stability robustness condition, a maximum deviation from the baseline control, and frequency-dependent controller-gain constraints. Alternately we may wish to improve the stability robustness subject to a performance constraint.

The tuning methodology is presented in Chapter 4 where definitions for the closed-loop cost, the stability robustness metric, deviation from baseline control metric and control channel gain metric will be presented. To make *problem 1* tractable the constraints are assumed soft and appended to an augmented cost. Further, the methodology results in a non convex nonlinear program which forces us to relax the problem statement to that of decreasing an augmented cost rather than finding a global minimum.

2.4 Summary

The general control problem is introduced. The MIMO extension of the SISO Nyquist stability robustness metric is explored and found to be necessary but not sufficient. Singular value analysis of the Sensitivity transfer matrix provides a conservative robust stability metric. In Chapter 4 these are combined to form a MIMO stability metric.

A control-design framework is detailed. The framework is based on successful control design experiments from the MACE program. Critical to the framework is the utilization of physics to determine if the plant can be decoupled to transform a global control problem into a set of simpler controllers. A tool for analyzing plant couplings is developed in Chapter 3. The control-design framework allows controller redesign if closed-loop requirements fail to be met or if certain controller characteristics are undesirable. A methodology for redesign based on controller tuning is proposed in Chapter 4. Further the tuning methodology allows the design to specify a general controller topology to take advantage of the natural system coupling as indicated by the application of the sensor/actuator indexing algorithm of Chapter 3.

Lastly, the central problem of this thesis research is formally specified in context of the control-design framework with the developed notation. The remainder of the thesis is devoted to solving the tuning problem and validating it with simulation and experiment..

Chapter 3

DECENTRALIZING THE CONTROL TOPOLOGY

In this chapter, a quantitative method is developed for decentralizing the control topology for controlling a dynamic system. The goal is to provide a tool for the designer which allows the control of a complex plant (many sensors and actuators) to be broken up into manageable local control loops each using subsets of the available sensors and actuators. The tool provides the control designer with a quantitative analysis of which sensors and actuators of the complex plant work together for effective control. A side result allows the designer to glean the penalty for neglecting sensor/actuator channels and determines the advantage of globalizing the control design. To maintain applicability to realistic plants, emphasis is placed on developing tools with good numerical robustness.

Linear controllers are assumed which can be written in state-space form as in Equation 2.5. In transfer function notation we can write the MIMO controller as a set of SISO transfer functions by

$$\begin{aligned} u_1 &= K_{11}y_1 + K_{12}y_2 + \ldots + K_{1n_y}y_{n_y} \\ u_2 &= K_{21}y_1 + K_{12}y_2 + \ldots + K_{2n_y}y_{n_y} \\ &\ldots \\ u_{n_u} &= K_{n_u1}y_1 + K_{n_u2}y_2 + \ldots + K_{n_un_y}y_{n_y} \end{aligned} , \tag{3.1}$$

where the K_{jk} SISO transfer function relates the k-th sensor to the j-th actuator. A constrained topology controller enforces that $K_{jk} = 0$ for certain sensor/actuator combinations. These topology constraints are useful since they may allow the global controller to be decentralized into a block diagonal form. The decentralized blocks can be designed loop-at-a-time, and implemented with decentralized real-time control computers.

The controller topology is often intuitively constrained by the large-scale control system designer. For example control for space telescopes is decoupled into (1) attitude control, with rate gyroscopes and star trackers as sensors and reaction wheels as actuators, and (2) optical control, with laser interferometers and wavefront tilt detectors as sensors and active optical elements as actuators. Typically the attitude control sensors will not provide information to the active optical elements. Topology constraints result in a loss of performance since global controllers are generally required for optimality (H_2 and H_∞).

In this chapter, a quantitative matrix linking each sensor to each actuator is computed from the system model. Large matrix entries correspond to sensor/actuator channels that are effective for control. The sensor/actuator linking matrix is proposed as a design tool to aid in the controller topology selection. Further utility of the sensor/actuator linking matrix allows the designer to observe the benefit of providing additional sensors information, or additional actuators to a decentralized local controller. Additional applications of the technique includes sensor and actuator placement (as opposed to selection) for control design and system identification.

[Mercadal, 1991] provides H_2 optimal first-order necessary conditions for block diagonal controller topologies. The necessary conditions are extended to the general topology case in Appendix B of this thesis. An optimization problem can be visualized where the H_2 cost is appended with a term to penalize the number of non-zero sensor/actuator channels. In practice, the constrained topology H_2 optimal controllers prove difficult to synthesize. In [Mallory and Miller, 2000] and Appendix A the closed-loop sensor evaluation problem is examined where the ability of each sensor to H_2 optimally estimate each of the system states is determined by a solution of a Riccati Equation. The dual LQR, actuator-at-a-time evaluation problem can be solved but the combination problem of grouping sensors and actuators in this context has proven to be difficult.

In [Kim and Junkins, 1991] controllability measures are combined with modal cost analysis [Skelton and Hughes, 1980] to place actuators with a strategy that accounts for disturbance and performance characteristics. In this chapter, a technique is presented which extends [Kim and Junkins, 1991] to the sensor problem, and then combines sensors and actuators to account for their joint action as a controller channel. Active isolation of uncontrollable modes from the performance is captured with the proposed technique.

The chapter begins with a section on preparing the model through proper scaling and model reduction. A technique to compute a sensor/actuator linking matrix based on performance weighted and disturbance weighted measures of the system's modal observability and controllability is developed and then refined to capture the potential of active output isolation. The algorithm is outlined and then applied to a model of an experiment taken from the actuator placement literature.

3.1 Model Preparation

Model-based control design requires the use of a design model. The order of the model should be small but capture the important dynamics, and the model should be input / output scaled to avoid numerical difficulties. Scaling should also capture the relative goodness of sensors and actuators relative to their respective sensor and actuator noises.

3.1.1 System Input/Output Scaling

Dynamic models of a plant are often presented with little attention to numerical conditioning. For example, sensors which measure nanometers are presented with a measurement in the units of meters, inducing a 10^{-9} scaling. Other sensors may, for example, measure angles of degrees with measurements in units of arcseconds, inducing a 3600 scaling. During nominal operation, the numeric output of these two sensors varies by over 12 orders of magnitude. The large deviation in the nominal measures from the sensors (and analogously from performance measures) causes numeric conditioning problems, and does not allow a fair comparison to determine each sensor's importance for a control objective, or for model reduction. Dual arguments hold for the actuators and disturbances. These problems motivate scaling the design plant.

Output Scaling

We assume the global design model is provided in the form of Equation 2.3 where, for convenience, all feedthrough terms are assumed to be zero. With the model, we are presented with n_y sensor resolutions, one for each sensor represented in C_y, as elements of the $n_y \times 1$ vector, R_y. For example, consider an interferometer with the i-th sensor measuring units of meters with a resolution of 1 nanometer then we have $R_y(i) = 10^9$. Similarly, we are presented with a $n_z \times 1$ vector of RMS performances, R_z.

To scale the sensors, we normalize the i-th sensor according to,

$$\bar{C}_{y,i} = R_y(i)C_{y,i} \tag{3.2}$$

where $C_{y,i}$ is the i-th row of C_y, and $\bar{C}_{y,i}$ is the i-th row of the corresponding scaled output matrix. In this manner, the sensors are scaled such that their resolution corresponds to a unity measure. All sensors can then be fairly compared in terms of their resolution.

To scale the performances, we employ a similar rule for the i-th performance,

$$\bar{C}_{z,i} = R_z(i)C_{z,i} \tag{3.3}$$

where $C_{z,i}$ is the i-th row of C_z, and $\bar{C}_{z,i}$ is the i-th row of the corresponding scaled output matrix. Thus performances are scaled such that the requirement is met by having an RMS performance of unity for each performance metric. All performances can then be fairly compared in terms of their requirements. Further, by invoking a design rule that sensors require a resolution on the order of ten times smaller than their closed-loop requirement we see that we can compare sensors and performances fairly (to within a factor of approximately 10).

Input Scaling

In a similar manner we scale the actuator input matrix B_u, and the disturbance input matrix, B_w. For scaling actuator inputs we use

$$\bar{B}_{u,i} = R_u(i)B_{u,i} \tag{3.4}$$

where $R_u(i)$ is the actuator resolution of the i-th actuator and $B_{u,i}$ corresponds to the i-th column of the B_u matrix. $R_u(i)$ is set such that an input measure of unity corresponds to the resolution of the actuator. For example if the i-th input of the nominal model expects force inputs in units of Newtons, and the resolution of the actuator is 1 mN, then $R_u(i) = 1000$. The resolution of an actuator depends of the actuator noise. Actuator noise enters the system at the actuator and corresponds to an error in the commanded control signal. An obvious source of actuator noise is quantization error, as discussed in Section 2.2.7. Actuator noise is not the LQR dual of Kalman filter sensor noise.

Similarly we scale the disturbance inputs as

$$\bar{B}_{w,i} = R_w(i)B_{w,i} \tag{3.5}$$

where $R_w(i)$ is chosen such that the true disturbance corresponds to a unit intensity white noise. The disturbance dynamics are assumed integrated with the model (pre-whitened) [Peebles, 1987].

The scaling can be represented pictorially as seen in Figure 3.1. Overbar quantities correspond to the scaled system where an identity covariance of $\bar{w}$ is the anticipated noise intensity, unity measures of $\bar{u}$ are the actuator resolutions, unity measures of $\bar{y}$ are sensor resolutions, and identity covariance of $\bar{z}$ is the performance requirement.

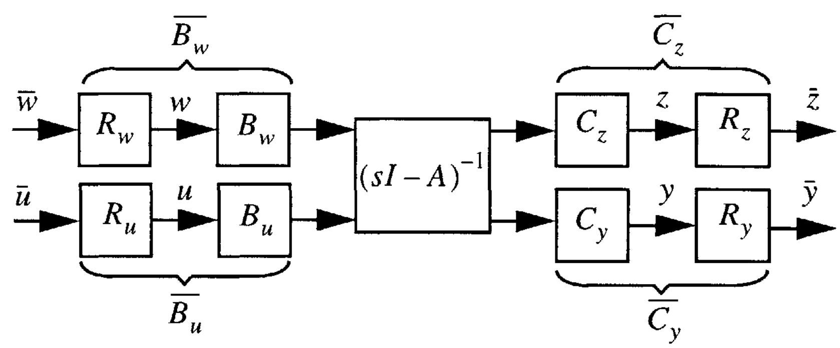

Figure 3.1 Scaling the design model for control design

Note that the designer must be aware of the scaling values, R_y, R_z, R_w, and R_u, since any controller designed with the scaled plant will need to be scaled in an inverse manner before the controller can be applied to the physical plant. Also, the proper representation of the units can be restored for analysis purposes.

3.1.2 Model Reduction

Prohibitively large models need to be reduced for controller synthesis since large models result in (1) numerical robustness and computational difficulties, and (2) large-order controllers. Balanced reduction is an accepted method for reducing the order of a model [Moore, 1981]. Ironically, the computation of a balanced realization for the large order model to be reduced can be computationally prohibitive and numerically unstable. In this section a numerically stable computation of the balanced realization is developed.

Balanced Reduction

Balanced realizations transform the system to normalize the influence of the inputs and outputs on the system states. In the balanced system, states which are marginally observable will be marginally controllable and they can be truncated to reduce the order of the system. We examine the procedure for balancing the system

$$\begin{aligned} \dot{x} &= Ax + Bu \\ y &= Cx \end{aligned} \tag{3.6}$$

as presented in [Zhou et al., 1996] to determine shortcomings of balanced reduction.

We assume the system is stable and minimal, and solve

$$AL_c + L_c A^T + BB^T = 0 \tag{3.7}$$

for the controllability Gramian L_c, and

$$A^T L_o + L_o A + C^T C = 0 \tag{3.8}$$

for the observability Gramian L_o.

Since the system is minimal and stable, the unique Gramians can be found, and are both positive definite. We use a singular value decomposition on L_c to write,

$$L_c = U_c \Lambda_c U_c^T. \tag{3.9}$$

The elements of diagonal matrix Λ_c are the sorted controllability singular values of the unbalanced system such that

$$\Lambda_c = \mathrm{diag}\{\sigma_{c1}, \sigma_{c2}, \ldots, \sigma_{cN}\} \tag{3.10}$$

with $\sigma_{ci} \geq \sigma_{cj}$ for $i > j$. Large singular values represent linear combinations of states which are highly controllable, and small singular values represent linear combinations of states which are slightly controllable. Slightly controllable states may still be important since they may be highly observable.

Similarly, a singular value decomposition is used on $U_c \Lambda_c^{\frac{1}{2}} L_o \Lambda_c^{\frac{1}{2}} U_c^T$ to write,

$$U_c \Lambda_c^{\frac{1}{2}} L_o \Lambda_c^{\frac{1}{2}} U_c^T = U_b \Lambda_b^2 U_b^T. \tag{3.11}$$

where the elements of the diagonal matrix Λ_b are such that

$$\Lambda_b = \mathrm{diag}\{\sigma_{b1}, \sigma_{b2}, \ldots, \sigma_{bN}\} \tag{3.12}$$

with $\sigma_{bi} \geq \sigma_{bj}$ for $i > j$.

We form a square transformation matrix T_b using,

$$T_b = \Lambda_b^{\frac{1}{2}} U_b^T U_c \Lambda_c^{\frac{1}{2}}. \tag{3.13}$$

The inverse can be directly computed using

$$T_b^{-1} = \Lambda_c^{-\frac{1}{2}} U_c^T U_b \Lambda_b^{-\frac{1}{2}}. \tag{3.14}$$

With this transformation we have a balanced system given by $A_b = T_b A T_b^{-1}$, $B_b = T_b B$, $C_b = C T_b^{-1}$. The controllability and observability Gramians become, $L_{cb} = T_b L_c T_b^T = \Lambda_b$ and $L_{ob} = T_b^{-T} L_o T_b^{-1} = \Lambda_b$. The elements of the balanced controllability and observability Gramian, Λ_b are the Hankel singular values.

The computation of the inverse of the transformation induces numerical difficulties since it requires inverting (1) the unbalanced controllability singular values, and (2) the Hankel singular values. The numerical conditioning is made poor by the inversion of the small singular values which we later intend to truncate. A technique which truncates during the balancing operation proves to be more numerically robust, and allows reduced-order models of flexible space structures to be computed when standard balanced reduction fails.

Numerically Robust Balanced Reduction

To make the balanced reduction more numerically robust we divide the reduction into two steps: (1) pre-balancing, and (2) balanced truncation.

Pre-balancing

In the balanced truncation step, we will be removing states which we find to be slightly controllable. The implicit assumption is that those states are not strongly observable. To ensure this, we apply a pre-balancing operation which balances the input/output of each mode.

To apply pre-balancing, we first transform the system into a modal form [Grocott, 1994]. We then balance the input/output of each complex-conjugate eigenvalue pair, and in the case of real eigenvalues each Jordan block, by considering the system part corresponding to those eigenvalues individually. Pre-balancing modes that are entirely uncontrollable and/or unobservable is numerically ill conditioned but since these modes will later be removed we need not pre-balance them.

Balanced truncation

The balanced truncation removes slightly controllable and slightly observable states as the system is balanced to maintain good numerical conditioning. The method is similar to replacing the inversions required in Equation 3.13 with a pseudo-inverse of T_b but allows the designer additional insight and direct manipulation of tolerances for removal of singular values.

We begin by approximating the decomposition of Equation 3.9 for the pre-balanced system by writing,

$$L_c \approx U_c \overline{\Lambda_c} U_c^T \tag{3.15}$$

where U_c follows from Equation 3.9 and $\overline{\Lambda_c}$ is a diagonal matrix of sorted singular values formed by keeping diagonal elements of Λ_c which are greater than a specified tolerance, and setting other elements to 0,

$$\overline{\Lambda_c} = \mathrm{diag}\{\sigma_{c1}, \sigma_{c2}, \ldots, \sigma_{cm}, 0, \ldots, 0\} \tag{3.16}$$

where $\sigma_{cj} < \mathrm{tol}_c, \forall j > m$. This action effectively removes linear combinations of states which are less controllable than the threshold set by tol_c. The pre-balancing operation ensures none of the removed states are highly observable. $\overline{\Lambda_c}^\dagger$ is the pseudo-inverse of Λ_c, formed by

$$\overline{\Lambda_c}^{\dagger} = \operatorname{diag}\left\{\frac{1}{\sigma_{c1}}, \frac{1}{\sigma_{c2}}, \ldots, \frac{1}{\sigma_{cm}}, 0, \ldots, 0\right\}. \tag{3.17}$$

We perform a similar operation on Λ_b, by rewriting Equation 3.13 as

$$U_c\Lambda_c^{\frac{1}{2}}L_o\Lambda_c^{\frac{1}{2}}U_c^T \approx U_b\overline{\Lambda_b}^2U_b^T \tag{3.18}$$

where,

$$\overline{\Lambda_b} = \operatorname{diag}\{\sigma_{b1}, \sigma_{b2}, \ldots, \sigma_{bq}, 0, \ldots, 0\}, \tag{3.19}$$

where $\sigma_{bj} < \mathrm{tol}_b, \forall j > q$. We form a pseudo-inverse of $\overline{\Lambda_b}$ using

$$\overline{\Lambda_b}^{\dagger} = \operatorname{diag}\left\{\frac{1}{\sigma_{b1}}, \frac{1}{\sigma_{b2}}, \ldots, \frac{1}{\sigma_{bq}}, 0, \ldots, 0\right\}. \tag{3.20}$$

To reduce the chance of removing a slightly controllable but highly observable state, we choose $\mathrm{tol}_b < \mathrm{tol}_c$ so that $q < m$. We then form a truncation matrix,

$$T_t = \begin{bmatrix} I_{q\times q} & 0_{q\times(n-q)} \end{bmatrix}. \tag{3.21}$$

The balanced truncation transformation is performed with the transformation matrix,

$$\overline{T_b} = T_t\overline{\Lambda_b}^{\frac{1}{2}}U_b^TU_c\overline{\Lambda_c}^{\frac{1}{2}}, \tag{3.22}$$

and the (pseudo) inverse transformation,

$$\overline{T_b}^{\dagger} = (\overline{\Lambda_c}^{\dagger})^{\frac{1}{2}}U_c^TU_b(\overline{\Lambda_b}^{\dagger})^{\frac{1}{2}}T_t^T. \tag{3.23}$$

The n-the order system is reduced to a balanced system of order q by transforming the system as $\overline{A_b} = \overline{T_b}A\overline{T_b}^{\dagger}$, $\overline{B_b} = \overline{T_b}B$, $\overline{C_b} = C\overline{T_b}^{\dagger}$, and $\overline{D_b} = D$. The controllability and observability Gramians become, $\overline{L_{cb}} = \overline{L_{ob}} = \overline{\Lambda_{br}}$ where

$$\overline{\Lambda_{br}} = \mathrm{diag}\{\sigma_{b1}, \sigma_{b2}, \ldots, \sigma_{bq}\} \tag{3.24}$$

are the Hankel singular values of the balanced and reduced system. We use the truncation operator to ensure that the $q+1$-th through n-th states are removed since our singular value truncation in forming $\overline{\Lambda_c}$ and $\overline{\Lambda_b}$ cause those higher states to lose accuracy.

Figure 3.2 is a plot of the transfer function of a channel from the reaction wheel disturbance to an internal optical pathlength measure for a model of the SIM spacecraft. The SIM model is further detailed in Chapter 7. Conventional balancing routines fail with the SIM model. The numerically robust balancing routine is able to balance the system whilst removing some uncontrollable/unobservable states. In the figure a 176 reduced order model agrees almost perfectly with the 270 state original model

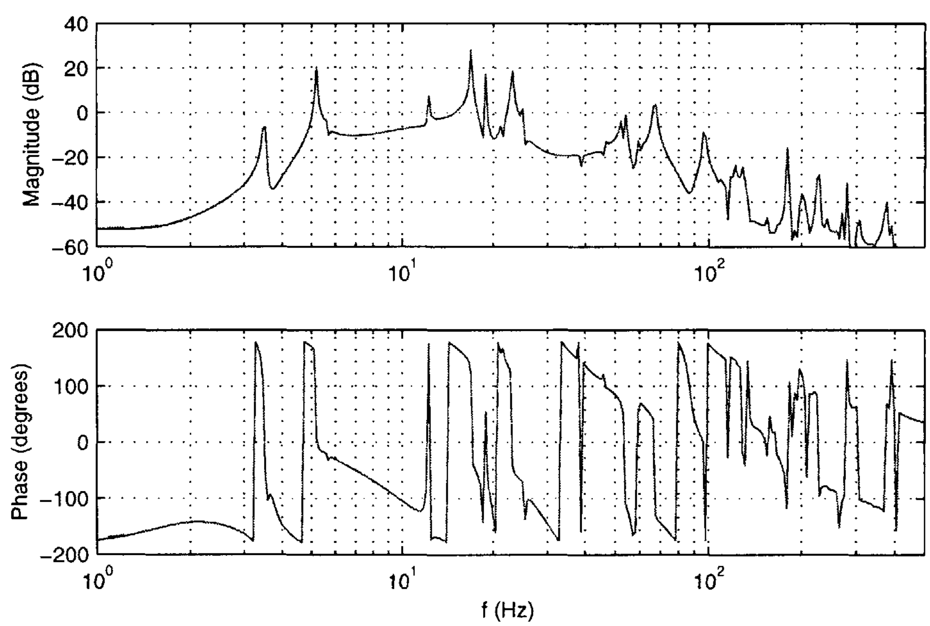

Figure 3.2 Channel transfer function of a balanced model. Phase is wrapped for plotting purposes. The 176 state balanced model (dashed) overlays the 270 state original model (solid). Without the numerically robust balancing technique the SIM model could not be balanced.

3.2 Controllability and Observability Based Technique

In this section, controllability and observability are used for the derivation of an index which quantifies the suitability of specific sensors and actuators for effective control. The four block regulation problem of Figure 2.1 and Equation 2.1 is considered. The selected strategy is open-loop which limits its use for predicting the effect of closed-loop control. The strategy uses H_2 modal costs in its development which indicates that it is best suited for determining the suitability of sensors and actuators for LQG control. The controllability is weighted to reflect the performance variables, z, and the observability is weighted to reflect the disturbance characteristics, w. These weighting are determined with H_2 norms which implicitly ties the technique to H_2 control. In Section 3.4 a flow diagram of the complete technique is presented that includes a patch to account for active output isolation.

3.2.1 A Measure of Controllability and Observability

Generally, controllability and observability is considered a binary yes/no characteristic of a system. The most well known test involves determining the rank of the Gramians of Equations 3.7 and 3.8. The loss in rank of the controllability Gramian corresponds to the number of uncontrollable states, and likewise, the loss in rank of the observability Gramian corresponds to the number of unobservable states. These tests depend on the realization of the system: in general a controllable system with unobservable states can be made observable and uncontrollable through an invertible state transformation. We begin with the development of an alternate test for controllability and observability.

For the system given by Equation 2.3, if we assume n-th order A has eigenvalues, $\{\lambda_i, i = 1, \ldots, n\}$ with a set of right eigenvectors $\{Ap_i = \lambda_i p_i, i = 1, \ldots, n\}$, and a set of left eigenvectors, $\{q_i^T A = \lambda_i q_i^T, i = 1, \ldots, n\}$. We consider a case where all eigenvalues have equal algebraic and geometric multiplicity with the exception of rigid-body modes. We normalize the eigenvectors to be biorthogonal,

$$q_i^H p_j = \delta_{ij}. \tag{3.25}$$

For the Popov, Belevitch and Hautus (PBH) eigenvector controllability test we note that the i-th state is uncontrollable if and only if

$$q_i^H B_u = 0. \tag{3.26}$$

Similarly, the i-th mode is unobservable if and only if

$$C_y p_i = 0. \tag{3.27}$$

Again, this test is of the yes/no type. A measure of controllability and observability is proposed in [Hamdan and Nayfeh, 1989]. For the i-th state's controllability from the j-th actuator we define,

$$f_{i,j} = \frac{q_i^H B_j}{\|q_i\|}, \tag{3.28}$$

which corresponds to the cosine of the angle between the i-left eigenvector and the j-th actuator, scaled by the magnitude of the actuator input column. Intuitively, the alignment of q_i and B_j corresponds to the efficiency with which the actuator can pump energy into the i-th state. The magnitude of B_j has been scaled in Section 3.1.1 with respect to the actuator noise such that the actuator's signal-to-noise ratio is captured. The larger the value of $\|f_{i,j}\|$, the larger the influence of the j-th actuator on the i-th state.

Following dual arguments, a measure of observability for the i-th mode from the k-th sensor can be defined as,

$$h_{i,k} = \frac{C_k p_i}{\|p_i\|}, \tag{3.29}$$

where C_k is the k-th row of C_y.

In the case of distinct eigenvalues we can expand the transfer matrix, $G_{yu}(s)$ as

$$G_{yu}(s) = \sum_{i=1}^{n} \frac{R_i}{s - \lambda_i} \tag{3.30}$$

where the residue matrix R_i is given by

$$R_i = C_y p_i q_i^T B_u \tag{3.31}$$

where the (k, j) element correspond to the k-th sensor and j-th actuator. We substitute Equations 3.28 and 3.29 to arrive at

$$\|R_i(k, j)\| = \frac{\|f_{i,j}\| \|h_{i,k}\|}{\|p_i\| \|q_i\|}. \tag{3.32}$$

Now in the special case where the eigenvalues are normalized by $\|p_i\| = \|q_i\| = 1$ we have

$$\|R_i(k, j)\| = \|f_{i,j}\| \|h_{i,k}\|. \tag{3.33}$$

The residues of the system are an input/output characteristic of the system and are invariant with respect to system state realization. Thus Equation 3.33 is invariant of realization. In this section have defined a measure of the controllability and observability and introduced an invariant method to combine these measures in terms of the design model's residues.

3.2.2 Modal Cost Analysis

The measures of controllability and observability, Equations 3.28 and 3.29, do not alone provide an assessment of the suitability of the actuators and sensors for the four block regulation problem. Additionally, the effect of the disturbance inputs through B_w, and performance variables through C_z, should be captured in the problem of assigning sensor and actuator sets for control. Following the [Kim and Junkins, 1991] treatment of actuator placement, the modal cost analysis of [Skelton and Hughes, 1980] can be used to weight the modal controllability and observability by the design model's modal disturbance and performance features.

Assuming a separation property holds we examine the modal cost properties of the full-information control problem and the state estimation problem separately. Given zero feedthrough matrix in Equation 2.3 the important system dynamics for the full information control system reduces to

$$\begin{aligned} \dot{x} &= Ax + B_u u \\ z &= C_z x \end{aligned} . \tag{3.34}$$

The open-loop cost is written as

$$J = \mathrm{tr}[XC_z^T C_z] \tag{3.35}$$

where

$$AX + XA^T + B_u B_u^T = 0 . \tag{3.36}$$

The cost function of the i-th state can be written as

$$J_i = [XC_z^T C_z]_{ii} . \tag{3.37}$$

Clearly

$$J = \sum_{i=1}^{n} J_i . \tag{3.38}$$

In the special case where the system is in a modal form the state costs, J_i are the modal costs. Intuitively, the input state costs, J_i, are large for states that make a large contribution to the performance cost and are stimulated by the actuators.

The dual, estimator problem uses

$$\begin{aligned} \dot{x} &= Ax + B_w w \\ y &= C_y x \end{aligned} \tag{3.39}$$

as the subset of Equation 2.3's dynamics. The open-loop cost can be written as

$$V = \mathrm{tr}[B_w B_w^T Y], \tag{3.40}$$

where

$$YA + A^T Y + C_y^T C_y = 0. \tag{3.41}$$

The cost of the i-th state can be written as,

$$V_i = [B_w B_w^T Y]_{ii}. \tag{3.42}$$

The output state costs are large for states that are both stimulated by the disturbance and measured by the sensors.

The solution of Lyapunov Equations 3.36 and 3.41 require an open-loop stable system. The more difficult approximations for the modal costs in the case of closed-loop systems are derived in [Skelton and DeLorenzo, 1983].

3.2.3 Combining the Controllability and Observability Measures

The measures of controllability and observability from Section 3.2.1 will be weighted by the modal costs of Section 3.2.2 to arrive at performance and disturbance weighted index of sensors/actuator groupings.

To apply the modal cost analysis, the plant must be stable. This requires careful manipulation and treatment of the rigid-body modes of flexible space structures. A technique will be applied to combine the weighted controllability and observability measures to assign each sensor/actuator grouping with an index. The larger the index, the more suited will be that sensor/actuator combination for control.

Rigid-Body Mode Manipulation

The modal cost analysis used in this work requires stable dynamics for the solution. A passive structure, such as an open-loop flexible space structures, will have stable, lightly-damped dynamics with the exception of rigid-body (RB) translation and rotation in three axes. We will choose to operate on RB modes separately when we scale and reduce the system. As such we require an efficient method to remove and replace RB modes.

To operate on the RB modes, first we transform the state-space system into a real block diagonal form. [Grocott, 1994] has a comprehensive treatment of the necessary transformation matrices. Complex modes are transformed into two-by-two A matrix blocks of the form

$$A_{rm}^{b} = \begin{bmatrix} -\zeta\omega & \omega\sqrt{1-\zeta^2} \\ -\omega\sqrt{1-\zeta^2} & -\zeta\omega \end{bmatrix}, \tag{3.43}$$

real modes are diagonalized as

$$A_{r}^{b} = -\lambda. \tag{3.44}$$

The multiple RB modes in a flexible spacecraft cause the system to be defective (each RB mode has a second order Jordan block) and derogatory (three translations and three rotations induce six 0 eigenvalues in the dynamics matrix), so care must be taken in the transformation [Horn and Johnson, 1985]. The resulting two-by-two rigid-body blocks are written as

$$A_{rb}^{b} = \begin{bmatrix} 0 & 1 \\ 0 & 0 \end{bmatrix}. \tag{3.45}$$

In this system we stack the rigid-body blocks in the top left diagonal, followed by the stable complex mode blocks, and then stable real states are included at the bottom right diagonal.

For a spaceborne telescope all rigid body translations will be unobservable for all sensors, and all performance metrics. Translational rigid bodies can be immediately truncated. The resulting system can be written as

$$\begin{aligned} \begin{bmatrix} \dot{x}_{RB} \\ \dot{x}_f \end{bmatrix} &= \begin{bmatrix} A_{RB} & 0 \\ 0 & A_f \end{bmatrix} \begin{bmatrix} x_{RB} \\ x_f \end{bmatrix} + \begin{bmatrix} B_{RBw} \\ B_{fw} \end{bmatrix} w + \begin{bmatrix} B_{RBu} \\ B_{fu} \end{bmatrix} u \\ \begin{bmatrix} z \\ y \end{bmatrix} &= \begin{bmatrix} C_{RBz} & C_{fz} \\ C_{RBy} & C_{fy} \end{bmatrix} \begin{bmatrix} x_{RB} \\ x_f \end{bmatrix} \end{aligned} , \tag{3.46}$$

where $(\cdot)_{RB}$ denotes the rotational rigid body dynamics, and $(\cdot)_f$ denotes the stable dynamics. The first n_{RB} states correspond to the n_{RB} rigid body states. By introducing the $n_{RB} \times n$ truncation operator

$$T_{RB} = \begin{bmatrix} I_{n_{RB} \times n_{RB}} & 0_{n_{RB} \times (n - n_{RB})} \end{bmatrix} \tag{3.47}$$

we can pick off the RB states using

$$x_{RB} = T_{RB} x . \tag{3.48}$$

We can form a state-space representation of the RB dynamics using, $A_{RB} = T_{RB} A T_{RB}^T$, $B_{RBw} = T_{RB} B_w$, $B_{RBu} = T_{RB} B_u$, $C_{RBz} = C_z T_{RB}^T$, $C_{RBy} = C_y T_{RB}^T$.

Similarly by defining the truncation operator

$$T_f = \begin{bmatrix} 0_{(n - n_f) \times n_f} & I_{(n - n_f) \times (n - n_f)} \end{bmatrix} \tag{3.49}$$

we can extract the non-RB states with

$$x_f = T_f x \tag{3.50}$$

and form a state-space representation of the stable non-RB dynamics using $A_f = T_f A T_f^T$, $B_{fw} = T_f B_w$, $B_{fu} = T_f B_u$, $C_{fz} = C_z T_f^T$, $C_{fy} = C_y T_f^T$.

If the states are not ordered with $x = \begin{bmatrix} x_{RB}^T & x_f^T \end{bmatrix}^T$, the truncation operators can still be used, but lose their simple forms of Equations 3.47 and 3.49. The use of the truncation operator is introduced since (1) it allows a mathematically clean operation for picking-off states, and (2) it can be used in an inverse manner to recombine the RB states, x_{RB}, and non-RB states, x_f into a single system.

Computing Modal Costs

We wish to determine the modal costs for each actuator and each sensor. For the input state cost of the j-th actuator we solve

$$AX_j + X_jA^T + B_{u,j}B_{u,j}^T = 0. \tag{3.51}$$

and form a n dimensional cost vector,

$$\underline{J}_j = \begin{bmatrix} J_{1,j} \\ J_{2,j} \\ \vdots \\ J_{n,j} \end{bmatrix} = \begin{bmatrix} [X_jC_z^TC_z]_{11} \\ [X_jC_z^TC_z]_{22} \\ \vdots \\ [X_jC_z^TC_z]_{nn} \end{bmatrix}. \tag{3.52}$$

In the presence of rigid body modes, the solution of Equation 3.51 is not well defined. With the partitioning of Equation 3.46, we can write a set of equations:

$$A_fX_{fj} + X_{fj}A_f^T + B_{fu,j}B_{fu,j}^T = 0 \tag{3.53}$$

$$A_{RB}X_{RBj} + X_{RBj}A_{RB}^T + B_{RBu,j}B_{RBu,j}^T = 0 \tag{3.54}$$

$$A_{RB}\overline{X_{Cj}} + \overline{X_{Cj}}A_f^T + B_{RBu,j}B_{fu,j}^T = 0 \tag{3.55}$$

where

$$X_j = \begin{bmatrix} X_{RBj} & \overline{X_{Cj}} \\ \overline{X_{Cj}}^T & X_{fj} \end{bmatrix}. \tag{3.56}$$

A_f is stable such that Equation 3.53 has a unique solution. Since the eigenvalues of A_{RB} and A_f are never equal, $\lambda_i(A_{RB}) = 0 \neq \lambda_k(A_f)$, then the Sylvester Equation 3.55 also has a unique solution for $\overline{X_{Cj}}$.

The solution for Equation 3.54 is ill-defined due to the non-stable rigid-body modes. To rectify this we replace the two-by-two blocks of Equation 3.45 by blocks

$$A^b_{drb} = \begin{bmatrix} 0 & 1 \\ -\omega^2_{RB} & -\sqrt{2}\omega_{RB} \end{bmatrix} \tag{3.57}$$

in the matrix A_{RB} to form a matrix A_{dRB}. These blocks correspond to a critically damped, $\zeta = 0.707$, mode at a frequency of ω_{RB} radians per second. ω_{RB} is chosen to be much smaller then the lowest frequency pole of A_f. To transform our artificially stabilized system into a real modal form as given by Equation 3.43, we use the transformation matrix for each mode,

$$T_\omega = \begin{bmatrix} 1 & 0 \\ 1 & \dfrac{-\sqrt{2}}{\omega_{RB}} \end{bmatrix} \tag{3.58}$$

and form a transformation matrix,

$$T_{mRB} = \begin{bmatrix} T_\omega & 0 & 0 \\ 0 & T_\omega & 0 \\ 0 & 0 & T_\omega \end{bmatrix} \tag{3.59}$$

which is a block diagonal matrix with a T_ω on each block corresponding to each RB mode. We transform the RB dynamics using, $A_{mRB} = T_{mRB}A_{dRB}T^{-1}_{mRB}$,

$B_{mRBw} = T_{mRB}B_{RBw}$, $B_{mRBu} = T_mB_{RBu}$, $C_{mRBz} = C_{RBz}T_{mRB}^{-1}$, $C_{mRBy} = C_{RBy}T_{mRB}^{-1}$. The RB system has been artificially stabilized and transformed to a modal form.

The full system now resembles,

$$\begin{aligned} \begin{bmatrix} \dot{x}_{mRB} \\ \dot{x}_f \end{bmatrix} &= \begin{bmatrix} A_{mRB} & 0 \\ 0 & A_f \end{bmatrix}\begin{bmatrix} x_{mRB} \\ x_f \end{bmatrix} + \begin{bmatrix} B_{mRBw} \\ B_{fw} \end{bmatrix} w + \begin{bmatrix} B_{mRBu} \\ B_{fu} \end{bmatrix} u \\ \begin{bmatrix} z \\ y \end{bmatrix} &= \begin{bmatrix} C_{mRBz} & C_{fz} \\ C_{mRBy} & C_{fy} \end{bmatrix}\begin{bmatrix} x_{mRB} \\ x_f \end{bmatrix} \end{aligned}, \tag{3.60}$$

To be consistent with the notation of Equation 2.3 we have a realization with

$$\begin{gathered} A = \begin{bmatrix} A_{mRB} & 0 \\ 0 & A_f \end{bmatrix}, B_w = \begin{bmatrix} B_{mRBw} \\ B_{fw} \end{bmatrix}, B_u = \begin{bmatrix} B_{mRBu} \\ B_{fu} \end{bmatrix}, \\ C_z = \begin{bmatrix} C_{mRBz} & C_{fz} \end{bmatrix}, C_y = \begin{bmatrix} C_{mRBz} & C_{fz} \end{bmatrix} \end{gathered} \tag{3.61}$$

Equation 3.54 is transformed to

$$A_{mRB}X_{mRBj} + X_{mRBj}A_{mRB}^T + B_{mRBu,j}B_{mRBu,j}^T = 0 \tag{3.62}$$

which has a unique solution, X_{mRBj}. Further, we rewrite Equation 3.55 as

$$T_{mRB}A_{RB}T_{mRB}^{-1}T_{mRB}\overline{X_{Cj}} + T_{mRB}\overline{X_{Cj}}A_f^T + T_{mRB}B_{RBu,j}B_{fu,j}^T = 0 \tag{3.63}$$

which justifies a transformed $X_{Cj} = T_{mRB}\overline{X_{Cj}}$ for a ω_{RB} parameterized solution. The complete Lyapunov Equation 3.51 solution is given by,

$$X_{mj} = \begin{bmatrix} X_{mRBj} & X_{Cj} \\ X_{Cj}^T & X_{fj} \end{bmatrix}, \tag{3.64}$$

where the RB modes have been stabilized by the ω_{RB} parameter, and the RB state-space dynamics have been transformed to a modal form (see Equation 3.58). The designer varies

ω_{RB} to weight the rigid-body control, the lower the value of ω_{RB}, the more emphasis is placed on sensors (actuators) that observe (control) RB modes. Solving the Lyapunov Equation 3.51 by breaking into sub-equations is advantageous since (1) Equation 3.53 is independent of ω_{RB} and needs only to be solved once, (2) Equation 3.55 is independent of ω_{RB} and needs only to be solved once to arrive at $\overline{X_{Cj}}$ which can be transformed by the simple transformation, T_{mRB}, and (3) Equation 3.54 is small, $n_{RB} \times n_{RB}$, and can be directly solved. To vary ω_{RB}, we need only a matrix multiplication and a $n_{RB} \times n_{RB}$ Lyapunov equation solution. Decoupling Equation 3.51 also eliminates the numeric difficulties which arise from an A matrix with very small eigenvalues, (on the order of ω_{RB}), and large eigenvalues (the higher structural modal frequencies).

Our modal cost analysis also requires the dual Lyapunov equation,

$$Y_k A + A^T Y_k + C_{y,k}^T C_{y,k} = 0 \tag{3.65}$$

be solved for each sensor, $\{k = 1, \ldots, n_y\}$. We form a n dimensional cost vector,

$$\underline{V_k} = \begin{bmatrix} V_{1,k} \\ V_{2,k} \\ \cdots \\ V_{n,k} \end{bmatrix} = \begin{bmatrix} [B_w B_w^T Y_k]_{11} \\ [B_w B_w^T Y_k]_{22} \\ \cdots \\ [B_w B_w^T Y_k]_{nn} \end{bmatrix}. \tag{3.66}$$

Using the partitioned and transformed system from Equations 3.60 and 3.61, we decouple Equation 3.65 into two Lyapunov Equations and a Sylvester Equation and for a solution given by

$$Y_{mk} = \begin{bmatrix} Y_{mRBk} & Y_{Ck} \\ Y_{Ck}^T & Y_{fk} \end{bmatrix}, \tag{3.67}$$

where

$$Y_{fk}A_f + A_f^T Y_{fk} + C_{fy,k}^T C_{fy,k} = 0 \tag{3.68}$$

$$Y_{mRBk}A_{mRB} + A_{mRB}^T Y_{mRBk} + C_{mRBy,k}^T C_{mRBy,k} = 0 \tag{3.69}$$

and

$$Y_{Ck} = T_{mRB}^{-T}\overline{Y_{Ck}} \tag{3.70}$$

where T_{mRB} is given in Equation 3.59, and $\overline{Y_{Ck}}$ is a solution of the Sylvester equation,

$$\overline{Y_{Ck}}A_f + A_{RB}\overline{Y_{Ck}} + C_{RB}^T C_f = 0\,. \tag{3.71}$$

Computing Sensor/Actuator Index

By combining the measures of controllability and observability from Section 3.2.1 with the performances, $\underline{J_j}$ and $\underline{V_k}$ from the previous section we can index the actuators in terms of their usefulness for the control problem, and likewise for the sensors. By combining these the sensor and actuator indices, we develop a sensor/actuator index.

We consider the system of Equation 3.60 where the rigid body modes have been artificially stabilized as discussed in the previous section. The A matrix is in a block diagonal form with two-by-two blocks for the complex modes, and one-by-one blocks for the real modes. For the complex modes, in the form of Equation 3.43, we set right eigenvectors (p_1 and p_2) and left eigenvectors (q_1, and q_2) to be given by,

$$p_{m1} = \begin{bmatrix} \frac{1}{\sqrt{2}} \\ i\frac{1}{\sqrt{2}} \end{bmatrix}, p_{m2} = \begin{bmatrix} \frac{1}{\sqrt{2}} \\ -i\frac{1}{\sqrt{2}} \end{bmatrix}, q_{m1} = \begin{bmatrix} \frac{1}{\sqrt{2}} \\ -i\frac{1}{\sqrt{2}} \end{bmatrix}, q_{m2} = \begin{bmatrix} \frac{1}{\sqrt{2}} \\ i\frac{1}{\sqrt{2}} \end{bmatrix} \tag{3.72}$$

The real modes have left and right eigenvectors set to

$$p_r = 1, q_r = 1\,. \tag{3.73}$$

Thus the eigenvector matrices of A are block diagonal in the same form of A with elements from Equation 3.72 corresponding to complex modes, and elements from Equation 3.73 for the real modes. The right eigenvectors of A are notated by $\{p_i, i = 1, \ldots, n\}$ and the left eigenvectors of A are notated by $\{q_i, i = 1, \ldots, n\}$.

Actuator Selection

For the actuator selection (or placement) problem we modify the measure described in [Kim and Junkins, 1991]. We generate an index for the j-th actuator. For the two states (i and $i+1$) corresponding to a complex mode we have

$$\begin{aligned}\alpha_{i,j} &= |f_{i,j}|^2(J_{i,j} + J_{i+1,j}) \\ \alpha_{i+1,j} &= |f_{i+1,j}|^2(J_{i,j} + J_{i+1,j})\end{aligned} \tag{3.74}$$

and for the state corresponding to a real mode we have,

$$\alpha_{i,j} = |f_{i,j}|^2(J_{i,j} + J_{i+1,j}) \tag{3.75}$$

where $J_{i,j}$ is given in Equation 3.52 and $f_{i,j}$ is given in Equation 3.28.

For the j-th index we sum over all states

$$\alpha_j = \sum_{i=1}^{n} \alpha_{i,j}. \tag{3.76}$$

The complex mode treatment of Equation 3.74 accounts for equal coupling between the two states that form the mode in the real modal form of Equation 3.43. We show this treatment results in an identical contribution to α_j then from a diagonal system.

Consider a 2×2 block system comprising a single complex mode. The system is in a real modal form with $A_m = A_{bm}^b$ as in Equation 3.43, and $B_m = \begin{bmatrix} b_1 & b_2 \end{bmatrix}^T$. By using the complex transformation matrix

$$T = \begin{bmatrix} 1 & -i \\ 1 & i \end{bmatrix} \tag{3.77}$$

we can transform to a diagonal form

$$A_d = TA_mT^{-1} = \begin{bmatrix} -\zeta\omega + i\omega\sqrt{1-\zeta^2} & 0 \\ 0 & -\zeta\omega - i\omega\sqrt{1-\zeta^2} \end{bmatrix}, B_d = TB_m = \begin{bmatrix} b_1 - ib_2 \\ b_1 + ib_2 \end{bmatrix} \tag{3.78}$$

The subscript $(\cdot)_m$ notates system matrices in modal form while $(\cdot)_d$ notates the system in diagonal form. Following Equation 3.28 we have for the modal and diagonal representations,

$$f_m = \begin{bmatrix} \frac{b_1}{\sqrt{2}} + i\frac{b_2}{\sqrt{2}} \\ \frac{b_1}{\sqrt{2}} - i\frac{b_2}{\sqrt{2}} \end{bmatrix} \text{ and } f_d = \begin{bmatrix} b_1 - ib_2 \\ b_1 + ib_2 \end{bmatrix}. \tag{3.79}$$

In modal form we write the matrix of Equation 3.52 as

$$X_m C_{z,m}^T C_{z,m} = \begin{bmatrix} X_{c1} & X_{c2} \\ X_{c2} & X_{c3} \end{bmatrix} \Rightarrow (\underline{J})_m = \begin{bmatrix} X_{c1} \\ X_{c3} \end{bmatrix} \tag{3.80}$$

where the diagonals elements are the elements of $\underline{J}_j$. In diagonal form we have:

$$\begin{aligned} X_d C_{z,d}^H C_{z,d} &= TX_m T^H T^{-H} C_{z,m}^T C_{z,m} T^{-1} \\ &= \begin{bmatrix} \frac{X_{c1} + X_{c3}}{2} & \frac{X_{c1} - X_{c3}}{2} - iX_{c2} \\ \frac{X_{c1} - X_{c3}}{2} + iX_{c2} & \frac{X_{c1} + X_{c3}}{2} \end{bmatrix} \Rightarrow (\underline{J})_d = \begin{bmatrix} \frac{X_{c1} + X_{c3}}{2} \\ \frac{X_{c1} + X_{c3}}{2} \end{bmatrix} \end{aligned} \tag{3.81}$$

where the solution of Lyapunov Equation 3.51 has been transformed according to $X_d = TX_mT^H$. Now, applying Equation 3.74 in the case of the modal representation, and

Equation 3.75 once for each state in the case of the diagonal representation, we have for both cases,

$$\begin{bmatrix} \alpha_1 \\ \alpha_2 \end{bmatrix} = \frac{1}{2}\begin{bmatrix} (b_1^2 + b_2^2)(X_{c1} + X_{c3}) \\ (b_1^2 + b_2^2)(X_{c1} + X_{c3}) \end{bmatrix}. \tag{3.82}$$

For actuator selection we rank actuators according to α_j. The larger the value of α_j the more well suited the actuator is for directly controlling modes weighted by their importance in the performance. In Section 3.3 a modification will be made to account for the additional spillover control action that results by indirectly controlling the coupling from the uncontrolled states to the performance.

Sensor Selection

For the sensor selection (or placement) problem we examine the dual of the actuator selection measure. We generate an index for the k-th sensor. For the two states (i and $i+1$) corresponding to a complex mode we have

$$\begin{aligned} \beta_{i,k} &= \frac{1}{4}|h_{i,k}|^2(V_{i,k} + V_{i+1,k}) \\ \beta_{i+1,k} &= \frac{1}{4}|h_{i+1,k}|^2(V_{i,k} + V_{i+1,k}) \end{aligned} \tag{3.83}$$

and for the state corresponding to a real mode we have,

$$\beta_{i,k} = |h_{i,k}|^2(V_{i,k} + V_{i+1,k}) \tag{3.84}$$

where $V_{i,k}$ is given in Equation 3.66 and $h_{i,k}$ is given in Equation 3.29.

For the k-th index we sum over all states

$$\beta_k = \sum_{i=1}^{n} \beta_{i,k}. \tag{3.85}$$

The equivalence of Equation 3.83, applied to a system in modal form, to Equation 3.84, applied to the two states of the system transformed into a diagonal form can be shown. Given an output matrix in modal form, $C_m = \begin{bmatrix} c_1 & c_2 \end{bmatrix}$, we have in diagonal form

$$C_d = \begin{bmatrix} \frac{c_1 + ic_2}{2} & \frac{c_1 - ic_2}{2} \end{bmatrix} \tag{3.86}$$

where the transformation of Equation 3.77 is used. Continuing, we can show,

$$h_m = \begin{bmatrix} \frac{c_1}{\sqrt{2}} + i\frac{c_2}{\sqrt{2}} \\ \frac{c_1}{\sqrt{2}} - i\frac{c_2}{\sqrt{2}} \end{bmatrix} \text{ and } h_d = \begin{bmatrix} \frac{c_1 + ic_2}{2} \\ \frac{c_1 - ic_2}{2} \end{bmatrix} \tag{3.87}$$

and given

$$B_{w,m}B_{w,m}^T Y_m = \begin{bmatrix} Y_{c1} & Y_{c2} \\ Y_{c2} & Y_{c3} \end{bmatrix} \Rightarrow (\underline{V})_m = \begin{bmatrix} Y_{c1} \\ Y_{c3} \end{bmatrix} \tag{3.88}$$

where Y_m satisfies Equation 3.65, we have

$$\begin{aligned} B_{w,d}B_{w,d}^H Y_d &= TB_{w,m}B_{w,m}^T T^H T^{-H} Y_m T^{-1} \\ &= \begin{bmatrix} \frac{Y_{c1} + Y_{c3}}{2} & \frac{Y_{c1} - Y_{c3}}{2} - iY_{c2} \\ \frac{Y_{c1} - Y_{c3}}{2} + iY_{c2} & \frac{Y_{c1} + Y_{c3}}{2} \end{bmatrix} \Rightarrow (\underline{V})_d = \begin{bmatrix} \frac{Y_{c1} + Y_{c3}}{2} \\ \frac{Y_{c1} + Y_{c3}}{2} \end{bmatrix}. \end{aligned} \tag{3.89}$$

Combining Equation 3.89 with Equation 3.87 according to Equations 3.83 for the modal representation and Equation 3.84 for both diagonal states, we verify the equivalence.

We rank sensors according to β_k. The greater the index value of β_k, the greater the suitability of the sensor for observing the system states, weighted by the disturbability of each state.

Sensor/Actuator Grouping for Control

For the sensor/actuator grouping problem we assign an index using the α and β indices from the two previous sections. We propose an index matrix $S \in \Re^{n_y \times n_u}$ with the (k, j)-th element given as

$$S(k,j) = \sum_{i=1}^{n} \alpha_{i,j}\beta_{i,k}. \tag{3.90}$$

Large values of the S index correspond to actuator/sensor combinations that efficiently actuate and measure states, weighted by the states' importance in the performance and susceptence to the disturbance.

The index S is entirely based on a weighted controllability and observability. We will see that additional controller performance can be achieved with an actuator which does not directly control modes. A modification to the index is made in Section 3.3 to account for these active output isolation actuators.

Sensor/Actuator Grouping for System Identification

In the case of a system identification problem for control we can specify (measure) a disturbance (B_w) and a performance (C_z) and the index S can be used to determine the best actuator and sensor types and locations. Again, S can be modified to account for active output isolation actuators. In this context the system identification problem, and the control actuator/sensor selection and placement problem can be solved with the same framework.

In the special case of modal identification, we can specify an actuator matrix B_u with column corresponding to all actuator locations, types and directions and a sensor matrix C_y with rows corresponding to all sensor locations, types and directions. A disturbance matrix B_w and performance matrix C_z are not specified. In this case the designer of the system identification experiment can select B_w and C_z to emphasize particular modes of interest. In the case where all modes are deemed interesting, $B_w = C_z = I$ can be used.

3.3 Correction for Active Output Isolation Actuators

In Section 3.2 an index matrix S was computed to determine actuator/sensor combinations that are effective for control. S is based on observability and controllability arguments. In some cases, control can be applied to decouple uncontrollable modes from the performance. In this case, an actuator which cannot control certain modes can still be effective in achieving a performance improvement. This section modifies S to account for control action on uncontrollable modes.

3.3.1 Performance Improvement from Uncontrollable Modes

To explore the action of a controller on uncontrollable modes we examine a system with dynamics given by

$$\begin{aligned} \begin{bmatrix} \dot{x}_c \\ \dot{x}_{nc} \end{bmatrix} &= \begin{bmatrix} A_{ct} & 0 \\ 0 & A_{nc} \end{bmatrix} \begin{bmatrix} x_{ct} \\ x_{nc} \end{bmatrix} + \begin{bmatrix} B_{wc} \\ B_{wnc} \end{bmatrix} w + \begin{bmatrix} B_{uc} \\ B_{unc} \end{bmatrix} u \\ z &= \begin{bmatrix} C_{zc} & C_{znc} \end{bmatrix} \begin{bmatrix} x_{ct} \\ x_{nc} \end{bmatrix} \end{aligned} \tag{3.91}$$

where subscript $(\cdot)_{ct}$ denotes dynamics controllable by actuator u, and subscript $(\cdot)_{nc}$ denoted dynamics uncontrollable by u. Without loss of generality the system is in a block diagonal form. The H_2 performance of the system can be determined using

$$J = \mathrm{tr}\left[\begin{bmatrix} C_{zc} & C_{znc} \end{bmatrix} X \begin{bmatrix} C_{zc} & C_{znc} \end{bmatrix}^T\right] \tag{3.92}$$

where

$$X = \begin{bmatrix} X_{ct} & X_{cpl} \\ X_{cpl}^T & X_{nc} \end{bmatrix} \tag{3.93}$$

satisfies the Lyapunov Equation,

$$\begin{bmatrix} A_{ct} & 0 \\ 0 & A_{nc} \end{bmatrix}\begin{bmatrix} X_{ct} & X_{cpl} \\ X_{cpl}^T & X_{nc} \end{bmatrix} + \begin{bmatrix} X_{ct} & X_{cpl} \\ X_{cpl}^T & X_{nc} \end{bmatrix}\begin{bmatrix} A_{ct}^T & 0 \\ 0 & A_{nc}^T \end{bmatrix} + \begin{bmatrix} B_{wc}B_{wc}^T & B_{wc}B_{wnc}^T \\ B_{wnc}B_{wc}^T & B_{wnc}B_{wnc}^T \end{bmatrix} = 0. \tag{3.94}$$

X_{cpl} is a term which couples the controllable states to the uncontrollable states. It represents covariance of the controllable and uncontrollable states. Equation 3.94 can be decoupled into three Equations (similar to Equations 3.53 to 3.55),

$$A_{ct}X_{ct} + X_{ct}A_{ct}^T + B_{wc}B_{wc}^T = 0 \tag{3.95}$$

$$A_{ct}X_{cpl} + X_{cpl}A_{nc}^T + B_{wc}B_{wnc}^T = 0 \tag{3.96}$$

$$A_{nc}X_{nc} + X_{nc}A_{nc}^T + B_{wnc}B_{wnc}^T = 0. \tag{3.97}$$

The cost can be written as,

$$J = \mathrm{tr}[C_{zc}X_{ct}C_{zc}^T] + 2\mathrm{tr}[C_{zc}X_{cpl}C_{znc}^T] + \mathrm{tr}[C_{znc}X_{nc}C_{znc}^T], \tag{3.98}$$

broken in three terms as contributions from (1) the controllable states, (2) the controllable / uncontrollable coupling, and (3) the uncontrollable states. The third term cannot be modified by control.

By applying a feedback law to the controllable states of the form

$$u = \begin{bmatrix} K_{ct} & 0 \end{bmatrix}\begin{bmatrix} x_{ct} \\ x_{nc} \end{bmatrix}, \tag{3.99}$$

we can modify the states to arrive at a closed loop A_{ct} given by

$$A_{ct} \to -\lambda I. \tag{3.100}$$

This pole placement is possible since all states of A_{ct} are assumed controllable. Lyapunov Equation 3.95 becomes

$$-\lambda X_{ct} - X_{ct}\lambda + B_{wc}B_{wc}^T = 0 \tag{3.101}$$

which has solution,

$$X_{ct} = \frac{B_{wc}B_{wc}^T}{2\lambda}. \tag{3.102}$$

Sylvester Equation 3.96 becomes

$$\begin{aligned} 0 &= -\lambda I X_{cpl} + X_{cpl}A_{nc}^T + B_{wc}B_{wnc}^T \\ &= X_{cpl}(-\lambda I) + X_{cpl}A_{nc}^T + B_{wc}B_{wnc}^T \\ &= X_{cpl}(A_{nc}^T - \lambda I) + B_{wc}B_{wnc}^T \end{aligned} \tag{3.103}$$

which has solution (if A_{nc} has no λ eigenvalues),

$$X_{cpl} = B_{wc}B_{wnc}^T(\lambda I - A_{nc}^T)^{-1}. \tag{3.104}$$

Thus both X_{ct} and X_{cpl} can be made arbitrarily small by choosing large λ. The cost of Equation 3.98 is reduced to

$$J \to \mathrm{tr}[C_{znc}X_{nc}C_{znc}^T]. \tag{3.105}$$

Feedback control from the controllable states allows a reduction in the controllable states' cost term and in the cost term representing coupling between controllable and uncontrollable states. By expanding the feedback law to allow feedback from the uncontrollable states,

$$u = \begin{bmatrix} K_{ct} & K_{nc} \end{bmatrix} \begin{bmatrix} x_{ct} \\ x_{nc} \end{bmatrix}, \tag{3.106}$$

a further cost reduction can be achieved since the second term in Equation 3.98 can be made negative. We can have

$$J < \mathrm{tr}[C_{znc} X_{nc} C_{znc}^T]. \tag{3.107}$$

This case is encountered in LQR control design when the uncontrollable disturbance states are available for full-state feedback [Kwakernaak and Sivan, 1972].

We have shown by the preceding simple example that the control of controllable states can have be used to actively decouple the uncontrollable states from the performance. A common control example is output isolation. In the case of an interferometer, a small mirror on a voice coil can be a very effective actuator for optical pathlength control. In this case the mirror's small mass does not couple to the structure, eliminating the possibility of structural control, but any measured disturbance within the actuator's bandwidth can be directly cancelled. This control approach is *active isolation*. Control performance can be realized from a sensor which observes many modes to an actuator which controls few modes but has an extended bandwidth. We will modify S to capture this control possibility by generating a modified actuator / sensor selection matrix, S_c.

By dual arguments (extending from the full state feedback case to the state estimation case) we can show that the effect of unobservable modes on the performance can be reduced by controlling the observable modes. Thus control performance can be realized from a sensor which observes few modes but has an extended bandwidth to an actuator which controls many modes. However this effect is neglected since experience shows that most sensors used for space telescopes (rate gyroscopes, laser interferometers, and wavefront sensors) have good modal observability properties which are already captured in S and S_c.

3.3.2 Effective Actuation Matrix Determination

If a disturbance is measured within the bandwidth of the actuator, then control action can be taken. In the case of structural control, the modes of the structure can be damped or shifted to have less contribution to the performance. The controllability/observability actuator/sensor index S quantifies the suitability of particular sensors and actuators for control in this case.

In the case of isolation, the actuator acts to cancel a measured disturbance without modifying modal behavior. To do this the actuator must have gain within the frequency region of interest. Further, the sensor must have gain and have an ability to observe the disturbance that is to be cancelled. To capture the effectiveness of the actuator for active isolation control we propose computing an *effective* input matrix Be_j which depends on the actuator gain. Using the effective input matrices for each actuator, an identical procedure to that used to compute S in Section 3.2 can be used to compute a modified sensor / actuator index matrix, S_c which captures actuators acting as active isolators.

The system is assumed to be in the realization described in Section 3.2.3. For the j-th actuator and k-th sensor we compute the effective input vector $Be_{j,k} \in \Re^{n \times 1}$. Since the effectiveness of an actuator for active isolation is sensor dependent an effective input vector for the j-th input is required for each sensor.

For a real state with eigenvalue, λ_l, we compute the l-th element of the vector $Be_{l,j,k}$ with the relation

$$\left.\left\{\left|\frac{C_{l,k}}{s+\lambda_l}\right| Be_{l,j,k} = \left|C_k(sI-A)^{-1}B_j\right|\right\}\right|_{s = i\lambda_l} \quad . \tag{3.108}$$

Thus we choose $Be_{l,j,k}$ to be the input vector value which would set a single state transfer function equal to the given multiple state transfer function, when evaluated at the eigenvalue of the l-th state. C_k is the row vector corresponding to the k-th sensor and B_j is the column vector corresponding to the j-th actuator. Thus $Be_{l,j,k}$ is chosen to have a measure of controllability on the l-th state with a magnitude reflecting the gain of the actuator-j/sensor-k channel. The expression for $Be_{l,j,k}$ in the case of the real state, λ_l, can be written as

$$Be_{l,j,k} = \frac{\sqrt{2}\left|\lambda_l C_k(i\lambda_l I - A)^{-1}B_j\right|}{|C_{l,k}|}. \tag{3.109}$$

For a real mode corresponding to the l-th and $l+1$-th state, a similar philosophy is adopted. From Equation 3.82 we see that the Pythagorean combination of the input vector elements is used to determine the α index corresponding to the mode. Thus, without loss of generality, we can set $Be_{l,j,k} = Be_{l+1,j,k}$. With this assumption we set

$$\left\{\left|\begin{bmatrix} C_{l,k} & C_{l+1,k}\end{bmatrix}\begin{bmatrix} sI - A^b_{rm}\Big|_{\zeta = \frac{1}{\sqrt{2}}}\end{bmatrix}^{-1}\begin{bmatrix}1\\1\end{bmatrix}\right| Be_{l,j,k} = \left|C_k(sI-A)^{-1}B_j\right|\right\}_{s = i\omega} \tag{3.110}$$

where A^b_{rm} is defined in Equation 3.43. We dereverberate the single mode of A^b_{rm} by setting, $\zeta = \frac{1}{\sqrt{2}}$. $Be_{l,j,k} = Be_{l+1,j,k}$ is set to be the value of the input vector which would equate the dereverberated single mode transfer function to the true transfer function at the natural frequency of the mode, ω. Dereverberation of the single mode ensures that $Be_{l,j,k} = Be_{l+1,j,k}$ is weighted by the height of the resonant peak. We write

$$Be_{l,j,k} = Be_{l+1,j,k} = \frac{\sqrt{2}\left|\omega C_k(sI-A)^{-1}B_j\right|}{\sqrt{3C^2_{l,k} + 2C_{l,k}C_{l+1,k} + C^2_{l+1,k}}}. \tag{3.111}$$

Note the similarities of Equations 3.109 and 3.111. With all elements of the vector $Be_{j,k}$ computed we use Equation 3.28 to calculate

$$fe_{i,j,k} = \frac{q_i^H Be_{i,j,k}}{\|q_i\|}. \tag{3.112}$$

Subsequently the index $\alpha e_{j,k}$ is computed with Equation 3.74 for complex modes and Equation 3.75 for real states. We can compute a sensor/actuator index matrix, S_c by modifying Equation 3.90 to read,

$$S_c(k,j) = \sum_{i=1}^{n} \alpha e_{i,j,k} \beta_{i,k}. \tag{3.113}$$

The final index matrix for sensor/actuator selection is defined by

$$S_t = S + \gamma S_c. \tag{3.114}$$

S_t is formed of the controllability/observability based index of Section 3.2, and corrected with a matrix S_c which accounts for actuators with good bandwidth but poor controllability properties. γ is a mixing parameter scale the terms with respect to each other. A mixing parameter of $\gamma = 1$ is found to work well in practice.

3.4 Controller Topology Determination Algorithm

Figure 3.3 is a flow diagram of the sensor/actuator indexing algorithm. Horizontal rows of blocks refer to operations that are computed dually for both actuators and sensors. Inputs and outputs of the model are found in Table 3.1. The algorithm generates an n_y by n_u index matrix, S_t. If (k,j) entry of S_t is large relative to other elements then the k-th sensor and j-th actuator are considered an effective pair for control.

The algorithm begins by scaling the system and in the case of very large systems, balancing and reducing the model (Section 3.1). The system is transformed to a real model form. For each actuator u_j, the open-loop performance is broken up into a set of modal contributions $\underline{J_j}$ (Equation 3.52). Dually, the modal contributions, $\underline{V_k}$, of the disturbance to the open-loop measure at each sensor, y_k, are computed (Equation 3.66). These quantities require the solution of Lyapunov Equations. Decoupling the Lyapunov Equations handles rigid body modes whose contribution to the sensor/actuator index matrix is subsequently determined by the designer with a single parameter, $\omega_{RB} > 0$ (Section 3.2.3). A small

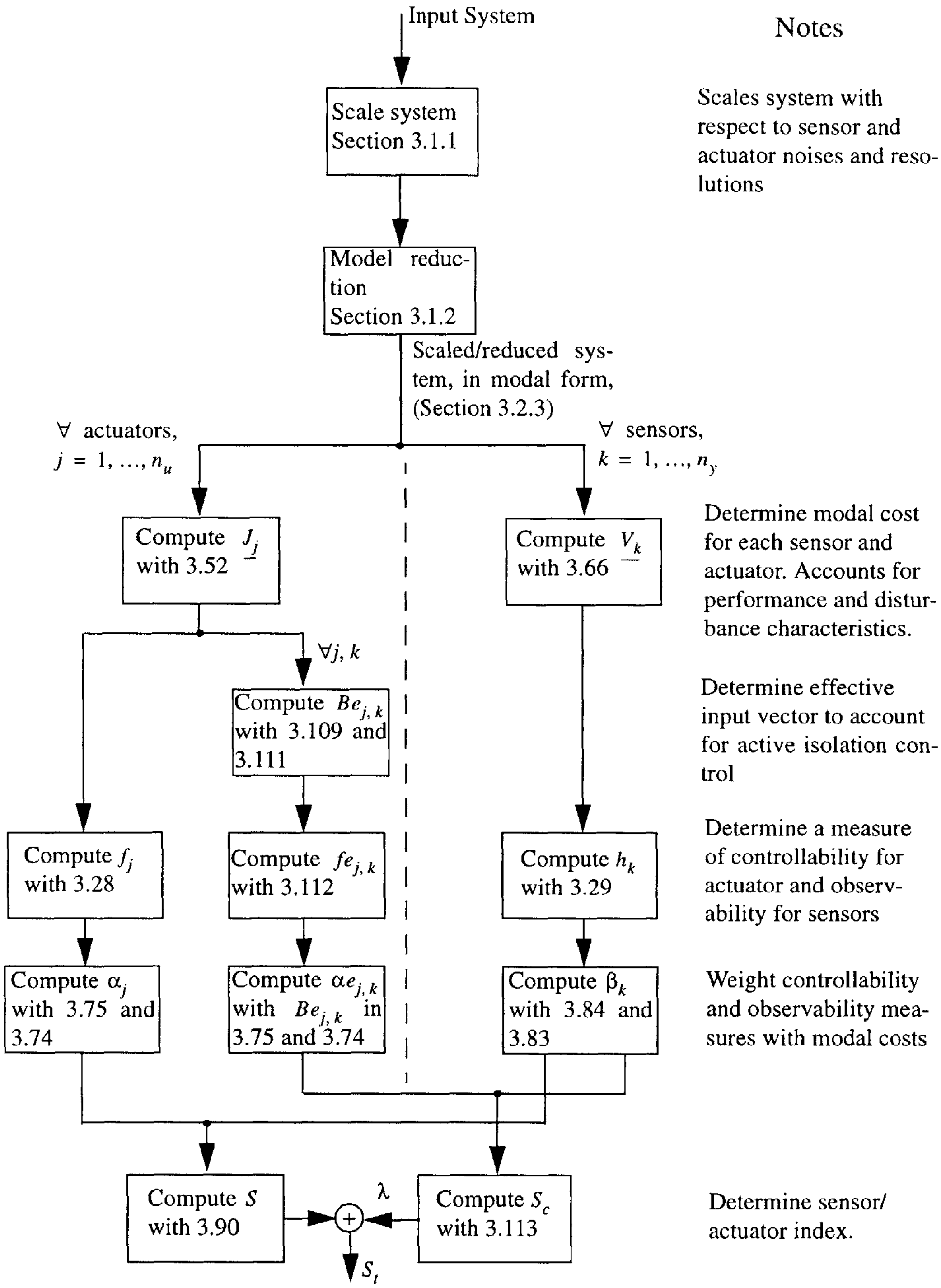

Figure 3.3 Simplified flow diagram of the sensor/actuator indexing algorithm. The manipulation of any rigid body modes is detailed in Section 3.2.3.

TABLE 3.1 Inputs and outputs for sensor/actuator indexing algorithm

Inputs	open-loop model	A, B_w, B_u, C_z, C_y	Equation 2.3
	scaling gains	R_w, R_u, R_z, R_y	Section 3.1.1
	rigid-body contribution parameter	ω_{RB}	Section 3.2.3
	output isolation mixing parameter	γ	Section 3.3.2
Outputs	sensor / actuator index matrix	S	Section 3.3.2

value of ω_{RB}, implies a heavy weighting on the rigid body modes in the indexing matrix S_t.

To handle the special case of actively decoupling uncontrollable modes from the performance (active output isolation) an effective input vector, $Be_{j,k}$, is computed for the j-th actuator and k-th sensor. $Be_{j,k}$ quantifies the suitability of an actuator for active output isolation in terms of modal controllability. The magnitude of the actuator-to-sensor transfer function, $|G_{yu,j,k}|$, is used as a weighting to ensure modes are weighted by the appropriate sensor/actuator gain (Section 3.3.2).

For each actuator, we compute a modal measure of controllability, f_j, which quantifies how the actuator controls each mode (Equation 3.28). Dually, a modal measure of observability, h_k, is computed (Equation 3.29). An effective measure of modal controllability, $fe_{j,k}$, is computed for the effective input vector to handle the active output isolation control case (Equation 3.112).

The next step of the algorithm, the modal measures of controllability (observability) are weighted by the modal performance (disturbance) contributions to form the weighted controllability (observability) vector, α_j (β_k) (Equations 3.76 and 3.85). To handle the active output isolation case an effective weighted controllability vector is computed, $\alpha_{j,k}$ (Section 3.3.2).

In the final step, the elements of thee sensor/actuator control effectiveness matrix, S, are calculated by computing the dot product of the weighted controllability and weighted observability vectors for each sensor and actuator (Equation 3.90). A corrective matrix, S_c, is computed using the effective weighted controllability to account for active output isolation capabilities of the actuators (Equation 3.113). Lastly, the index matrix S_t is computed by mixing S and S_c (Equation 3.114).

3.5 Demonstration on a Simple Grid Structure

To demonstrate the sensor/actuator indexing algorithm we examine its applicability to the model of a simple structure. The selected structure provides a tradeoff between reasonable complexity and an example where engineering intuition can be validated with the sensor/actuator selection algorithm. The discussed example demonstrates the use of the sensor/actuator indexing matrix for the placement of a small set of sensors and actuators for LQG structural control. The sensor/actuator index results are compared with three other methods in terms of performance and computational efficiency.

3.5.1 Structural Model

A simple grid structure which has been previously used to validate an actuator placement algorithm is selected [Kim and Junkins, 1991]. The structure is seen in Figure 3.4.

The structure is made up from a grid of 1/8" thick aluminum beams, clamped at one end. The numbered nodes on the structure represent locations where sensors or actuators can be placed. Displacement sensors, and both x and y torque actuators (modeled as reaction wheels) are selected. The structure is modeled with a FEM of Bernoulli-Euler beam elements. At each grid node location, a lumped mass is placed to account for the mass of sensors and actuator. In this manner the model does not change with the sensors or actuators selected. The first ten flexible modes of the structure are kept. The material properties of the model are listed in Table 3.2.

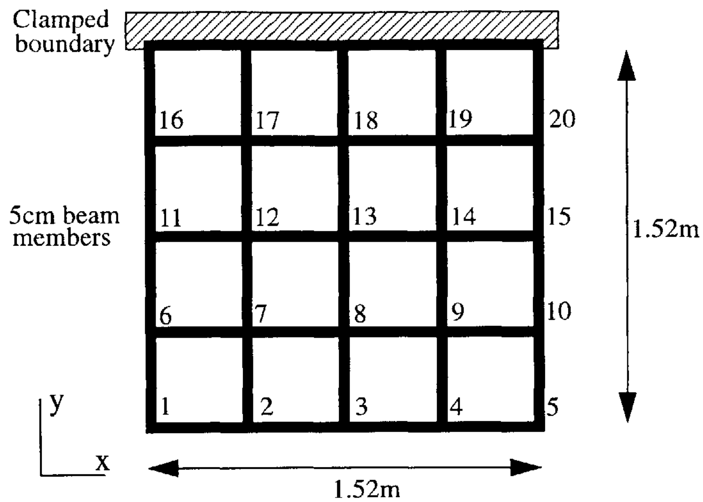

Figure 3.4 Test model for validating sensor/actuator indexing. Node locations for sensors and actuators are numbered. Taken from [Kim and Junkins, 1991].

TABLE 3.2 Material properties of grid model, [Kim and Junkins, 1991].

Bending stiffness	EI	$9.35\ \mathrm{N \cdot m^2}$
Torsional stiffness	GJ	$14.19\ \mathrm{N \cdot m^2}$
Mass distribution	ρA	0.447 kg/m
Inertia distribution	ρI_p	$9.65\mathrm{x}10^{-4}\ \mathrm{kg \cdot m}$

3.5.2 Problem Statement: Sensor/Actuator Placement

In this example the sensor/actuator placement for control problem is solved. The problem can be phrased: given a control strategy and a set of sensors and actuators, select N_s sensors and N_u actuators which achieve optimal control performance.

We select an LQG (H_2 optimal) control strategy in this example. The H_2 control synthesis procedure is detailed in Appendix C, Section C.1. For the grid we can define,

$$B_u = \begin{bmatrix} B_{u,1} & B_{u,2} & \dots & B_{u,n_u} \end{bmatrix} \in \Re^{n \times n_u} \tag{3.115}$$

where B_u has a column from the FEM for each of n_u possible actuators. Defining a projection matrix,

$$\Lambda = \begin{bmatrix} \lambda_1 & \dots & 0 \\ \vdots & \ddots & \vdots \\ 0 & \dots & \lambda_{n_u} \end{bmatrix} \in \Re^{n_u \times n_u} \tag{3.116}$$

where λ_j is unity if an actuator is selected or zero if it is not selected. The matrix $B_u\Lambda$ is the input matrix of selected actuators. Dually, we define,

$$C_y = \begin{bmatrix} C_{y,1}^T & C_{y,2}^T & \dots & C_{y,n_u}^T \end{bmatrix}^T \in \Re^{n_y \times n} \tag{3.117}$$

where C_y has a row from the FEM for each possible sensor. We define

$$\Gamma = \begin{bmatrix} \gamma_1 & \dots & 0 \\ \vdots & \ddots & \vdots \\ 0 & \dots & \gamma_{n_y} \end{bmatrix} \in \Re^{n_y \times n_y} \tag{3.118}$$

where γ_k is unity if a sensor is selected or zero if it is not selected. The matrix ΓC_y is the output matrix of selected sensors.

Sample Problem Statement

We consider an actuator and sensor placement problem. Given the actuator cost penalty and sensor noise intensity, we wish to select the set of N_u actuators from n_u available, and the set of N_y sensors from n_y available, to minimize the closed-loop H_2 cost in Equation C.2. Standard assumptions of reachability and detectability for all sensor/actuator combinations hold. Using definitions 3.116 and 3.118 with the disturbance-to-performance dynamics from the FEM, (A, B_w, C_z), we can quantify the problem statement in terms of Riccati equations.

$$\{\lambda_j^*, \gamma_k^*\} = \underset{\{\lambda_j, \gamma_k\}}{\arg\min} \ \mathrm{Tr}\left[XB_wB_w^T + \frac{1}{\rho}YXB_u\Lambda B_u^T X\right] \tag{3.119}$$

where X and Y solve modified versions of Riccati Equations C.10 and C.11,

$$0 = XA + AX + R_{xx} - \frac{1}{\rho} X B_u \Lambda B_u{}^T X \tag{3.120}$$

$$0 = AY + YA^T + V_{xx} - \frac{1}{\mu} Y C_y{}^T \Gamma C_y Y. \tag{3.121}$$

ρ and μ weight control use and sensor noise respectively. Additional constraints are the binary constraints

$$\begin{aligned} \lambda_j &= 0 \text{ or } 1, j = 1, \ldots, n_u \\ \gamma_k &= 0 \text{ or } 1, k = 1, \ldots, n_y \end{aligned}, \tag{3.122}$$

and the number of sensor and actuator constraints

$$\begin{aligned} \mathrm{Tr}[\Lambda] &= N_u \\ \mathrm{Tr}[\Gamma] &= N_y \end{aligned}. \tag{3.123}$$

Equations 3.119 through 3.123 define a nonlinear (quadratic) integer programming problem.

3.5.3 Possible Solution Techniques

Four methods to solve the nonlinear integer programming method will be explored: (1) complete enumeration (2) branch and bound integer programming, (3) simulated annealing, and (4) the developed sensor/actuator indexing algorithm. Given a set of λ_j's and γ_k's that satisfy constraint 3.122, the cost can be evaluated through the solution of the two Riccati equations 3.120 and 3.121. This simple cost evaluation is possible since we are considering a *fully connected* control topology. The four methods are described below.

Complete Enumeration

This brute force approach simply uses Equations 3.119 through 3.121 to compute the H_2 cost of all possible sets of $\{\lambda_j, \gamma_k\}$ which satisfy the constraints 3.122 and 3.123. This method will find the true global optimum. The computational cost is prohibitive however since the number of cost evaluations is given by

$$N_J = \binom{n_u}{N_u}\binom{n_y}{N_y}. \tag{3.124}$$

For example, on the simple structure with $n_u = 40$ actuator possibilities, and $n_y = 20$ sensor locations, choosing the optimal set of $N_u = 3$ actuators and $N_y = 3$ sensors will require an infeasible 11×10^6 solutions of both Riccati equations 3.120 and 3.121.

Branch and Bound

Branch and bound techniques can be used to efficiently solve linear integer programming problems [Hillier and Lieberman, 1995]. In our nonlinear integer program we can use branch and bound techniques to increase the efficiency of finding the true optimum over the complete enumeration.

We start with a feasible first guess at the solution with cost J_o. Begin by setting all $\{\lambda_j, \gamma_k\}$ to unity. In the branch step we set a λ_j or a γ_k parameter to zero. In the bound step, we *relax* the Constraint 3.123. With Constraint 3.123 relaxed, the optimal solution is to set all remaining λ_j and γ_k to unity and to solve Equations 3.119 to 3.121 for a cost J (since an additional sensor or actuator cannot degrade optimal performance). If $J > J_o$ then the our branch is *fathomed* and our zero-set parameter must be unity in the solution. We traverse the feasible tree by repeating these steps. By fathoming the feasible tree we reduce the number of cases before we need to appeal to a complete enumeration.

This branch and bound strategy fails to provide a significant improvement over the complete enumeration because for increased efficiency (1) it requires a good starting guess (which we can find with the sensor/actuator indexing algorithm), and (2) it requires that specific sensors and actuators dominate the achieved performance. Enhancing this branch and bound technique is a topic of further research.

Simulated Annealing

Simulated annealing is a method to solve discrete optimization problems [Press et al., 1992]. We begin with an initial randomly generated $\{\lambda_j, \gamma_k\}$ and compute J_o. Then with each successive iteration, we perturb the current $\{\lambda_j, \gamma_k\}_m$ to get $\{\lambda_j, \gamma_k\}_{m+1}$ and compute J_{m+1}. If $J_{m+1} < J_m$ then we accept $\{\lambda_j, \gamma_k\}_{m+1}$, *i.e.* $\{\lambda_j, \gamma_k\}_{m+1} \to \{\lambda_j, \gamma_k\}_m$. If $J_{m+1} > J_m$ then we accept $\{\lambda_j, \gamma_k\}_{m+1}$ with some probability $p(J) \propto \exp\left(-\frac{J}{T}\right)$ where T is the temperature, a parameter which decreases with successive iterations. The temperature controls the rate with which parameters with greater cost are accepted. The ability to accept greater costs reduces the chance that the solver will be trapped in a local minimum.

Simulated annealing does not guarantee a global minimum but is more efficient than complete enumeration for finding a good solution. The number of iterations is controlled by the cooling rate (*i.e.* the amount that T is decreased per iteration).

Sensor/Actuator Indexing Algorithm

By analyzing the sensor/actuator (S/A) index S_t we can choose sensors and actuators effective for control. We solve,

$$\{\lambda_j^{sa}, \gamma_k^{sa}\} = \arg\max_{\{\lambda_j, \gamma_k\}} \sum_{l=1}^{n_y} \sum_{m=1}^{n_u} \Gamma S_t \Lambda \tag{3.125}$$

where S_t, Λ and Γ are defined in Equations 3.114, 3.116 and 3.118 respectively. We can solve this problem quickly with simple logic to arrive at a set of sensors and actuators, $\{\lambda_j^{sa}, \gamma_k^{sa}\}$. The selected set is not guaranteed to be optimal since the S/A selecting index predicts control performance based on open-loop calculations. In the next section we compare the application of the S/A indexing algorithm to the three previously mentioned methods in terms of performance and computational efficiency.

3.5.4 Method Comparison

The methods discussed in the precious section will be applied to the structure of Figure 3.4 to determine the optimal set of sensors and actuators for LQG control.

In Table 3.3 S/A indexing is used to determine the best set of $N_y = 3$ sensors and $N_u = 3$ actuators for control. The problem involves the rejection of a x-direction white disturbance torque applied at Node 3, while the performance to be minimized is the RMS displacement at Node 3. For the $n = 20$ state system, 588×10^6 floating point operations (flops) are required. This number of flops allows simulated annealing with only 8 iterations to determine the solution, and does not even allow the complete enumeration (or branch and bound) of a system with $n_y = 4$ sensors and $n_u = 4$ actuators.

TABLE 3.3 Comparison of sensor/actuator indexing with simulated annealing and complete enumeration when the total flops is held constant. A unity white noise disturbance torque added at node 3 about the x axis. The performance is to minimize the RMS displacement of node 3.

Method	**Flops/step** (10^6)	**Steps**	**Flops**[a] (10^6)	**Actuator Locations**[b]	**Sensor Locations**[c]	**J** (10^{-2})	**Notes**
S / A indexing	588	1	588	x2,x3,x4	2,3,4	4.60	
simulated annealing	78	8	624	x18,x19,y9 x3,x5,x12 x1,x3,x14 x3,x6,y13 x3,x15,y3	6,11,19 3,6,17 1,4,13 4,6,10 3,7,9	6.54 5.17 4.91 5.19 5.29	5 simulated annealing trials. Note that 8 iterations is not enough for the optimizer to anneal and corresponds to a premature end for the algorithm
complete enumeration[d]	78	8	624	N/A	N/A	N/A	No design available since 8 steps does not even allow $n_u = n_y = 4$

a. each method adjusted for approximately an equal number of floating point operations (flops)

b. x# - letter indicates direction for applied moment, number indicates node location

c. number indicates node number where a sensor is placed

d. similar conclusions apply for the branch and bound technique

S/A indexing suggests the intuitive result that x-direction torque actuators should be included at Nodes 3, 4 and 5, with displacement sensors at Nodes 3, 4 and 5. The achieved performance for this configuration is superior to any determined by the simulated annealing with 8 iterations. These results highlight the relative computational efficiency of the S/A indexing algorithm.

To compare the S/A indexing solution to the true globally optimal set of $N_y = 3$ sensors and $N_u = 3$ actuators we appeal to a complete enumeration. The initial problem with $n_u = 40$ actuator and $n_y = 20$ sensor possibilities has a prohibitive 11×10^6 possible cases. We reduce the set of sensors and actuators to: x-direction and y-direction torque actuators, and displacement sensors at nodes 1, 3, 5, 11, 13, and 15. This $n_y = 6$, and $n_u = 12$ subset has 4400 possible cases to enumerate.

In Figure 3.5 the cost for each possible solution is ranked and plotted in terms of descending cost. Again the problem involves the rejection of a x-direction white disturbance torque applied at Node 3, where the performance to be minimized is the RMS displacement at Node 3. Three sets of control penalties (ρ) and sensor noise intensities (μ) are plotted. The S/A indexing result is plotted with an asterisk. In two cases the S/A indexing solution is indeed globally optimal. In the $\rho = \mu = 0.0001$ case the S/A indexing algorithm solution is not globally optimal but remains a good solution with cost (relative to worse cases) near the optimal cost value.

Table 3.4 compares the S/A indexing algorithm to the global optimum found by complete enumeration for three disturbance/performance specifications, each with three control penalty/sensor noise intensity settings. The S/A indexing algorithm finds the global optimal in 5 of the 9 cases. In the non-optimal cases the performance calculated for the S/A indexing algorithm configurations is close to the optimal performance, relative to the open-loop performance and to the worse cases of the enumeration. It is important to note that for the enumeration of this subset of the possible sensor and actuator locations, the S/A algorithm requires 584 times fewer flops. The branch and bound technique also returns the global optimal but is not found to provide significant computational saving over the complete enumeration.

Table 3.5 compares the S/A indexing algorithm solutions to those found with the simulated annealing method. The full $n_u = 40$ and $n_y = 20$ case is used. Five fifty-iteration simulated annealing trials were performed for each of the nine cases from Table 3.4. The

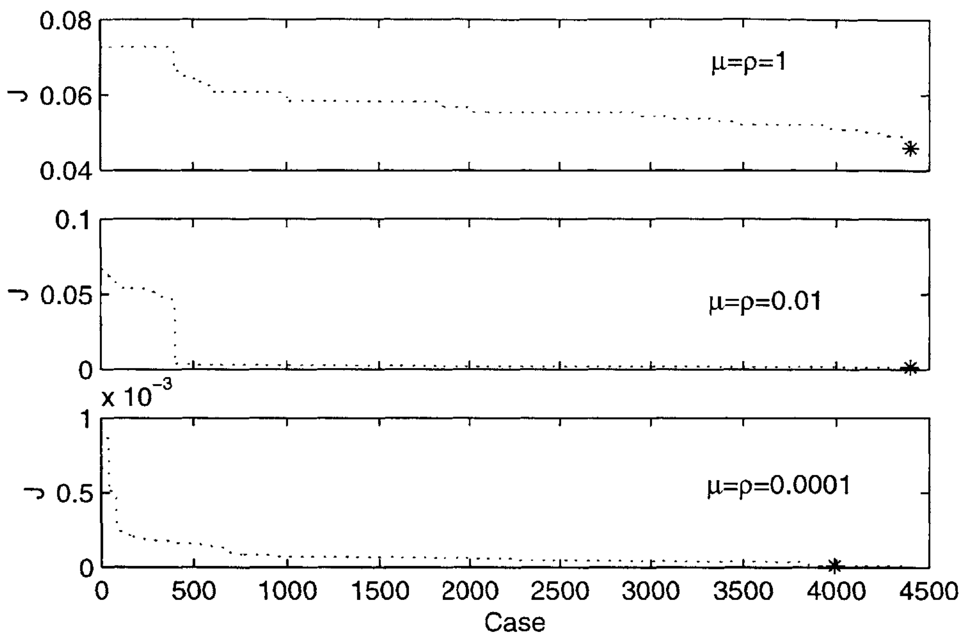

Figure 3.5 Complete enumeration of a reduced set of actuators and sensors for three control penalty/sensor noise settings. A unity white noise disturbance torque added at node 3 about the x axis. The performance is to minimize the RMS displacement of node 3. The sensor/actuator indexing algorithm choice is indicated by *.

best of the five trials was kept as the solution. Each simulated annealing solution required 33 times the flops required for the S/A indexing. In six cases the S/A indexing solutions is superior to that found with simulated annealing. In the other three cases simulated annealing provides a marginal improvement in performance but with an increased computation price.

The usefulness of the S/A algorithm for solving the problem of sensor/actuator selection for full-state LQG control has been demonstrated. This problem is one application of the S/A index matrix, S_t. Though the S/A indexing solution is not necessary a global optimum, in the included sample cases it is a good solution with relative cost near that of the global optimum. Using the S/A index for this problem compares well to using simulated annealing. Further, the S/A index computation increases only linearly with the number of possible sensor and actuator locations compared with: (1) a factorial increase in possibilities for the complete enumeration (2) a factorial increase in feasible set size for the simu-

TABLE 3.4 Comparison of sensor/actuator indexing with complete enumeration. Three disturbance/performance cases are tried, each at three levels of LQG control. Each complete evaluation finds global optimum but requires 584 times more flops than the sensor/actuator indexing algorithm.

Dist.[a]	Perf.[b]	J_{ol}	$\mu = \rho$	Sensor Actuator Indexing			Complete Enumeration[c]		
				Actuator Loc.	Sensor Loc.	J	Actuator Loc.	Sensor Loc.	J
x3	3	7.3×10^{-2}	1	x1,x3,x5	1,3,5	4.6×10^{-2}	x1,x3,x5	1,3,5	4.6×10^{-2}
			1×10^{-2}	x1,x3,x5	1,3,5	1.4×10^{-3}	x1,x3,x5	1,3,5	1.4×10^{-3}
			1×10^{-4}	x1,x3,x5	1,3,5	9.9×10^{-6}	x3,y1,y5	3,5,13	9.2×10^{-6}
x3,y3	12 − 13, 14 − 13, 8 − 13	1.2×10^{-2}	1	x1,x3,x5	1,3,5	1.1×10^{-2}	x1,x3,x5	1,3,5	1.1×10^{-2}
			1×10^{-2}	x1,x3,x5	1,3,5	2.0×10^{-3}	x1,x5,y3	1,5,11	1.7×10^{-3}
			1×10^{-4}	x1,x3,x5	1,3,5	8.6×10^{-5}	x1,x3,y13	1,3,6	2.8×10^{-5}
y3	1 − 5	7.5×10^{-2}	1	y1,y3,y5	1,5,6	7.0×10^{-2}	y1,y3,y5	1,5,11	7.0×10^{-2}
			1×10^{-2}	y1,y3,y5	1,5,6	3.5×10^{-3}	x1,y1,y3	1,5,15	3.5×10^{-2}
			1×10^{-4}	y1,y3,y5	1,5,6	9.7×10^{-6}	x1,y1,y5	1,5,15	8.8×10^{-6}

a. x# - letter indicates direction for applied moment, number indicates node location

b. number indicates node number where a sensor is placed

c. the computational burden of the complete enumeration requires the use of a subset of available sensors and actuators

lated annealing and (3) a factorial increase in tree size for the branch and bound. The number of computations dependence on the system order n is less for the S/A indexing (solving Lyapunov Equations 3.51 and 3.65 n_u and n_y times respectively) than the other methods (solving Riccati Equations 3.120 and 3.121 for each cost-determination iteration).

3.6 Demonstration on a Simple Mass/Spring System

As a second design example, the sensor/actuator assessment matrix, S_t, is determined for a two degree-of-freedom (dof) mass/spring problem with two sensors and two actuators. The best sensor/actuator pair as predicted by S_t is compared with the best sensor/actuator pair as determined by designing SISO LQG controllers for each of the four sensor/actuator

TABLE 3.5 Comparison of sensor/actuator indexing with simulated annealing. Three disturbance/performance cases are tried, each at three levels of LQG control. The best of five 50 iteration simulated annealing runs is displayed for each case. Each simulated annealing solution requires 33 times more flops than the sensor/actuator indexing.

Dist.[a]	Perf.[b]	J_{ol}	$\mu = \rho$	Sensor Actuator Indexing			Simulated Annealing		
				Actuator Loc.	Sensor Loc.	J	Actuator Loc.	Sensor Loc.	J
x3	3	7.3×10^{-2}	1	x1,x3,x5	1,3,5	4.6×10^{-2}	x5,x14,x19	1,4,9	5.0×10^{-2}
			1×10^{-2}	x1,x3,x5	1,3,5	1.4×10^{-3}	x3,x4,x5	1,3,12	1.5×10^{-3}
			1×10^{-4}	x1,x3,x5	1,3,5	9.9×10^{-6}	x3,x14,y1	2,8,16	9.4×10^{-6}
x3,y3	12 – 13, 14 – 13, 8 – 13	1.2×10^{-2}	1	x1,x3,x5	1,3,5	1.1×10^{-2}	x1,x4,y8	8,16,20	1.1×10^{-2}
			1×10^{-2}	x1,x3,x5	1,3,5	2.0×10^{-3}	x3,x6,y4	4,11,20	1.9×10^{-3}
			1×10^{-4}	x1,x3,x5	1,3,5	8.6×10^{-5}	x3,y8,y19	1,7,8	3.6×10^{-5}
y3	1 – 5	7.5×10^{-2}	1	y2,y3,y4	1,5,6	6.8×10^{-2}	x18,y3,y6	1,10,11	7.1×10^{-2}
			1×10^{-2}	y2,y3,y4	1,5,6	3.4×10^{-3}	x12,y3,y11	1,5,6	3.7×10^{-3}
			1×10^{-4}	y2,y3,y4	1,5,6	1.4×10^{-5}	x5,x12,y15	2,4,5	2.6×10^{-6}

a. x# - letter indicates direction for applied moment, number indicates node location

b. number indicates node number where a sensor is placed

combinations. The LQG designs validate the predictions of S_t which are contrary to design intuition. A figure of the sample problem is found in Figure 3.6.

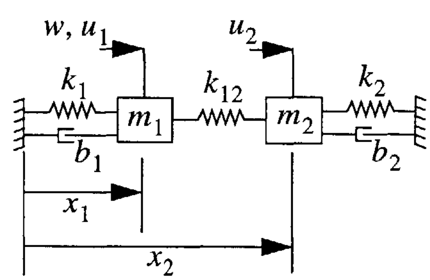

Figure 3.6 Two mass/spring design example to demonstrate the application of the sensor/actuator assessment matrix for selecting sensor and actuators for the LQG control problem.

The structural parameters and the signals for the four-block control problem are presented in Table 3.6.

TABLE 3.6 System parameters and input/output signals for 2-dof sensor/actuator effectiveness assessment example

Parameters	$m_1 = m_2 = 1$.,$k_1 = k_2 = 1$, $k_{12} = 10^{-4}$, $b_1 = b_2 = 10^{-3}$
Disturbance	w : force on m_1
Performance	$z = x_2$: position of m_2
Actuators	u_1 : force on m_1 , and u_2 : force on m_2
Sensors	$y_1 = x_1$: position of m_1 , and $y_2 = x_2$: position of m_2

We set up a sample problem whereby the control designer selects one of the two sensors and one of the two actuators for SISO rejection of the disturbance, w, as measured in the performance, z. Three intuitive sensor/actuator sets are obvious:

1. *Input isolation*: select the collocated pair u_1 and y_1 to actively decouple the disturbance from the performance.
2. *Output isolation*: select the collocated pair u_2 and y_2 to actively decouple the performance from the disturbance.
3. *Input/Output analogous*: select the input analogous actuator, u_1, to directly control the disturbance and output analogous sensor, y_2 to directly measure the sensor.

We compare these intuitive selections with the prediction of the sensor/actuator effectiveness matrix.

A four-state state-space model for the system is developed. Both sensors and both actuators are scaled identically and the sensor/actuator assessment matrix is computed and $\log(S_t)$ is plotted in Table 3.7.

The larger the element in Table 3.7, the greater the predicted effectiveness of that sensor/actuator combination for closed-loop control. Contrary to the intuitive predictions, S_t indicates that u_2 and y_1 are the most effective sensor and actuator for SISO control.

TABLE 3.7 Sensor/Actuator matrix, S_t, for 2-dof sensor/actuator effectiveness assessment. The channel deemed best is shaded.

	y_1	y_2
u_1	7.9	3.2
u_2	8.2	7.9

To validate the predictions, a SISO LQG controller is designed for each of the four sensor/actuator possibilities. For comparison purposes each controller is designed with the same sensor noise and control penalty. The resulting LQG costs are presented in Table 3.8.

TABLE 3.8 H_2 cost for SISO LQG controllers designed for 2-dof sensor/actuator effectiveness assessment. The channel calculated to be best is shaded.

	y_1	y_2
u_1	0.111	0.241
u_2	0.003	0.111

We see that the relative costs agree exactly with the relative magnitude of the elements of S_t from Table 3.7 (small LQG costs correspond to large elements on S_t). The S_t prediction of u_2 and y_1 is validated and each of the three intuitive strategies fails. The y_1-to-u_2 control strategy achieves its performance by (1) locating the sensor directly at the disturbance input which provides the most direct estimate of the disturbance, and (2) by locating the actuator directly at the performance measure which provides the most direct control of the performance variable.

On a simple 2-dof system the sensor/actuator assessment matrix demonstrates its utility for determining the effective sensor and actuator sets for control, despite a contradiction with standard design intuition. The predictions of the S_t matrix are shown to agree with the costs determined by LQG controllers.

3.7 Summary

This chapter has detailed an algorithm which computes an index which quantifies the suitability of a particular sensor/actuator pair for control. Relevant applications of the indexing to this thesis include (1) breaking a global system into sensor and actuators set for local control (Note (a) in Figure 1.3), and (2) quantifying the suitability of particular sensor to actuator control channels for controller tuning (Note (d) in Figure 1.3).

The indexing is based on modal controllability weighted by modal contributions to the performance, and on modal observability weighted by modal contributions by the disturbance. The inclusion of performance and disturbance weighting allow a controllability/observability technique to be used with the four-block regulation problem. An additional patch is added to handle actuators which are effective for active output isolation. The final indexing technique is validated with an example of a sensor/actuator selection for LQG control problem. It is shown to perform favorably with little computational burden when compared with other solution methods. As an open-loop technique, the algorithm is limited as a predictor of closed-loop behavior. An example of the limitations will be presented in Section 6.4.5.

Chapter 4

CONTROLLER TUNING

In this chapter, a methodology is developed and detailed which synthesizes a controller using an optimization-based approach that preserves the heritage of conventional control designs. A tuning method is developed whereby the tuned controller achieves improved performance, and/or improved stability robustness, given some allowable deviation from a baseline controller.

Two classes of tuning are developed in parallel:

- *Model-based tuning*: A state-space design model of the plant is available (A, B, C, D). Where possible, cost expressions and gradients are expressed exactly in terms of state-space variables. Absolute stability is evaluated by checking closed-loop eigenvalues.
- *Data-based tuning*: Frequency response data is available for the plant $G(s)$. Cost expressions and gradients are written at a discrete number of frequency points. Absolute stability is evaluated with graphical methods such as the MIMO Nyquist criteria.

The tuning strategy is developed for both of these cases in parallel. The tuning methodology is developed by forming a cost function which is made up of metrics which quantify: performance, stability robustness, deviation from the baseline controller, and controller channel gain.

In the chapter, the costs are quantified and gradient expressions with respect to control parameters are derived for both model-based and data-based tuning. A general parameterization of a controller is presented. A nonlinear program used for decreasing the augmented cost is discussed. Applications of the tuning method will be presented for: (1) augmenting the controller by adding states, (2) controlling the closed-loop bandwidth, (3) adding or removing control channels, and (4) controlling the actuator use over specific bands. As a special case, the tuning of Sensitivity-weighted LQG controllers will be discussed.

4.1 Closed-Loop Tuning Costs and Gradients

To tune the baseline controller an optimization cost must be formed. Based on the ideal constrained optimization *Problem 1* described by Equation 2.32 we form a simplified cost that allows the solution of an unconstrained optimization problem. We form an augmented cost:

$$J_A(p) \;=\; J(p) + S_R(p) + d(p) + M(p) \tag{4.1}$$

The terms of the augmented cost are described in Table 4.1.

TABLE 4.1 Description of the terms of the augmented tuning cost. Included are references to the equations of the mathematical definitions of the cost components for both model-based and data-based tuning.

Cost terms	Description	Definition model	Definition data
J	Closed loop performance. Smaller magnitude indicates improved performance	Eq. 4.40	Eq. 4.52
S_R	Stability margin. Formed from a combination of two stability robustness measures(S_S and S_{cr}). Smaller magnitude indicates better robustness.	(S_S) : Eq. 4.9 (S_{cr}) : Eq. 4.37	Eq. 4.9 Eq. 4.37
d	Deviation from nominal controller. Smaller magnitude indicates less deviation.	Eq. 4.57	Eq. 4.62
M	Control channel magnitudes weighting. Smaller magnitude indicates that the designer-selected control channel have decreased their gain.	Eq. 4.64	Eq. 4.71

By minimizing the augmented cost of Equation 4.1 we indirectly solve the constrained optimization *Problem 1* specified in Equation 2.32. Selection of relative weighting vectors allows the control tuner to trade performance, stability robustness, deviation from the baseline control and control gain. We elect to tune with this unconstrained cost for three reasons: (1) unconstrained optimization steps are computationally simpler, (2) relaxed constraints allow the tuner to explore more of the controller space, and (3) relaxed constraints allow systems trades between the terms of the augmented cost, *e.g.* trading performance with stability robustness. The third reason is important for conceptual system design as will be demonstrated on a one-dimensional interferometer model in Chapter 5.

The vector, p, parameterizes the tuned controller. A function P is defined such that

$$K(s,p) = P(K_b(s),p). \tag{4.2}$$

Thus, given the constant baseline controller K_b, the tuned controller is uniquely determined by the parameter vector, p.

The gradients of the augmented cost can be written as,

$$\nabla J_A(p) = \nabla J(p) + \nabla S_R(p) + \nabla d(p) + \nabla M(p). \tag{4.3}$$

where the gradient operator, $\nabla(\cdot)$, represents a vector formed of partial derivatives with respect to controller parameters,

$$\nabla(\cdot) \equiv \begin{bmatrix} \dfrac{\partial(\cdot)}{\partial p_1} & \cdots & \dfrac{\partial(\cdot)}{\partial p_{n_p}} \end{bmatrix}^T. \tag{4.4}$$

In this section each term of the augmented cost will be mathematically defined as it applies to both model-based and data-based tuning. Further, the expressions for the gradients for each of the cost terms will be developed.

4.1.1 Stability Robustness Metrics

The second term in the augmented cost of Equation 4.1 corresponds to a measure of the stability robustness of the system. We develop two metrics of stability robustness in this section which are combined as

$$S_R = (1-\gamma_{cr})S_S + \gamma_{cr}S_{cr} \tag{4.5}$$

to form the stability term of Equation 4.1. $S_S > 0$ is a scalar which quantifies the deviation of the maximum singular value of the system's Sensitivity transfer matrix over a threshold in a bandwidth of interest. $S_{cr} > 0$ is a scalar which corresponds to the distance of the Nyquist locus from the critical point integrated over a bandwidth of interest (generally near crossover). The mixing parameter $\gamma_{cr} \in [0, 1]$ allows the two stability metrics to be combined in a specified ratio. Figure 4.1 is a graphical example of the two stability metrics.

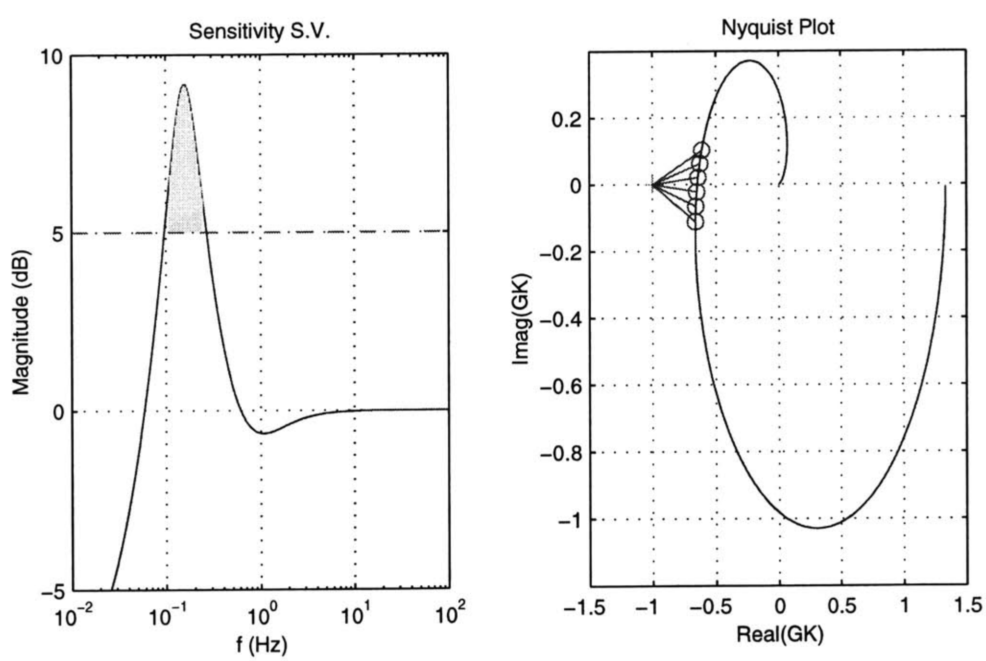

Figure 4.1 Two measures of stability robustness: The left plot corresponds to S_s where the shaded area measures the deviation of the maximum singular value of the Sensitivity over the 5 dB threshold. The right plot demonstrates S_{cr} which measures the sum of the distances from the (-1,0) critical point to the critical Nyquist locus points marked with circles.

The S_S metric follows from the small gain theorem and the MIMO gain and phase margin (Section 2.1.3). These margins are often very conservative but the MACE program demonstrated the peaks in the maximum singular value of the sensitivity correspond to potential instabilities in practice. As a rule of thumb peaks greater than 10 dB, at frequencies where we have less confidence in the model, indicate a poor controller design [Miller et al., 1996]. The S_{cr} metric follows from a SISO argument that crossing over away from the critical point (on the Nyquist plot) ensures good stability margins. In general, the SISO logic does not extend to MIMO systems [Grocott, 1994], but in practice, near passes of the critical point often do lead to poor stability margins and should be avoided. [Masters, 1997] demonstrated the usefulness of this type of stability robustness metric by manually tuning the controller parameters to increase robustness, with little degradation of performance. The controller poles where perturbed to expand small loops and near encirclements of the critical point, increasing robustness enough to allow implementation of the controller.

The following development quantifies both stability robustness metrics, and derives their gradients with respect to the controller parameters.

A) Maximum Sensitivity Singular Value Stability Metric

To determine the sensitivity of the stability robustness of the closed-loop system with respect to the controller parameters, we appeal to the Sensitivity transfer matrix as discussed in Chapter 2. We can derive expressions for the sensitivity of $S(j\omega, p)$ with respect to the parameters, p, and the frequency ω. We assume that: (1) that the system is closed-loop and stable, and (2) that $S(j\omega, p)$ is an analytic function of p and ω. Note that undamped poles will force $S(j\omega, p)$ to not be an analytic function of ω, but that our stability assumption (1) forbids this. Our particular interest is with the maximum singular value of the sensitivity $\sigma_{\max}(S(j\omega, p))$ since the conservative MIMO gain and phase margin expressions depend on the maximum singular value of the Sensitivity transfer matrix (Equations 2.25 and 2.26)

For analytic computation reasons an area metric is chosen to approximate the peak value of $\sigma_{max}(S(j\omega, p))$.

$$S_S(p) = \frac{1}{\pi}\int_0^\infty g(\sigma_{max}(S(j\omega, p)))d\omega \tag{4.6}$$

Due to the Bode integral theorem, there is a fundamental conservation of the net area of $S(j\omega, p)$ computed in decibels (dB) with respect to 0 dB (Freudenberg and Looze, 1985). To circumvent this limitation we wish to compute the area of the $\sigma_{max}(S(j\omega, p))$ curve which lies greater than some frequency dependent threshold, $T_S(\omega) \geq 0$. The threshold can be large where confidence in the model (data) is good (typically low frequency), and should be lower near crossover and where confidence in the model is less. Thus we trade an increase in $\sigma_{max}(S(j\omega, p))$ up to the threshold $T_S(\omega)$ to push down $\sigma_{max}(S(j\omega, p))$ in frequency regions where $\sigma_{max}(S(j\omega, p)) \geq T_S(\omega)$. Tuning to improve the stability robustness is dependent on the designer's selection of $T_S(\omega)$.

From the above discussion we note that a simple implementation of the threshold is to use logic:

$$g(x) = \begin{matrix} x^2 \text{ for } x > T_S(\omega) \\ 0 \text{ for } x \leq T_S(\omega) \end{matrix} . \tag{4.7}$$

where $x = \sigma_{max}(S(j\omega, p))$. However, to allow the computation of gradients with respect to controller parameters we need to preserve differentiability in the threshold. We approximate the function of Equation 4.7 using the smooth function

$$g(x) = x^2\left[\frac{\arctan(\alpha\{\ln(x) - T_S(\omega)\})}{\pi} + \frac{1}{2}\right]. \tag{4.8}$$

To visualize the effect of the smooth function we plot a sample case in Figure 4.2. The lower figure plots $\left[\frac{\arctan(\alpha\{\ln(x) - T_S(\omega)\})}{\pi} + \frac{1}{2}\right]$ for $x = 20\log_{10}(\sigma_{max}(S))$ and $T_S(\omega) = 5\text{dB}\ \forall\omega$ as α is varied. As α is increased the function approaches the desired switching function of Equation 4.7. α must not set too large since near-singular gradients at the $x = T_S(\omega)$ points will result.

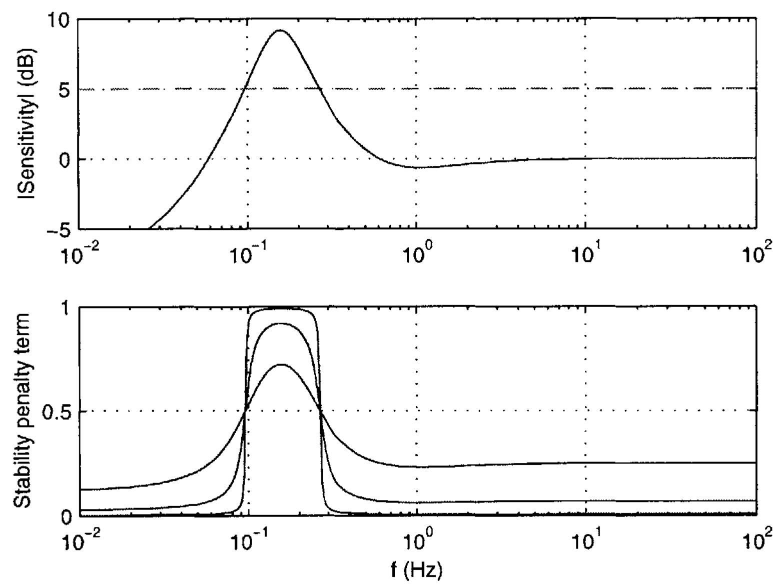

Figure 4.2 Stability penalty term of Equation 4.8. Upper plot: Maximum s.v. of a Sensitivity Transfer Matrix. Bottom plot: stability penalty term plotted for three values of α. As α is increased the stability penalty for deviations greater than the 5 dB threshold is made sharper (*i.e.* small deviations are penalized like large deviations)

Our stability robustness cost is computed numerically by approximating the integral of Equation 4.6 with a summation over a discrete set of n_ω frequencies, $\{\omega_k\}$

$$S_S(p) = \frac{1}{\pi}\sum_{k=1}^{n_\omega} W_S(\omega)(\sigma_{\max}(S))^2\left[\frac{\arctan(\alpha\{\ln(\sigma_{\max}(S)) - T_S(\omega)\})}{\pi} + \frac{1}{2}\right]\Delta\omega_k \tag{4.9}$$

where the ω and p dependence of the sensitivity, S, has been dropped for convenience and $W_S(\omega)$ is a designer-defined frequency-dependent weighting function. $W_S(\omega)$ allows the designer to trade the relative weight of $S_S(p)$ with the other terms of J_A, and with $T_S(\omega)$ to control the bandwidth of the controller by penalizing any spikes in $\sigma_{\max}(S)$ at a frequency greater than crossover.

We compute the gradient of $S_S(p)$ with respect to the i-th parameter

$$\frac{\partial S_S}{\partial p_i} = \frac{1}{\pi^2}\sum_{k=1}^{n_\omega} W_S\sigma_{\max}(S)\left[2\arctan(\alpha[\Delta S]) + \frac{\alpha}{1+(\alpha[\Delta S])^2} + \pi\right]\frac{\partial\sigma_{\max}(S)}{\partial p_i}\Delta\omega_k \quad (4.10)$$

where $\Delta S = \ln(\sigma_{\max}(S)) - T_S(\omega)$. To evaluate this gradient we require an expression for the gradient of the maximum singular value of the sensitivity with respect to the controller parameters, $\frac{\partial\sigma_{\max}(S)}{\partial p_i}$. The following development outlines that calculation.

Singular Value Sensitivity

We determine a relationship for the sensitivity of the singular values of a transfer matrix, $G(j\omega, p) \in C^{n_o \times n_i}$ with respect to a parameter vector p. In our case, p is a vector corresponding to the controller parameters which will be tuned. We let $n_l = \min(n_o, n_i)$. We begin by decomposing $G(j\omega, p)$ with a Singular Value Decomposition (SVD), [Press et al., 1992],

$$G(j\omega, p) = U(j\omega, p)\Lambda(j\omega, p)V^H(j\omega, p) \quad (4.11)$$

where $U(j\omega, p) \in C^{n_o \times n_o}$ and $V(j\omega, p) \in C^{n_i \times n_i}$ are unitary matrices: $UU^H = I$, and $VV^H = I$, and $\Lambda(j\omega, p) = diag[\sigma_1, \sigma_2, \ldots, \sigma_{n_l}] \in C^{n_o \times n_i}$ is formed from diagonal entries, namely the non-zero singular values, $\sigma_l(j\omega, p), l = 1, \ldots, n_l$ and zero blocks such that the dimensions are commensurate. $(\cdot)^H$ is the Hermitian (conjugate, transpose) operator. We rewrite Equation 4.11, with a summation as,

$$G(j\omega, p) = \sum_{l=1}^{n_l} u_l(j\omega, p)\sigma_l(j\omega, p)v_l^H(j\omega, p) \quad (4.12)$$

where, for convenience, the summation is carried only over non-zero singular values. By taking advantage of the unitary nature of U and V we can write,

$$G(j\omega, p)v_l(j\omega, p) = \sigma_l(j\omega, p)u_l(j\omega, p) \ , \quad (4.13)$$

and by taking the Hermitian of Equation 4.12, we write

$$G^H(j\omega, p)u_l(j\omega, p) = \sigma_l(j\omega, p)v_l(j\omega, p) \quad . \tag{4.14}$$

Now we take derivatives with respect to the parameter, p, of Equations 4.13 and 4.14 respectively to arrive at,

$$\frac{\partial G}{\partial p_i}v_l + G\frac{\partial v_l}{\partial p_i} = \frac{\partial u_l}{\partial p_i}\sigma_l + u_l\frac{\partial \sigma_l}{\partial p_i} \tag{4.15}$$

and,

$$\frac{\partial G^H}{\partial p_i}u_l + G^H\frac{\partial u_l}{\partial p_i} = \frac{\partial v_l}{\partial p_i}\sigma_l + v_l\frac{\partial \sigma_l}{\partial p_i} \tag{4.16}$$

where we have dropped the $(j\omega, p)$ dependence for compactness. Here we have assumed that the singular values and singular vectors are analytic (*i.e.* the above derivatives exist). In general they are [Sun, 1988], though three difficulties exist: (1) small singular values need not be analytic, *e.g.* the singular value of the scalar α is $|\alpha|$ which is not analytic near 0, and (2) we must pay close attention to the ordering of singular values to preserve analyticity, and (3) the derivation holds for simple (non repeated) singular values. We continue the derivation by assuming these three conditions are held, an assumption that will be justified in our application of the result.

We pre-multiply Equation 4.15 by u_l^H to arrive at,

$$u_l^H\frac{\partial G}{\partial p_i}v_l + u_l^H G\frac{\partial v_l}{\partial p_i} = \sigma_l u_l^H\frac{\partial u_l}{\partial p_i} + \frac{\partial \sigma_l}{\partial p_i} , \tag{4.17}$$

where $u_l^H u_l = 1$ has been used. Similarly we pre-multiply Equation 4.16 by v_l^H to arrive at,

$$v_l^H\frac{\partial G^H}{\partial p_i}u_l + v_l^H G^H\frac{\partial u_l}{\partial p_i} = \sigma_l v_l^H\frac{\partial v_l}{\partial p_i} + \frac{\partial \sigma_l}{\partial p_i} . \tag{4.18}$$

In Equation 4.17 we substitute the Hermitian of Equation 4.14, $u_l^H G = \sigma_l v_l^H$, to get

$$u_l^H \frac{\partial G}{\partial p_i} v_l + \sigma_l v_l^H \frac{\partial v_l}{\partial p_i} = \sigma_l u_l^H \frac{\partial u_l}{\partial p_i} + \frac{\partial \sigma_l}{\partial p_i}, \tag{4.19}$$

and in Equation 4.18 we substitute the Hermitian of Equation 4.13, $v_l^H G^H = \sigma_l u_l^H$, to get

$$v_l^H \frac{\partial G^H}{\partial p_i} u_l + \sigma_l u_l^H \frac{\partial u_l}{\partial p_i} = \sigma_l v_l^H \frac{\partial v_l}{\partial p_i} + \frac{\partial \sigma_l}{\partial p_i} \tag{4.20}$$

We add Equations 4.19 and 4.20, and cancel like terms to arrive at,

$$2\frac{\partial \sigma_l}{\partial p_i} = u_l^H \frac{\partial G}{\partial p_i} v_l + v_l^H \frac{\partial G^H}{\partial p_i} u_l . \tag{4.21}$$

By manipulation of Equation 4.21 we have the desired result:

$$\frac{\partial}{\partial p_i}\sigma_l(j\omega, p) = \mathrm{Re}\left(u_l^H(j\omega, p)\frac{\partial}{\partial p_i}G(j\omega, p)v_l(j\omega, p)\right). \tag{4.22}$$

This very useful result is proved in a more rigorous manner in [Sun, 1988] using the Implicit Function Theorem. Alternate expressions for the singular value sensitivity based on the generalized sine of the singular value vectors are derived in [Stewart and Sun, 1990].

Using the result of Equation 4.22 we can derive the sensitivity of the maximum singular value of the Sensitivity Transfer Matrix. We divide our derivation into two cases:

(1) Design Model

In the first case, we have a state-space representation of the design model $\{A, B_u, C_y, D_{yu}\}$ and of the controller of Equation 2.5, $\{A_c(p), B_c(p), C_c(p)\}$. We can determine the state-space representation of $S(j\omega, p)$, $\{A_s(p), B_s(p), C_s(p), D_s\}$ using Equation 2.16. We can write the Sensitivity as

$$S(j\omega, p) = C_s(p)(j\omega I - A_s(p))^{-1}B_s(p) + I \ , \tag{4.23}$$

where we have set $D_s = I$.

We note that by writing $MM^{-1} = I$ for an invertible matrix M, we can apply the product rule to write

$$\frac{dM}{dp_i}M^{-1} + M\frac{dM^{-1}}{dp_i} = 0 \tag{4.24}$$

which can be reduced to,

$$\frac{dM^{-1}}{dp_i} = -M^{-1}\frac{dM}{dp_i}M^{-1} \ . \tag{4.25}$$

By applying the chain rule to Equation 4.23 and substituting $M = sI - A_s$ in Equation 4.25, we arrive at

$$\begin{aligned}\frac{\partial S}{\partial p_i} = {} & \frac{\partial C_s}{\partial p_i}(j\omega I - A_s)^{-1}B_s + C_s(j\omega I - A_s)^{-1}\frac{\partial A_s}{\partial p_i}(j\omega I - A_s)^{-1}B_s \\ & + C_s(j\omega I - A_s)^{-1}\frac{\partial B_s}{\partial p_i}\end{aligned} \tag{4.26}$$

where we have dropped the $(j\omega, p)$ dependence for convenience. From Equation 2.16 we have

$$\frac{\partial A_s}{\partial p_i} = \begin{bmatrix} 0 & B_u\frac{\partial C_c}{\partial p_i} \\ \frac{\partial B_c}{\partial p_i}C_y \ \frac{\partial A_c}{\partial p_i} + \frac{\partial B_c}{\partial p_i}D_{yu}C_c + B_cD_{yu}\frac{\partial C_c}{\partial p_i} \end{bmatrix}, \frac{\partial B_s}{\partial p_i} = \begin{bmatrix} 0 \\ \frac{\partial B_c}{\partial p_i} \end{bmatrix}, \frac{\partial C_s}{\partial p_i} = \begin{bmatrix} 0 & D_{yu}\frac{\partial C_c}{\partial p_i} \end{bmatrix} \ . \tag{4.27}$$

By substituting $S(j\omega, p) = G(j\omega, p)$ in Equation 4.11 and by using Equation 4.26 in Equation 4.22, we have a closed form expression for the sensitivity of the singular values of $S(j\omega, p)$ with respect to the parameter p, $\frac{\partial}{\partial p_i}\sigma_l(S(j\omega, p))$.

In a similar manner, by using

$$\frac{\partial}{\partial \omega}S(j\omega, p) = -jC_s(p)(j\omega I - A_s(p))^{-2}B_s(p) \tag{4.28}$$

in place of Equation 4.26, we can derive an expression for the sensitivity of the singular values with respect to the frequency ω, $\frac{\partial}{\partial \omega}\sigma_l(S(j\omega, p))$.

(2) Measurement Data

By identifying our plant with a spectrum analyzer, we can experimentally determine a measurement model for the $G_{yu}(s)$ transfer matrix. $G_{yu}(j\omega_k)$ is measured at a set of frequencies $\{\omega_k, k = 1, \ldots, n_\omega\}$. We use Equation 2.9 with our measurement model to derive a pseudo-measured Sensitivity transfer matrix,

$$S(j\omega_k, p) = (I - G_{yu}(j\omega_k)K(j\omega_k, p))^{-1}, k = 1, \ldots, n_\omega \tag{4.29}$$

By substituting the state-space controller notation of Equation 2.5 we have,

$$S\,(j\omega_k, p) = (I - G_{yu}(j\omega_k)C_c(p)(j\omega_k I - A_c(p))^{-1}B_c(p))^{-1}. \tag{4.30}$$

We will ensure parameter p enters the controller matrices $\{A_c(p), B_c(p), C_c(p)\}$ analytically so that $S(j\omega_k, p)$ is an analytic function of p. We apply the rule of Equation 4.25 to the derivative of the transfer matrix corresponding to the controller and find,

$$\begin{aligned}\frac{\partial K}{\partial p_i} &= \frac{\partial C_c}{\partial p_i}(j\omega I - A_c)^{-1}B_c + C_c(j\omega I - A_c)^{-1}\frac{\partial A_c}{\partial p_i}(j\omega I - A_c)^{-1}B_c \\ &+ C_c(j\omega I - A_c)^{-1}\frac{\partial B_c}{\partial p_i} \\ &= \frac{\partial C_c}{\partial p_i}\Phi_c B_c + C_c\Phi_c\frac{\partial A_c}{\partial p_i}\Phi_c B_c + C_c\Phi_c\frac{\partial B_c}{\partial p_i}\end{aligned} \tag{4.31}$$

where we have dropped the written dependence on $(j\omega_k, p)$ for convenience, substituted the notation $\Phi_c(j\omega_k, p) = (j\omega_k I - A_c(p))^{-1}$. To determine the sensitivity of $S(j\omega_k, p)$ with respect to p again we apply the rule of Equation 4.25 and find

$$\begin{aligned}\frac{\partial S}{\partial p_i} &= (I - G_{yu}K)^{-1}\left[\frac{\partial}{\partial p_i}(I - G_{yu}C_c(j\omega_k I - A_c)^{-1}B_c)\right](I - G_{yu}K)^{-1} \\ &= S(j\omega_k, p)G_{yu}(j\omega_k)\left(\frac{\partial}{\partial p_i}K(j\omega_k, p)\right)S(j\omega_k, p)\end{aligned} \tag{4.32}$$

where we have defined $S(j\omega_k, p)$ as in Equation 4.30.

By substituting Equation 4.30 into Equation 4.11 and Equation 4.32 into Equation 4.22 we have the desired singular value sensitivities, $\frac{\partial}{\partial p_i}\sigma_l(S(j\omega_k, p))$. We should note that since $G_{yu}(j\omega_k)$ is defined only for a discrete set of frequency points, ω_i, then $S(j\omega_k, p)$ is not an analytic function of ω and analytic expressions for $\frac{\partial}{\partial\omega}\sigma(S(j\omega_k, p))$ do not exist.

Computational Algorithm

Based on the expressions of the two previous subsections, we are prepared to outline an algorithm for determining the sensitivity of the maximum singular value of $S(s)$ at a vector of frequency points, $\{\omega_k, k = 1, \ldots, n_\omega\}$ in both the design model and measurement model cases. We outline steps that are taken to increase computational efficiency. Figure 4.3 is a flowchart of the algorithm.

The flowchart treats both design model and measurement model with a decision at the top. We iterate over each frequency, ω_k, to compute the Sensitivity transfer matrix, evaluated

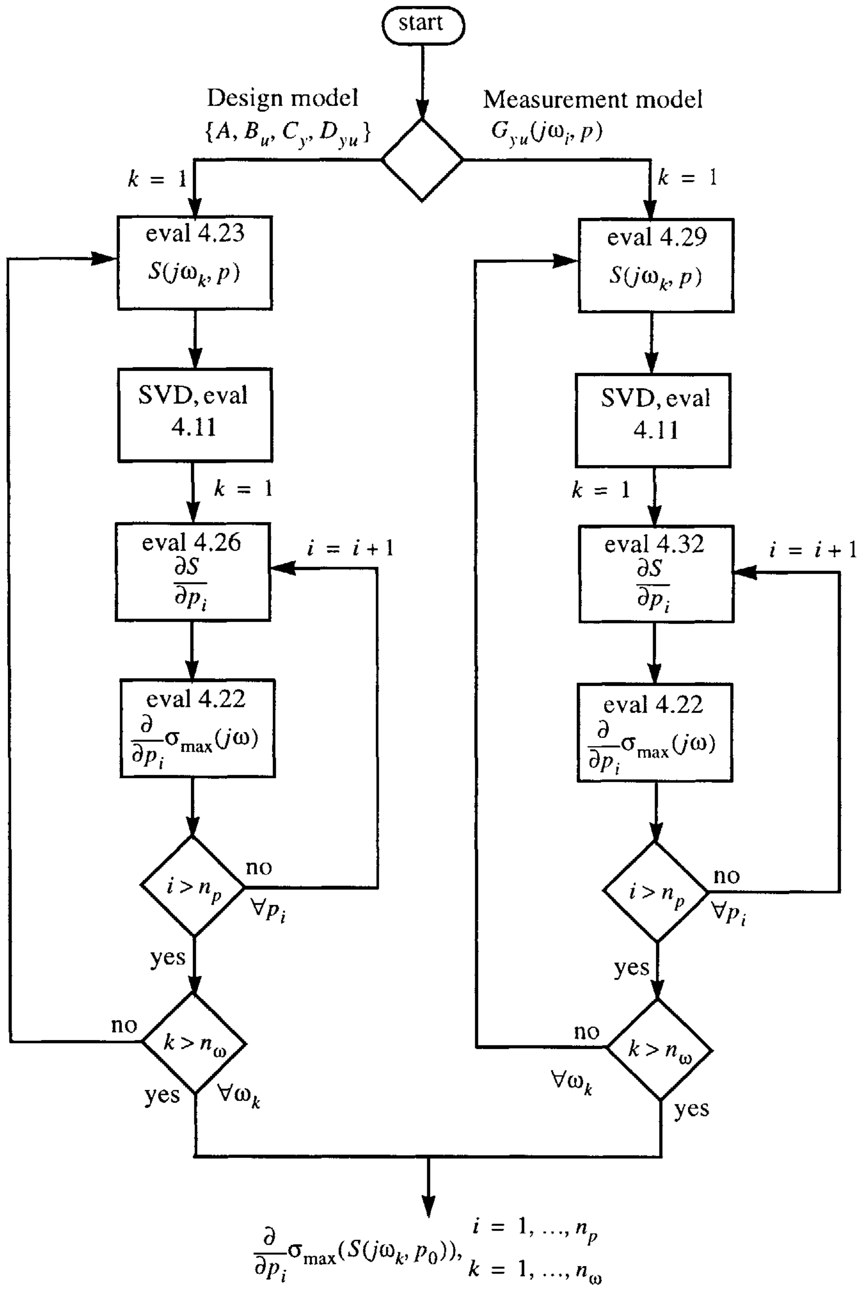

Figure 4.3 Flow chart for an algorithm to compute the sensitivity of the maximum singular value of the Sensitivity transfer matrix with respect to controller parameters. Both design model and measurement model cases are presented.

at ω_k, and the corresponding singular value decomposition. We then iterate over each parameter, p_j for $j = 1, \ldots, n_p$ and evaluate $\frac{\partial S}{\partial p_j}$ using Equation 4.26 in the design model case, or Equation 4.32 in the measurement model case. Equation 4.22 is used to evaluate $\frac{\partial}{\partial p_i}\sigma_{\max}(j\omega)$.

Computing a resolvant, $\Phi(\omega_k) = (j\omega_k I - A_r)^{-1}$, for $k = 1, \ldots, n_m$ is computationally intensive. We assume A_r has no repeated eigenvalues, such that it can be diagonalized as

$$A_r = V_r \Lambda_r V_r^{-1} \tag{4.33}$$

where Λ_r is a matrix with the eigenvalues, $\{\lambda_l\}$, of A_r along the diagonal, and V_r is a matrix of the corresponding eigenvectors. We rewrite the resolvant as,

$$\begin{aligned} \Phi(\omega_k) &= (j\omega_k I - A_r)^{-1} \\ &= (j\omega_k V_r^{-1} V_r - V_r^{-1} \Lambda_r V_r)^{-1} \\ &= V_r^{-1} \operatorname{diag}\left(\frac{1}{j\omega_k - \lambda_l}\right) V_r \end{aligned} \tag{4.34}$$

where $\operatorname{diag}(v)$ is an operator which forms a matrix with the elements of the vector v along the diagonal. Thus, a costly matrix inverse is transformed into a set of scalar division with a sparse matrix multiplication. The eigenvalue decomposition needs only to be performed once, independent of the frequency points ω_k.

Figure 4.4 is a plot of the maximum and minimum singular values of the sensitivity of a plant and the sensitivity as computed analytically and with finite differences. The two methods for computing are in agreement, validating our analytic expressions for the sensitivity. At a frequency of 0.033 Hz there is a discontinuity in the maximum singular value of the sensitivity transfer matrix. The gradient is not defined at exactly the discontinuity frequency, but the effect is very local. In our case, the discontinuities are ignored since they occur at an exact evaluation frequency with an insignificant probability. In practice, this oversight has not led to problems with the examples in the thesis. Subgradients [Boyd and Barratt, 1991] can handle the discontinuities with sophistication but practical examples have not warranted the added complexity of their implementation.

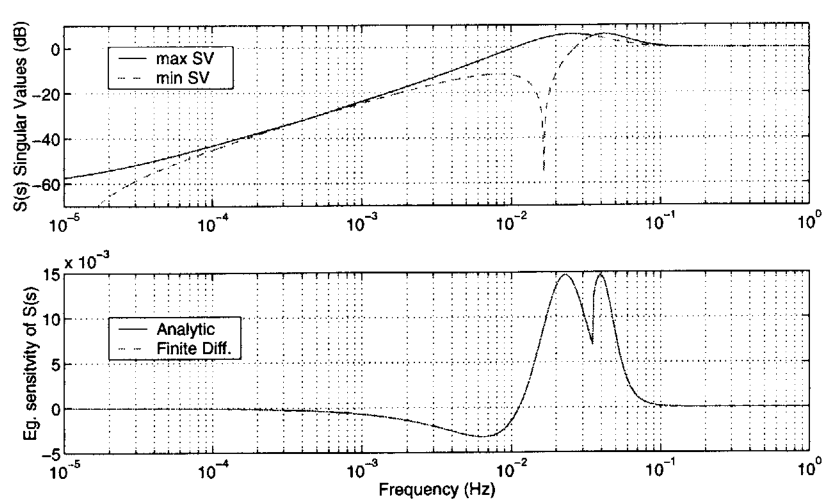

Figure 4.4 Top: singular values of a sample sensitivity transfer matrix, Bottom: sensitivity of the singular values with respect to a controller parameter. Analytic and finite difference calculation is shown.

B) Critical Point Distance Metric

A second stability metric is the distance of the MIMO Nyquist locus from the critical point. Though [Grocott, 1994] has demonstrated that the MIMO Nyquist locus does not provide a stability margin metric in a strict theoretical sense, in practice the distance to the critical point does quantify stability robustness to a multiplicative uncertainty. Thus a metric is created which quantifies stability robustness in terms of the minimum distance to the critical point.

The Nyquist function is defined in Equation 2.29 to be given by

$$H_n(j\omega) = -1 + \det(I - G_{yu}(j\omega)K(j\omega)). \tag{4.35}$$

Where $H_n(j\omega) = \mathrm{Re}\{H_n(j\omega)\} + i\mathrm{Im}\{H_n(j\omega)\}$. The critical point is given by $P_{cr} = -1$ such that the distance from the Nyquist locus to the critical point is

$$\begin{aligned} d_{cr}^2(j\omega) &= [P_{cr} - H_n(j\omega)][P_{cr} - H_n(j\omega)]^H \\ &= [\det(I - G_{yu}(j\omega)K(j\omega))][\det(I - G_{yu}(j\omega)K(j\omega))]^H \end{aligned}. \tag{4.36}$$

A metric which captures the distance from the Nyquist curve to the critical point is defined to be:

$$S_{cr} = \frac{1}{\pi} \sum_{k=1}^{n_\omega} W_{cr}(\omega_k) \frac{1}{d_{cr}^2(j\omega_k)} \Delta\omega_k . \tag{4.37}$$

Thus we penalize a close pass to the critical point.

In the case of a non-singular matrix $M(p)$ with distinct eigenvalues the following result can be shown [Athans and Schweppe, 1965]:

$$\begin{aligned} \frac{d}{dp}\det[M(p)] &= \mathrm{trace}\left[M(p)^\dagger \frac{d}{dp}M(p)\right] \\ &= \det[M(p)]\,\mathrm{trace}\left[M(p)^{-1}\frac{d}{dp}M(p)\right] \end{aligned} \tag{4.38}$$

where $(\cdot)^\dagger$ represents the adjoint of a matrix which can be written as $(\cdot)^\dagger = \det(\cdot)(\cdot)^{-1}$ in the case of an invertible matrix (*i.e.* consistent with our assumption on non-singularity).

By applying Equation 4.38 to the metric of Equation 4.37 under the practical assumption that for the frequencies of interest, $\{\omega_k, k = 1, \ldots, n_\omega\}$, $H_n(j\omega_k)$ is non-singular and with distinct eigenvalues, we have

$$\frac{\partial S_{cr}}{\partial p_i} = \frac{2}{\pi} \sum_{k=1}^{n_\omega} W_{cr}(\omega_k) \frac{1}{d_{cr}^2(j\omega_k)} \mathrm{Re}\left((I - G_{yu}K)^{-1} G_{yu} \frac{\partial}{\partial p_i} K(p)\right) \Delta\omega_k \tag{4.39}$$

where $\frac{\partial}{\partial p_i}K(p)$ is computed with Equation 4.31.

The S_{cr} stability robustness metric is defined at a discrete number of frequency points and is not obviously extended to a continuous metric. Thus the model-based and data-based representations of the metric are identical.

Stability Robustness Metric – Limitations

Both measures of stability robustness, S_S and S_{cr}, represent a trade between accuracy and computational complexity. The application of the augmented cost in an iterative nonlinear program requires that the stability robustness metric be computed quickly. Further, the nonlinear program requires that the gradients of the stability metric be readily computable. Both of these required characteristics limit the choice of a metric of stability robustness and preclude modern measures of stability robustness such as μ.

The developed stability robustness metrics, S_S and S_{cr} capture multiplicative (and divisive uncertainty). For most examples in the thesis, including SIM (and also NGST), the G_{yu} transfer matrix corresponds to active optics which do not strongly couple to the structure. G_{yu} is simple, without structural flexibility, and the developed stability metrics capture stability robustness of the active optics loops.

In Chapter 5 S_S and S_{cr} are used on a one-dimensional interferometer model to capture structural uncertainty. There are limitations, however. For example, a slight perturbation in the frequency of a flexible mode may cause a large spike in the maximum singular value of the Sensitivity transfer matrix, while prior to the perturbation, the Sensitivity s.v. was smooth. Examples of this type of system behavior are documented in [Miller et al., 1996] and are common to the structural control of flexible systems. For parametric uncertainty, the structured singular value, μ [Zhou et al., 1996], and its easier-to-compute derivatives, such as Popov [How, 1993] have been developed. To safeguard against the limitations of S_S and S_{cr}, as stability robustness metrics the use of the parametric stability robustness measures is recommended in the evaluation of the tuned controllers (see Section 2.2.6).

4.1.2 Performance Metric

We derive an expression for the sensitivity of the performance, $J(K(p))$, as a function of the controller parameters, p. To formulate the problem, we implicitly assume a regulator control problem, and further we will use an H_2 (RMS) performance metric. Again, we assume the system is (1) stable so that the H_2 norm exists and (2) that $J(K(j\omega, p))$ is an analytic function of p. Again, we continue our derivation for two cases:

(1) Design Model

In this case, we have a state-space representation of the design model $\{A, B_u, C_y, D_{yu}\}$ and of the controller of Equation 2.5, $\{A_c(p), B_c(p), C_c(p)\}$. A similar derivation can be found in [Gutierrez, 1999]. We set up the state-space system for the closed-loop as in Equation 2.7. The H_2 performance can be written as,

$$J(K(p)) = \mathrm{tr}[C_z^{(cl)}(p)\Sigma_{xx}(p)(C_z^{(cl)}(p))^T] \tag{4.40}$$

where $\Sigma_{xx}(p)$ is the solution of the Lyapunov Equation,

$$A^{(cl)}(p)\Sigma_{xx}(p) + \Sigma_{xx}(p)(A^{(cl)}(p))^T + B_w^{(cl)}(p)(B_w^{(cl)}(p))^T = 0 . \tag{4.41}$$

We form an augmented cost by appending Equation 4.41 with a Lagrange Multiplier matrix, L,

$$J(K(p)) = \mathrm{tr}[C_z^{(cl)}\Sigma_{xx}(C_z^{(cl)})^T] + \mathrm{tr}[L(A^{(cl)}\Sigma_{xx} + \Sigma_{xx}(A^{(cl)})^T + B_w^{(cl)}(B_w^{(cl)})^T)] \tag{4.42}$$

where the explicit dependence on the controller parameters, p is dropped for notational convenience.

To determine sensitivities, we take partial derivatives of the augmented cost with respect to our set of variables, L, Σ_{xx}, and p. The partial with respect to the Lagrange Multiplier, $\frac{\partial}{\partial L}J(K(p))$ recovers the Constraint Equation 4.41. The partial with respect to the closed-loop state covariance is 0 along the optimal trajectory and calculated as,

$$\begin{aligned} \frac{\partial}{\partial \Sigma_{xx}}J(K(p)) &= \frac{\partial}{\partial \Sigma_{xx}}\mathrm{tr}[C_z^{(cl)}\Sigma_{xx}(C_z^{(cl)})^T] + \frac{\partial}{\partial \Sigma_{xx}}\mathrm{tr}[LA^{(cl)}\Sigma_{xx}] + \frac{\partial}{\partial \Sigma_{xx}}\mathrm{tr}[L\Sigma_{xx}(A^{(cl)})^T] \\ &= (C_z^{(cl)})^T C_z^{(cl)} + LA^{(cl)} + (A^{(cl)})^T L \\ &= 0 \end{aligned} \tag{4.43}$$

where we have taken advantage of the properties of the trace operator. Finally we form the partial with respect to the i-th parameter, p_i, $i = 1, \ldots, n_p$, to arrive at,

$$\begin{aligned}\frac{\partial}{\partial p_i}J(K(p)) &= \operatorname{tr}\left[\Sigma_{xx}\frac{\partial}{\partial p_i}\left\{C_z^{(cl)}(C_z^{(cl)})^T\right\}\right] \\ &\quad + \operatorname{tr}\left[L\frac{\partial A^{(cl)}}{\partial p_i}\Sigma_{xx} + L\Sigma_{xx}\frac{\partial (A^{(cl)})^T}{\partial p_i} + L\frac{\partial}{\partial p_i}\left\{B_w^{(cl)}(B_w^{(cl)})^T\right\}\right]\end{aligned} \tag{4.44}$$

where

$$\frac{\partial A^{(cl)}}{\partial p_i} = \frac{\partial A_s}{\partial p_i}, \frac{\partial B_w^{(cl)}}{\partial p_i} = \begin{bmatrix} 0 \\ \frac{\partial B_c}{\partial p_i}D_{yw} \end{bmatrix}, \frac{\partial C_z^{(cl)}}{\partial p_i} = \begin{bmatrix} 0 & D_{zu}\frac{\partial C_c}{\partial p_i} \end{bmatrix} \tag{4.45}$$

(Compare with Equation 4.27). To recap, we solve Constraint Equation 4.41 for $\Sigma_{xx}(p)$, then we solve auxiliary Equation 4.43 for Lagrange Multiplier, L, and lastly, we evaluate Equation 4.44 for each parameter, p_i. The Lagrange Multiplier based method requires the solution of two $(n + n_c)$ order Lyapunov equations whereas direct methods (taking gradients of the closed-loop matrices of Equation 2.7) require the solution of $n_p + 1$ $(n + n_c)$ order Lyapunov equations.

(2) Measured Data

We have measured data for the plant transfer matrix, $G(j\omega_k)$ where $\{\omega_k, k = 1, \ldots, n_m\}$ is the set of measurement frequency points. The performance can be experimentally determined using Equation 2.6 such that,

$$\begin{aligned} z(j\omega_k) &= [G_{zw}(j\omega_k) + G_{zu}(j\omega_k)K(j\omega_k)(I - G_{yu}(j\omega_k)K(j\omega_k))^{-1}G_{yw}(j\omega_k)]w(j\omega_k) \\ &= H^{(cl)}(j\omega_k)w(j\omega_k)\end{aligned} \tag{4.46}$$

The experimental H_2 cost can be written with,

$$\begin{aligned} J(K(p)) &= E\left[\sum_{k=1}^{n_\omega} \mathrm{trace}\{z(j\omega_k)z(j\omega_k)^H\}\Delta\omega_k\right] \\ &= E\left[\sum_{k=1}^{n_\omega} \mathrm{trace}\left\{H^{(cl)}(j\omega_k)w(j\omega_k)w(j\omega_k)^H H^{(cl)}(j\omega_k)^H\right\}\Delta\omega_k\right] \\ &= \sum_{k=1}^{n_\omega} \mathrm{trace}\left\{H^{(cl)}(j\omega_k)\Sigma_{ww}(j\omega_k)H^{(cl)}(j\omega_k)^H\Delta\omega_k\right\} \end{aligned} \tag{4.47}$$

where, experimentally, we assume ergodicity and approach the expectation operator, $E(\cdot)$, by averaging over multiple measures. $\Delta\omega_k$ represents the spacing between frequency samples. We have defined the power spectral density of w as $\Sigma_{ww}(j\omega_k) = E(w(j\omega_k)w(j\omega_k)^H)$. Generally, we have no direct measure of the exogenous disturbance, w, though we can measure its effects through the power spectral densities,

$$\Sigma_{zw}(j\omega_k) = G_{zw}(j\omega_k)\Sigma_{ww}(j\omega_k)G_{zw}(j\omega_k)^H , \tag{4.48}$$

$$\Sigma_{yw}(j\omega_k) = G_{yw}(j\omega_k)\Sigma_{ww}(j\omega_k)G_{yw}(j\omega_k)^H . \tag{4.49}$$

We may also have little knowledge of the form of Σ_{ww}. We resolve this by assuming Σ_{ww} can be written as unit intensity white noise, $w^{(w)}$ with $\Sigma_{ww}^{(w)} = I$, driving a whitening filter. If we cascade the whitening filter with the dynamics, Equations 4.48 and 4.49 become

$$\Sigma_{zw}(j\omega_k) = G_{zw}^{(w)}(j\omega_k)G_{zw}^{(w)}(j\omega_k)^H \tag{4.50}$$

$$\Sigma_{yw}(j\omega_k) = G_{yw}^{(w)}(j\omega_k)G_{yw}^{(w)}(j\omega_k)^H \tag{4.51}$$

where in these transfer matrices, the $(\cdot)^{(w)}$ superscript implies plant dynamics concatenated with the whitening dynamics. To extract transfer matrices, $G_{zw}^{(w)}(j\omega_k)$ and $G_{yw}^{(w)}(j\omega_k)$ from power spectral densities, $\Sigma_{zw}(j\omega_k)$ and $\Sigma_{yw}(j\omega_k)$, we assume stable, minimum phase dynamics. We rewrite the cost, Equation 4.47, with the whitening dynamics as,

$$J(K(p)) = \frac{1}{\pi}\sum_{k=1}^{n_\omega} \mathrm{tr}\left\{H^{(cl)}(j\omega_k)H^{(cl)}(j\omega_k)^H\right\}\Delta\omega_k \tag{4.52}$$

where $H^{(cl)}(j\omega_k)$ is defined by substituting $G_{zw}^{(w)}(j\omega_k)$ and $G_{yw}^{(w)}(j\omega_k)$ into Equation 4.46. By applying the product rule to Equation 4.52 we have,

$$\frac{\partial}{\partial p}J(K(p)) = \frac{2}{\pi}\sum_{k=1}^{n_\omega} \mathrm{tr}\left\{Re\left(\left[\frac{\partial}{\partial p}H^{(cl)}(j\omega_k)\right]H^{(cl)}(j\omega_k)^H\right)\Delta\omega_k\right\} \tag{4.53}$$

where

$$\begin{aligned}\frac{\partial H^{(cl)}}{\partial p} &= G_{zu}\frac{\partial K}{\partial p}SG_{yw}^{(w)} + G_{zu}K\frac{\partial S}{\partial p}G_{yw}^{(w)} \\ &= G_{zu}\left[\frac{\partial K}{\partial p}S + K\frac{\partial S}{\partial p}\right]G_{yw}^{(w)}\end{aligned} \tag{4.54}$$

where the $(j\omega_k)$ dependence has been dropped. $S(j\omega_k)$ is the Sensitivity transfer matrix, Equation 4.30. We compute $\frac{\partial}{\partial p}K(j\omega_k, p)$ with Equation 4.31, and $\frac{\partial}{\partial p}S(j\omega_k, p)$ with Equation 4.32.

4.1.3 Compensator Deviation Metric

The deviation of the tuned controller, $K(s, p)$ from the baseline controller, $K_b(s)$, is defined by,

$$d(p) = \alpha_d\|K(s,p) - K_b(s)\| \tag{4.55}$$

In the case of a metric comparing the baseline and tuned compensator no distinction is made between data-based and model-based design. We can devise metrics which use Lyapunov-based exact continuous computation or alternately a metric which evaluates the

the deviation metric at the frequencies of interest. For computational ease, the 2-norm is used. The penalty for the use of the 2-norm is that the high control gain frequency regions are weighted disproportionately strongly. The logarithmic cost function of [Jacques, 1995] could be used to allow the weight controller zeros. Alternately, deviations of the loop gain, $G_{yu}(s)K(s)$, corresponding to the baseline and tuned controller could be used as a metric to allow a scaling by the plant.

The continuous computation fits naturally with model-based tuning whereas the discrete computation fits with data-based tuning. Both cases are developed here.

(1) Continuous Computation (Stable Controller)

The state-space representation of the controllers is given by: $\{A_c(p), B_c(p), C_c(p)\}$ for $K(s, p)$, and $\{A_{cb}, B_{cb}, C_{cb}\}$ for $K_b(s)$. We assume both controllers are stable. To compute the deviation we form an augmented state-space system with

$$A_d = \begin{bmatrix} A_c(p) & 0 \\ 0 & A_{cb} \end{bmatrix}, B_d = \begin{bmatrix} B_c(p) \\ B_{cb} \end{bmatrix}, C_d = \begin{bmatrix} C_c(p) & -C_{cb} \end{bmatrix}. \tag{4.56}$$

The deviation can be computed using,

$$d(p) = \alpha_d \text{trace}[X_d C_d^T C_d] \tag{4.57}$$

where X_b satisfies the Lyapunov Equation

$$A_d X_d + X_d A_d^T + B_d B_d^T = 0. \tag{4.58}$$

By taking derivatives with respect to the i-th parameter p_i we find

$$\frac{\partial}{\partial p_i} d(p) = \alpha_d \text{trace}\left[\frac{\partial X_d}{\partial p_i} C_d^T C_d + X_d \frac{\partial C_d^T}{\partial p_i} C_d + X_d C_d^T \frac{\partial C_d}{\partial p_i}\right] \tag{4.59}$$

where,

$$A_d\frac{\partial X_d}{\partial p_i}+\frac{\partial X_d}{\partial p_i}A_d^T+\frac{\partial A_d}{\partial p_i}X_d+X_d\frac{\partial A_d^T}{\partial p_i}+\frac{\partial B_d}{\partial p_i}B_d^T+B_d\frac{\partial B_d^T}{\partial p_i} = 0 \tag{4.60}$$

with

$$\frac{\partial A_d}{\partial p_i} = \begin{bmatrix}\frac{\partial}{\partial p_i}A_c(p) & 0\\ 0 & 0\end{bmatrix}, \frac{\partial B_d}{\partial p_i} = \begin{bmatrix}\frac{\partial}{\partial p_i}B_c(p)\\ 0\end{bmatrix}, \frac{\partial C_d}{\partial p_i} = \begin{bmatrix}\frac{\partial}{\partial p_i}C_c(p) & 0\end{bmatrix}. \tag{4.61}$$

(2) Discrete Frequencies (Continuous Case: Unstable Controller)

To discretely determine the deviation on the set of frequencies, $\{\omega_k, k = 1, \ldots, n_m\}$, consistent with those used with the measurement model, we numerically compute the 2-Norm using,

$$\begin{aligned} d(p) &= \frac{\alpha_d}{\pi}\sum_{k=1}^{n_\omega}\|K(j\omega_k, p) - K_b(j\omega_k)\|^2\Delta\omega_k \\ &= \frac{\alpha_d}{\pi}\sum_{k=1}^{n_\omega}\mathrm{trace}[(K(j\omega_k, p)-K_b(j\omega_k))^H(K(j\omega_k, p)-K_b(j\omega_k))]\Delta\omega_k \end{aligned}. \tag{4.62}$$

We note that this deviation is identical in the case of (1) a design model and (2) a measurement model. By taking derivatives with respect to the i-th parameter p_i, we have,

$$\begin{aligned} \frac{\partial}{\partial p_i}d(p) &= \frac{\alpha_d}{\pi}\sum_{k=1}^{n_\omega}\mathrm{trace}\left\{\left(\frac{\partial K}{\partial p_i}\right)^H(K(p)-K_b)+(K(p)-K_b)^H\left(\frac{\partial K}{\partial p_i}\right)\right\}\Delta\omega_k \\ &= \frac{2\alpha_d}{\pi}\sum_{k=1}^{n_\omega}\mathrm{trace}\left\{Re\left[\left\{\frac{\partial}{\partial p_i}K(j\omega_k, p)\right\}^H(K(j\omega_k, p)-K_b)\right]\right\}\Delta\omega_k \end{aligned}. \tag{4.63}$$

4.1.4 Compensator Channel Magnitude Metric

We may wish to tune a controller to modify the gain in a particular control channel. For example, we may wish to reduce the expected control signals below actuator saturation levels while maintaining stability robustness and performance. Alternately, a controller can be decentralized by decreasing the gain in particular channels until those channels can be removed from the controller without adversely affecting the stability or performance.

The control magnitude metric is defined using a weighted sum of the energy (H_2 norm) of the control channels,

$$M = \frac{1}{\pi}\sum_{m=1}^{n_y}\sum_{l=1}^{n_u}\int_0^{\infty} W_{M,ml}(\omega)\left|K_{ml}(j\omega)\right|^2 d\omega . \tag{4.64}$$

The $n_y \times n_u$ weighting matrix $W_M(\omega)$, is chosen to individually weight control channels whose energy is to be included in the optimization cost function. The ml-th subscript indicates the $m \times l$ controller channel is picked off. The frequency weight allows the designer to shape the controller magnitude as a function of frequency, for example: to avoid DC saturation of small-stroke actuators, or to specify the control bandwidth.

In the case of the metric evaluating the gain of a tuned compensator no distinction is made between data-based and model-based design. Again, we can devise metrics which use Lyapunov-based exact continuous computation or alternately a metric which evaluates the the deviation metric at the frequencies of interest.

(1) Continuous Computation (Stable Controller)

In the case of a stable continuous controller, if possible, we append the stable state-space weighting $W_{\sqrt{M},ml}(s)$ to the ml-th control channel, where

$$W_{\sqrt{M},ml}(s)W_{\sqrt{M},ml}(s)^H = W_{M,ml}(\omega) \tag{4.65}$$

to arrive at an augmented, weighted controller, given by the state-space triplet $\{A_{ca}(p), B_{ca}(p), C_{ca}(p)\}$. If the weighting cannot be represented by the state-space model we appeal to the Discrete Frequencies case developed below.

The cost of the $\{j, l\}$ channel is given by solving the Lyapunov equation,

$$A_{ca}X_{ca,jl} + X_{ca,jl}A_{ca}^T + B_{ca,l}B_{ca,l}^T = 0 \tag{4.66}$$

where $B_{ca,l}$ is the l-th column of the augmented controller input matrix, and evaluating

$$\|K_{a,jl}\|_2^2 = C_{ca,j}X_{ca,jl}C_{ca,j}^T \tag{4.67}$$

where $C_{ca,j}$ is the j-th row of the augmented controller output matrix and $K_{a,jl}$ is the jl-th entry of the augmented controller.

The gradient of M with respect to the i-th controller parameter is given by,

$$\frac{\partial M}{\partial p_i} = \sum_{j=1}^{n_y}\sum_{l=1}^{n_u}\frac{\partial\|K_{a,jl}\|_2^2}{\partial p_i} \tag{4.68}$$

where

$$\frac{\partial\|K_{a,jl}\|_2^2}{\partial p_i} = \frac{\partial C_{ca,j}}{\partial p_i}X_{ca,jl}C_{ca,j}^T + C_{ca,j}\frac{\partial X_{ca,jl}}{\partial p_i}C_{ca,j}^T + C_{ca,j}X_{ca,jl}\frac{\partial C_{ca,j}^T}{\partial p_i} \tag{4.69}$$

with $\frac{\partial X_{ca,jl}}{\partial p_i}$ satisfying the Lyapunov equation

$$\begin{aligned} A_{ca}\frac{\partial X_{ca,jl}}{\partial p_i} + \frac{\partial X_{ca,jl}}{\partial p_i}A_{ca}^T + \frac{\partial A_{ca}}{\partial p_i}X_{ca,jl} + X_{ca,jl}\frac{\partial A_{ca}^T}{\partial p_i} \\ + \frac{\partial B_{ca,l}}{\partial p_i}B_{ca,l}^T + B_{ca,l}\frac{\partial B_{ca,l}^T}{\partial p_i} = 0 \end{aligned}. \tag{4.70}$$

(2) Discrete Frequencies (or Continuous Case; Unstable Controller)

In the case of a discrete set of frequencies, $\{\omega_k\}$, we evaluate Equation 4.64 using

$$M = \frac{1}{\pi}\sum_{m=1}^{n_y}\sum_{l=1}^{n_u}\sum_{k=1}^{n_\omega} W_{M,ml}(\omega)|K_{ml}(j\omega)|^2\Delta\omega_k. \tag{4.71}$$

The gradient of M with respect to the i-th controller parameter can be evaluated using

$$\frac{\partial M}{\partial p_i} = \frac{2}{\pi}\sum_{m=1}^{n_y}\sum_{l=1}^{n_u}\sum_{k=1}^{n_\omega} W_{M,ml}(\omega)\mathrm{Re}\left(\frac{\partial K_{jl}(j\omega)}{\partial p_i}K_{jl}^H(j\omega)\right)\Delta\omega_k \tag{4.72}$$

in conjunction with Equation 4.31.

Equation 4.72 can be used for critically stable controllers as long as no $\omega_k \neq 0$.

4.1.5 Tuning Costs and Gradients: Summary

In Section 4.1.1 through Section 4.1.4, the four terms which combine to form the augmented tuning cost J_a have been defined, and their gradients with respect to the controller parameters have been computed. The resulting cost expressions are summarized in Table 4.2 with equation labels pointing to the introduction of the cost term in the text. If continuous and discrete expressions (or expressions for use with design models and expressions for use with measured data) are available for the cost terms, both are presented in the table.

The design weights and thresholds which act as knobs for the designer to control the tuning are reviewed in Table 4.2. Each term in the augmented cost function can be scaled to modify their relative weights. Further, where possible, a frequency weighted scaling on the cost terms is introduced to specify the control bandwidth.

4.2 Controller Parameterization

The controller is broken into a set of basis functions for efficient tuning. The elements of the state-space representation is chosen as a suitable set. Linearity and orthonormality is sacrificed for a minimal number of parameters (basis functions) to represent a controller of order n_c. The number of parameters is further decreased by sacrificing some numerical conditioning and requiring that the controller be represented in a particular form. This sec-

TABLE 4.2 Summary of the terms of the augmented cost function. The table lists expressions for the cost terms when either a state-space model is available, or when measured data only is available. Designer thresholds and weights are all noted with an asterisk (*).

<table>
<tr><th colspan="2" rowspan="2">Cost Term</th><th colspan="2">Expression</th></tr>
<tr><th>Design Model or Continuous Computation</th><th>Measured Data or Discrete Computation</th></tr>
<tr><td colspan="2">J</td><td>$\text{trace}[C_z^{(cl)}\Sigma_{xx}(C_z^{(cl)})^T]$ with
$A^{(cl)}\Sigma_{xx}+\Sigma_{xx}(A^{(cl)})^T+B_w^{(cl)}(B_w^{(cl)})^T=0$
(see Eq. 4.40 and 4.41)
$A^{(cl)}, B_w^{(cl)}, C_z^{(cl)}$ are closed-loop quantitates which include performance appended state-space frequency scaling.</td><td>$\frac{1}{\pi}\sum_{k=1}^{n_m}\text{trace}\left\{H^{(cl)}(j\omega_k)H^{(cl)}(j\omega_k)^H\right\}\Delta\omega_k$
(see Eq. 4.52)
Assume a white noise disturbance input. Summation of the closed-loop cost over the frequency samples. $H^{(cl,\,m)}$ is a closed-loop metric relating w to z.</td></tr>
<tr><td rowspan="3">$S_R =$
$(1-\gamma_{cr})S_S$
$+\gamma_{cr}S_{cr}$</td><td rowspan="2">S_S</td><td colspan="2">$\frac{1}{\pi}\sum_{i=1}^{n_\omega}W_S(\omega)(\sigma_{\max}(S))^2\left[\frac{\arctan(\alpha\{\ln(\sigma_{\max}(S))-T_S(\omega)\})}{\pi}+\frac{1}{2}\right]\Delta\omega_k$ (see Eq. 4.9)[a]
Summation of the deviation of the maximum s.v. of the Sensitivity $\sigma_{\max}(S)$ *over* a threshold in a frequency band of interest.
$W_S(\omega)$ * weights the stability robustness penalty as a function of frequency, and weights the relative contribution of the S_S term to the total cost J_A. Used to specify the control bandwidth
$T_S(\omega)$ * threshold over which spikes in $\sigma_{\max}(S)$ are penalized. Can be used to capture uncertainty in the model or measured data (a low threshold implies less model confidence)</td></tr>
<tr><td colspan="2">α * weights the penalty for deviation of the maximum s.v. above $T_S(\omega)$. As α is increased slight deviations are penalized as strongly as large deviations.</td></tr>
<tr><td>S_{cr}</td><td colspan="2">$\frac{1}{\pi}\sum_{k=1}^{n_\omega}W_{cr}(\omega_k)\frac{1}{d_{cr}^2(j\omega_k)}\Delta\omega_k$ (see Eq. 4.37)[a]
Summation of the inverse of the distance from the MIMO Nyquist locus to the critical point over a frequency band of interest. For good stability robustness we maximize this distance near crossover.
$W_{cr}(\omega)$ * weights and selects the frequency values of interest, and weights the relative contribution of the S_{cr} term to the total cost J_A. Can be used to push importance frequency points away from the critical point.
$d_{cr}(j\omega_k)$ is the distance from the Nyquist locus to the critical point at frequency ω_k.</td></tr>
<tr><td colspan="2" rowspan="2">d</td><td>$\alpha_d\text{trace}[X_dC_d^TC_d]$with
$A_dX_d+X_dA_d^T+B_dB_d^T=0$
(see Eq.4.57, 4.58)
Form an augmented state-space system (A_d, B_d, C_d) which subtracts the outputs of the two (stable) controllers.</td><td>$\frac{\alpha_d}{\pi}\sum_{k=1}^{n_\omega}\lVert K(j\omega_k,p)-K_b(j\omega_k)\rVert^2\Delta\omega_k$ o
(see Eq. 4.62)
Approximate the H_2 norm of the difference between the two controllers evaluated at the set of critical frequencies.</td></tr>
<tr><td colspan="2">α_d * weights the relative contribution of the d term to the total cost J_A.</td></tr>
</table>

TABLE 4.2 Summary of the terms of the augmented cost function. The table lists expressions for the cost terms when either a state-space model is available, or when measured data only is available. Designer thresholds and weights are all noted with an asterisk (*).

Cost Term	Expression	
	Design Model or Continuous Computation	**Measured Data or Discrete Computation**
M	$\frac{1}{\pi}\sum_{m=1}^{n_y}\sum_{l=1}^{n_u}\int_0^{\infty} W_{M,ml}(\omega)\lvert K_{ml}(j\omega)\rvert^2 d\omega$ (see Eq. 4.64)	$\frac{1}{\pi}\sum_{m=1}^{n_y}\sum_{l=1}^{n_u}\sum_{k=1}^{n_\omega} W_{M,ml}(\omega)\lvert K_{ml}(j\omega)\rvert^2 \Delta\omega_k$ (see Eq. 4.71)
	Penalize the sum of the areas under the magnitude of each controller channel. Solved with Lyapunov Eq. 4.66 and 4.67	Summation of the area under the magnitude of each weighted controller channel.
	W_M * is a frequency weight appended to the state-space model to penalize control magnitude and weights the relative contribution of the M term to the total cost J_A. Can be used to limit actuator use over critical frequency bands.	W_M * weights the individual controller channels as a function of frequency and weights the relative contribution of the M term to the total cost J_A. Can be used to limit actuator use over critical frequency bands.

a. A continuous computation of the stability robustness metrics has not been developed

tion presents the controller parameterization for the full and constrained-topology controller.

4.2.1 Full State-Space Parameterization

We form a full parameterization of the state-space representation of the controller given by Equation 2.5. Since state-space realizations are not unique, there are an infinite number of ways to parameterize the controller.

Jordan (diagonal) state-space form

To understand the number of parameters required to specify the state-space system, we assume it is diagonalizable, and perform a state transformation to convert to a MIMO Jordan (or diagonal) form as seen in Figure 4.5.

We define the Jordan canonical form state-space matrices as

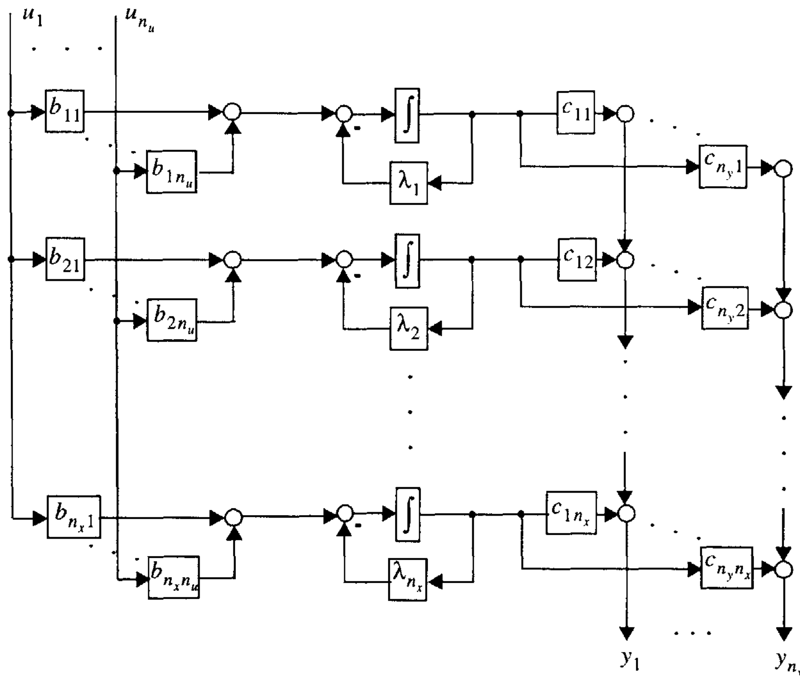

Figure 4.5 Jordan (diagonal) form for an order n_x MIMO system with n_u inputs and n_y outputs.

$$A_c^J = \begin{bmatrix} \lambda_1 & 0 & \dots & 0 \\ 0 & \lambda_2 & \dots & 0 \\ \vdots & \vdots & \ddots & \vdots \\ 0 & \dots & \dots & \lambda_{n_x} \end{bmatrix}, B_c^J = \begin{bmatrix} b_{11} & \dots & b_{1n_u} \\ b_{21} & \dots & b_{2n_u} \\ \vdots & \ddots & \vdots \\ b_{n_x1} & \dots & b_{n_xn_u} \end{bmatrix}, C_c^J = \begin{bmatrix} c_{11} & c_{12} & \dots & c_{1n_x} \\ \vdots & \vdots & \ddots & \vdots \\ c_{n_y1} & c_{n_y2} & \dots & c_{n_yn_x} \end{bmatrix}. \tag{4.73}$$

We see that n_x eigenvalue parameters, λ_i, are necessary to specify the dynamic matrix. For this system with n_u inputs and n_y outputs, the input matrix, B_c^J, requires $n_x \times n_u$ parameters and the output matrix, C_c^J, requires $n_x \times n_y$ parameters. The total number of parameters is,

$$n_p = n_x(n_u + n_y + 1) \tag{4.74}$$

which over-parameterizes the system. By constraining two rows of C_c^J to be made up of 1 and 0, the number of parameters to completely specify of state-space system is given by [Ly et al., 1985]:

$$n_p = n_x(n_u + n_y - 1), \text{ for } n_u \geq 2\,. \tag{4.75}$$

The Jordan canonical form is useful for understanding the form of the parameterization, but for our purposes it has two flaws: (1) not all systems can be diagonalized, and (2) some eigenvalues come in complex conjugate pairs, and as such each λ_i are not independent, and made up of a real scalar and a complex scalar. The possible complex nature of the λ_i makes the real/complex transition of the eigenvalues of A_c^J awkward. We alter the Jordan form slightly to alleviate these difficulties.

Near-modal state-space form

By forcing n_x to be even, we can group complex conjugate eigenvalues, $\{\lambda_{i,\,i+1}^c = \sigma_i \pm j\omega_i\}$, together and group real eigenvalues in pairs, $\{\lambda_i^r, \lambda_{i+1}^r\}$ where $\lambda_i^r \neq \lambda_{i+1}^r$. We then appeal to a second-order form whose dynamic matrix is given by,

$$A_c^{nm} = \text{diag}[A_i^b],\, i = 1, \ldots, \frac{n_x}{2}, \tag{4.76}$$

where the $\text{diag}[A_i^b]$ forms a block diagonal matrix with the matrix components, A_i^b along the diagonal. The 2×2 blocks are of the form,

$$A_i^b = \begin{bmatrix} 0 & 1 \\ a_{1i} & a_{2i} \end{bmatrix} \tag{4.77}$$

where in the case of complex eigenvalues, $a_{1i} = -(\sigma_i^2 + \omega_i^2) = -\omega_{ni}^2$ and $a_{2i} = -2\sigma_i = -2\zeta_i\omega_{ni}$ where ω_{ni} and ζ_i are the respective natural frequency and damping ratio. In the case of real poles $a_{1i} = -\lambda_i^r\lambda_{i+1}^r$ and $a_{2i} = -(\lambda_i^r + \lambda_{i+1}^r)$. The input and output matrices, B_c^{nm} and C_c^{nm}, remain parameterized as in Equation 4.73, though the components of the matrices will be transformed. Because of its resemblance to modal form with the inclusion of even pairs of real poles, we term this state-space representation as near-modal form.

By breaking the dynamics matrix into 2×2 blocks corresponding to factors of the characteristic equation, $s^2 + a_{2i}s + a_{1i}$ where a_{1i} and a_{2i} are real, we maintain a smooth transition from real to complex conjugate poles. Further, most structural systems can be transformed into this form.

For transforming the state-space system into this form we treat real and complex-conjugate poles separately. For complex-conjugate poles, the form is a common real modal form, and the transformation is achieved by manipulating the appropriate eigenvectors as discussed [Grocott, 1994]. For the real eigenvalues, we group them into non-equal pairs, and then we concatenate two transformations. First we diagonalize using the eigenvectors, resulting in a 2×2 block of the form

$$A_i^d = \begin{bmatrix} \lambda_i^r & 0 \\ 0 & \lambda_{i+1}^r \end{bmatrix} \tag{4.78}$$

we then apply a transformation matrix of the form

$$T = \begin{bmatrix} \begin{bmatrix} 1 \\ 1 \end{bmatrix} & A_i^d \begin{bmatrix} 1 \\ 1 \end{bmatrix} \end{bmatrix} = \begin{bmatrix} 1 & \lambda_i^r \\ 1 & \lambda_{i+1}^r \end{bmatrix}, \tag{4.79}$$

such that

$$A_i^b = T A_i^d T^{-1}. \tag{4.80}$$

We have defined a state-space transformation which specifies a unique A_c^{nm} matrix, but because of the non-unique normalization of the eigenvectors used in the transformation, does not specify a unique B_c^{nm} or C_c^{nm} matrix. To uniquely specify them, and improve numerical conditioning, we scale them such that the 2-Norm of the two rows of B_c^{nm} and the two columns of C_c^{nm}, corresponding to the 2×2 A_i^b blocks, are equal. The scaling uniquely specifies the near-modal state-space form, but complicates the parameterization considerably. For controller tuning purposes, we choose to relax the input/output scaling and leave the controller slightly over parameterized with $n_p = n_x(n_u + n_y + 1)$ parameters non-uniquely specifying the controller.

The controller parameters are written in terms of a perturbation from their nominal value: *e.g.* $a_{11} = a_{11,b} + \delta a_{11}$, where the $(\cdot)_b$ notation indicates the nominal (baseline) value and δa_{11} indicates the tuning parameter. The tuning parameters are placed in a vector of the form

$$p = \begin{bmatrix} \delta a_{11} \; \delta a_{21} \; \ldots \; \delta a_{1\frac{n_x}{2}} \; \delta a_{2\frac{n_x}{2}} \; \delta b_{11} \; \ldots \; \delta b_{n_x 1} \; \delta b_{12} \; \ldots \; \delta b_{n_x n_u} \\ \ldots \; \delta c_{11} \; \ldots \; \delta c_{1n_x} \; \delta c_{21} \; \ldots \; \delta c_{n_y n_x} \end{bmatrix}^T , \qquad (4.81)$$

where we refer to the i-th element of this vector as p_i.

Our near-modal form is similar to the tridiagonal form suggested in the direct controller design work of [Ly et al., 1985]. The principal difference is that Ly constrains the form to be unique by setting elements of C_c to be unity or zero. In this way, Ly's form has the minimal number of parameters for a unique state-space parameterization (Equation 4.75). In our parameterization, we sacrifice uniqueness for improved numerical conditioning by allowing the elements of B_c and C_c flexibility in maintaining similar numerical values. The near modal parameterization requires $n_p = n_x(n_u + n_y + 1)$ parameters. The tridiagonal parameterization of [Ly et al., 1985] (similar to our near-modal parameterization) compares favorably in terms of performance and computational efficiency to a full parameterization [Collins and Sadhukhan, 1998].

Near-modal form derivatives

The derivatives of the state-space representation of the controller are required to compute $\frac{\partial K}{\partial p_i}$ as required for all of the gradient computations of Section 4.1. The preceding statement follows from the chain rule since the controller, $K(s, p)$, affects all closed-loop characteristics of the system the we monitor, and since $K(s, p)$ depends explicitly on the parameters, p.

The near-modal form exhibits particularly simple derivatives. For example, the derivative of the state-space matrices with respect to $p_1 = a_{11}$ are given by,

$$\frac{\partial A_c^{nm}}{\partial p_1} = \begin{bmatrix} 0 & 0 & \dots & 0 \\ 1 & 0 & 0 & 0 \\ \vdots & \vdots & \ddots & \vdots \\ 0 & 0 & \dots & 0 \end{bmatrix}, \frac{\partial B_c^{nm}}{\partial p_1} = [0], \frac{\partial C_c^{nm}}{\partial p_1} = [0]. \tag{4.82}$$

As another example, the derivative of the state-space matrices with respect to $p_{n_x+1} = b_{11}$ is given by

$$\frac{\partial A_c^{nm}}{\partial p_{n_x+1}} = [0], \frac{\partial B_c^{nm}}{\partial p_{n_x+1}} = \begin{bmatrix} 1 & 0 & \dots & 0 \\ 0 & 0 & \dots & 0 \\ \vdots & \vdots & \ddots & \vdots \\ 0 & 0 & \dots & 0 \end{bmatrix}, \frac{\partial C_c^{nm}}{\partial p_{n_x+1}} = [0]. \tag{4.83}$$

In each case we find that two of the state-space matrices are zero matrices while the third has only a single entry of unity. The sparsity of these derivative matrices can be exploited for numerical efficiency.

We can write the state-space matrices for the tuned controller in terms of the baseline controller by computing

$$\begin{gathered} A_c(p) = A_{c,b} + \sum_{i=1}^{n_p} \frac{\partial A_c^{nm}}{\partial p_i} p_i, \quad B_c p = B_{c,b} + \sum_{i=1}^{n_p} \frac{\partial B_c^{nm}}{\partial p_i} p_i, \\ C_c(p) = C_{c,b} + \sum_{i=1}^{n_p} \frac{\partial C_c^{nm}}{\partial p_i} p_i \end{gathered} . \tag{4.84}$$

Example: 4th order 2×2 controller

We parameterize the controller as:

$$A_c = \begin{bmatrix} 0 & 1 & 0 & 0 \\ a_{11} & a_{21} & 0 & 0 \\ 0 & 0 & 0 & 1 \\ 0 & 0 & a_{21} & a_{22} \end{bmatrix}, B_c = \begin{bmatrix} b_{11} & b_{12} \\ b_{21} & b_{22} \\ b_{31} & b_{32} \\ b_{41} & b_{42} \end{bmatrix}, C_c = \begin{bmatrix} c_{11} & c_{12} & c_{13} & c_{14} \\ c_{21} & c_{22} & c_{23} & c_{24} \end{bmatrix} \tag{4.85}$$

noting each parameter can be written as the sum of the nominal (baseline) parameter summed with a perturbation *e.g.* $a_{11} = a_{11,b} + \delta a_{11}$. The parameter vector is given by Equation 4.81 with $n_p = 20$ parameters.

4.2.2 Constrained Topology Parameterization

By fixing certain parameters in the free-topology controller parameterization of the previous section, the controller topology can be constrained. Block diagonal controller topologies are generated by removing some controller parameters from the vector of tunable parameters, p.

We limit the allowable controller topologies to be in a block form. A more general sensor/actuator constrained topology can be written using the constrained Markov parameters discussed in Section B.1. However, general constraints can over-constrain the controller and lead to complex constraint equations. The block form avoids the extra complexity without sacrificing too much generality.

Each block corresponds to a subset of sensors that actuate a subset of actuators through the action of the controller. To specify a constrained controller topology first we decide on a number of sensor /actuator blocks $\{\beta_l, l = 1, \ldots, n_\beta\}$ and for each block we assign an *even* number of states, $n_{\beta, l}$. Each pair of states is in the near-modal form. The states that are free for tuning are included as the first elements of the p vector. For each sensor channel we determine which blocks of states are affected. The corresponding parameters of the

B_c matrix are the next parameters of the p vector. Similarly, we determine which blocks of states control each actuator. The corresponding elements of the C_c matrix are included as the final parameters of the p vector.

Example: 2nd order SISO controller with integral action

We wish to put a controller of the form

$$K(s) = \frac{\beta}{s(s+\alpha)} \tag{4.86}$$

into our constrained topology while maintaining integral action. The controller matrices can be written as

$$A_c = \begin{bmatrix} 0 & 1 \\ 0 & -\alpha \end{bmatrix}, B_c = \begin{bmatrix} b_{11} \\ b_{21} \end{bmatrix}, C_c = \begin{bmatrix} c_{11} & c_{12} \end{bmatrix} \tag{4.87}$$

with a parameter vector given by $p = \begin{bmatrix} \delta\alpha & \delta b_{11} & \delta b_{21} & \delta c_{11} & \delta c_{12} \end{bmatrix}$. The 0 in the $A_c(2, 1)$ location ensures the preservation of integral action.

Example: 4th order 2×2 controller with sensor/actuator constraints

In this example we wish to have a 2×2 controller where the first sensor controls both actuators and where the second sensor only controls the second actuator. We divide the 4 states into two 2-state blocks and write the controller in the form:

$$A_c = \begin{bmatrix} 0 & 1 & 0 & 0 \\ a_{11} & a_{21} & 0 & 0 \\ 0 & 0 & 0 & 1 \\ 0 & 0 & a_{21} & a_{22} \end{bmatrix}, B_c = \begin{bmatrix} b_{11} & 0 \\ b_{21} & 0 \\ b_{31} & b_{32} \\ b_{41} & b_{42} \end{bmatrix}, C_c = \begin{bmatrix} c_{11} & c_{12} & 0 & 0 \\ 0 & 0 & c_{23} & c_{24} \end{bmatrix}. \tag{4.88}$$

The tuning parameterization has been reduced from $n_p = 20$ to $n_p = 14$ parameters.

4.3 Tuning Iterations

The iterative Boyden-Fletcher-Goldfard-Shanno (BFGS) [Bazaraa et al., 1993] nonlinear descent method is employed to reduce the cost of Equation 4.1. With each step, the gradients of the cost are computed with respect to the control parameters of Section 4.2 using the relations derived in Section 4.1. The selection of the step-size is modified from the standard algorithm to ensure that closed-loop stability (and optionally, controller stability) is maintained. A similar nonlinear program was used for multi-model control synthesis by [MacMartin et al., 1991] and for the MACE program [Campbell et al., 1999]. An expert algorithm to determine stability from measured data (*i.e.* without evaluating the eigenvalues) is developed.

4.3.1 Stepping Algorithm

The standard sum-of-squares curve fitting technique is the Levenberg-Marquardt (LM) algorithm [Bazaraa et al., 1993 and Jacques, 1995]. However, for our controller tuning a BFGS *variable metric* descent is used to tune the controller with the aim of minimizing the augmented cost of Equation 4.1. The method requires that the gradient, ∇J_a, be computed at arbitrary points using the expressions developed in Section 4.1.

The BFGS algorithm is selected over the LM algorithm for four reasons: (1) model-based costs are not necessarily written using a sum-of-squares (Section 4.1), (2) data-based tuning examples show the LM tends to rapidly converge to a greater-cost controller than the BFGS, (3) the LM requires a $n_p \times n_p$ matrix inversion with each iteration, and (4) the standard LM approximation of the Hessian (ignoring second derivatives [Press et al., 1992]) does not hold since the controller tuning problem does not necessarily go to a negligibly small cost. The BFGS algorithm is chosen over other descent methods (*e.g.* gradient descent) based on an informal comparison of performance and computational complexity with the developed tuning algorithms. The superiority (performance versus computational complexity) of the BFGS algorithm is collaborated in a similar study comparing direct reduced-order H_2 designs [Collins and Sadhukhan, 1998].

Following the implementation of the BFGS algorithm outlined in [Press et al., 1992], the BFGS algorithm is coded to iteratively compute the next controller parameter vector, p_{k+1}, given the current p_k,

$$p_{k+1} = p_k + \mu_{k+1}(\delta p_k) \tag{4.89}$$

where μ_k is the adaptively selected stepsize, and

$$\delta p_k = -\mathrm{H}_k \nabla J_{a,k}. \tag{4.90}$$

The BFGS updating formula for the inverse of the Hessian is written as

$$\begin{aligned} \mathrm{H}_{k+1} = \mathrm{H}_k &+ \frac{(p_{k+1}-p_k)(p_{k+1}-p_k)^T}{(p_{k+1}-p_k)^T(\nabla J_{a,k+1}-\nabla J_{a,k})} \\ &- \frac{[\mathrm{H}_k(\nabla J_{a,k+1}-\nabla J_{a,k})][\mathrm{H}_k(\nabla J_{a,k+1}-\nabla J_{a,k})]^T}{(\nabla J_{a,k+1}-\nabla J_{a,k})^T\mathrm{H}_k(\nabla J_{a,k+1}-\nabla J_{a,k})} \\ &+ (\nabla J_{a,k+1}-\nabla J_{a,k})^T\mathrm{H}_k(\nabla J_{a,k+1}-\nabla J_{a,k})uu^T \end{aligned} \tag{4.91}$$

where

$$u = \frac{(p_{k+1}-p_k)}{(p_{k+1}-p_k)^T(\nabla J_{a,k+1}-\nabla J_{a,k})} - \frac{\mathrm{H}_k(\nabla J_{a,k+1}-\nabla J_{a,k})}{(\nabla J_{a,k+1}-\nabla J_{a,k})^T\mathrm{H}_k(\nabla J_{a,k+1}-\nabla J_{a,k})}. \tag{4.92}$$

With each successive step of the BFGS algorithm an approximation of the inverse of the Hessian is iteratively constructed using Equations 4.91 and 4.92. We start the algorithm with the baseline controller $p_1 = 0$ and with $\mathrm{H}_1 = I$.

4.3.2 Stepsize Determination: Stability Preservation

The stepsize, μ_k, is adaptively selected. A standard cubic spline line search [Press et al., 1992] is modified to ensure closed-loop stability is preserved. The initial stepsize is bisected until the controller at p_{k+1} (given by Equation 4.89) displays a stable closed-loop. In addition, the designer may wish to preserve the stability of the controller itself.

The bisection limits the stepsize so that the tuned controller resulting from each iteration stabilizes the plant. A backtracking algorithm is used to further refine the stepsize to ensure the objective function, $J_a(p_{k+1})$ is decreased: (1) if the given stepsize increases the objective function then we backtrack along the direction of descent $\nabla J_a(p_{k+1})$, (2) we solve for the minimum of the cubic spline made up from our initial point, first step, and backtrack step. We iterate on subsequent splines until a suitable decrease in the objective function is made.

Determining the stability of the closed-loop system is essential to computing the appropriate stepsize. We determine the stability in both cases: (1) when the design model of the plant is available, and (2) when frequency transfer matrix data for the plant is available.

(1) Model stability determination

In the case of model-based controller tuning, the open-loop model is available. In this case, determining stability is a matter of ensuring all of the closed-loop poles in the left hand plane. Mathematically for the controller at p_k,

$$\begin{aligned} \max(\mathrm{Re}[\mathrm{eig}(A^{(cl)}(p_k))]) &\le -\varepsilon \Rightarrow \text{stable} \\ &> -\varepsilon \Rightarrow \text{unstable (conservative)} \end{aligned} \tag{4.93}$$

where ε is a tolerance for adjusting the allowable proximity to the $j\omega$-axis for the closed-loop system to be considered stable. The determination of stability is conservative since a stable closed loop may be considered unstable if it's eigenvalues are to close to the $j\omega$-axis.

The compensator stability can always be considered with a model-based test of the eigenvalues of $A_c(p_k)$. In general though, pure integrators are allowed in the controller which implies that $\varepsilon = 0$ must be used in the test of Equation 4.93.

(2) Data-based stability determination

When the model is unavailable, a graphical determination of stability is used. A knowledge-based algorithm is to developed to automatically implement the rules of the MIMO stability criterion to determine stability.

The MIMO Nyquist function can be determined at each frequency point, $\{\omega_k, k = 1, \ldots, n_\omega\}$,

$$H(j\omega) = -1 + \det[I + G_{yu}(j\omega)\{-K(j\omega)\}] \tag{4.94}$$

where, as per the convention for graphical stability determination, negative feedback is employed. The MIMO Nyquist stability requirement is that the *net* number of counter-clockwise encirclements of the critical point (-1) made by the locus of $H(j\omega)$ on the complex plane must be equal to the number of unstable poles in the open loop system $G_{yu}(j\omega)K(j\omega)$ [Lehtomaki et al., 1981 and Grocott, 1994].

To simplify the stability determination, the locus of $H(j\omega)$ can be plotted as log-magnitude versus phase, commonly referred to as a Nichols plot. In the Nichols plot, encirclements in the Nyquist plot become passes of the locus of $H(j\omega)$ over the critical points found at a magnitude of 1 with phase $-180 \pm n360$ degrees. It is much simpler to code a rule which counts passes over the critical point than it is to count encirclements. For stability with the Nichols plot, the *net* number of left to right (lower to higher phase) passes of the locus of $H(j\omega)$ over the critical points must be equal to the number of unstable poles in the open loop system $G_{yu}(j\omega)K(j\omega)$.

The stability determination algorithm works by comparing subsequent points, $H_k = H(j\omega_k)$ and $H_{k+1} = H(j\omega_{k+1})$. The points are placed in their respective quadrant using:

$$\begin{aligned} 0 < \angle H_k < 90 \Rightarrow q(H_k) &= 1 \\ 90 < \angle H_k < 180 \Rightarrow q(H_k) &= 2 \\ -180 < \angle H_k < -90 \Rightarrow q(H_k) &= 3 \\ -90 < \angle H_k < 0 \Rightarrow q(H_k) &= 4 \end{aligned} \tag{4.95}$$

A right to left pass of a critical point corresponds to traversing from quadrant 3 to quadrant 2. A left to right pass corresponds to traversing from quadrant 2 to quadrant 3. Based on this, the following rules are implemented to determine passes over the critical point:

$$\begin{aligned} &|H_k| > 1, |H_{k+1}| > 1, q(H_k) = 3, q(H_{k+1}) = 2 \Rightarrow \text{Right to left pass} \\ &|H_k| > 1, |H_{k+1}| > 1, q(H_k) = 2, q(H_{k+1}) = 3 \Rightarrow \text{ Left to right pass} \end{aligned}. \tag{4.96}$$

In the case where the locus passes from quadrant 2 to quadrant 3 (or from quadrant 3 to quadrant 2) and the magnitude of one of the points is greater than 1 then it is impossible to determine if the locus has passed over or under the critical point. In this case a linear interpolation is used to generate points between ω_k and ω_{k+1}. The algorithm is then recursively applied to determine whether a critical point crossing has occurred. Mathematically,

$$\begin{aligned} &|H_k| > 1, |H_{k+1}| < 1, q(H_k) = 3, q(H_{k+1}) = 2 \Rightarrow \text{ Interpolate} \\ &|H_k| > 1, |H_{k+1}| < 1, q(H_k) = 2, q(H_{k+1}) = 3 \Rightarrow \text{ Interpolate} \\ &|H_k| < 1, |H_{k+1}| > 1, q(H_k) = 3, q(H_{k+1}) = 2 \Rightarrow \text{ Interpolate} \\ &|H_k| < 1, |H_{k+1}| > 1, q(H_k) = 2, q(H_{k+1}) = 3 \Rightarrow \text{ Interpolate} \end{aligned}. \tag{4.97}$$

In the case where consecutive points skip a quadrant (*e.g.* $q(H_k) = 1$ and $q(H_{k+1}) = 3$) and the magnitude of one of the points is greater than unity, then the data is considered to be bad. We have

$$|H_k| > 1 \text{ or } |H_{k+1}| > 1, \text{ quadrant skipped } \Rightarrow \text{Sparse data}. \tag{4.98}$$

By assessing the net number of right to left crossings of the critical point and by comparing to the number of open-loop unstable poles, the stability of the closed-loop is determined.

Limitations of a stability-preserving step

The stability-preserving step is essential to guarantee a stable closed loop. It does however limit the feasible space of available controllers. Consider Figure 4.6, a simplified example where all controllers which can be described by two parameters, p_1 and p_2. The resulting controllers are marked as stability preserving (stabilizing) and non-stabilizing.

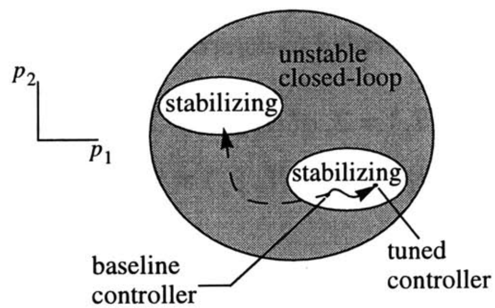

Figure 4.6 Space of parameterized controllers, two parameter example

Consider a baseline controller which by assumption lies in a stable set. By applying the tuning algorithm a cost is minimized to determine the tuned controller. The stability-preserving step ensures that all iterations occur within the stable ball that contains the baseline controller. The dashed trajectory is not possible even if a better controller could be found in the alternate stable ball. The limitation results from the fact that in general the parameterization of stability-preserving controllers is not a convex set.

The limitation of the stability-preserving step highlights the dependence of the tuned controller on the baseline design.

4.3.3 Controller Tuning: Summary

The tuning methodology can now be summarized with the help of the flow chart of Figure 4.7.

We begin a tuning problem by specifying the augmented control cost by setting the design control knobs listed in Table 4.2. We initialize out iteration counter, k to be zero and our

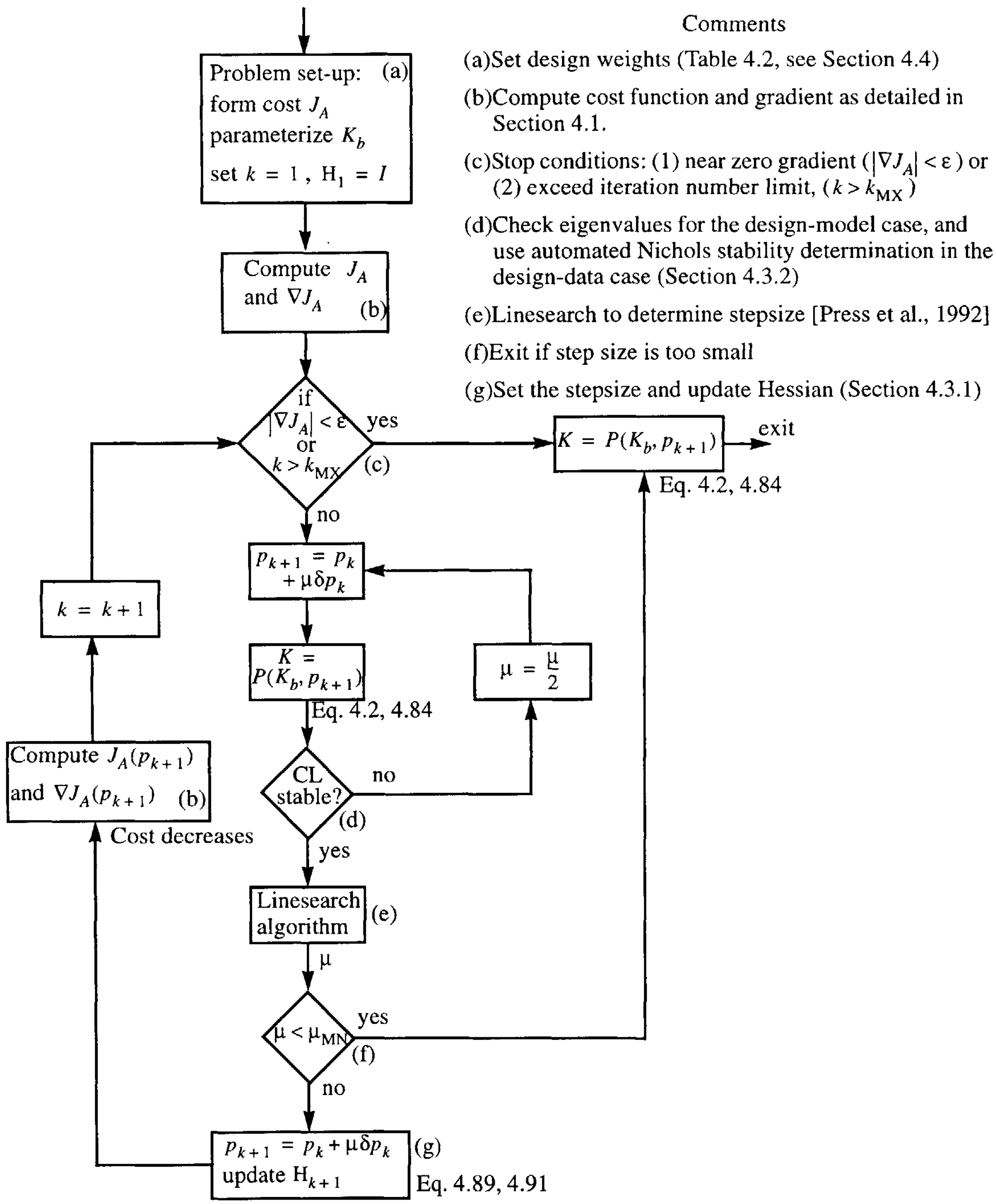

Figure 4.7 Flow diagram of the tuning methodology including the iterative cost minimization

initial Hessian value to be the identity, $H_1 = I$. The controller is parameterized following the guidelines developed in Section 4.2. We determine the initial cost, $J_A(p_1)$ and gradient, $\nabla J_A(p_1)$ with the relations introduced and derived in Section 4.1.

The tuning iteration can now begin. Three stop conditions are defined to end the tuning iterations: (1) the gradient magnitude can fall below a stopping threshold, i.e. $|\nabla J_A| < \varepsilon$ indicating that further tuning steps will not affect the cost (convergence), (2) the maximum number of iterations is exceeded, *i.e.* $k > k_{MX}$, or (3) the stepsize falls below a threshold *i.e.* $\mu < \mu_{MN}$. For each iteration the tuning steps of Section 4.3.1 are performed: (1) a step size is selected, (2) the parameter vector is updated to p_{k+1} by Equation 4.89, (3) the estimate of the inverse Hessian is updated with Equation 4.91, (4) the cost $(J_A(p_{k+1}))$ and gradient $(\nabla J_A(p_{k+1}))$ are evaluated, (5) the counting index, k, is updated, and (6) the stopping criteria are checked.

For each tuning the step, the stepsize, μ, must be computed. We begin with $\mu = 1$, compute the updated parameter vector using Equation 4.89. Then the stability of the closed-loop system, and optionally that of the controller itself can be computed. Stability is verified by checking the eigenvalues if the design model is available, or by using the MIMO Nyquist criteria if we have only plant data as discussed in Section 4.3.2. If we have an unstable closed-loop then the stepsize, μ, is decreased until we maintain stability. Our assumption of a stabilizing baseline controller ensures that generally we can find μ small enough to maintain a stable closed-loop. Upon finding a maximal μ that maintains stability, a linesearch algorithm [Press et al., 1992] selects the final stepsize to ensure that taking the tuning step will decrease the augmented cost, J_A. If the stepsize falls below a threshold then we exit the tuning iteration loop.

Once the tuning loop is exited, a tuned controller is formed from the parameter using Equation 4.84.

The application of the tuning algorithm to a state-space model or to a measured data set is limited by the possibility of overtraining. If the tuning algorithm is aggressively applied to achieve a great decrease in the augmented cost then the controller may become tuned to a particular data set and not perform well should the plant change slightly (time variation or slight nonlinearity). An amplitude nonlinearity in the MACE experiment demonstrated the danger of overtraining a control design to a particular data set [Miller et al., 1996].

4.4 Controller Architecture Modifications

The tuning methodology allows the designer to make major changes to the controller architecture. In this section we present the capability of the methodology to: increase the controller order, specify the use of an actuator over a band, modify the controller topology (*i.e.* which sensors feed to which actuators), and alter the closed-loop bandwidth.

The flexibility of modifying the controller architecture in an optimization framework is a strong advantage of the proposed tuning methodology. In classical control synthesis the designer specifies an architecture (presumably made up of SISO control channels) and manually tunes each channel, one-at-a-time until good closed-loop characteristics are obtained. In the proposed framework any MIMO architecture may be specified and optimally tuned. Further, beginning with a SISO channel classical design, sensor/actuator control channels can be opened for improved performance/stability robustness. In modern model-based design ($H_{2/\infty}$) the designer has little control over the controller order (identical to that of the design plant) and control topology (generally fully connected from all sensors to all actuators).

4.4.1 Modifying Controller Order

The tridiagonal controller parameterization of Section 4.2 allows us to easily add states to the tuned controller. To maintain the even number of states required by the parameterization we must add states two-at-a-time.

As an example, given the state-space representation of the initial controller (A_c, B_c, C_c) which stabilizes the plant, we append two states to arrive at the increased-order controller:

$$A_c^i = \begin{bmatrix} A_c & 0 & 0 \\ 0 & 0 & 1 \\ 0 & a_{1i} & a_{2i} \end{bmatrix}, B_c^i = \begin{bmatrix} & B_c & \\ b_{i,1} & \dots & b_{i,n_y} \\ b_{i+1,1} & \dots & b_{i+1,n_y} \end{bmatrix}, C_c^{(i)} = \begin{bmatrix} & c_{1,i} & c_{1,i+1} \\ C_c & \vdots & \vdots \\ & c_{n_u,i} & c_{n_u,i+1} \end{bmatrix}. \quad (4.99)$$

By specifying a_{1i} and a_{2i} the designer can set the initial pole locations (frequency and damping).

To maintain stability we ensure that the added are either unobservable or uncontrollable such that the controller with appended states has an identical transfer function to the initial controller. For example we can set $b_{i,1}, \dots, b_{i+1,n_y} = 0$ or alternately, $c_{1,i}, \dots, c_{n_u,i+1} = 0$.

It is important to not set both $b_{i,1}, \dots, b_{i+1,n_y} = 0$ and $c_{1,i}, \dots, c_{n_u,i+1} = 0$, otherwise the ubiquitous gradient $\frac{\partial K}{\partial p_i}$ of Equation 4.31 vanishes for the parameters corresponding to the added states. The result is that the added state parameters will not be tuned.

To add extra states the following procedure is employed:

1. Add states (two-at-a-time) as shown in Equation 4.99
2. Set the (stable) pole locations for the added states
3. Set $b_{i,1}, \dots, b_{i+1,n_y} = 0$ corresponding to the added states
4. Set $c_{1,i}, \dots, c_{n_u,i+1}$ to values such the elements of the gradient of the augmented cost with respect to the controller parameters corresponding to $c_{1,i}, \dots, c_{n_u,i+1}$ are similar in magnitude to the gradient with respect to the original controller parameters.

With this procedure we add poles at the desired frequency and ensure by setting the initial values of $c_{1,i}, \dots, c_{n_u,i+1}$ such that ∇J_A for the added parameters will allow the added parameters to play a significant role in subsequent tuning.

4.4.2 Specifying Actuator Use

The fourth term, M, in the augmented cost expression of Equation 4.1 is used to penalize control channel use. In particular we use the weighting matrix $W_M(\omega)$ to select channel and frequency bands where control gain is penalized. This type of tuning allows us to handle physical stroke and bandwidth limitations of actuators. Several examples are presented here:

- *Removing DC gain for a control actuator*: Some actuators are limited at low-frequencies. To limit the l-th actuator's use at low frequency we increase $W_{M,\,il}(\omega)$, $i = 1, \ldots, n_y$ to be a large value for the low-frequency band of interest.
- *Decreasing the use of a stroke-limited actuator*: Actuators may have limitations on their stroke. We can use the W_M weighting to limit the use of the l-th actuator. The designer can examine $u = Ky$ in the closed-loop system to determine which control channel over which frequency band is causing the actuator to saturate. A heavy penalty on that W_M channel can be set over the appropriate frequency band and tuning will ensure that the problem gain of actuator will be decreased with minimal adverse effect on J_A.

4.4.3 Modifying the Controller Topology

The tuning methodology provides a framework to remove sensor/actuator channels from the controller (decentralizing) and to add sensor/actuator channels to the controller (centralizing). Channels are removed with minimal negative impact and added with the greatest possible impact on the augmented performance.

- *Removing a control channel*: Given a controller topology it is sometimes desirable to remove a sensor/actuator connection. For example we may wish to decentralize a fully connected controller. In fact removing channels from a global controller may be easier than directly designing a constrained-topology controller. The direct design of constrained-topology controllers is presented in Appendix B. The tuning methodology provides a means for removing controller channels (if possible) such that stability is maintained and performance is affected minimally. Using the penalty on controller gain, M we set the design weight for the ml-th channel in question ($W_{M,\,ml}$) to be progressively greater. With each successive increase in $W_{M,\,ml}$ we tune the controller until the gain of the ml-th channel is small enough that we can set the channel to 0 without affect the performance or stability robustness.

- *Adding a control channel*: A controller can achieve greater performance as it becomes increasingly connected. For this reason, given a constrained control topology it may be desirable to open sensor/ actuator channels in the tuned design. The methodology provides a framework for this by simply expanding the constrained topology parameterization (Section 4.2.2) to include parameters for the control channel that the designer wishes to add. Applying the tuning methodology will bring in the added channel to maximize its impact on the augmented performance.

4.4.4 Altering Closed-Loop Bandwidth

The tuning methodology provides two principal methods for controlling the closed-loop bandwidth: (1) a heavy penalty on stability non-robustness ($S_S(\omega)$) at frequencies greater than crossover, and (2) a heavy penalty on control channel use ($W_M(\omega)$) at frequencies greater than crossover.

- *Stability robustness bandwidth specification*: The stability robustness term in the augmented cost can be used to specify the closed-loop bandwidth. Generally, a pop-up (greater than 0 dB) in the maximum singular value of the Sensitivity transfer matrix is exhibited near crossover. To lower the crossover frequency we specify the bandwidth by using our stability robustness penalty S_S to push the pop-up feature lower in frequency. This is done by setting a low threshold, $T_S(\omega)$ and high penalty weight, $W_S(\omega)$ for frequencies greater than the desired crossover frequency. Applying the tuning methodology will then decrease the closed-loop bandwidth. To increase the bandwidth we relax our stability robustness constraint and increase the emphasis on performance improvement in J_A. The bandwidth will naturally increase as the controller is tuned.
- *Control channel use bandwidth specification*: The frequency weighting on the gain of the control channels can be used to specify the control bandwidth by forcing the controller to roll off. For each of the appropriate channels we increase $W_M(\omega)$ for frequencies greater than the desired cutoff frequency. Applying the tuning methodology will force the controller channels to roll off with minimal adverse effect on the closed loop performance/stability robustness.

This section demonstrates the flexibility of the tuning methodology. With specification of the designer-defined control knobs, the tuning methodology can be used to indirectly shape the controller. Performance and stability limitations cannot be circumvented, but the flexibility afforded by the tuning methodology is a desired feature.

4.5 Special Example: SWLQG

Sensitivity-weighted LQG (SWLQG) control design [Grocott, 1994] provides us with a case where the tuning strategy can be modified to take advantage of the special properties of SWLQG controllers. The development is detailed in Appendix C.

We can parameterize the controller with the sensitivity weights rather than the standard control parameterization, p. For each setting of the sensitivity weights a modified LQG synthesis returns a controller that is guaranteed to stabilize the state-space design model. Generally, the designer manually chooses the sensitivity weights. We can form a tuning cost as described in Section 4.1 and compute the gradients of the cost with respect to the sensitivity weights. The gradients require the solution of a well-behaved Lyapunov equation. The tuning methodology can be used to select the sensitivity weights which uniquely determine the controller. Further, we can employ measured data to determine the stability robustness penalty.

In Appendix C controllers are designed for the MACE test article. The tuned SWLQG controller is shown to achieve better performance with better stability robustness than a baseline LQG controller. The tuning of SWLQG controllers is complicated by a restriction that the LQG state cost matrix must be positive definite which requires the sensitivity weights be positive (or only slightly negative).

4.6 Summary

A methodology has been developed for tuning a baseline controller. The methodology allows trades of: (1) performance, (2) stability robustness, (3) deviation of tuned and baseline controller, and (4) control channel gain by forming an augmented cost with weighted contributions from each of these. A unconstrained nonlinear program iteratively reduces the augmented cost while ensuring closed-loop stability. The tuning methodology can be applied to a plant state-space design model, or directly to measured plant data. In the remainder of the thesis the tuning methodology will be validated on a one-dimensional interferometer sample problem, experimentally on a space-telescope-like test article, and on a full-order model of a future spaceborne telescope.

Chapter 5

1-D INTERFEROMETER EXAMPLE

In this chapter a low-order one-dimensional interferometer is modeled and used as a sample problem to demonstrate the sensor/actuator topology selection algorithm from Chapter 3 and the controller tuning strategies from Chapter 4. The low-order interferometer model captures many elements of the SIM control problem and with twelve states is a non-trivial sample problem. The model includes a rigid body mode, a non-white disturbance spectrum, and low-fidelity models of optical elements.

The model will be detailed and the application of the sensor/actuator selection algorithm will be demonstrated. A constrained-topology baseline controller will be classically designed. The classical baseline controller will be tuned to explicitly demonstrate the use of the two stability robustness metrics of Section 4.1.1. By trading stability robustness and performance, adding states, and opening sensor/actuator control channels a family of tuned controllers will be generated from the classically-designed baseline controller. Similarly, a global LQG-designed modern baseline controller will be designed. By applying the tuning algorithm with the sensor/actuator index as guidance, a family of tuned controllers will be designed with increasingly more restrictive topology.

This chapter demonstrates the flexibility and application of the tuning methodology, and how a control designer might apply the techniques developed in the thesis.

5.1 Low-Order Sample Plant

Figure 5.1 is a block diagram of a one-dimensional model of a space-based interferometer that will be used extensively as a sample problem to demonstrate the techniques developed in this thesis. The model considers three main masses: a combiner (m_1) joined through springs to two collectors (m_2 and m_4). Connected through a spring on each collector is a mass (m_3 and m_5) which corresponds to a voice-coil activated mirror. The actuation of the voice coils is modeled through a relative force (f_2 and f_3). The interferometer reaction wheels are modeled with an inertial force.

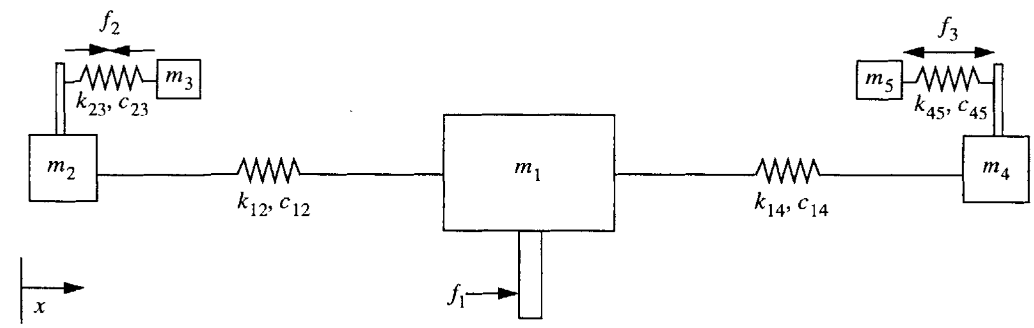

Figure 5.1 1-D Interferometer Sample Problem. Masses and springs are labeled. The position of the masses is noted by x_s where s is the mass' subscript.

Table 5.1 contains the values of the parameters indicated in Figure 5.1.

TABLE 5.1 Parameter values for the 1-D Interferometer Sample Problem.

Parameter Type	Parameter Values	Units
Mass	$m_1 = 100, m_2 = 10, m_3 = 0.1, m_4 = 9.9, m_5 = 0.1$	kg
Stiffness	$k_{12} = k_{14} = k_{23} = k_{45} = 1 \times 10^5$	N/m
Damping	$c_{12} = c_{14} = 17, c_{23} = c_{45} = 20$	N•s/m

The dynamics of the model can be determined. The vibrational modes of the 1-D interferometer are listed in Table 5.2. The arms have approximately 1% damping. The masses of the collectors are slightly different to provide a greater separation of the symmetric and antisymmetric arm modes at 15.9 and 17.3 Hz respectively. The voice coil mirrors have approximately 10% damping and have bandwidths greater than 100 Hz.

TABLE 5.2 Structural modes of the 1-D interferometer model

Mode		f_n (Hz)	ζ (%)
Rigid body		0	NA
Arm symmetric	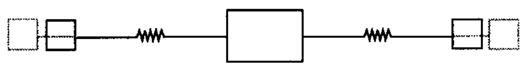	15.9	0.85
Arm antisymmetric	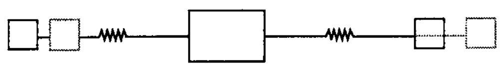	17.3	0.93
m_5 voice coil mode		160.7	10.0
m_3 voice coil mode		160.7	10.0

The force input is split to include the rigid body actuation and the higher frequency disturbance. A prewhitening filter is appended at the force input f_1 to simulate the disturbance of a reaction wheel imbalance. The prewhitening filter is a bandpass given by

$$F_d(s) = \frac{As}{s^2 + 2\pi\zeta_d\omega_d + \omega_d^2} \tag{5.1}$$

with $\omega_d = 2\pi \cdot 16$ radian/s and $\zeta_d = 30\,\%$. The second order filter is appended to the dynamics of the model resulting in a 12 state model. Figure 5.2 is a schematic of the reaction wheel as actuator and disturbance.

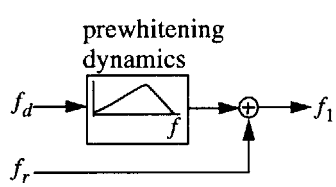

Figure 5.2 The inertial force, f_l. f_d is a disturbance force passing through pre-whitening dynamics. f_r is the rigid-body actuator.

The sensors and actuators of the one-dimensional interferometer are listed in Table 5.3. Included are the process noise disturbances and the performance variables. These inputs and outputs represent the signals for the four-block regulation problem (Section 2.1.1) that will be investigated in this chapter.

TABLE 5.3 Input and output signals for the 1-D interferometer. Resolutions are included for the sensors and actuators, intensities for the disturbances and requirements for the performances.

Signal Type	Abbreviation	Description	Symbol	Resolution[a]
Disturbance[b] w	RWAd	Reaction wheel imbalance disturbance[c]	f_d	1 N
Actuators u	RWA	Inertial reaction wheel[c]	f_r	0.01 N
	VCL	Left voice coil, relative force	f_2	0.0001 N
	VCR	Right voice coil, relative force	f_3	0.0001 N
Performance, z	RBz	Rigid body. Position of m_1	x_1	10 cm
	DPLz	Differential pathlength	$x_5 - x_3$	0.1 mm
Sensors, y	ST	Star tracker analogue[c]	x_1	30 mm
	RG	Rate gyroscope analogue[c]	$\dot{x}_1$	1 mm/s
	DPL	Laser interferometer	$x_5 - x_3$	10 μm

a. The term 'resolution' applies for the actuators and the sensors. For the disturbance, 'intensity' is more appropriate and for the performance, 'requirement' is more appropriate.

b. Additional disturbances include an actuator noise for each actuator and a sensor noise for each sensor.

c. Reaction wheels actuate torques and star trackers and rate gyroscopes measure angular quantities. In this 1-D example the translation analogue is intended. The names RWA, ST and RG are intended only for comparison with the SIM spacecraft of Chapter 7.

Figure 5.3 is a plot of the magnitudes of the transfer function matrix of the 1-D interferometer model. In the transfer functions we see the strong observability and controllability of the symmetric and/or antisymmetric interferometer arm modes. At higher frequency the voice coil modes are noted in the transfer functions. The shape of the disturbance spectrum is noted by the RWAd to DPL transfer function. The voice coil to DPL transfer functions show little controllability to the interferometer arm modes, but good authority in the bandwidth of the disturbance.

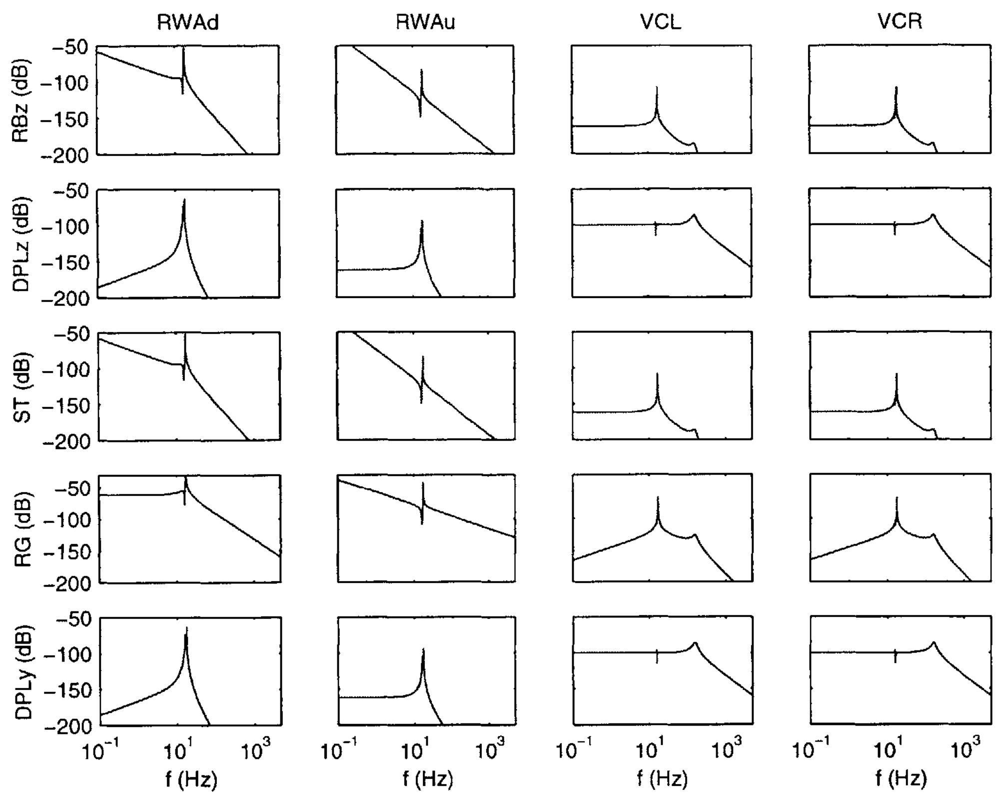

Figure 5.3 Magnitudes of transfer functions for the 1-D interferometer sample problem

5.2 Sensor/Actuator Assessment

The sensor/actuator algorithm of Chapter 3 is applied to the one-dimensional interferometer model. The resulting sensor/actuator indexing matrix, S_t, shows which sets of sensors and actuators are most effective for control, and will be later exploited to (1) determine which channels of the baseline controllers will benefit most from controller tuning, and (2) which channels in a fully-connected controller contribute little and can be removed.

The 1-D interferometer of Section 5.1 is cast into the four-block control problem with the disturbance, actuator, performance and sensor variables outlined in Table 5.3. For each of the three actuators, an actuation noise is added to the disturbance variables. The algorithm of Chapter 3 can now be applied. The user must supply four sets of information as shown in Table 3.1. For the one-dimensional interferometer example:

1. The plant model is delivered in a four-block state-space form, (A, B_w, B_u, C_z, C_y).
2. The scaling gains, R_u, R_y, R_w, R_z are set using the resolutions (for u and y variables), intensities (for w variables), and performance requirements (for z variables) which are listed in Table 5.3. These scaling factors to weight the relative importance of the sensors and actuators by capturing the anticipated signal-to-noise. The resulting sensor/actuator indices depend on the square of the scaling factors.
3. The standard value of $\gamma = 1$ is used for the output isolation mixing parameter (Equation 3.114).
4. The relative importance of the rigid body modes must be assigned by setting the ω_{RM} parameter (Section 3.2.3). The reaction wheel control the rigid body mode and the star tracker observed the rigid body mode indicating that the RWA to ST index will be ω_{RM}-dependent. The rate gyro also observes the rigid body mode which ensures the RG to RWA index will be ω_{RM}-dependent (though its ω_{RM} dependence is weaker than for the ST since the RG measures only the velocity state of the rigid body mode). The importance of the rigid body mode is set by selecting ω_{RM} by equating the greatest ω_{RM}-dependent S_t index with the greatest non ω_{RM}-dependent S_t index. This setting implicitly balances rigid-body and structural control importance.

Table 5.4 displays the logarithm of the sensor/actuator indexing matrix, $\log_{10}(S_t)$ for the 1-D interferometer.

TABLE 5.4 Sensor/Actuator matrix, S_t, for 1-D Interferometer Model. Shaded blocks represent channels in used for a classically-designed local controller.

	ST	RG	DPL
RW	18.9[a]	12.7	9.1
VCL	1.5	15.7	18.9
VCR	1.4	15.7	18.9

a. ω_{RB} tuned until the RWA to ST index matches the VCR - DPL index.

The largest entries in Table 5.4 are shaded. The shaded channels are deemed most effective for control and can be used to guide the topology of a local, classically-designed controller. The ST-to-RWA channel and the RG-to-RWA channel are both dependent on the

ω_{RM} parameter indicating these channels' suitability for rigid-body control. The ST-to-RWA channel is necessary to stabilize the rigid body mode which explains its greater magnitude. The high indices for the RG sensor to all actuators indicate that it is a sensor that is useful for attitude *and* optical control. The DPL sensor couples strongly with the voice coil actuators for optical control. The voice coil actuators provide an example where the output isolation correction of Section 3.3 is important. Figure 5.3 shows that the interferometer arm modes (15.9 Hz and 17.3 Hz) are not controllable by the voice coil actuators. The actuator does have authority in the frequency region of these modes however, and can thus act as an output isolator. The low index for the ST to voice coil channels confirms that the rigid body mode measured by the ST is not controllable by the voice coils. The low index for the DPL to RWA channel results from the DPL being a relative measure that is not controllable from the inertial RWA actuator.

The sensor/actuator matrix will be used to decouple the system into attitude (rigid body) control and optical control. S_t will be used to determine sensor to actuator channels that can be opened (or removed) to improve (or least affect) controller performance.

5.3 Example: Classically-Designed Baseline Controller

In this section a baseline controller for the 1-D interferometer sample problem will be designed with classical techniques. The baseline controller will be tuned resulting in a controller with better performance and improved stability robustness. Lastly, the use of the stability metrics from Section 4.1.1 will be demonstrated.

5.3.1 Baseline Controller Design

The classical controller is designed by decoupling the system into sets of sensors and actuators that are effective for control. To determine the suitability of particular sensor/actuator combinations for control the S_t index of Table 5.4 is used. The largest index entries are shaded, suggesting a controller topology. The intuitive decoupling of attitude control (ST - to-RWA) and optical control (DPL-to-VCL and DPL-to-VCR)

The low-effort controller is designed using sequential loop closure of two SISO loops:

Attitude control: ST to RWA

The attitude controller is designed to stabilize the rigid body modes, and is comprised of:

- A 1^{st} order lead to provide phase margin with a break frequency a factor of three below the crossover frequency,
- A 2^{nd} order lag to provide adequate roll-off with near-critical damping and a break frequency a factor of three above the crossover frequency,
- A gain adjusted for a crossover frequency of 1 Hz.

Optical Control: DPL to VCL & VCR:

The two optical loops from DPL to VCL and form DPL to VCR are simplified to a SISO loop by considering $VCL - VCR$ as a differential actuator. The simplification is valid since the optical sensor and performance (DPL) is a relative measure of optical pathlength. The optical controller is comprised of:

- A low-frequency 2^{nd} order lag to provide gain at low frequency,
- A 1^{st} order lead to provide gain over the frequency region where the disturbance significantly injects energy in the performance metric,
- A 2^{nd} order lead at the break frequency of the voice coil mass/spring mode to counter the phase loss of the actuator dynamics,
- a 2^{nd} order lag with a break frequency after crossover to provide adequate roll-off.

We note that the optical controller is an example of active output isolation. Small controllability prevents the voice coil masses from effectively modifying the frequency or damping of the structural arm modes (though structural instability is possible). Control performance is achieved by taking advantage of the small structural coupling to directly cancel the disturbances effect in the performance without adversely affecting the structure.

5.3.2 Family of Tuned Controllers

Starting from the classically-designed baseline controller, a family of tuned controllers can be designed. Successive controllers are designed by tuning the parameters of the previous design. Features can be added to change the controller topology: states can be added, sensor/actuator channels can be opened (or closed). The incremental approach allows us to monitor the progress of the tuning algorithm as features of the controller are modified one-at-a-time.

The tuning cost function is introduced in Chapter 4 and repeated here for convenience:

$$J_A(p) = J(p) + S_R(p) + d(p) + M(p). \tag{5.2}$$

The settings of the terms of the tuning cost are tabulated in Table 5.5.

TABLE 5.5 Tuning terms (from Equation 5.2) for OT tuned controller family

Term		Setting
RMS Performance	$J(p)$	Weighted RMS of the DPLz for white-noise disturbance at the RWAd input[a]
Stability Robustness	$S_R(p)$	Penalize all maximum s.v. of sensitivity deviations > 10 dB threshold. Critical point distance metric is not used, *i.e.* $\gamma_{cr} = 0$.
Controller Deviation	$d(p)$	Not used
Controller Magnitude	$M(p)$	Not used

a. The optical performance is the critical performance metric. The baseline controller stabilizes the rigid body mode and thus RBz need not be considered in the tuning cost.

The control objective is to minimize the RMS DPL jitter subject to a reaction-wheel-induced disturbance. The stability robustness metric is set to penalize maximum Sensitivity singular value spikes greater than a 10 dB threshold. The 10 dB threshold is set based on an experimental determination of stable and robust controllers from the MACE program [Miller et al., 1996].

The family of controllers resulting from the application of the tuning methodology to the classically-designed baseline controller is diagrammed in Figure 5.4.

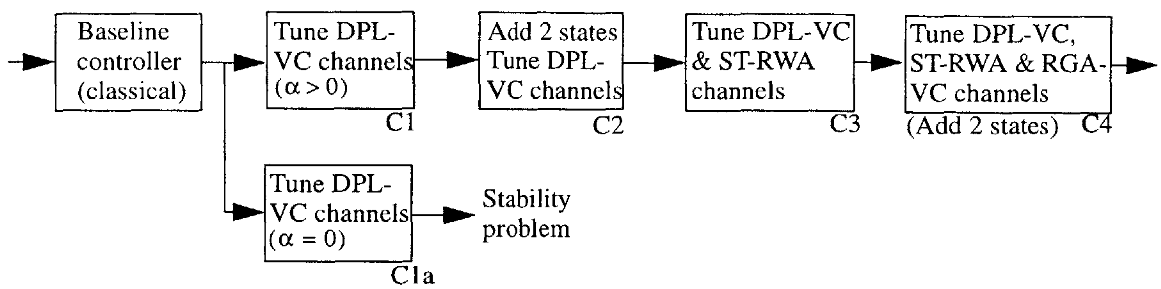

Figure 5.4 A family of tuned controllers for the 1-D interferometer sample problem: starting with the classically-designed baseline controller, states are added and additional controls channels are added to result in a final tuned controller C4. Controllers are designed by tuning the previous controller in the diagram.

We follow the sensor/actuator index matrix of Table 5.4 to choose which channels will benefit from tuning. First we tune the DPL-to-VC channels. Beginning with the baseline controller, we apply the tuning algorithm to improve the performance, with no penalty on the stability robustness. The resulting controller, C1a, is subsequently rejected for poor stability robustness. By adding a penalty on stability non-robustness, the controller C1 results. We then add two states by appending a second-order mode (with an initial frequency where G_{zw} is a maximum) to controller C1 and tune to result in controller C2. Then we choose to open up our tuning to the ST-to-RWA channel and we tune the ST-to-RWA and DPL-to-VC channels of C2 simultaneously, resulting in controller C3. Lastly, we add 2 more states and open the RGA-to-VC channels for tuning. The resulting controller also has nonzero gain in the ST-to-VC channels, but we force those channels to be zero, resulting in the controller C4.

Table 5.6 lists the RMS performance and maximum singular value of the Sensitivity transfer matrix (a measure of stability robustness) for the family of controllers from Figure 5.4. In Figure 5.5 the information from Table 5.6 is displayed graphically. The tuned controllers are able to achieve improved performance with improved stability robustness. The C1a controller, designed without a stability robustness penalty, corresponds to the large spike in the maximum singular value. Further tuning of controller C1a was not performed.

TABLE 5.6 Performance and stability robustness of the family of controller of Figure 5.4.

Controller	n_c [a]	Perf. (mm)	$[\sigma_{max}(S)]_\infty$ [b] (dB)	Notes
None	N/A	0.1306	N/A	
BC	8	0.0176	9.0	
C1a	8	0.0046	20.3	Tune DPL - VC channels with no stability robustness penalty, i.e. $\alpha = 0$.
C1	8	0.0068	7.5	Tune DPL - VC channels with a stability robustness penalty.
C2	10	0.0025	4.0	Add 2 states and tune DPL - VC channels with a stability robustness penalty.
C3	10	0.0022	4.3	Tune DPL - VC and ST - RWA channels
C4	12	0.0011	4.6	Add 2 states. Tune all channels with the exception of RGA - RWA and DPL - RWA. Remove ST - VC channels form resulting controller. We are left with a tuned controller with nonzero DPL - VC, ST - RWA and RG - VC channels.

a. Number of controller states

b. Maximum singular value of the Sensitivity for $f > 10$ Hz.

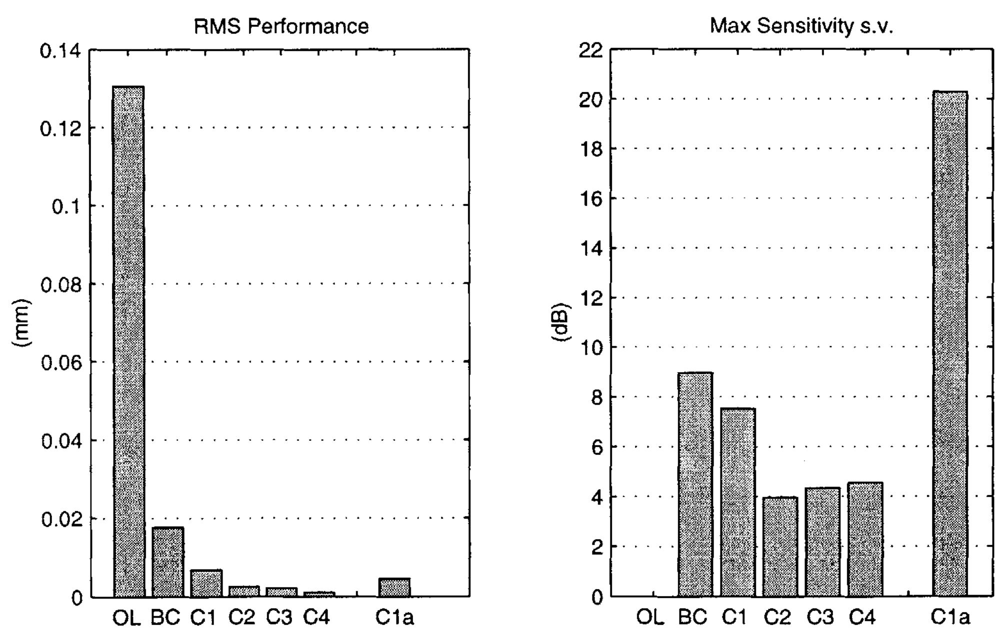

Figure 5.5 Performance and maximum s.v. of the Sensitivity (for f>10 Hz) for the family of constrained-topology controllers of Figure 5.4.

Figure 5.6 plots the performance, maximum singular values of the Sensitivity and the MIMO Nichols plot for the classically-designed baseline controller and for the tuned controller C4. The tuned controller sacrifices closed-loop performance at low and high frequency to increase its effectiveness in the critical 17 Hz range. Controller C4 achieves a 41.5 dB performance improvement compared with 17.4 dB for the baseline controller. The tuned controller eliminates the sensitivity spike corresponding to the interferometer arm modes at 17 Hz and reduces the spike corresponding to the voice coil modes at 160 Hz. The trade-off is extended bandwidth: controller C4 has a MIMO gain crossover of 107.8 Hz, compared to 55.9 Hz for the baseline controller, and a MIMO phase crossover at 321.8 Hz, compared to the baseline at 172.3Hz.

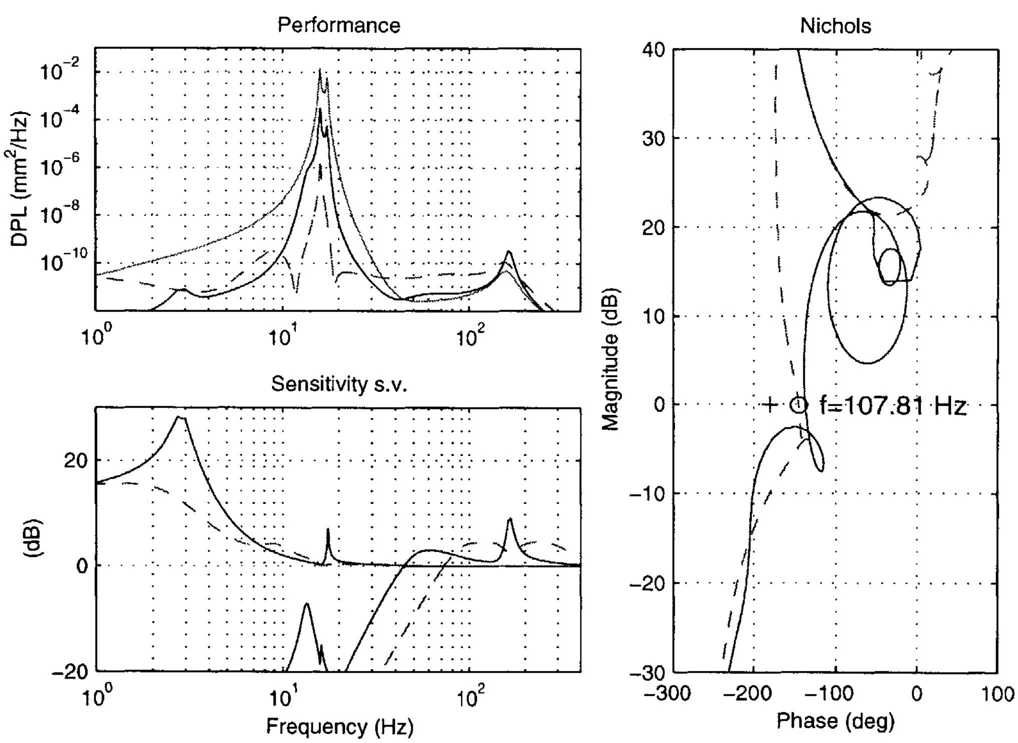

Figure 5.6 Performance (top left), maximum and minimum singular values of the Sensitivity (bottom left) and MIMO Nichols plot (right) for baseline classical controller (solid) and a tuned controller C4 (dashed). Open loop performance is indicated with a light solid line.

Figure 5.7 is a plot of the magnitudes of the controller transfer functions for the classically-designed baseline controller and the tuned controller, C4. The tuned controller exhibits a higher gain in the DPL-to-VC channels, corresponding greatly to the improved performance. In particular, a lightly damped mode in the performance critical 17 Hz frequency range is apparent. A zero near the frequency of the mass-spring voice coil mode corresponds to a robust pole/zero cancellation for extending the DPL-to-VC channel bandwidth. The ST-to-RWA attitude control channel remains mostly unchanged. Opening the RG-to-VC channels has resulted in low-pass filters in these channels for the tuned controller.

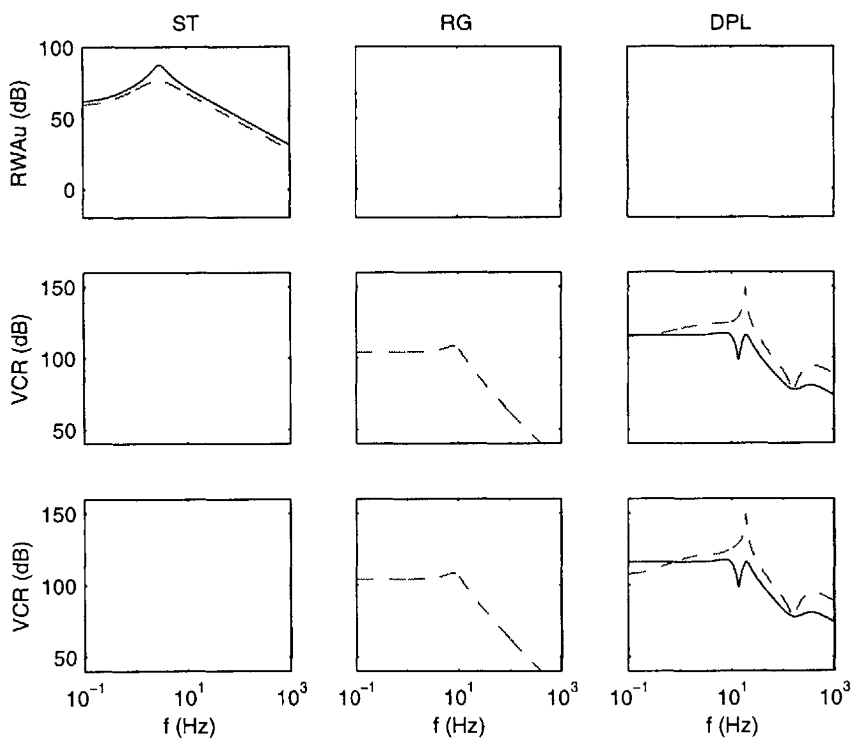

Figure 5.7 Transfer function magnitudes for the baseline classical controller (solid) and C4 tuned controller (dashed).

5.3.3 Stability Robustness Tuning: Demonstration

It is instructive to analyze the particular effects of the stability non-robustness penalty, $S_R(p)$ on tuning the controller. Recall from Equation 4.5 that $S_R(p)$ is made up from two stability robustness metrics as

$$S_R = (1-\gamma_{cr})S_S + \gamma_{cr}S_{cr} \tag{5.3}$$

where S_S penalizes the maximum singular values of the Sensitivity transfer matrix above a threshold, and S_{cr} penalizes the inverse of the distance of MIMO Nyquist locus from the critical point. In this section the use of both stability metrics will be demonstrated.

Maximum Singular Value of Sensitivity

As a demonstration of the application of the S_S stability metric a set of controllers is tuned from the classically-designed baseline. We set $\gamma_{cr} = 0$ in Equation 5.3. The S_S metric is set as indicated in Table 5.5 with a threshold to penalize singular value spikes greater than 10 dB. The S_S penalty is gained by a factor, β and the controller is tuned for various β.

Figure 5.8 displays the maximum singular value magnitude versus the β value for a set of tuned controllers with constant performance. Also displayed is the maximum Sensitivity singular value (s.v.) as a function of frequency for various values of β.

We see that as the factor β is increased that for a given performance the maximum amplitude of the maximum Sensitivity singular value drops. This indicates improved stability robustness to unstructured uncertainty [Lehtomaki et al., 1981]. From the plot on the right we see that improving performance with only a small stability robustness penalty results in a Sensitivity maximum s.v. spike at ~ 75 Hz, approximately corresponding to the baseline crossover frequency. A second spike at ~ 160 Hz pops up as well and corresponds to the mass/spring mode of the voice coil actuators. In fact as β increases the voice coil spike pops up. It is important for the designer understand the nature of the spikes in the maximum s.v. of the Sensitivity. Smooth crossover spikes such as that at 75 Hz indicate that unstructured uncertainty in the transfer matrix at that frequency may cause instability.

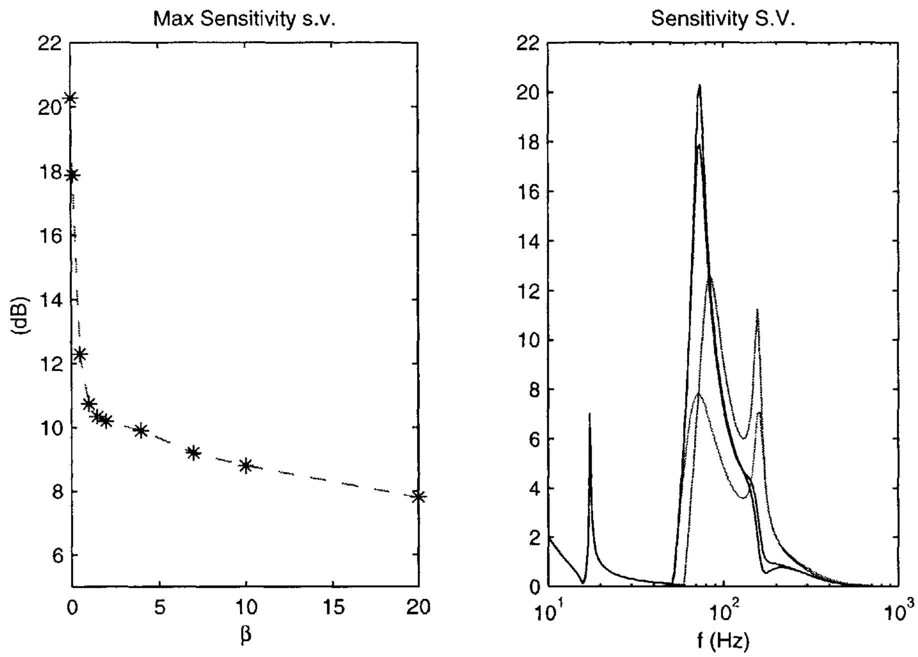

Figure 5.8 A family of controllers designed to maintain performance as stability robustness is improved. The left figure plots the maximum spike in the Sensitivity s.v. versus the stability robustness tuning parameter, β. The right figure plots the maximum s.v. of the Sensitivity as β is increased (increasing β corresponds to lighter curves)

The probabilistic chance that the physical plant allows such a deviation may be very small though. On the other hand, for the 160 Hz spike corresponding to the voice coil mode, a physically-probable change in damping or frequency in the voice coil mass/spring mode may result in instability. These examples demonstrate the potential conservatism of the maximum Sensitivity singular value as a stability robustness metric (Section 2.1.3). It is important that the designer distinguish bad spikes in the maximum Sensitivity s.v. from acceptable ones. The following rules can be used as a guide: (1) sharp spikes tend to correspond to a lightly damped pole or to a pole/zero cancellation and should be avoided, (2) spikes should be avoided wherever there is mismatch between the design model (or design data) and true plant dynamics, (3) wherever a spike corresponds to a pole/zero in the plant which may have uncertain frequency or damping. Future research should address an uncertainty model for spaceborne telescopes and link the uncertainty to the stability robustness metrics of this thesis.

Pushing the Nyquist Locus from the Critical Point

The S_{cr} stability robustness metric attempts to push the Nyquist locus away from the critical point. We demonstrate its application with two examples.

Example 1: Robust to miss-modeled actuator dynamics

By setting $\gamma_{cr} = 1$ (see Equation 5.3) and by choosing W_{cr} to be nonzero in the $f \approx 160$ Hz range, we penalize the inverse of the distance from the MIMO Nyquist locus to the critical point near the frequency of the voice coil mass/spring mode. Thus, the tuned controller is made more robust to miss-modelling the frequency and damping of the voice coil model.

Figure 5.9 is a one-sided MIMO Nyquist plot of the baseline control and the tuned controller. The loop near the critical point of the baseline control case (solid) corresponds to the voice coil mode. By decreasing the size of the voice-coil-mode-induced loop the tuned controller (dashed) passes farther from the critical point in the 160 Hz range.

Figure 5.10 is a plot of the performance, maximum s.v. of the Sensitivity and Nichols plot for the baseline and improved-robustness controller. The tuned controller exhibits a performance of 0.0096 mm, 5.3 dB better than the baseline controller. In the Nichols plot, we note that the loop near the gain crossover (which corresponds to the voice coil mode) is pushed well into the roll-off for the tuned controller. The trade-off is that the tuned locus has a gain crossover which passes more closely to the critical point. The voice-coil mode spike at 160 Hz in the maximum s.v. of the Sensitivity is pushed down, indicating a connection between the S_R and S_{cr} stability robustness metrics. It is interesting to note that at 55.9 Hz, the tuned gain-crossover frequency is the same as for the baseline controller.

Example 2: Robust to structural damping overestimates

By again setting $\gamma_{cr} = 1$ and by choosing W_{cr} to be nonzero in the $f \approx 17$ Hz range, we penalize the inverse of the distance from the MIMO Nyquist locus to the critical point near the frequencies of the interferometer arm modes. The physical case corresponds to a

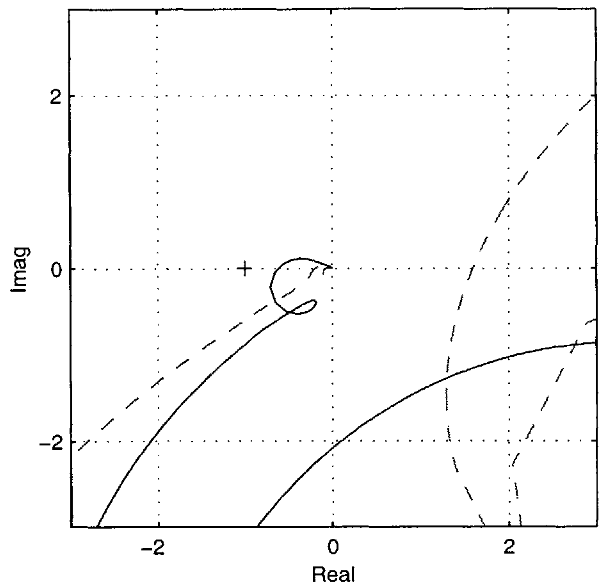

Figure 5.9 Multivariable Nyquist plot. The classical baseline controller is solid. The controller tuned to push the locus away from the critical point at frequencies greater than the VC mode (~160 Hz) is dashed.

designer's concern that the structural damping may be underestimated. In this example, we examine the applicability of the S_{cr} stability robustness metric to capture a parametric uncertainty in the damping of a structural mode.

Figure 5.11 plots the performance, maximum s.v. of the Sensitivity transfer matrix and the MIMO Nichols plot for the classically-designed baseline controller and for the controller tuned to be robust to structural damping overestimates.

The tuned controller exhibits a performance of 0.0117 mm, 3.5 dB better than the baseline controller. In the Nichols plot, the loop corresponding to the arm modes are pulled away from the critical point as indicated by the arrow. At higher frequencies the tuned controller approaches the baseline. The maximum s.v. of the Sensitivity transfer matrix also remains unchanged.

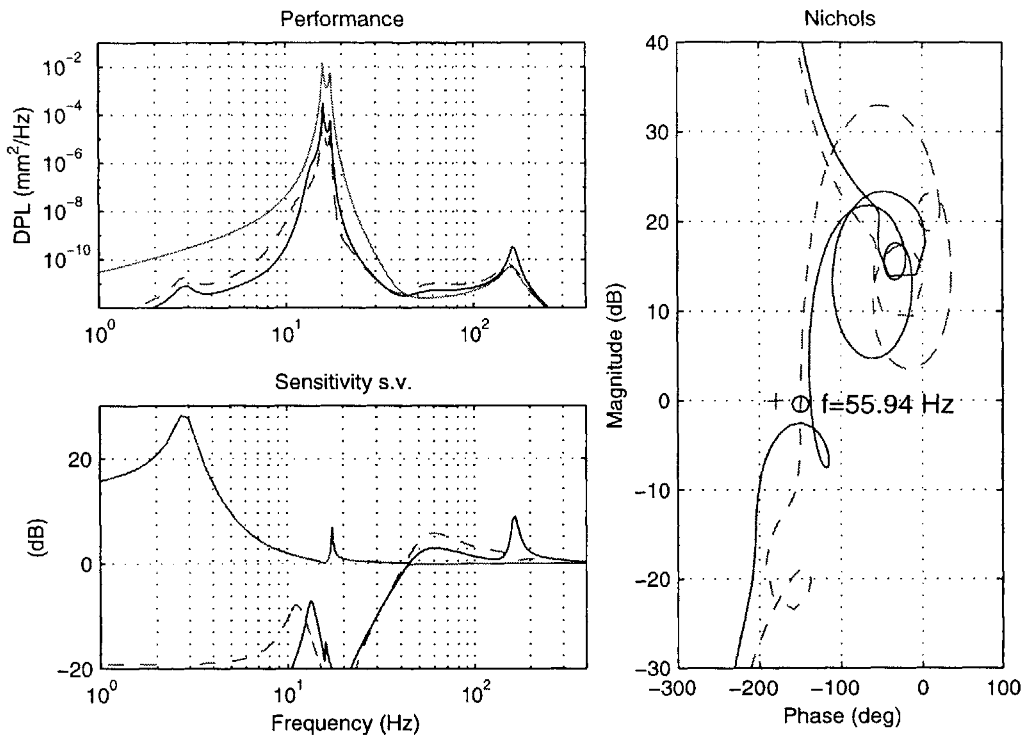

Figure 5.10 Performance (top left), maximum and minimum singular values of the Sensitivity (bottom left) and MIMO Nichols plot (right) for baseline classical controller (dark) and a tuned controller (dashed). The tuned controller penalizes the distance from the critical point for f>150 Hz. Open loop performance is indicated with a light solid line.

To verify that the action of the S_{cr} cost penalty does indeed improve the stability robustness, Figure 5.12 repeats the Nichols plot of Figure 5.11 for three damping ratios of the structural arm modes (ζ=1%, 0.01%, and 0). The resulting curves show that as ζ is decreased the radius of the loop corresponding to the arm modes increases. The baseline case encircles the critical point and exhibits instability for sufficiently low ζ. The tuned controller has a stable closed loop for all ζ, indicating an improved robustness.

One critical feature of the metric S_{cr} is that it should be applied very locally in frequency.

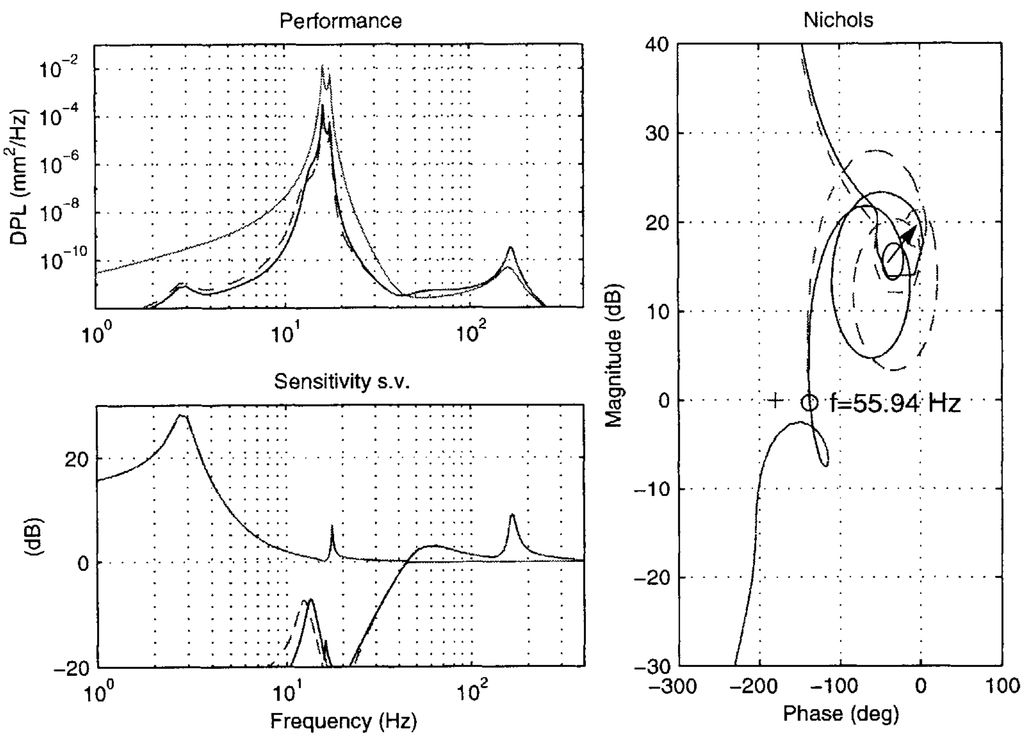

Figure 5.11 Performance (top left), maximum and minimum singular values of the Sensitivity (bottom left) and MIMO Nichols plot (right) for baseline classical controller (dark) and a tuned controller (dashed). The tuned controller penalizes the distance from the critical point for frequencies near the arm modes (*i.e.* $f \approx 16$ Hz.). The arrow in the right plot indicates a shifting away from the critical point of the loop corresponding to the interferometer arm modes. Open loop performance is indicated with a light solid line.

5.4 Example: LQG-Designed Baseline Controller

In this section an LQG baseline controller for the 1-D interferometer sample problem will be designed. The baseline controller will be tuned resulting in a controller with better performance, similar stability robustness and a simplified sensor/actuator topology.

5.4.1 Baseline Controller Design

An LQG control problem is set up by specifying the weights required in the LQG synthesis framework of [Lublin et al., 1996]. The synthesis of LQG controllers is briefly covered in Section C.1. The design weights for the baseline LQG controller are listed in Table 5.7.

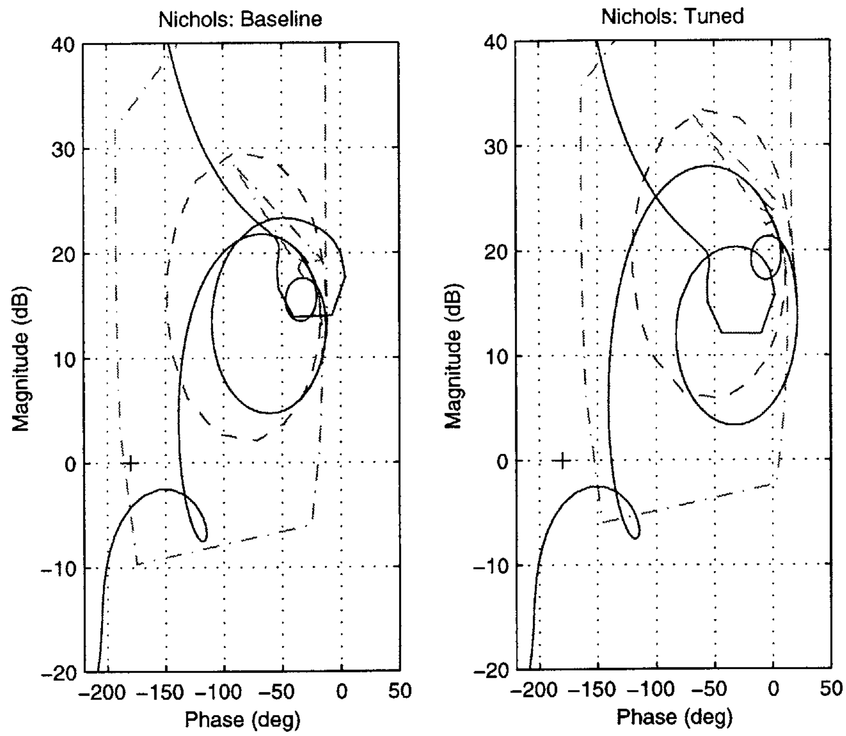

Figure 5.12 Nichols stability plots of the baseline (left) and tuned (right) case as damping of the symmetric and antisymmetric arm modes is varied. ζ=1% is solid, ζ=0.01% is dashed and ζ=0 is dash-dotted. The tuned controller is designed to be more robust to uncertainty in the arm modes than the baseline controller by penalizing the distance from the critical point for frequencies near the arm modes (*i.e.* $f \approx 16$ Hz)

TABLE 5.7 Weights for the baseline LQG controller

Weight	Design weights	Notes
Performance z	DPLz is weighted with a unit intensity. RBz is weighted less with respect to DPLz.	Penalizes DPL error at the interferometer arm modes
Disturbance w	Unit intensity	Pre-whitened in scaling for Section 5.2
Control Use u	$\rho_{RWA} = 3.5 \times 10^{-4}$ [a] $\rho_{VCL} = \rho_{VCL} = 3.5 \times 10^{-4}$	Ratio of ρ weights identical to the ratio of actuator noises in Table 5.3. The absolute weights are tuned until the LQG baseline controller and the classically-designed baseline controller have identical performance.
Sensor Noise y	$\mu_{ST} = 3 \cdot 10^{-2}, \mu_{RG} = 10^{-3}$ $\mu_{DPL} = 10^{-5}$ [b]	μ set with the sensor noises of Table 5.3

a. R_{uu} from Equation C.2 is formed as $R_{uu} = \mathrm{diag}\left[\rho_{RWA}^2 \ \rho_{VCL}^2 \ \rho_{VCR}^2\right]$

b. V_{yy} from Equation C.4 is formed as $V_{yy} = \text{diag}\left[\mu_{\text{ST}}^2\ \mu_{\text{RG}}^2\ \mu_{\text{DPLy}}^2\right]$

It is required for LQG synthesis that non-stable modes are observable by the sensors and performance measures, and that all non-stable modes are controllable by the disturbances and the actuators. If these conditions are not met, LQG synthesis will fail. The tuning methodology does not require these strict controllability and observability requirements. We do assume the plant is stabilized by the baseline controller however, and if a mode is uncontrollable or unobservable the automated test for stability (for direct-data tuning) may fail.

The baseline LQG controllers are global and allow dynamic gain from each sensor to each actuator. The RG to RWA control channel is a low-pass filter. The DPL to voice coil channels display a high gain in the performance-critical 16 Hz frequency range. A zero near the frequency of the voice coil modes serves the same function as a similar zero in the classically-designed baseline controller: reduce the Sensitivity of the optical loop near the voice coil resonance. The zero-channels in the classical design are non-zero for the LQG controller. The use and necessity of the channels that are deemed non-critical by the sensor to actuator indexing (Section 5.2) will be examined.

The potential increase in performance of the LQG controllers over the classical designs is achieved with a cost: (1) an increase in the number of states, and (2) a shift from a local topology to a global controller topology.

5.4.2 Family of Tuned Controllers

Starting from the LQG baseline controller another family of tuned controllers can be designed. The settings of the terms of the tuning cost (Equation 5.2) are tabulated in Table 5.8.

The family of controllers resulting from the application of the tuning methodology to the LQG-designed baseline controller is diagrammed in Figure 5.13. Controllers are tuned from the previous controller in the figure. Beginning with the baseline LQG controller we

TABLE 5.8 Tuning terms (from Equation 5.2) for OT tuned controller family

Term		Setting
RMS Performance	$J(p)$	Weighted RMS of the DPLz for white-noise disturbance at the RWAd input[a]
Stability Robustness	$S_R(p)$	Penalize all maximum s.v. of sensitivity deviations > 10 dB threshold. Critical point distance metric is not used, *i.e.* $\gamma_{cr} = 0$.
Controller Deviation	$d(p)$	Not used
Controller Magnitude	$M(p)$	Used to selectively penalize control use for particular sensor/actuator channels The penalized channels can subsequently be removed.

a. The optical performance is the critical performance metric. The baseline controller stabilizes the rigid body mode and thus RBz need not be considered in the tuning cost.

tune all of the parameters to arrive at controller K1. We now use the indices of the sensor/actuator index matrix to determine which control channels are unnecessary. From controller K1, we set $M(p)$ to penalize gain in the ST-to-VC channels (the smallest elements of S_t) resulting in controller K2. Controller K2a results from penalizing the gain of the DPL-to-VC channel (the largest elements of S_t). Controller K2a exhibits poor stability robustness and is not further tuned. Following the element size of the S_t entries, we penalize the gain of the DPL-RWA channel of controller K2, resulting in controller K3. Lastly the RG-RWA gain of controller K3 is penalized resulting in tuned controller K4.

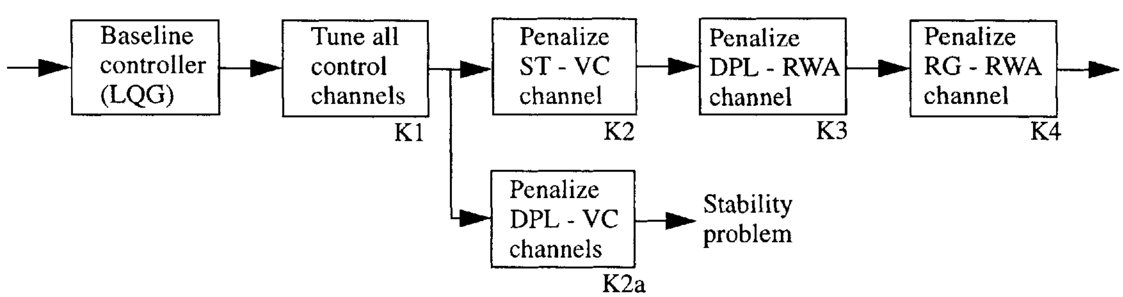

Figure 5.13 A family of tuned controllers for the 1-D interferometer sample problem: starting with the baseline LQG controller, particular control channels are penalized and removed from the controller. Each controller is tuned from the previous controller in the diagram.

Table 5.9 records the performance and maximum singular value of the Sensitivity for each controller in the family of Figure 5.13. Two cases are presented where appropriate: a fully connected case (all non-zero control channels), and a constrained topology case. The constrained topology case corresponds to forcing sensor/actuator channels of the control to 0. Figure 5.14 is a graphical display of the information of Table 5.9 for the constrained topology case. We see that as we move along the family of controllers, the performance is improved with little change in the stability robustness metric. The exception (case K2a) results when we attempt to force a large-S_t index channel to zero. The resulting controller has poor robustness as seen by a large spike in the maximum Sensitivity singular value. We have demonstrated how to use the tuning technique to remove control channels as guided by the sensor/actuator index matrix. Channels with a low index can be tuned out of the controller without adversely affecting the performance and stability robustness. The constrained-topology controller K4 is the same order and input/output topology as controller C4 (Figure 5.4) and achieves the same performance and stability robustness.

TABLE 5.9 Performance and stability robustness of the family of controller of Figure 5.13. Both the fully connected and constrained topology (channels set to 0) controller cases are considered. All controllers have 12 states.

Controller	Fully connected topology		Constrained topology		
	Perf. (mm)	$[\sigma_{max}(S)]_\infty$ [a] **(dB)**	**Perf. (mm)**	$[\sigma_{max}(S)]_\infty$ [a] **(dB)**	**Notes**
None	0.13	N/A	N/A	N/A	No controller
BC	0.017	2.2	N/A	N/A	global controller (no i/o constraint)
K1	0.0029	4.5	N/A	N/A	global controller (no i/o constraint)
K2	0.0028	2.3	0.0028	2.3	ST - VC channels set to 0
K2a	0.0017	0.7	0.0230	11.3	DPL - VC channel set to 0. Sharp spikes appears in $\sigma_{max}(S)$
K3	0.0014	4.1	0.0015	4.1	ST - VC channels and DPL - RWA channel set to 0
K4	0.0011	4.6	0.0012	4.6	ST - VC, DPL - RWA, and RG - RWA channels set to 0

a. Maximum singular value of the Sensitivity for $f > 10$ Hz.

Figure 5.15 plots the performance, maximum singular values of the Sensitivity and the MIMO Nichols plot for the classically-designed baseline controller and for the tuned controller K4. The tuned controller demonstrates greater performance in the critical 17 Hz

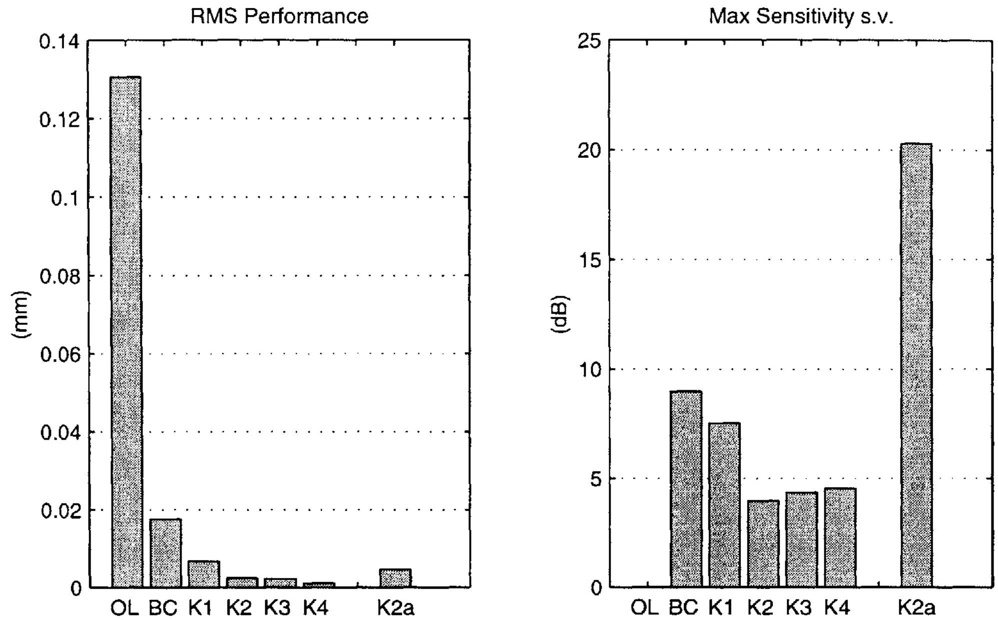

Figure 5.14 Performance and maximum s.v. of the Sensitivity (for $f > 10$ Hz) for the family of constrained-topology controllers of Figure 5.13.

range, and achieves 40.7 dB compared with 17.7 dB. Compared with the classically-designed baseline controllers (compare with Figure 5.6) the maximum Sensitivity singular value of the LQG designs are much smoother. The activity in the Sensitivity singular value plot at 18 Hz corresponds to the interferometer arm modes. The trade-off for the improved performance and fewer control channels in K4 is that the tuned design has higher low-frequency sensitivity than does the baseline design. Note that although the LQG-tuned controller K4 and the classically-designed tuned controller C4 have identical structure (order and input/output topology) and achieve the same performance with similar stability robustness, controller K4, with a gain-crossover frequency of 18 Hz, does so with much less bandwidth.

Figure 5.16 is a plot of the magnitudes of the controller transfer functions for the LQG-designed baseline controller and the tuned controller K4. The tuned controller has a constrained topology as seen by the zero channels. The tuned controller exhibits a higher low-frequency gain in the DPL-to-VC channels, corresponding to the improved performance.

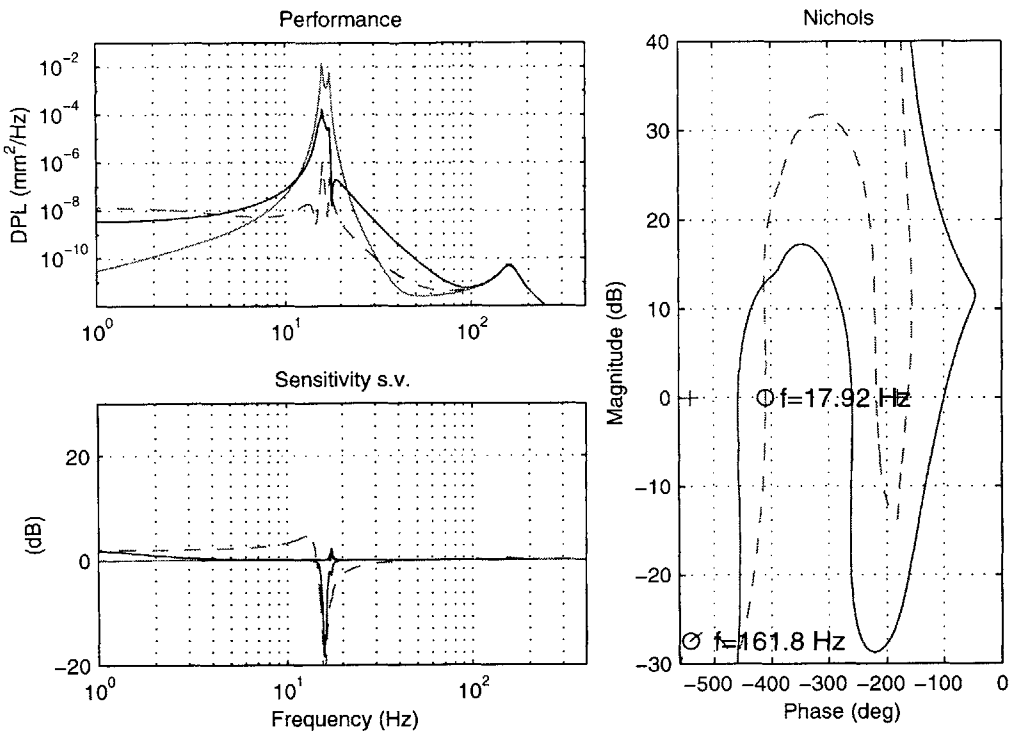

Figure 5.15 Performance (top left), maximum and minimum singular values of the Sensitivity (bottom left) and MIMO Nichols plot (right) for baseline classical controller (dark) and a tuned controller K4 (dashed). Open loop performance is indicated with a light solid line.

The bandwidth of the tuned ST to RWA attitude control is increased. The RG-to-VC channels exhibit lightly damped modes in the performance-critical 17 Hz frequency range. Comparing with Figure 5.7 we see that in general the LQG-tuned controller has smaller gains than its classically-designed counter-part. The LQG-tuned design uses its gain more efficiently.

5.5 Summary

A one-dimensional interferometer sample problem is introduced and modeled. The model captures key elements of future spaceborne telescopes including: band-pass disturbance, lightly-damped structure, active optics and rigid-body modes. The effectiveness of the sensors and actuators for control is determined by applying the algorithm of Chapter 3.

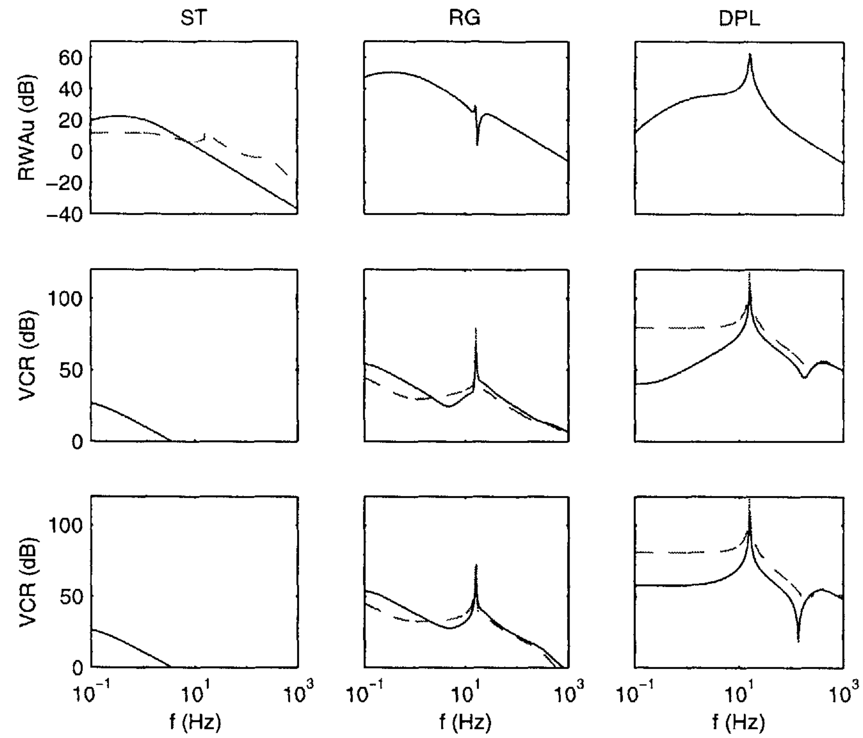

Figure 5.16 Transfer function magnitudes for the baseline LQG controller (solid) and K5 constrained-topology tuned controller (dashed).

A baseline controller is designed with classical techniques. Starting from the classically-designed baseline controller the tuning methodology was applied to add states, improve performance, improve stability robustness and open control channels. The resulting controllers are compared with the baseline design and shown to have improved performance with improved stability robustness. Special examples are presented to highlight the use of the tuning methodology's stability robustness metrics. In one example both stability metrics are shown to result in similar tuned controllers. Limitations of the stability metrics are presented.

A baseline controller is also designed with LQG synthesis. Starting from the LQG-designed baseline controller the tuning methodology is applied to improve performance and to remove sensor/actuator controller channels without adversely affecting the stability robustness. The sensor/actuator effectiveness matrix provides a guideline for which channels can be removed. The final tuned controller has an identical structure (order and input/output topology) to the classical-designed tuned controller, and achieves the same performance and stability robustness with less control bandwidth. Extrapolating to SIM suggests the possible advantage of a tuned-LQG control strategy. The difference between the tuned controllers indicates the dependence of the final tuned design on the baseline controller.

With satisfactory performance on a non-trivial sample problem, we are now prepared to experimentally validate the tuning methodology on a test article relevant to future space-borne telescopes.

Chapter 6

EXPERIMENTAL VALIDATION

In this chapter, we demonstrate experimental validation of the controller tuning technique on a laboratory test article representative of future space-based telescopes. We begin the chapter with a high-level description of space telescope control. Then a detailed description of the Origins Testbed is provided. The Origins Testbed captures the dynamics and control of space-based telescopes, and allows traceable implementation of the all elements of high-level space telescope control. A baseline controller for the Origins Testbed is then presented. Lastly, the tuning techniques are applied to the baseline controller to arrive at a family of tuned control designs.

6.1 Space Telescope Control

Space telescopes observe astronomical targets, and thus their performance can be quantified in terms of optical performance metrics. Two distinct, but coupled, optical performance metrics can be identified: pointing and phasing. Pointing is an angular metric measured in units of root-mean-squared (RMS) arc-second pointing, and refers to the jitter present in the angular tracking of a target. In terms of science light, the pointing metric is related to wavefront tilt. The second metric, phasing, refers to the optical differential path-length (DPL), measured as an RMS distance, between analogous optical paths. In the case of an interferometer, the phase error is an RMS measure of the DPL between the two interfered signals. For a filled-aperture telescope, the phasing metric is more difficult to apply.

One simplification is to consider the focus of the secondary (at a detector) as analogous to a combiner in the interferometer case.

Three operational events have been identified as being common to space telescopes including NGST and SIM:

1. **Optical Capture**: The mode of operation, after deployment or a disturbance, where the wavefront error is too large for fine optical control. A coarse control algorithm must reduce the error to within a tolerance before the optical control is effective. The optical fine control algorithm then maintains capture of the fringe (image) while minimizing disturbance effects.
2. **Observation**: An extended interval of quiet operation where the telescope is integrating an astronomical image. Disturbance-induced jitter (generated onboard and externally) must be kept small to maintain resolution throughout the period of observation. The wavefront error is minimized using optical pathlength control and structural control as required.
3. **Slewing**: An operation of movement while the telescope acquires a new target. In the case of SIM, (2) and (3) are combined, since SIM executes a constant rate rotational maneuver during its imaging mode.

These operational events are captured in a block diagram of Figure 6.1.

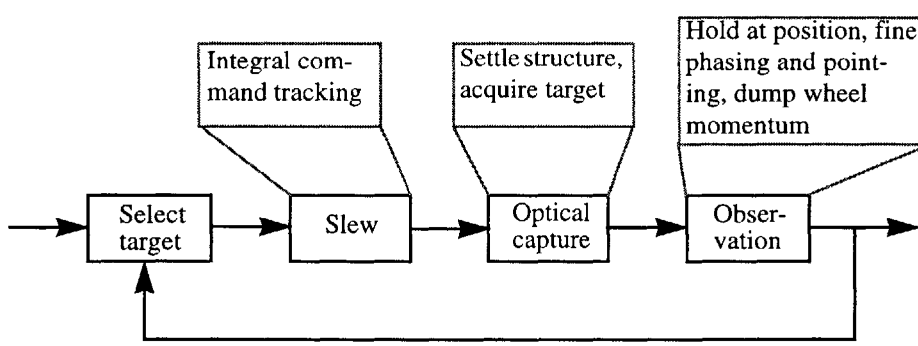

Figure 6.1 Space telescope / Origins Testbed control block diagram

The control requirements for the three telescope operational events are presented in Table 6.1. In the thesis, Slew Control and Observation Control of space telescopes are investigated.

TABLE 6.1 Control requirements for space-based telescopes

Operational Event	Control Requirements
Optical Capture	Alignment algorithm: scan optical components through a range of motion in a set pattern to align optical components. Optical capture will not be developed in this Thesis, though an alignment algorithm is introduced in [Mallory et al., 2000].
Observation	Regulation and noise rejection: the telescope is holding in position as controlled by the slew controller, and fine phasing and fine-pointing control are enabled. The principal disturbance source is from the RWA.
Slew	Low bandwidth integral tracking control with zero steady state error to point the telescope at a target. Nonlinear logic controls thrusters to dump RWA momentum.

6.2 Origins Testbed

The Origins Testbed (OT) is a laboratory test article that incorporates the same quality of dynamics and control problems that are anticipated by the Origins observatories. The OT has the capability to operate in the three operational events Section 6.1, and is the first spacecraft-type testbed with the capability to address the impact of slewing on nanometer phasing and sub-arcsecond pointing. The OT evolved from the MIT Multipoint alignment testbed, a stationary tetrahedral truss for investigating the dynamics and control of flexible space structures [Blackwood et al., 1991] and belongs in a family of control testbeds described in [Miller and Mallory, 1998]. The primary science objective of the OT research program is:

To address challenges faced by NASA's Origins Program telescopes in areas related to dynamics and control, and to ensure that the results are traceable to these missions.

A description of the requirements that drove the design of the OT is found in [deBlonk et al., 1996]. A detailed description of the testbed and its research program is found in [Mallory et al., 2000].

Figure 6.2 is a photograph of the Origins Testbed. The OT is formed by a truss structure with four arms separated by ninety degrees, lying in a plane. Each arm is 1.375 meters in length from the center of the testbed. The tower rises 2 meters from the top of the arms and is constructed from identical truss elements (struts and nodes). The arms and tower are connected, and the entire truss is bolted to an aluminum frame. While the truss forms the quiet, optical side of the testbed, the aluminum frame forms the spacecraft bus. The spacecraft bus is connected through a two-axis gimbal to a large support mount, fixed to the laboratory floor. The gimbal houses a high-resolution encoder, which provides a measure of the slew angle with respect the laboratory reference frame. A DC motor is housed in the gimbal providing low-frequency torque about the slew axis. The weight of the testbed is off-loaded from the gimbal with a bearing mechanism, which limits the slew maneuver to a single axis. Housed at the base of the spacecraft bus is a reaction wheel mount with two reaction wheels aligned such that their axis of rotation is parallel to the slew axis. The OT is mass-balanced about the center of rotation to simulate the neutrally stable dynamics of a spacecraft. To simulate the low-frequency dynamics of solar panels and heat shields, two brass beams with 2 Hz fundamental vibration modes have been fixed to the testbed. The vibration of these beams dominates the testbed's low-frequency response, and couples significantly with the OT's pointing response.

The testbed's optical system is responsible for measuring the fine phasing and pointing performance. Optical elements are placed along two opposing arms, at the center of the testbed where all four arms and the tower meet, and at the top of the tower. Three channels of a laser interferometer allow a high frequency, high resolution measure of the DPL. Two flat mirrors fixed to the laboratory ceiling provides an external reference. A CCD system provides a measure of the pointing performance by recording the position of a laser spot.

6.2.1 Structure

The truss structure is composed of aluminum tubes of 3/8" outer diameter and 0.058" wall thickness, bolted to aluminum nodes. The struts have been designed to have local bending resonances greater than 200 Hz, higher than the 100 Hz bandwidth of the structural and optical control. The uncontrollable local resonances are high enough in frequency that

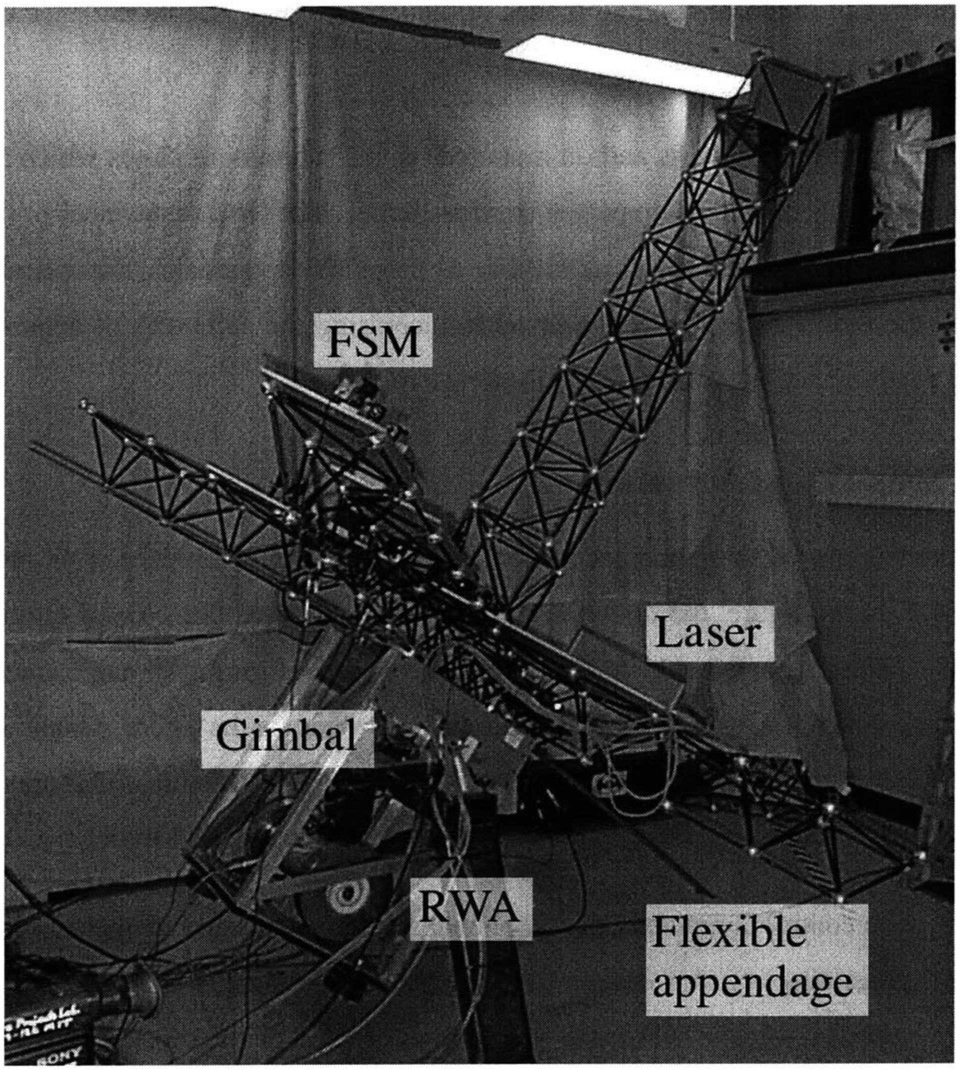

Figure 6.2 Origins Testbed

they do not present a design limitation for the lower bandwidth control design. The arm truss lattice is composed of bays of square based pyramids. Adjacent apexes are joined by a longeron. The tower is composed of cubic bays with diagonal longerons on each face. Detail on the characteristics of the struts, and on a finite element model of the OT is provided in [Mallory et al., 1998].

The cross-sectional dimensions of the aluminum members of the spacecraft bus portion of the testbed were chosen to ensure that the local bending modes of the bus are as high as the frequency of the local bending modes of the lattice struts. The mount appears rigid in the control bandwidth of interest.

Optics are fixed to 1/4" posts and on mounted on 1/4" aluminum plates which are bolted to aluminum balls that make up part of the truss lattice. The local resonances of the optical posts have been measured as low as 110 Hz. At these low frequencies, the optical post resonances are close to the control bandwidth, increasing the difficulty of achieving good control performance while maintaining stability robustness.

6.2.2 Sensors and Actuators

A block diagram of the principal sensor and actuator suite for the OT is provided in Figure 6.3. In the figure, the direction of the arrow represents the flow of information or actuation. Information from the testbed is obtained by measuring slew angle and rate, optical phasing, and optical pointing. In addition to the sensors in the figure, a bank of accelerometers and strain gauges, which can be placed on the structure, measure structural vibration. The wheel tachometer provides a measure of the reaction wheel speed.

The real-time control computer closes the feedback loop by gathering the sensor information, and generating actuator commands. The testbed slew angle and speed is controlled with the reaction wheels, while the gimbal motor provides a thruster-like momentum dump for the wheels. Optical phasing is controlled with an optical delay line. Optical pointing is controlled by the fast steering mirrors, and is coupled to the slew angle.

In Table 6.2 and Table 6.3, the testbed actuator and sensor suites are respectively detailed. The corresponding analogue for the SIM and NGST telescopes are provided.

6.2.3 Optical System

SIM and NGST are both telescopes whose performance is quantified optically. To this end, the optical system for the OT is highly important, and will be further detailed. The Testbed optical system is divided into a phasing system and a pointing system which are

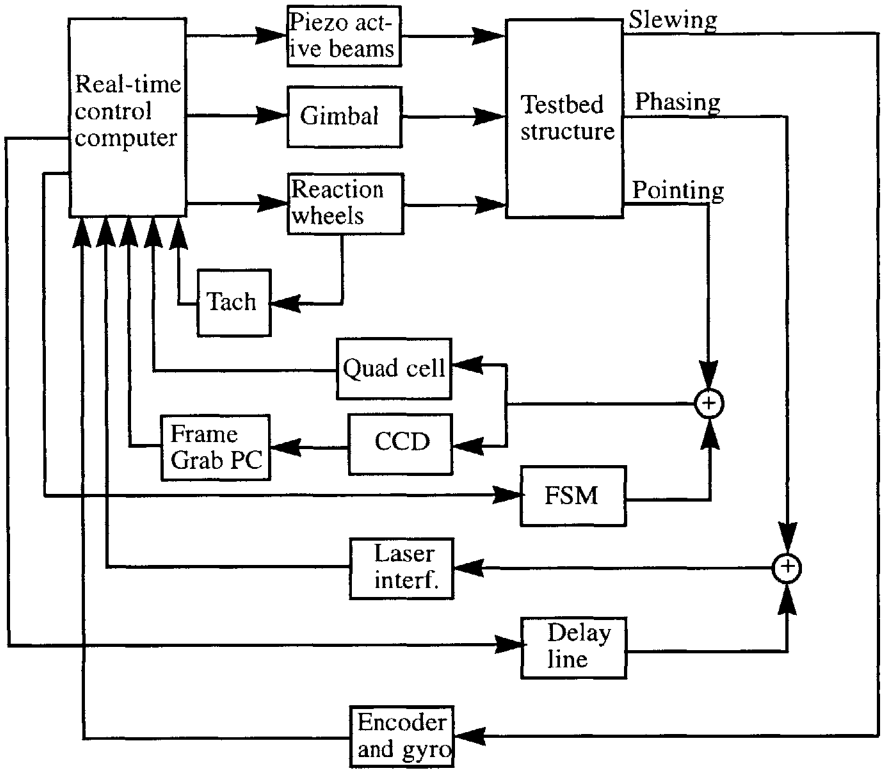

Figure 6.3 Origins Testbed subsystems block diagram

TABLE 6.2 Origins Testbed actuator suite

Actuator	Stroke	Resolution	Primary Function	Secondary Function	SIM Analogue	NGST Analogue
Reaction wheels	3.9 N · m	0.0020 N · m	Slew spacecraft	Realistic disturbance source	4 wheels	4 wheels
Gimbal motor	2.9 N · m	0.0014 N · m	Momentum dump for wheels	N/A	Thrusters	Thrusters
Optical delay line: Coarse (voice coil)	730 μm	0.36 μm	Coarse phasing control	Optical capture	Voice coils	No direct analogue. Active primary
Optical delay line: Fine (piezo mirror)	43.8 μm	46.5 nm	Fine phasing control	N/A	Piezo Mirrors	No direct analogue. Active primary
Fast steering mirrors	2850 arcsec	1.4 arcsec	Fine pointing control	Optical capture	Fast steering mirrors	Fast steering mirrors
Solar panel actuator	1000 με	0.5 με	Solar panel active damping	Pointing disturbance source	None	None

TABLE 6.3 Origins Testbed sensor suite

Sensor	Range	Resolution	Function	SIM Analogue	NGST Analogue
Encoder	60 degrees	4 arcsec	Rigid body slew angle	Star tracker	Star tracker
Angular rate gyro	20.5 deg/sec	0.01 deg/sec	Rigid body slew velocity	Angular rate gyro	Angular rate gyro
Wheel tachometer	3333 rpm	1.7 rpm	Reaction wheel speed	Wheel tachometer	Wheel tachometer
Laser interferometer	10 m	50 nm	Phasing measure	Laser interferometer	Laser metrology
CCD camera	195 arcsec	0.1 arcsec	Fine pointing measure (slow sample)	Tilt sensor	Tilt sensor
Quad cell photodiode	194 arcsec	1.2 arcsec	Fine pointing measure (fast sample)	Tilt sensor	Tilt sensor
Solar panel strain gauge	20500 $\mu\varepsilon$	10 $\mu\varepsilon$	Solar panel strain	None	None

used as both control systems sensors and as performance monitors. A photograph of the OT optical system is seen in Figure 6.4, and a block diagram of the optical elements is found in Figure 6.5. In these figures, we see that the optical paths are concentrated on two arms of the testbed, called the optical arms.

Phasing is implemented with a heterodyne laser interferometer with a 50 nm resolution. A laser source is mounted to the testbed. Beam splitter optics split the laser source into three channels, providing a measure of three relevant DPL's. The internal channel, DPL_i serves as an internal reference, measures the DPL of the two optics arms, and is typically used as a sensor. The external channel, DPL_e is used for measurements with respect to the lab frame, measures the DPL of the two optics arms as well as a contribution to a testbed-external lab ceiling mirror and can be used as a measure of performance. A third channel, DPL_t, an internal channel which includes a testbed tower measure, is not used in the experiments for this thesis. By forming linear combinations of the three interferometry channels, distinct optical phasing paths for SIM and NGST can be formed as detailed in [Mallory et al., 2000]. Both DPL_i and DPL_e pass through the optical delay line of

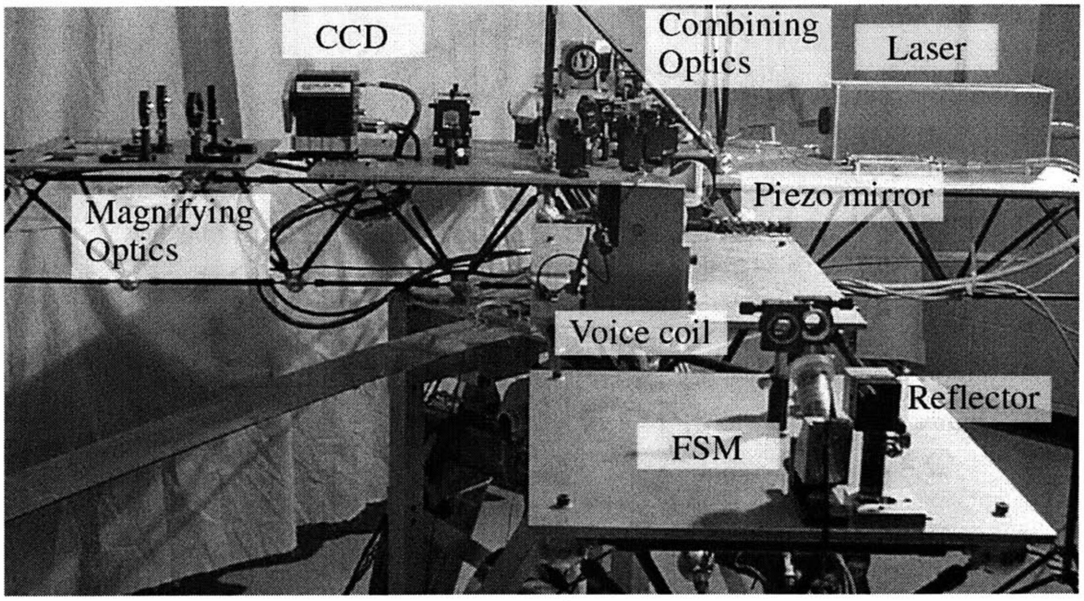

Figure 6.4 Origins Testbed: optical system block diagram

Figure 6.6. The delay line includes a mirror mounted on a voice coil for large-stroke coarse control and a mirror mounted on a piezo stack for fine control.

The fine-pointing optics are split off the external DPL_e path as seen in Figure 6.5. Beam splitters extract light from the external path, pass it through a focusing lens, and reflect it from a convex mirror onto a CCD camera. Both optical arms generate a dot on the CCD camera. The convex mirror acts as an optical amplifier to increase the system's sensitivity to jitter. A PC, fitted with a framegrabber, processes the images with a centroiding algorithm and passes the (x, y) position corresponding to each dot to the real-time control computer. Before reaching the CCD camera, some light from each channel is redirected with a beamsplitter onto a pair of quad-cell photodiodes. The quad cells provide a second measure of fine pointing. The CCD has a low bandwidth and high resolution while the quad cell photodiodes have a high bandwidth and low resolution. Details on the fine-pointing system, the centroiding algorithm, and an automated optical alignment algorithm are found in [Mallory et al., 2000]. A small mirror mounted on a tip/tilt piezo stack acts as a fine steering mirror (FSM) actuator for the pointing channels.

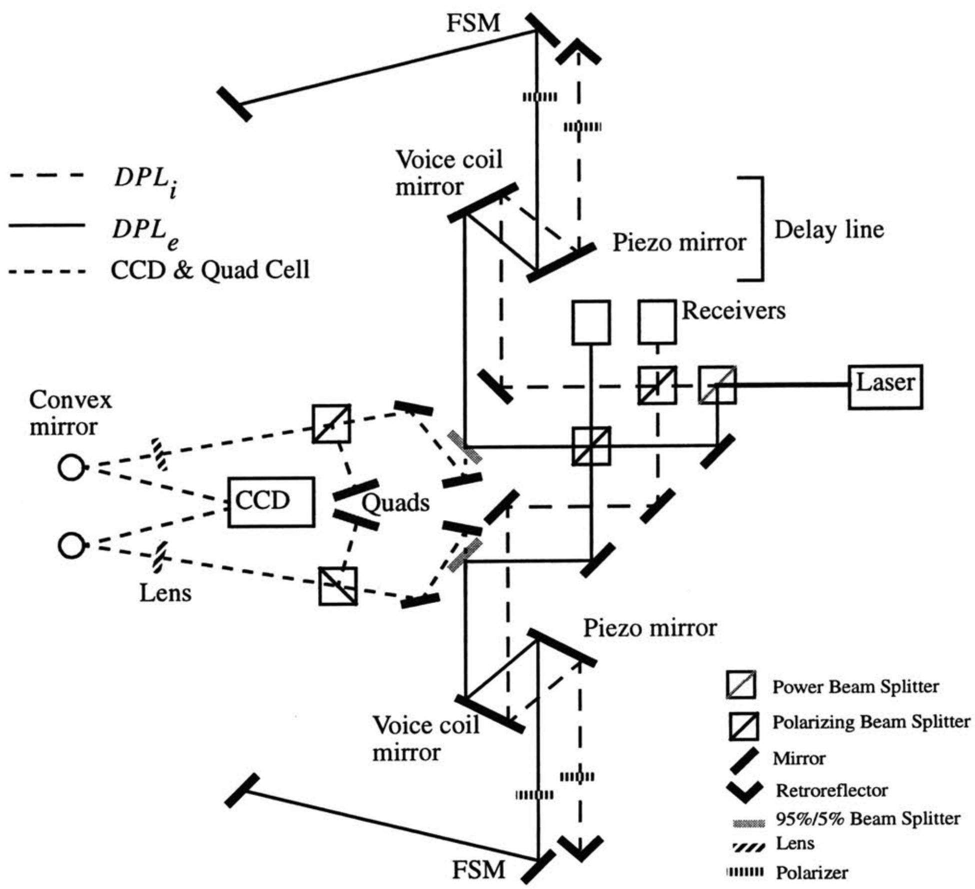

Figure 6.5 Origins Testbed: optical system block diagram

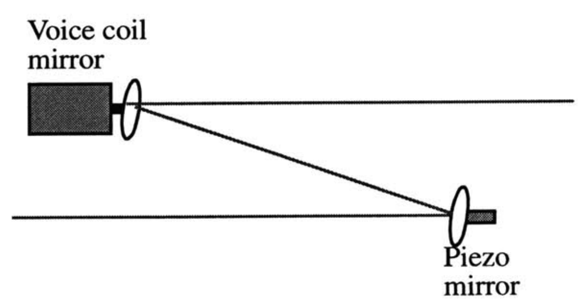

Figure 6.6 Optical delay line implementation

6.3 Testbed Identification and Sensor/Actuator Assessment

To assess the suitability of the Origins Testbed's sensor/actuator sets for control, the analysis techniques developed in Chapter 3, will be applied. The resulting sensor/actuator indexing matrix, S_t, shows which sets of sensors and actuators are most effective for control, and will be later exploited to determine which channels of the baseline controllers will benefit most from controller tuning. The sensor/actuator indexing algorithm requires a state-space model. This section will present the identification of a state-space measurement model of the OT, and analyze the application of the OT's sensor/actuator suite for control.

6.3.1 Control Problem Specification

Section 6.1 details three modes of operation for telescope control. In the thesis we will design controllers for the *observation* mode of operation. An attitude (*slew*) control is required to coarsely point the telescope during the observation. *Optical capture* for the Origins Testbed is introduced in [Mallory et al., 2000]

A subset of the actuators and sensors of Table 6.2 and Table 6.3 respectively, are selected for the observation control examples. We specify the four-block telescope observation control problem in Table 6.4.

Observation control for the Origins Testbed is a MIMO control problem with four actuators and four sensors. The observation control problem is a regulator problem with the goal of minimizing the transmission of the reaction wheel imbalance disturbance f_d to the optical performance metrics, z_{DPL}, and z_{QC}.

6.3.2 Open Loop Dynamics and System Identification

The open loop dynamics of the OT can be determined. A rudimentary finite element model is discussed in [Mallory et al., 1998] but not adopted in this thesis. Control tuning will be performed directly on measured data, without a model. This section discusses the measurement of the OT dynamics, and develops a technique for identifying a state-space measurement model when disturbance transfer matrices cannot be directly measured.

TABLE 6.4 Signal definitions for the four-block control problem for the Origins Testbed observation control. Resolutions are included for the sensors and actuators, intensities for the disturbances and requirements for the performances.

Signal Type	Abbreviation	Description	Resolution[a]
Disturbance[b] w	RWAd	Reaction wheel imbalance disturbance	1 V
Actuators u	RWAu	Inertial reaction wheel	10.0 mV
	VC	Mirror on voice coil, relative force	4.9 mV
	PZT	Mirror on piezo stack, relative force	4.9 mV
	FSM	Single axis of a fast steering mirror	4.9 mV
Performance z	DPL	Internal laser interferometer	250 nm
	QC	Single axis of quad cell pointing sensor	5 arcsec
Sensors y	ENC	Star tracker analogue	4 arcsec
	RGA	Rate gyroscope assembly	0.01 deg/s
	DPL	Laser interferometer	50 nm
	QC	Laser interferometer	1.2 arcsec

a. The term 'resolution' applies for the actuators and the sensors. For the disturbance, 'intensity' is more appropriate and for the performance, 'requirement' is more appropriate.

b. Additional disturbances include an actuator noise for each actuator, sensor noise for each sensor, and room noise from building disturbances. The reaction wheel imbalance strongly dominates the other disturbance sources.

Measuring Testbed Dynamics

Transfer function identification is typically performed using a signal analyzer. White noise is applied to each actuator, one-at-a-time, and the corresponding sensor output is transformed to a transfer function measure. Averaging improves the transfer function signal-to-noise. These techniques can be applied to measure the transfer matrices from the actuators to the sensors, $G_{yu}(\omega_k)$ and from the actuators to the performance variables, $G_{zu}(\omega_k)$, where $\{\omega_k, k = 1, \ldots, n_\omega\}$ is the set of measured frequency points. The magnitudes of the $G_{yu}(\omega_k)$ transfer matrix are plotted in Figure 6.7.

Note that the input units of each actuator are given in terms of actuation Volts applied to the amplifier. We verify the presence of the rigid body mode in the RWA to ENC transfer

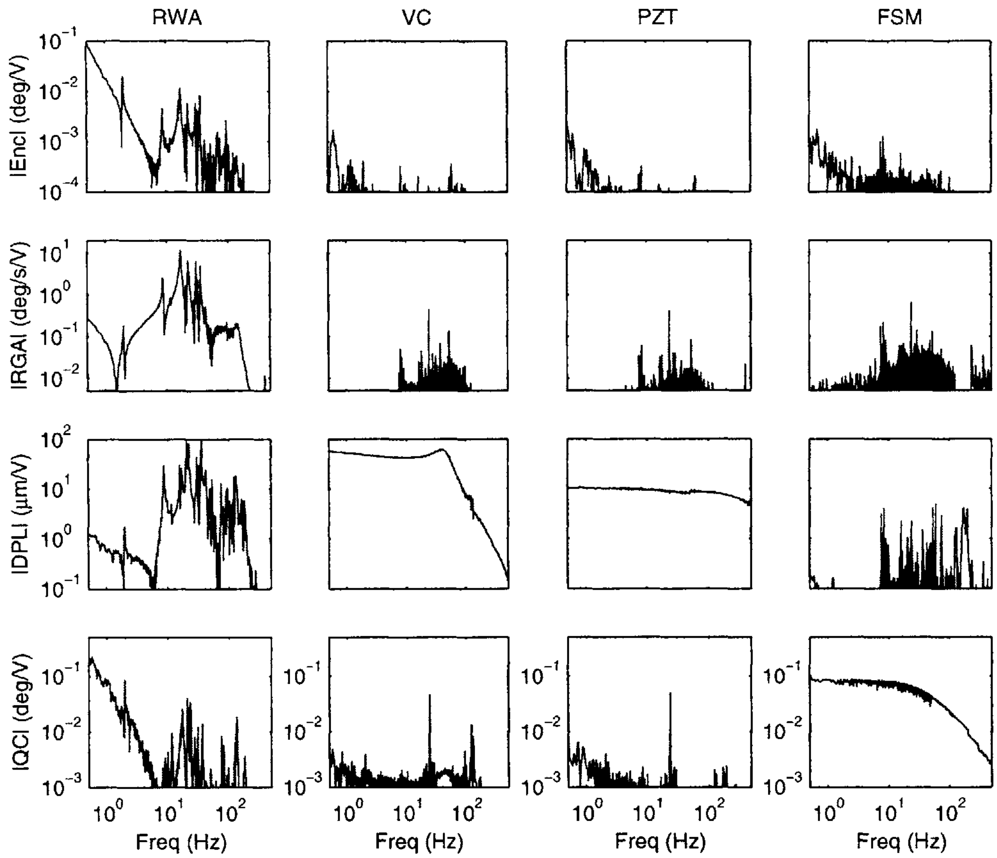

Figure 6.7 Measured $G_{yu}(\omega_k)$ magnitudes for the Origins Testbed. A low frequency loop (bandwidth ~ 0.1 Hz) is closed from the encoder to gimbal to remove rigid-body drift during system identification.

function with a –40 dB/decade slope at low frequency. Similarly the RWA-to-RGA function has a –20 dB/decade slope (angular velocity), and the RWA-to-QC function has a –40 dB/decade slope. The optical actuators, VC, PZT and FSM are decoupled from the ENC and RGA measure, due to their small actuated mass. The phasing actuators, VC and PZT, are strongly coupled to the DPL sensor, while the fine pointing actuator, FSM is only lightly coupled to DPL. Likewise for the fine pointing sensors, the FSM is strongly coupled to QC, while the VC and PZT are weakly coupled. The natural sensor/actuator decoupling is a desired feature of a telescope system since it simplifies control design. The reaction wheel couples strongly to all sensors indicating a strong disturbance in the performance measures.

The optics actuators, VC, PZT and FSM do not couple strongly with the dynamics of the structure as seen by their simple G_{yu} transfer matrix. These actuators are effective for active output isolation though. Further, the simple G_{yu} transfer matrix indicates that the active optics are unlikely to destabilize the structural modes despite the possibility of modal (parametric) uncertainty. For these active optics channels our developed metrics of stability robustness, S_S and S_{cr} are adequate.

As mentioned in Section 4.1.2, in most physical systems the disturbance node is not exposed and we cannot apply white noise to an actuator to directly measure the $G_{yw}(\omega)$ and $G_{zw}(\omega)$ transfer matrices. *Input analogous* systems are an exception (where the control actuators double as the disturbance source). The OT reaction wheels act as both control actuator and the primary disturbance source, but are not input analogous. The physical mechanism that actuates and disturbs the system are not the same. The actuation is achieved through a single torque axis, and is a torque proportional to the acceleration of the wheel, whereas the disturbance enters the system through the two remaining torque axes and three relative force axes, and are engendered by wheel imbalances and bearing noise. Without a physical model of the OT, the disturbance inputs are not accessible for system identification.

By measuring data as the wheels wind-up through a simulated observation, the power spectral density of each sensor can be measured and is plotted in Figure 6.8.

The auto-spectra are the product of the transfer-matrices under the assumption of a pre-whitening filter. Thus, for the i-th sensor and the j-th disturbance

$$A_{y_i w_j}(\omega_k) = G_{y_i w_j}(\omega) G_{y_i w_j}(\omega)^* = \left|G_{y_i w_j}(\omega)\right|^2. \tag{6.1}$$

Similar relations hold for the elements of $G_{z\omega}(\omega)$. The magnitudes of the transfer functions are measured, but phase information is lost. We will use the transfer function magnitudes for measured-data control design.

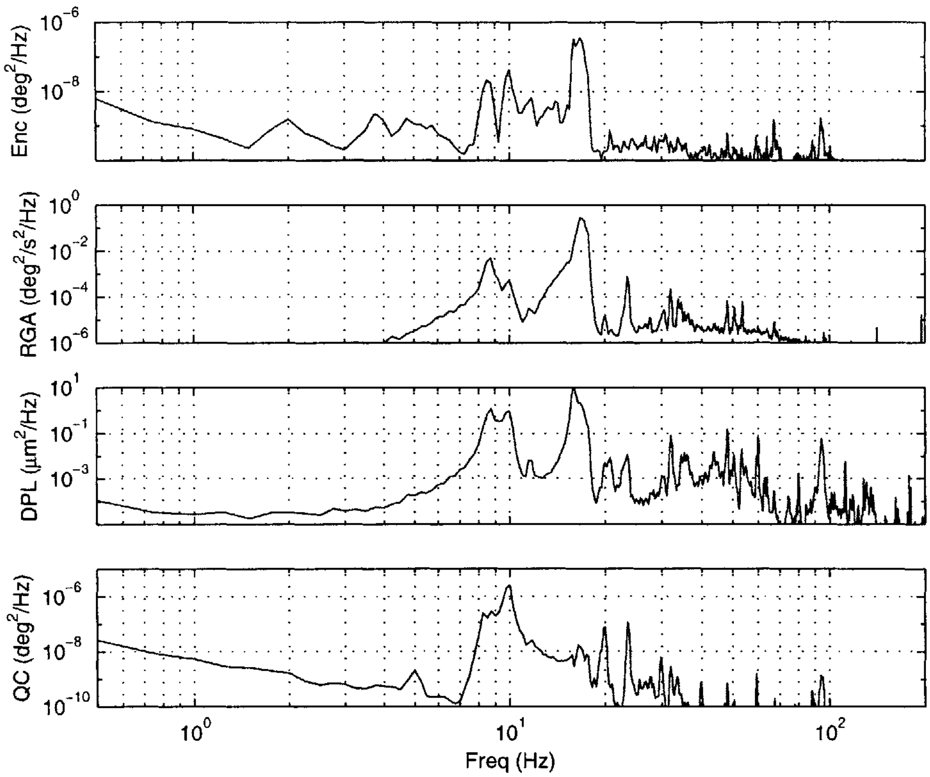

Figure 6.8 Autospectra of output measures during an observation. The disturbance is the average effect of the wheel imbalance as the wheel winds up to maintain accurate pointing.

Determining a State-Space Model

In the case where a state-space model is required we now develop a technique for fitting a model to the measured auto-spectra data. Though control design and tuning will be performed without a model, the sensor/actuator selection algorithm requires a state-space model.

In our case the complex transfer function data can be directly measured for the actuator-to-sensor channels, but not for the disturbance-to-sensor channels. [Jacques, 1995] presents a brief discussion on the identification of G_{yw} which is expanded here. By taking the square root of the disturbance-to-performance autospectra however, the magnitude of G_{yw} can be determined. By concatenating the measured $|G_{yw}|$ real data with the measured G_{yu} complex data a measured-data matrix is formed. The state-space measurement model can be computed by fitting frequency response data using the Frequency Domain Observability Range Space Extraction (FORSE) algorithm coupled with logarithmic least squares tuning as detailed in [Jacques, 1995]. We must be careful to ensure that the missing phase information corresponding to the $|G_{yw}|$ does not corrupt the fit. Careful iteration accomplishes this. Further, numerous non-structural states, corresponding to the disturbance model states, must be added to our fit.

Our state-space model fits the measured data reasonably well, but is empirical and not physics-based. An example of the fit is seen in Figure 6.9 which overlays the measured autospectra to the identified state-space autospectra. Actuator to sensor channels are also well fit with additional emphasis place on fitting the phase.

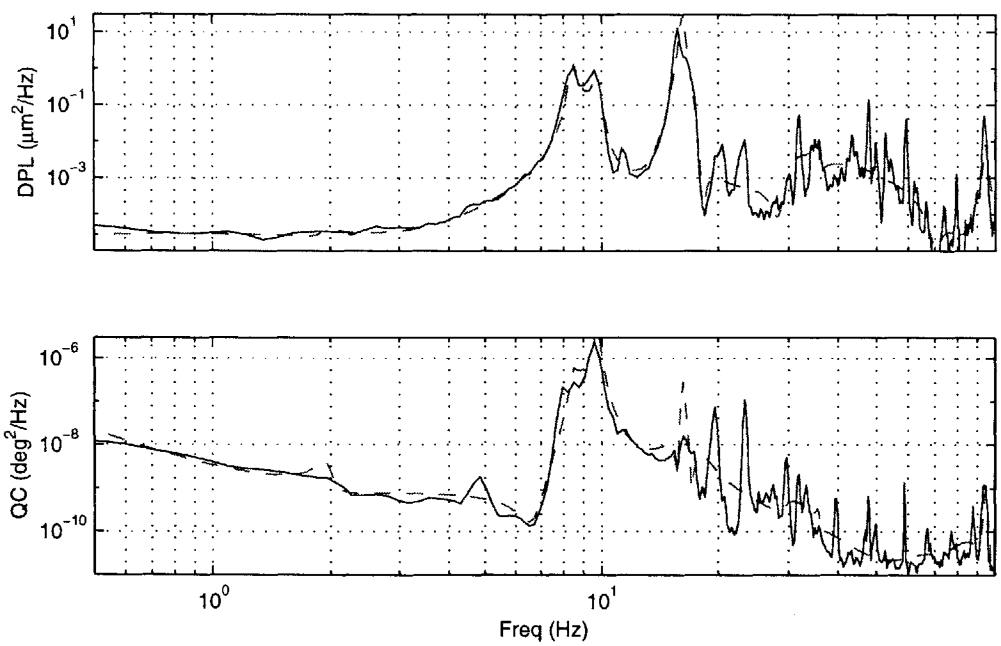

Figure 6.9 Measured (solid) and identified (dashed) disturbance to performance autospectra

An alternate technique which relies on a physical model of the reaction wheel disturbance to identify a state-space model to the measured data is developed in Appendix D. The physics-based technique relies on a state-space approximation to the anticipated wheel spectrum which does not allow an adequate high-frequency roll-off and does not prove to be as accurate as the direct identification presented in this section. The identified model will now be used with the sensor/actuator algorithm of Chapter 3 to identify sets of sensors and actuators that are effective for control.

6.3.3 Origins Testbed Sensor/Actuator Index

The sensor/actuator algorithm of Chapter 3 is applied to the OT. The resulting sensor/actuator indexing matrix, S_t, shows which sets of sensors and actuators are most effective for control, and will be later exploited to determine which channels of the baseline controllers will benefit most from controller tuning.

The OT is cast into the four-block control problem with the disturbance, actuator, performance and sensor variables outlined in Table 6.4. The model identified with the technique developed in Section 6.3.2 is used. The algorithm of Chapter 3 can now be applied. The user must supply four sets of information as shown in Table 3.1. For the OT example:

1. The plant model is delivered in a four-block state-space form, (A, B_w, B_u, C_z, C_y) (Section 6.3.2).
2. The scaling gains, R_u, R_y, R_w, R_z are set using the resolutions (for u and y variables), intensities (for w variables), and performance requirements (for z variables) which are listed in Table 6.4. These scaling factors to weight the relative importance of the sensors and actuators by capturing the anticipated signal-to-noise. The resulting sensor/actuator indices depend on the square of the scaling factors.
3. The standard value of $\gamma = 1$ is used for the output isolation mixing parameter (Equation 3.114).
4. The relative importance of the rigid body modes must be assigned by setting the ω_{RM} parameter (Section 3.2.3). In the OT control example, ω_{RM} is set to $0.1/2\pi$ rad/sec corresponding to the anticipated 0.1 Hz bandwidth of the attitude control loop. The disturbance-to-performance spectra (the DPL and QC plots of Figure 6.8) do not exhibit a strong dependence on the OT rigid body since the wheel disturbance has greatest energy at higher wheel speeds. For this reason, the S_t matrix for the OT is not very sensitive to the ω_{RM} parameter.

To determine the suitability of particular sensor/actuator combinations for control the S_t index is used. Table 6.5 displays the sensor/actuator effectiveness matrix ($\log_{10}(S_t)$) for the OT.

TABLE 6.5 Sensor and Actuator indexing matrix for OT Model.

	ENC	RGA	DPL	QC
RWA	20.3[a]	19.1[a]	12.2	17.4[b]
VC	5.0	8.8	22.8[c]	8.9
PZT	10.2	12.7	26.3[c]	13.7
FSM	6.3	11.4	14.5	20.6[d]

a. Attitude control sensor and actuator. The low relative magnitude corresponds to the unimportance of the rigid body mode in this particular OT control problem.

b. Use QC with RWA for active disturbance isolation

c. Phasing control sensor and actuators.

d. Fine pointing control sensor and actuator

The largest index entries are indicated with superscripts, suggesting a controller topology. When interpretating the S_t matrix we must recall the defined performance variables: a combination of the modeled wheel disturbance to DPL and of the wheel disturbance to QC. Attitude control is not included in the performance. The intuitive decoupling of phasing control (DPL to VC and DPL to PZT) and fine-pointing control (QC to FSM) is apparent. The highest value in the matrix corresponds to the use of the high-bandwidth PZT with the low-noise DPL. The ENC and RGA couple strongly with the RWA for control of the rigid body and 2 Hz solar panel mode that are strongly observable in the QC. The table indicates the QC could also be used with the RWA for a strategy whereby the wheel is used with the RGA to cancel disturbance at the source (the wheel). This strategy is not adopted due to interference with the attitude control loop

6.4 Baseline Testbed Controller

Using classical control techniques, a fully decoupled, baseline controller (BC) for the observation operational mode has been designed and implemented on the OT. The BC has been broken up into attitude control and optical control. Optical control is further broken up into phasing control and fine-pointing control. The sensors/actuators for the three stages of observation control for the testbed: (1) attitude control, (2) phasing control, and (3) fine pointing control, are summarized, with abbreviations, in Table 6.6:

TABLE 6.6 Actuators and sensors for the Origins Testbed control examples

Control Stage	Actuators	Sensors
Attitude[a]	Reaction wheel (RWA)	Encoder (ENC) Rate Gyro (RGA)[b]
Phasing	Mirror on voice coil (VC) Mirror on piezo stack (PZT)	Internal laser interferometer (DPL)
Fine pointing	One fast-steering mirror axis (FSM)	One quad-cell fine-pointing axis (QC)

a. Not included in the table are the gimbal motor actuator and the RWA tachometer sensor. These are used together for momentum dumping the RWA and are treated as an external disturbance to the attitude control loop.

b. The rate gyro sensor is traditionally used with attitude control. Its utility for phasing and fine-pointing control will be investigated in the sequel.

The closed-loop performance of the four-block control problem is given by Equation 2.6. In the special case where the performance variables are a linear combination of the sensor variables, $z = Ny$ (*output analogous*), we have,

$$y = G_{yw}w + G_{yu}u \Rightarrow z = Ny = NG_{yw}w + NG_{yu}u \tag{6.2}$$

which implies $G_{zw} = NG_{yw}$ and $G_{zu} = NG_{zw}$. Substituting into Equation 2.6 results in

$$\begin{aligned} z &= [G_{zw}(s) + G_{zu}(s)K(s)(I - G_{yu}(s)K(s))^{-1}G_{yw}(s)]w \\ &= [NG_{yw}(s) + NG_{yu}(s)K(s)(I - G_{yu}(s)K(s))^{-1}G_{yw}(s)]w \\ &= N[I + G_{yu}(s)K(s)(I - G_{yu}(s)K(s))^{-1}]G_{yw}(s)w \end{aligned} \tag{6.3}$$

which, by the application of the Matrix Inversion Lemma, results in

$$z = N[I - G_{yu}(s)K(s)]^{-1}G_{yw}(s)w. \tag{6.4}$$

Figure 6.10 is a block diagram representation of Equation 6.4.

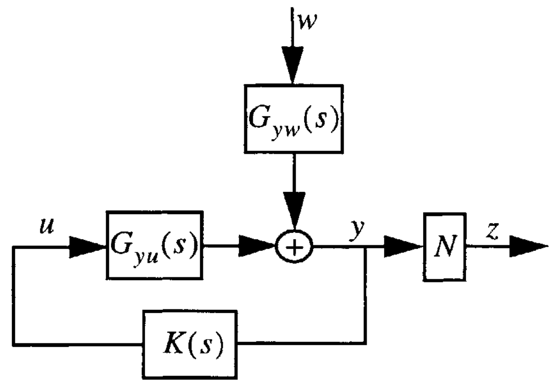

Figure 6.10 Block diagram of output analogous control

In this case the control objective (minimize the effect of w on z) can be achieved by having a high controller gain over the bandwidth of interest. Effectively we minimize the $[I - G_{yu}(s)K(s)]^{-1}$ factor to actively decouple w from z. This active output isolation is achieved regardless of the spectral shape G_{yw}. If $|G_{yw}|$ is known then performance can be enhanced by choosing $K(s)$ to ensure that $[I - G_{yu}(s)K(s)]^{-1}$ is minimized in the bandwidth where the magnitude of G_{yw} is large. Active output isolation is independent of the phase of G_{yw}. If the phase of G_{yw} is known then the controller can approach a pole/zero cancellation strategy to achieve performance with less control authority. The baseline controller employs an output isolation control strategy.

The BC structure is given by,

$$\begin{bmatrix} u_{sc} \\ u_{ph} \\ u_{pn} \end{bmatrix} = \begin{bmatrix} K_{sc} & 0 & 0 \\ 0 & K_{ph} & 0 \\ 0 & 0 & K_{pn} \end{bmatrix} \begin{bmatrix} y_{sc} \\ y_{ph} \\ y_{pn} \end{bmatrix}, \tag{6.5}$$

where u corresponds to actuator inputs, y to sensor outputs, and K to controller transfer matrices. The subscript sc corresponds to slew control, ph to phasing control, and pn to fine-pointing control such that u_{sc} is the command to the RWA, u_{ph} are the commands to the VC and PZT, u_{pn} is the command to the FSM, y_{sc} is the measured ENC signal, y_{ph} is the measured DPL signal and y_{pn} is the measured fine-pointing signal. The RG is not used by the BC. We note the presence of the zeros, enforcing the decoupled nature of the BC.

Implementation Consideration

Section 2.2.7 highlights implementation considerations for running a controller on a digital control system, including the Origins Testbed.

The controller is converted from the continuous design to a discrete design by employing the nonlinear weighted least-squares identification software designed for [Jacques, 1995]. A frequency response of the continuous controller is generated and fit with a discrete model. A logarithmic cost function is used to fit zeros well. In practice, system-ID based continuous-to-discrete conversion performs better than standard (ZOH, Tustin, *etc.*) methods with the additional computational cost of the nonlinear optimization.

6.4.1 Slew Control

To design a slew controller for the OT, (K_{sc} from Equation 6.5) we begin by measuring the slew dynamics of the OT and fitting them with a low-order measurement model. Classical control synthesis is used to design the controller, which is then tested on the OT. The design of the baseline slew controller is completely decoupled from the phasing and fine-pointing controllers. We further break up the slew controller into a component with the RWA as an actuator, $K_{sc,\,w}$, and a component with the gimbal motor as an actuator, $K_{sc,\,g}$, A block diagram of the slew control structure is found in Figure 6.11.

$K_{sc,\,w}$ generates a torque for the RWA, τ_w, based on an error, $e = \theta_r - \theta_{sc}$, between a reference command, θ_r, and the OT encoder angle, θ_{sc}. Through the inertia of the wheels, I_w, τ_w causes the RWA to rotate at an angular velocity of $\dot{\theta}_w$. $K_{sc,\,g}$ generates a

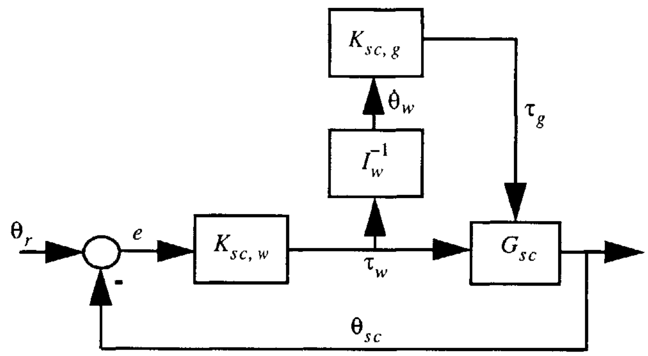

Figure 6.11 Baseline slew controller structure

torque for the gimbal actuator, τ_g, based on $\dot{\theta}_w$. In the figure, G_{sc} are the OT slew dynamics.

Origins Testbed Slew Dynamics

The slew dynamics of the OT are identified by applying white noise to the RWA and recording the encoder angle and rate gyro angular velocity. A spectrum analyzer is used to record the transfer functions from the RWA to encoder and RWA to rate gyro. The resulting transfer functions are plotted in Figure 6.12

The RWA-to-ENC transfer function displays a -40 dB/decade rolloff at low frequency, characteristic of the angular position measure of a rigid body, given a torque input. At 2 Hz we see the first resonance of the OT's solar panels (brass beams) which couple in to the pointing transfer function. At 10 Hz, we see an increase in modal density. The encoder data becomes noisy at higher frequency. The RAW-to-RG transfer function displays a -20 dB/decade rolloff at low frequency, characteristic of the angular rate measure of a rigid body, given a torque input. Again we see the solar panel 2 Hz mode. At frequencies above 10 Hz we have an increase in modal density corresponding to the flexible modes of the reaction wheel assembly.

A 22 state high-order model fits the transfer functions of Figure 6.12 almost exactly. For the slew controller, when we use the encoder as the primary feedback sensor, a much lower order model can be used for controller design. A fourth order model is selected,

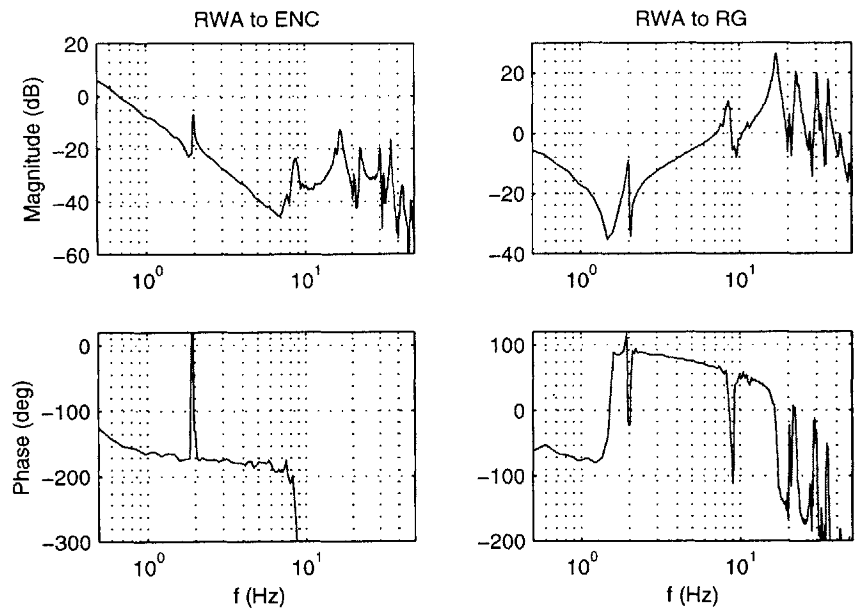

Figure 6.12 Origins Testbed slew dynamics

with 2 states corresponding to the OT rigid body mode and 2 states assigned to the observable brass beam resonance mode. We determine a model of the form,

$$G_{sc,w}(s) = \frac{K(s^2 + 2\zeta_{nm}\omega_{nm}s + \omega_{nm}^2)}{(s^2 + 2\zeta_{rb}\omega_{rb}s + \omega_{rb}^2)(s^2 + 2\zeta_{bb}\omega_{bb}s + \omega_{bb}^2)} + d_m \tag{6.6}$$

where s is the Laplace Transform variable. We fit the model to the transfer function and find $K = 2.5$. A zero in the system response is governed by: $\zeta_{nm} = 0.47\,\%$, $\omega_{nm} = 2\pi \cdot 1.90$. Due to friction, the OT slewing rigid body is modeled with a low-frequency, heavily damped pole with $\zeta_{rb} = 70\,\%$, $\omega_{rb} = 2\pi \cdot 0.1$. The brass beam flexibility is modeled with a lightly-damped pole with $\zeta_{rb} = 1\,\%$, $\omega_{rb} = 2\pi \cdot 2$. A static correction $d_m = -1.25\times10^{-3}$ is added to account for the low frequency effect of the neglected higher-order dynamics.

RWA Slew Controller

To design the RWA slew controller, $K_{sc,w}$, we formulate the design requirement as: track targets with zero steady-state error to a step while maintaining good stability margins. For a sensor we select the angular encoder (4 arcsecond resolution) and for the actuator the reaction wheels.

The SISO control design consists of:

- a pure integrator which eliminates steady-state tracking error to a step at the expense of stability margin,
- a 2nd order lead filter provides phase at cross-over, negating the phase loss from the integrator, and providing good stability margins, and
- a 2nd order lag filter at high frequency to avoid exciting neglected high-frequency dynamics.

The controller is thus in the form,

$$K_{sc,\,w}(s) = \frac{K_k(s^2 + 2\zeta_{kn}\omega_{kn}s + \omega_{kn}^2)}{s(s^2 + 2\zeta_{kd}\omega_{kd}s + \omega_{kd}^2)} \tag{6.7}$$

with $K_k = 170$, $\zeta_{kn} = 70.7\,\%$, $\omega_{kn} = 2\pi \cdot 0.1$, $\zeta_{kn} = 70.7\,\%$, and $\omega_{kn} = 2\pi \cdot 4$. contains the controller transfer function.

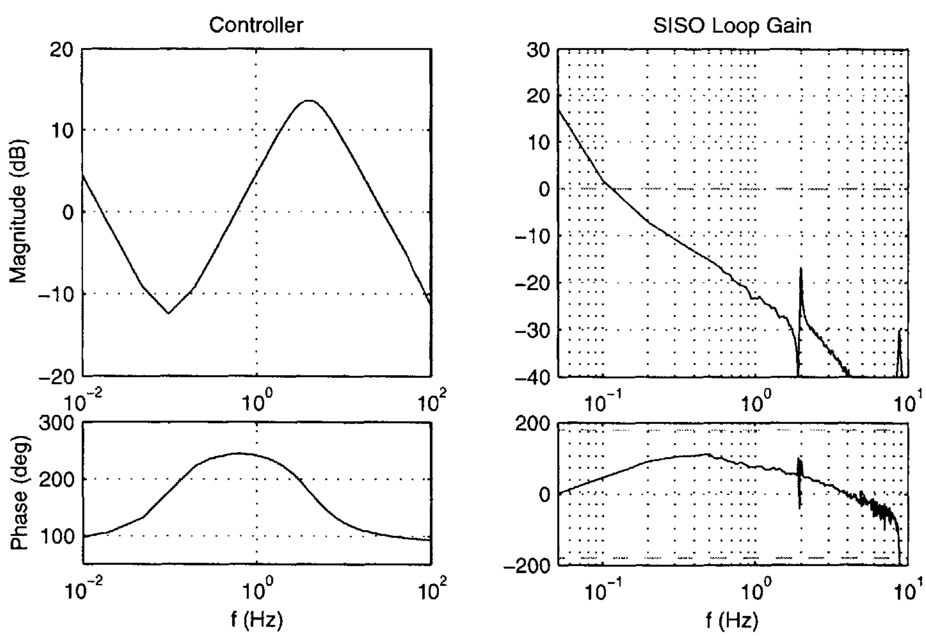

Figure 6.13 Baseline RWA slew controller, $K_{sc,w}$ and encoder to RWA control loop gain, calculated with measured data.

Momentum Dumping

To hold the OT in position while countering residual gravity and friction torques, the reaction wheel speed to wind up. The gimbal actuator is controlled to desaturate the RWA through $K_{sc,\,g}$. The OT wheel desaturation is analogous to the spacecraft case where thrusters are fired to desaturate the wheels. We select the reaction wheel tachometer as the sensor and the gimbal torque motor as the actuator.

Nonlinear switching logic controls the gimbal actuation with the rules,

- If $\dot{\theta}_w > \bar{\omega}$ then apply a step to the gimbal and hold until $\dot{\theta}_w < \underline{\omega}$.
- If $\dot{\theta}_w < -\bar{\omega}$ then apply a negative step to the gimbal and hold until $\dot{\theta}_w > -\underline{\omega}$

where $\bar{\omega}$ is an upper wheel speed threshold, and $\underline{\omega}$ is a lower speed threshold.

The gimbal step is prefiltered with a fourth order filter which is shaped to minimize interaction with the RWA/encoder loop. The SISO prefilter design consists of:

- a 2$^{\text{nd}}$ order notch at the frequency where the RWA-to-ENC pointing is most sensitive to the gimbal torque, τ_g, and
- a 2$^{\text{nd}}$ order lag at high frequency to eliminate high frequency torque spikes.

The pre-filter dynamics and the τ_g to RWA-to-ENC pointing loop dynamics, with the ENC-to-RWA loop closed, are seen in Figure 6.14. To the RWA-to-ENC loop, the gimbal torque appears as a disturbance. The presence of the integrator eliminates low-frequency coupling from τ_g to θ_{sc}.

The pre-filter is in the form,

$$K_{sc,\,w}(s) = \frac{K_w(s^2 + 2\zeta_{gn}\omega_{gn} + \omega_{gn}^2)}{(s^2 + 2\zeta_{g1}\omega_{g1} + \omega_{g1}^2)(s^2 + 2\zeta_{g2}\omega_{g2} + \omega_{g2}^2)} \tag{6.8}$$

with $K_w = 0.032$, $\zeta_{g1} = 0.7$, $\omega_{g1} = 2\pi \cdot 0.07$, $\zeta_{g2} = 0.7$, $\omega_{g2} = 2\pi \cdot 0.04$, $\zeta_{gn} = 0.1$, and $\omega_{gn} = 2\pi \cdot 0.05$.

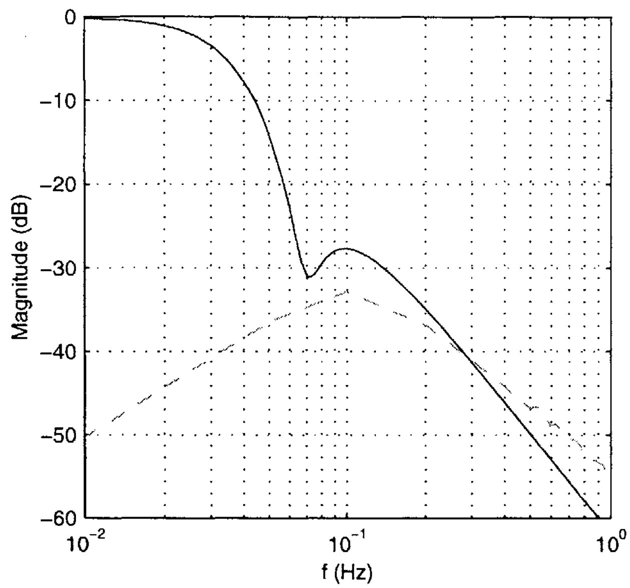

Figure 6.14 Gimbal momentum dump prefilter. Dashed: gimbal torque to RWA-to-ENC pointing with ENC-to-RWA loop closed, and solid: gimbal pre-filter magnitude dynamics

Performance and Stability

Figure 6.15 is a plot of the time-domain data for representative actions of the slew controller. The testbed slews to a 30° position, holds 130 seconds, returns to its initial position and holds for 100 seconds. At 60 seconds the wheel pass the speed threshold and the gimbal turns on. The wheel speed shows reaction to rotation of the testbed, holding torques, and gimbal torques.

The stability of the τ_g to θ_{sc} loop can be determined from a SISO attitude control gain/phase plot with a realistic assumption that the phasing and fine pointing actuators do not have couple enough with the structure at low frequency to destabilize the attitude loop. Further, we assume that the gimbal momentum dump appears as an external disturbance (despite the presence of the wheel speed driven nonlinear feedback logic). The 2 Hz mode of the brass beams is gain stabilized above the bandwidth of the control loop. Since this is a SISO loop, we determine stability margins of 40 dB gain margin and 40° phase margin directly from the plot.

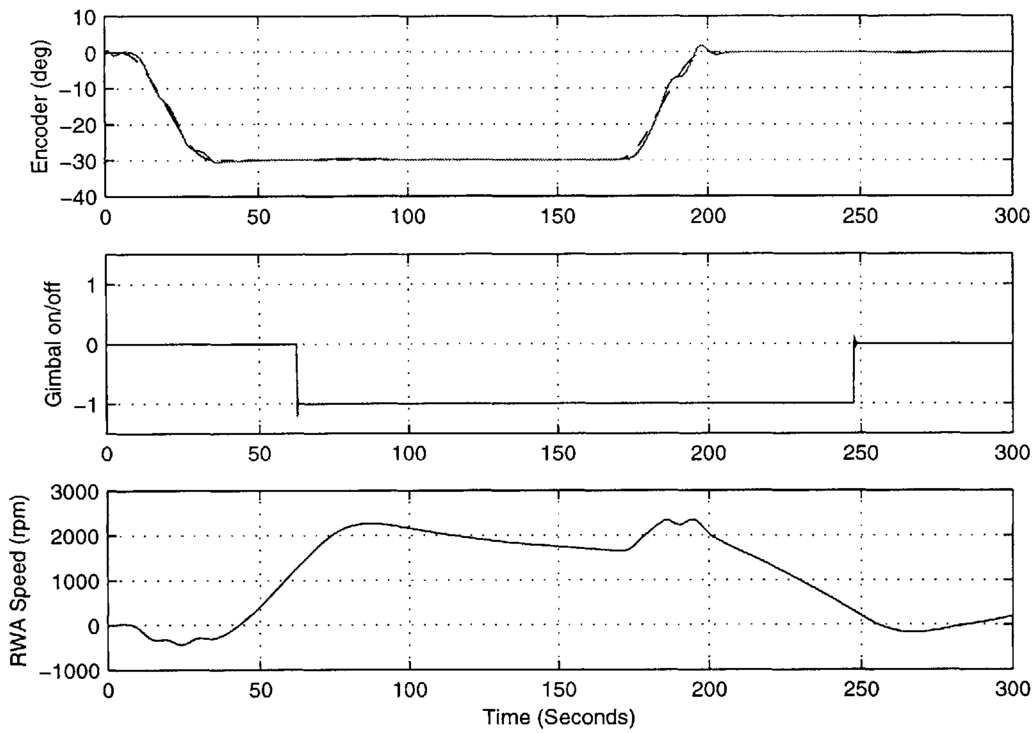

Figure 6.15 Measured slew control performance. Top: testbed pointing angle with reference (dashed), Middle: gimbal action, Bottom: reaction wheel speed

6.4.2 Phasing Control

To design the phasing control, K_{ph}, we choose a structure from the literature with heritage on several interferometry testbeds [Melody and Neat, 1999, Masters, 1997, and O'Neal and Spanos, 1991]. This control structure is also used for the baseline SIM phasing controller in Chapter 7. The phasing control structure is seen in Figure 6.16.

Phasing control is achieved through the delay line. We divide the phasing control amongst two actuators, a mirror mounted on a voice coil (denoted with a subscript v), and a mirror mounted on a piezo stack (denoted with a subscript p). An internal loop is formed by feeding back the internal metrology interferometer measure, $\mathrm{DPL_i}$ to a voice coil filter, $K_{ph,\,v}$, and a piezo filter $K_{ph,\,p}$ connected in parallel. The respective plant dynamics are

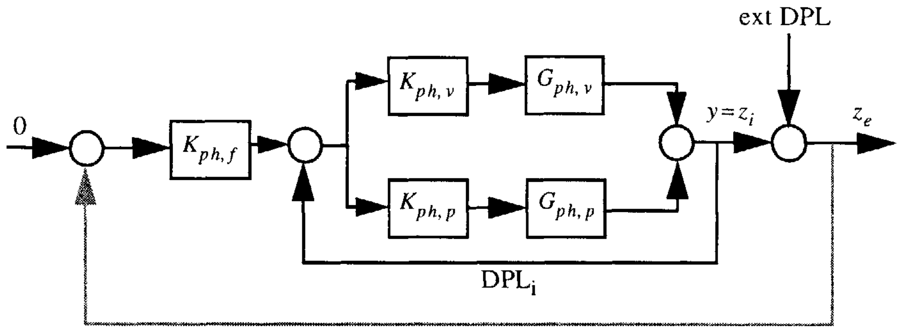

Figure 6.16 Baseline phasing controller structure. The loop indicated with the light line is closed in the SIM control strategy, but will not be closed in the simplified OT demonstration experiments.

denoted by $G_{ph,v}$ and $G_{ph,p}$ for the voice coil and the piezo mirror respectively. The internal loop is corrupted by the external contribution to differential pathlength, ext. DPL.

In the experiments that will be detailed in this chapter, the internal DPL is the differential pathlength performance metric, *i.e.* $z_{DPL} = z_i = \mathrm{DPL}_\mathrm{i}$. In the above figure, the baseline controller is formed by cutting the external z_e feedback, and for simplicity by setting $K_{ph,f} = 1$.

The higher bandwidth piezo controller is designed first with:

- a 1st order lead at $f = 0$ Hz to eliminate DC gain,
- a 1st order lag to flatten gain over region of desired authority,
- a 1st order lead to provide phase lead at crossover,
- a 1st order lag to roll-off after crossover, and
- a 2nd order lag for increased roll-off.

The resulting controller has the form,

$$K_{ph,p}(s) = \frac{K_{ph,p}s(s+\omega_{pz})}{(s+\omega_{p1})(s+\omega_{p2})(s^2+2\zeta_p\omega_{p3}+\omega_{p3}^2)} \tag{6.9}$$

with $K_{ph,p} = 1500$, $\omega_{p2} = 2\pi\cdot 20$, $\omega_{pz} = 2\pi\cdot 50$, $\omega_{p1} = 2\pi\cdot 60$, $\zeta_{gn} = 0.4$, and $\omega_{gn} = 2\pi\cdot 120$.

The piezo control loop achieves performance over the 15 to 40 Hz range while the voice coil is used over the 0 to 20 Hz range. The lower bandwidth voice coil loop is designed with:

- a low frequency 2nd order lag well below crossover,
- a 1st order lead to provide phase near crossover,
- a 2nd order lead to negate the phase lag of the 2nd order voice coil mass/ spring dynamics, and
- a 2nd order lag after crossover to provide adequate roll-off.

The resulting controller is in the form,

$$K_{ph,v}(s) = \frac{K_{ph,v}(s+\omega_{vz})(s^2+2\omega_{vn}+\omega_{vn}^2)}{(s^2+2\zeta_{v1}\omega_{v1}+\omega_{v1}^2)(s^2+2\zeta_{v2}\omega_{v2}+\omega_{v2}^2)} \tag{6.10}$$

with $K_{ph,v} = 1800$, $\zeta_{v1} = 0.9$, $\omega_{v1} = 2\pi \cdot 2$, $\omega_{vz} = 2\pi \cdot 23$, $\omega_{vn} = 2\pi \cdot 40$, $\zeta_{v2} = 0.7$, and $\omega_{v2} = 2\pi \cdot 320$.

The voice coil and piezo controller transfer functions are plotted in Figure 6.17 along with the loop gain cut at the sensor (single channel DPL),

The bandwidth of the phasing control loop can be measured to be ~45 Hz with a gain margin of 10 dB, and a phase margin of ~40 degrees. (Note that by measuring stability of the phasing loop we are implicitly neglecting interaction with the attitude and fine-pointing loops)

6.4.3 Fine-Pointing Control

The fine-pointing controller employs the structure of Figure 6.10. From Figure 6.8 we see that the G_{zw} for the fine-pointing loop is maximum over the 10 to 20 Hz band. The fine-pointing controller, $K_{fpn}(s)$, is designed to have gain over that frequency region.

The controller is designed with:

- a 1st order lead at $f = 0.1$ Hz to eliminate DC gain,

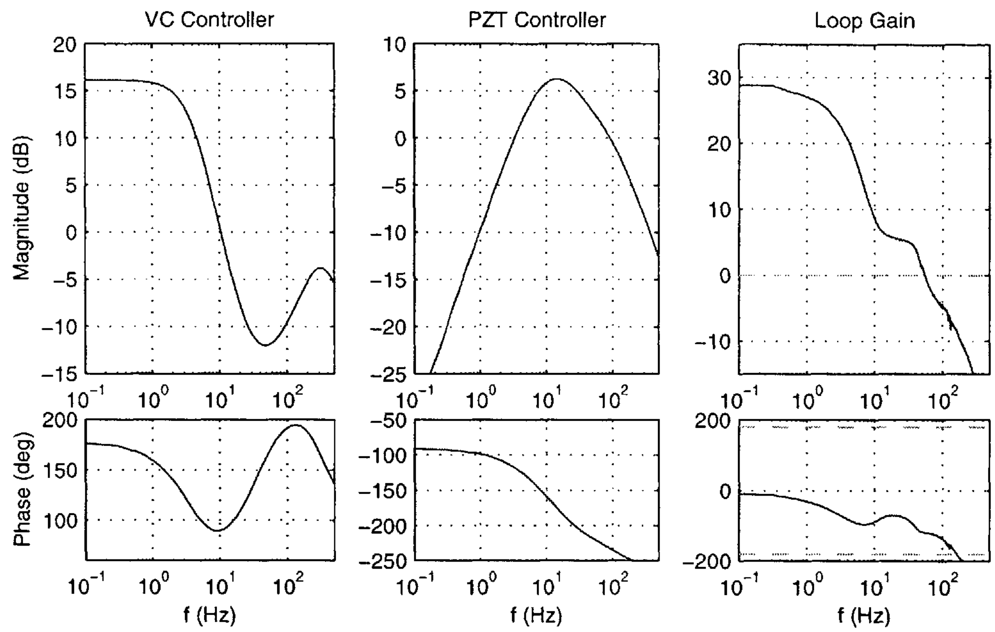

Figure 6.17 Baseline phasing controller for the voice coil actuator, $K_{ph,v}$, baseline controller for the piezo mirror actuator $K_{ph,p}$, and the phasing loop gain

- a 2^{st} order lag well below crossover,
- a 1^{st} order lead to provide phase lead near crossover, and
- a 2^{nd} order lag after crossover for adequate roll-off

The resulting controller is in the form,

$$K_{fpn}(s) = \frac{K_{fpn}(s+\omega_{fz})(s+\omega_{fn})}{(s^2+2\zeta_{f1}\omega_{f1}+\omega_{f1}^2)(s^2+2\zeta_{f2}\omega_{f2}+\omega_{f2}^2)} \tag{6.11}$$

with $K_{fpn} = 6\times10^5$, $\omega_{fz} = 2\pi\cdot0.1$, $\zeta_{f1} = 0.9$, $\omega_{f1} = 2\pi\cdot6$, $\omega_{fn} = 2\pi\cdot90$, $\zeta_{f2} = 0.9$, and $\omega_{f2} = 2\pi\cdot400$.

The fine-pointing controller transfer function and the associated loop gain transfer function is plotted in Figure 6.18.

The bandwidth of the fine-pointing control loop can be measured to be from 2 to 70 Hz with a gain margin of 9 dB, and a phase margin of ~40 degrees. (Note that by measuring

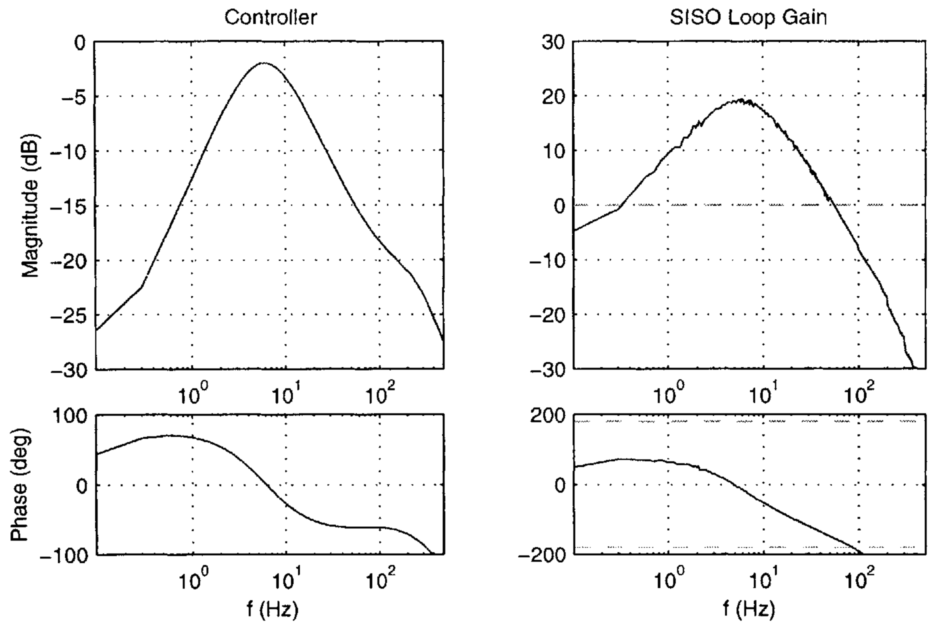

Figure 6.18 Baseline fine-pointing controller and fine-pointing loop gain

stability of the fine pointing loop we are implicitly neglecting interaction with the attitude and phasing loops)

6.4.4 Baseline Performance and Stability

In this section we present the optical performance and global stability robustness of the BC applied to the Origins Testbed.

Figure 6.19 is a plot of the autospectra of the DPL and the QC, and compares the open-loop (straight line) and the closed-loop (dashed line) performance. We see that the phasing and fine-pointing controllers achieve performance in the 10 to 20 Hz band where the disturbance is dominant. At high frequency, after controller roll-off there is no observed performance change.

The broadband performance of the baseline controller is summarized in Table 6.7.

From studying Figure 6.19 we see that most performance is obtained by decreasing the disturbance of moderately narrow spikes at 9 and 18 Hz. The baseline level of perfor-

TABLE 6.7 Measured and predicted performance of baseline controller

	OL RMS Performance		BC RMS Performance		
Perf Variable	**Predict**	**Meas**	**Predict**	**Meas**	**Meas. imp. over OL**
DPL	4.31 μm	4.77 μm	1.81 μm	1.62 μm	9.4 dB
QC	6.97[a] arcsec	7.05 arcsec	1.64 arcsec	1.81 arcsec	11.8 dB

a. The data is measured by averaging 40 spectra allowing the quad cell resolution to surpass the instantaneous resolution of 0.1 arcseconds (asec).

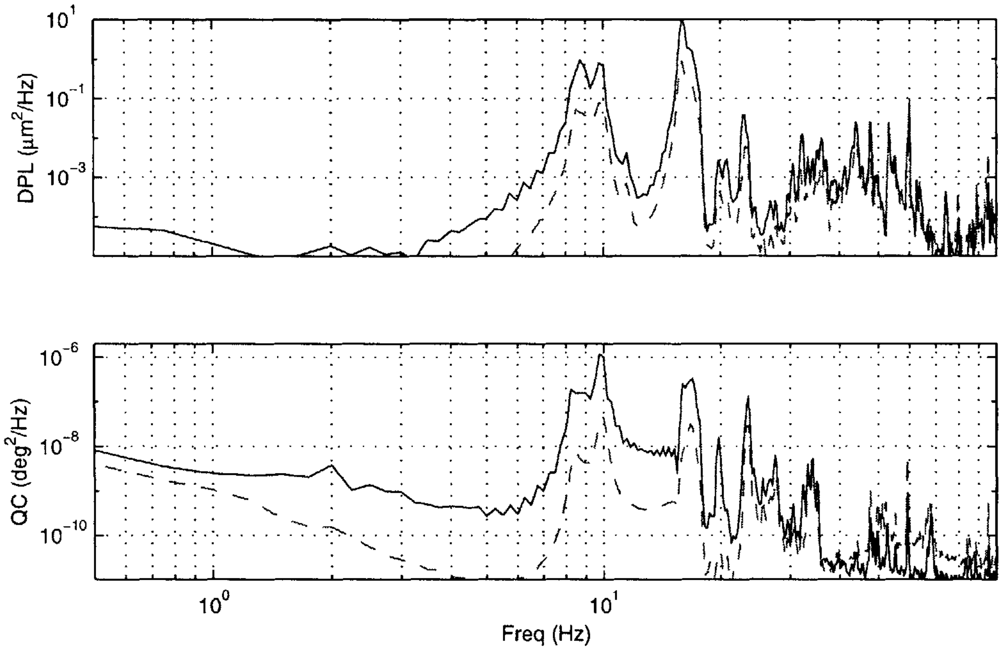

Figure 6.19 Open-loop (solid) and closed-loop (dashed) performance of the baseline controller for the differential pathlength and fine pointing metrics as measured by the laser interferometer (DPL) and the quad cell (QC)

mance achieves an approximately factor of four improvement over the open-loop. The baseline performance achieved on the OT is less than achieved by Neat *et al.* on JPL's Micro-Precision Interferometer (MPI) testbed [Melody and Neat, 1999], [Neat and O'Brien, 1996]. Multiple factors contribute to the difference in achieved performance:

1. Figure 6.19 shows that the performance autospectra of the OT have negligible energy at low frequency. Contrarily, MPI has 76% of its performance energy below 10 Hz. The low-pass nature of the classical MPI controllers

allows considerable performance to be achieved at these easy-to-control low frequencies.

2. The natural bandwidth of the MPI actuators allows a 500 Hz crossover of the phasing loop, compared to 70 Hz for the OT. The fundamental limit is the mass of the mirror affixed to the PZT that causes a roll-off (*i.e.* phase loss) of the PZT to DPL channel at ~ 170 Hz.
3. The MPI sensors have higher resolutions and bandwidths than their OT counterparts, corresponding to a capability for higher bandwidth control and less sensor noise injected by closing the loop.
4. The OT control computer is sampling at 1000 Hz, forcing a practical control bandwidth of 200 Hz. MPI's control computer samples at 8000 Hz.
5. The OT disturbance is a real-world, difficult-to-model reaction wheel imbalance disturbance. The MPI testbed uses a shaker to emulate the reaction wheel disturbance which allows for a direct measure of G_{yw} and G_{zw}, and a good understanding of the disturbance source.
6. The phasing control of MPI has an additional low-frequency actuator to form a three-tier delay line, compared to the two-tier delay line of the OT (VC and PZT).

The nature of the OT disturbance source and bandwidth limitations of the OT sensors and actuators do not allow the fidelity of the MPI testbed. Based on these physical constraints, we conclude that the OT baseline control performs well and provides a suitable platform for the demonstration of the tuning methodology. Future work should include a demonstration applying the tuning methodology to the MPI baseline controller presented in [Melody and Neat, 1999] and [Neat and O'Brien, 1996].

Figure 6.20 plots the MIMO Nyquist locus of the BC applied to the OT and the corresponding maximum and minimum singular values of the sensitivity transfer matrix. The Nichols plot shows a bandwidth of approximately 68 Hz with a roll-off at higher frequencies. Small spikes in the maximum singular value correspond to frequency points with measurement noise. The large, smooth spike near crossover (~68 Hz) corresponds to a pop-up region where noise may be amplified.

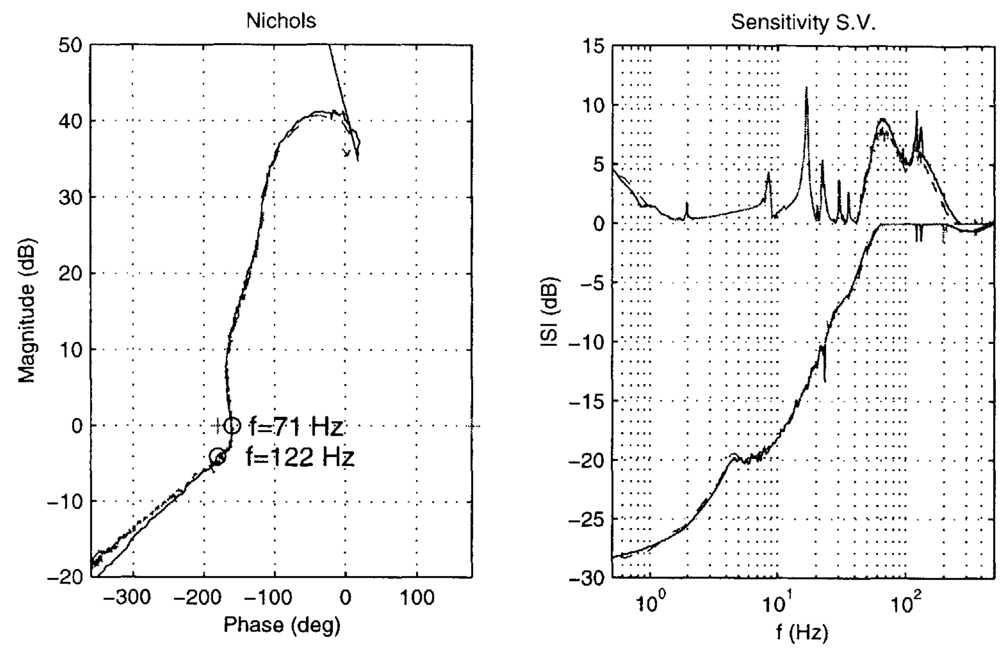

Figure 6.20 Absolute stability and robustness of the baseline controller: simulated with data from the Origins Testbed, and experimentally measured (dashed)

6.4.5 Baseline Control: Sensor/Actuator Index

Upon the application of the baseline controller, the input/output characteristics of the plant change. The sensor/actuator indexing algorithm can be applied to the closed loop system to provide a guide for further tuning. Figure 6.21 is a block diagram of the system used for sensor/actuator indexing in the presence of a feedback controller. The sensor and actuator noise are denoted by w_y and w_u respectively.

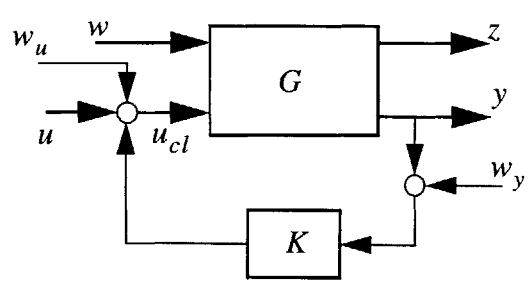

Figure 6.21 Sensor Actuator Indexing in the presence of a controller

In the closed-loop case, the sensor noise is fed back, and enters the plant as additional actuator noise. The closed loop actuator signal is written as

$$u_{cl} = Ky + Kw_y + w_u + u\,. \tag{6.12}$$

The first term (Ky) can be rewritten into the closed loop dynamics as in Equation 2.6. The fourth term (u) is the closed-loop actuator command signal. The second and third term $(Kw_y + w_u)$ enter as the actuator noise. In the algorithm of Chapter 3 the importance of scaling with the sensor and actuator resolutions (noises) is emphasized. In the closed-loop case we must capture the degradation of actuator resolution brought by feeding back the sensor noise. We adopt a worse-case strategy to write for the j-th actuator noise standard deviation, $\frac{1}{R_u(j)}$:

$$\frac{1}{R_u(j)} = \sum_{i=1}^{n_y} K_{ij}^{\infty}\frac{1}{R_y(i)} + \left(\frac{1}{R_u(j)}\right)_o, \tag{6.13}$$

where K_{ij}^{∞} is the maximum (over frequency) absolute value of the ij-th channel of the controller, $1/(R_y(i))$ is the standard deviation of the i-th sensor noise (the notation is introduced in Section 3.1.1), and $(1/(R_u(j)))_o$ is the standard deviation of the j-th open-loop actuator noise. With the modified input scaling the sensor/actuator indexing algorithm can be applied to the closed loop system. For the OT example with the baseline controller in place the resulting indexing matrix is shown in Table 6.8.

TABLE 6.8 Modified Sensor and Actuator indexing matrix for the closed-loop, baseline-controlled OT Model

	ENC	RGA	DPL	QC
RWA	12.3	17.8	10.1	8.0
VC	5.1	9.4	21.9	9.9
PZT	10.3	12.7	26.3	13.4
FSM	6.2	11.4	14.4	19.0

Comparing the BC case of Table 6.8 to the OL case of Table 6.5 we note several differences: (1) The ENC-to-RWA index has decreased as the rigid body mode is controlled, (2) the DPL-to-VC and QC-to-FSM indices have dropped indicating a slight decrease in their potential for additional control benefit (3) No change in the DPL-to-PZT channel reflects the low PZT control gain.

The sensor/actuator index matrix of Table 6.8 can be used as a guideline for tuning the baseline controller. With each tuned controller a further sensor/actuator index matrix can be computed to ascertain which sensors and actuators can be employed for further tuning. Some problems with the algorithm are associated with this:

1. As detailed in Chapter 3 the sensor/actuator indexing algorithm is an open-loop method and does not attempt to capture the effect of loop closing.
2. The plant scaling is based on an implicit assumption that the actuator and sensor noises are white. Feeding back the sensor noise as actuator noise in the manner of Equation 6.13 does not capture the spectral shape that the controller applies to the fed back sensor noise.
3. The sensor/actuator indexing algorithm is a guideline and has no capability to capture the real world nonlinearities in the sensors and actuators. For example, the saturation limit of the PZT limits its use for control, but is not captured by the algorithm.
4. The sensor/actuator indexing algorithm is a guideline and has no capability to capture the stability limitations of poorly modeled (measured) dynamics, or missing and nonminimum phase zeros in structural control systems.

Future research should address the resolution of these limitations.

6.5 Tuned Controllers

Starting from the baseline controller, a family of controllers for the OT is designed. Successive controllers are designed by tuning the parameters of the previous controller while adding features to change the controller topology: adding states, actuators, sensors and control channels. This incremental approach is favored for two reasons: (1) it is instructive to monitor the synthesis of the tuning technique as features are changed and added and (2) it is computationally simpler to tune individual control channels separately before combining to tune the controller globally. The second reason allows the tuning algorithm to be less likely to falter in a local minimum.

The tuning cost function is introduced in Chapter 4 and repeated here for convenience:

$$J_A(p) = J(p) + S_R(p) + d(p) + M(p). \tag{6.14}$$

The settings of the terms of the tuning cost are tabulated in Table 6.9.

TABLE 6.9 Tuning terms (from Equation 6.14) for OT tuned controller family

Term		Setting
RMS Performance	$J(p)$	Weighted RMS of the phasing (DPL) and pointing (QC) autospectra from a observation RWA disturbance
Stability Robustness	$S_R(p)$	Penalize all maximum s.v. of sensitivity deviations > 10 dB threshold. Increase penalty at $f > 100$ Hz to provide margin near roll-off. Critical point distance metric is not used, *i.e.* $\gamma_{cr} = 0$.
Controller Deviation	$d(p)$	Not used in the OT examples
Controller Magnitude	$M(p)$	Penalize low-frequency ($f < 1$ Hz) PZT and FSM use (avoid saturating small-stroke actuators with DC control)

The control objective is to minimize the RMS performance of the phasing and fine pointing while maintaining similar stability robustness to the baseline controller. As such the stability robustness weighting vector, ($W_S(\omega)$), is adjusted to maintain robustness. Based on engineering conclusions from the MACE program, a 10 dB threshold is set as the accepted maximum Sensitivity singular value at frequencies where the plant is not well measured or modeled [Miller et al., 1996]. A penalty on the low frequency control magnitude of the piezo actuators (PZT and FSM) is used to ensure that the small-stroke actuators are not saturated with DC control.

The interrelation of the controllers forming the family of controllers for the OT are shown in the block diagram of Figure 6.22. Table 6.10 lists the performance (predicted and experimental) for the tuned controllers and details the incremental changes to the controller topology.

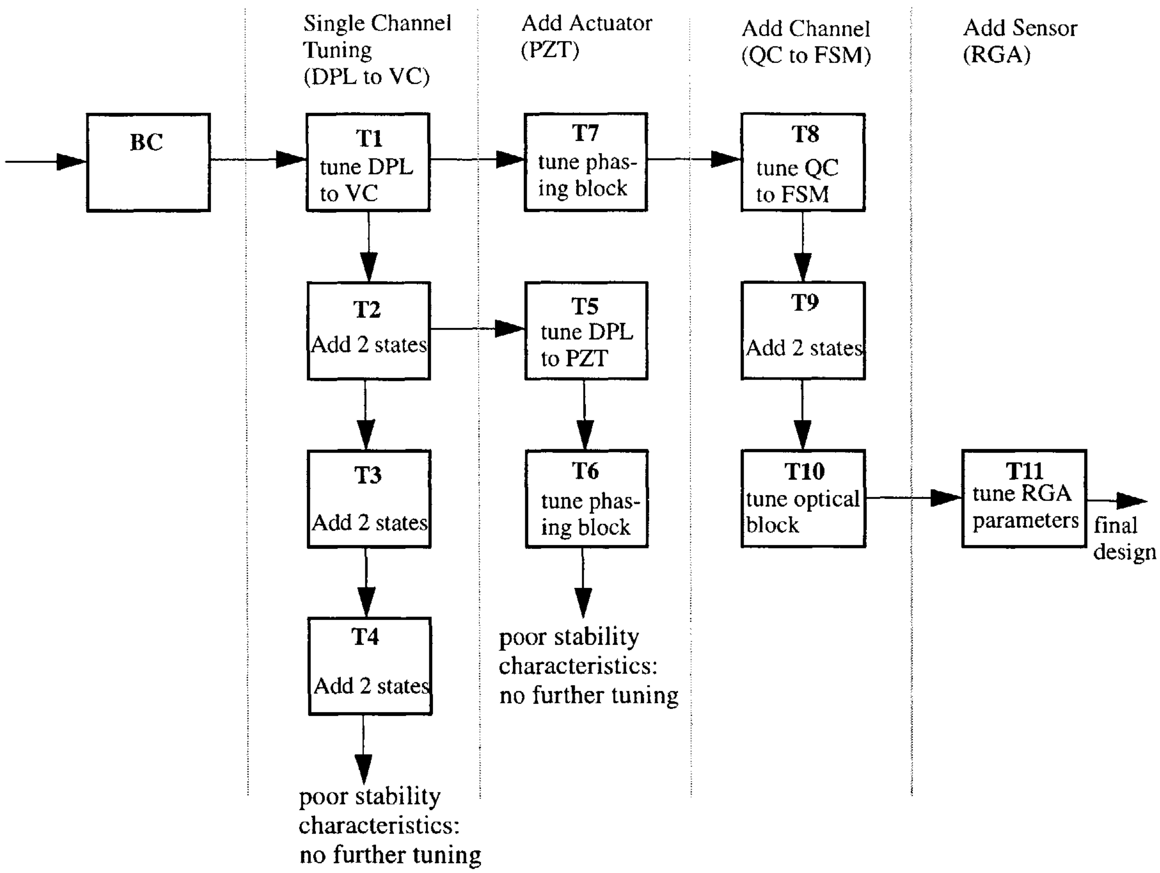

Figure 6.22 OT tuned controller family: controllers are synthesized by tuning the previous controller in the block diagram.

The path through Figure 6.22 from the baseline controller (BC) to a tuned design is chosen based on information from the sensor/actuator indexing matrix of Table 6.8. We are tuning the optical control block which corresponds to the lower 3×3 block of the indexing matrix. In this block, we see that the DPL-to-PZT and DPL-to-VC channels have the highest entry, motivating our initial tuning to focus on phasing control. Though the DPL-to-PZT block has the greatest entry in the indexing matrix, we are concerned with the nonlinear saturation limitation of the PZT and thus we choose to initially tune the DPL-to-VC block, resulting in the second column of Figure 6.22. In the third column PZT tuning is performed, where we are careful to avoid saturation. The third column also corresponds to tuning the entire optical control block, *i.e.* simultaneous tuning of the DPL-to-VC and DPL-to-PZT channel. Again where care must be take to avoid saturating the PZT. Con-

TABLE 6.10 OT tuned controller family: description and performance

Controller	Tuned from	RMS DPL Perf Predict (μm)	RMS DPL Perf Meas (μm)	RMS QC Perf. Predict (arcsec)	RMS QC Perf. Meas (arcsec)	# tuned param. n_p	# cont. states n_c	Notes
None	N/A	4.31	4.77	6.97	7.05	N/A	N/A	Closed-loop predictions and controller tuning is based on the open-loop data
BC	N/A	1.81	1.62	1.64	1.81	N/A	20	Classically designed controller, detailed in Section 6.4
T1	BC	1.47	1.29	1.59	1.63	12	20	Tune DPL-to-VC channel
T2	T1	1.09	0.97	1.60	1.68	18	22	Add 2 states and tune DPL-to-VC channel
T3	T2	0.97	0.89	1.56	1.62	24	24	Add 2 additional states and tune DPL-to-VC channel
T4	T3	0.90	0.87	1.56	1.70	30	26	Add 2 additional states and tune DPL-to-VC channel
T5	T2	1.06	0.98	1.59	1.68	12	22	Tune DPL-to-PZT channel. Penalize PZT use at low frequency.
T6	T2	0.81	0.66	1.58	1.85	40	22	Tune phasing block: DPL-to-VC & PZT block. Penalize PZT use at low frequency
T7	T1	0.86	0.76	1.55	1.88	40	22	Add 2 states. Tune phasing block: DPL-to-VC & PZT block. Penalize PZT use at low frequency
T8	T7	0.86	0.71	1.19	1.34	12	22	Tune QC-to-FSM block. Penalize FSM use at low frequency.
T9	T8	0.86	0.69	1.02	1.18	18	24	Add 2 states and tune QC-to-FSM block. Penalize FSM use at low frequency.
T10	T9	0.86	0.76	0.98	1.00	96	24	Tune entire optical control block: DPL & QC-to-VC, PZT and FSM. Penalize PZT and FSM use at low frequency.
T11	T10	0.66	0.77	0.86	0.98	16	24	Tune RGA parameters for the optical control block. Penalize PZT and FSM use at low frequency.

tinuing, the fourth column of Figure 6.22 corresponds to the next highest value in the indexing matrix block; the QC-to-FSM channel. Lastly (in the fifth column) we add the RGA sensor.

Appendix E compiles the result of applying the tuned controllers, T1 through T11, to the Origins Testbed. For each controller the controller gains, measured performance autospectra, and measured stability robustness plots are recorded. Where appropriate either the measured and predicted results, or the current and previous controller (from Figure 6.22) results are compared.

Figure 6.23 is a plot of the performance autospectra for the final controller, T11. For comparison purposes, the open-loop DPL and QC autospectra are plotted as well as those corresponding to the baseline controller. From the autospectra plots, we see that the tuned controller achieves a significant level of performance over the baseline controller by targeting the peaks in the autospectra. From Table 6.10 we see the improved performance is achieved with 4 more states than the order of the baseline controller.

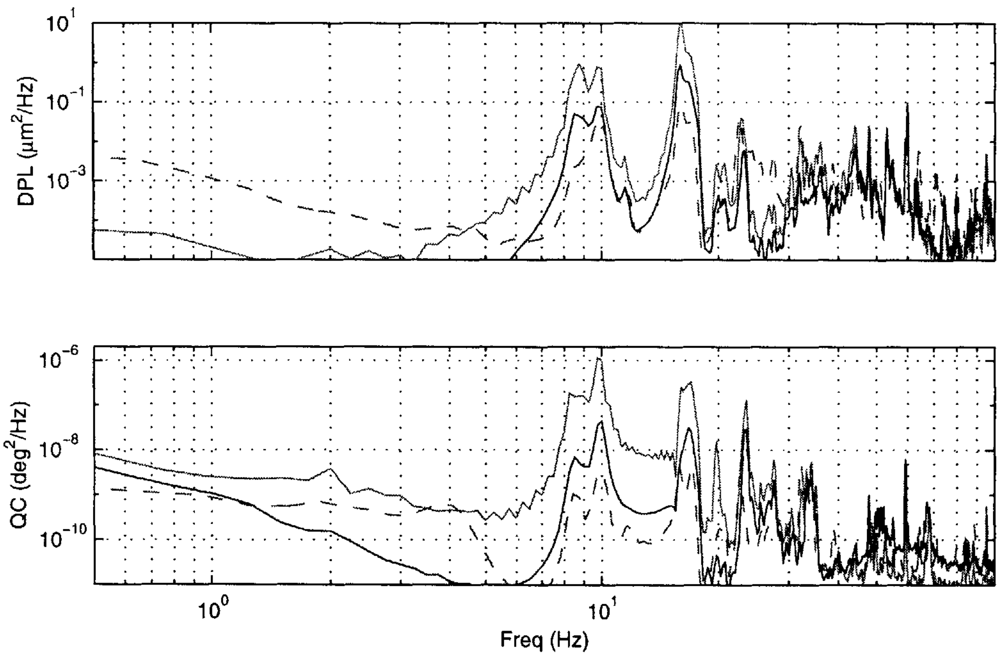

Figure 6.23 Experimental performance autospectra: open-loop (light), baseline controller (solid), T11 controller (dashed)

Figure 6.24 is a plot of the stability of the final T11 design. Also plotted is the stability plot of a design which achieves the same theoretical performance as T11, but which is designed by tuning the BC without penalizing our stability metric (*i.e.* by setting $W_S(\omega) = 0 \forall \omega$). In the Nichols plot, we see that the locus passes very close to the critical point. This corresponds to a 15 dB spike at in the maximum singular value of the sensitivity at 75 Hz. The high sensitivity spike is an indication of likely stability problems and for safety the controller was not implemented on the OT. The tendency towards designs with poor stability reinforces the need to tune with a penalty on stability non-robustness.

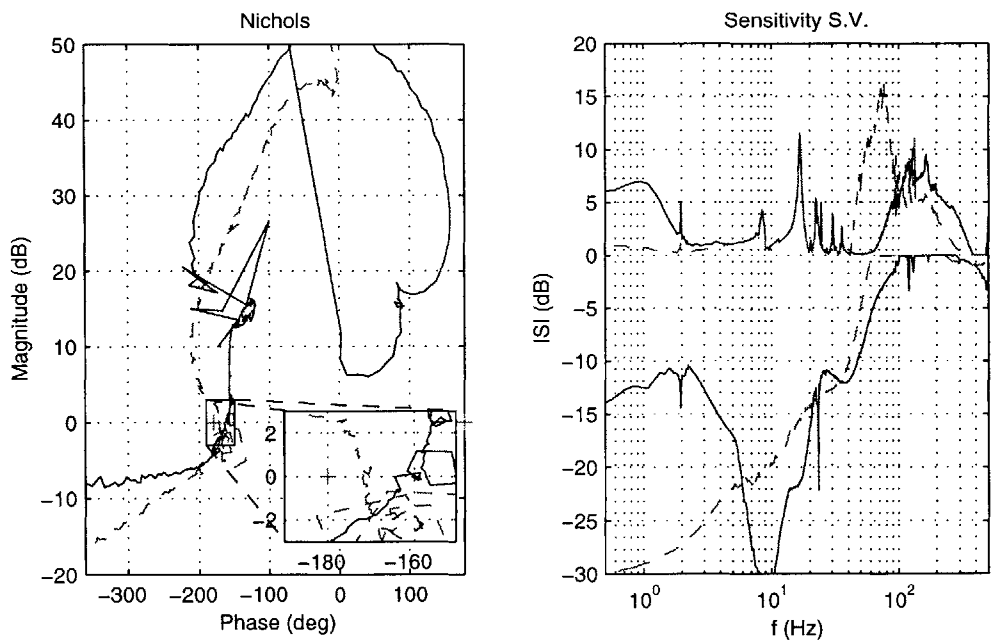

Figure 6.24 Stability plots for T11 controller (solid) compared with a controller designed without the stability penalty, *i.e.* $W_S(\omega) = 0 \forall \omega$, (dashed) that achieves similar simulated performance. An expanded view new the critical point of the Nichols plot shows the dashed curve approaching dangerously close to the critical point.

Figure 6.25 summarizes the performance attained by the tuned controllers as listed in Table 6.10 and plots the maximum singular value of the Sensitivity transfer matrix, a measure of stability robustness. For presentation purposes, the family of tuned controllers are broken up into three sets. Each set corresponds to a pass along the arrows of Figure 6.22.

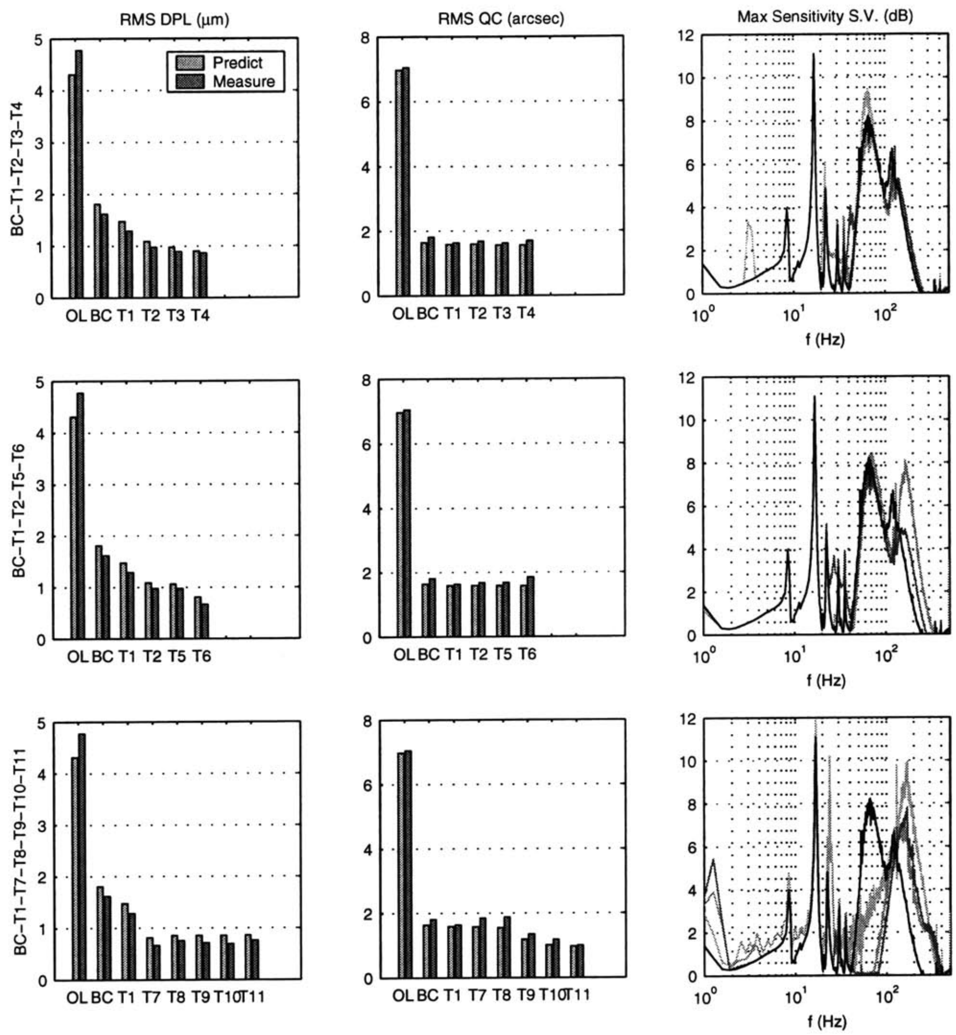

Figure 6.25 Plots of performance and maximum Sensitivity s.v. for each of three incremental tuner controller designs from the controller family of Figure 6.22 (following arrows). RMS DPL and QC performance are listed with predicted and measured values. For the maximum Sensitivity s.v., progression along a path in Figure 6.22 is indicated with a progression towards a lighter curve. For presentation purposes not all maximum s.v. plots in the set of controllers are displayed.

The initial set begins with the baseline controller and ends at controller T4: BC-T1-T2-T3-T4 and involves progressive tuning of the DPL-to-VC control channel. The DPL performance increases for the controllers while the QC performance remains approximately constant. As we progress along this set of controllers, a spike in the maximum s.v. of the

Sensitivity transfer matrix ($\bar{\sigma}(S)$) at 60 Hz indicates that we may have decreasing stability robustness should we tune further. The second set of controllers is: BC-T1-T2-T5-T6 which involves successively complicated tuning of the phasing loop (DPL to VC and DPL to PZT). A spike in ($\bar{\sigma}(S)$) at 190 Hz cause us to abandon this set. The final set begins with phasing control tuning, followed by fine-pointing control tuning, and ends with the addition of the RG sensor. The set includes: BC-T1-T7-T8-T9-T10-T11. Spikes in ($\bar{\sigma}(S)$) at 22 Hz and 190 Hz cause us to finish tuning with controller T11. The performance curves show that this tuning set has achieved considerable performance improvement over the baseline controller for both the DPL and QC performance channel (6.5 dB and 5.4 dB respectively).

6.6 Summary

The Origins Testbed was developed as a ground-based test article which captures the dynamics and control issues of future space telescopes. The OT was detailed with particular emphasis on its traceablility to SIM and NGST in terms of its dynamics, sensor suite, and actuator suite. The OT was modeled with state-space dynamics and the sensor/actuator indexing algorithm of Chapter 3 was applied to rank the effectiveness of sets of actuators and sensors for control. From the sensor/actuator indexing, the topology of the baseline controller was selected. The baseline controller design was detailed as a demonstration of the OT control complexity, and its performance experimentally measured. The baseline OT control is compared to the control of JPL's MPI test article. From the baseline controller, the tuning algorithms of Chapter 4 are applied to create a family of tuned controllers for the OT. The effect of the addition of states and sensor/actuator control channels are demonstrated and experimentally validated on the OT. With an experimental validation of the tuning algorithms on the traceable test article, we are now confident to apply the methodology to the control of the SIM spacecraft model.

Chapter 7

APPLICATION TO SIM

In this chapter, the tuning framework is demonstrated on a model of the Space Interferometry Mission (SIM) spacecraft. The applicability of the developed tools to large-order flexible models is confirmed. In particular, the tuning strategy allows an improved performance with little stability robustness degradation over the JPL-designed baseline controller, emphasizing its usefulness for future spaceborne telescopes.

The chapter begins with a quick introduction to the SIM and the SIM spacecraft. The conceptual FEM model of the SIM Classic spacecraft is introduced and prepared for use with the tuning framework. Techniques used for improving the numerical conditioning of the model are presented. The sensor/actuator suite of the conditioned model is analyzed for control effectiveness and a block-decoupled control structure is shown to be effective. A baseline controller is designed that includes elements from a JPL-designed controller. Lastly, the baseline controller is tuned and significant improvements in performance are achieved with little degradation in stability robustness.

7.1 SIM Description

The Space Interferometry Mission (SIM) is the first observatory in NASA's Origins program. It is a spaceborne 10 m baseline Michelson optical interferometer. The SIM science goals include furthering astrometry by (1) searching for planetary companions to nearby stars, and (2) providing 4 μarcsec precision absolute star position measures. Further, SIM will provide a technology demonstration for other telescopes in the Origins family including the Next Generation Space Telescope (NGST) and the Terrestrial Planet Finder (TPF). Both optical (such as the nulling interferometer mode for TPF) and controlled-structure (such as quieting a spacecraft to nm RMS levels of phasing jitter) technologies will be necessary for the operation of SIM, and will be demonstrated on SIM for application to future missions. Further details on SIM science goals can be found in [Unwin et al., 1999].

Figure 7.1 is a concept drawing of the SIM Classic spacecraft.[1] The optical side of the spacecraft is formed from a truss structure with seven collector apertures. In the standard observation mode, the collectors work in pairs, with two pairs imaging bright guide stars, and the third pair imaging the science target. The seventh aperture is redundant. A metrology tower rises from the truss structure. Four beam launchers at the tip of the tower are used to provide four measures of the position of each of the collectors. At the base of the telescope is the spacecraft bus, housing the attitude control system, communication hardware and electronics.

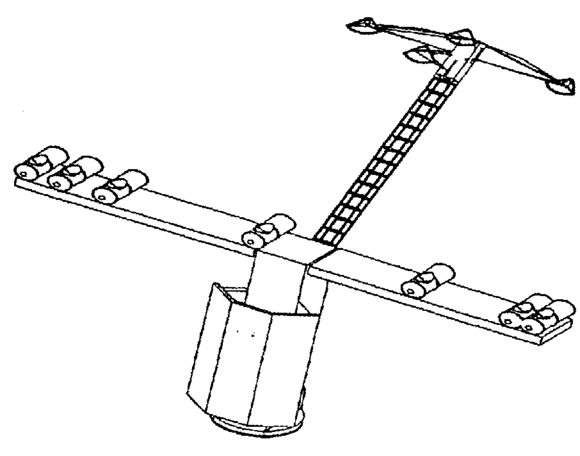

Figure 7.1 SIM Classic: one Possible design of the Space Interferometry Mission spacecraft. (Graphic courtesy of JPL)

1. The SIM model and ensuing description is for SIM Classic, an early SIM design concept. Current design iterations may result in a spacecraft physically quite different from this. The techniques applied to the SIM classic model are general enough to be applied to future SIM models and other large-scale systems.

The control actuators for the SIM spacecraft include mirrors mounted on voice coils, mirrors mounted on piezo stacks, fast-steering mirrors, and reaction wheels. The sensors include star trackers, rate gyroscopes, interferometers, wavefront tilt sensors and fringe trackers. Physical descriptions of the sensors and actuators are found in [Gutierrez, 1999].

The control problem that will be considered is the regulation problem of minimizing root-mean-square performance jitter as the telescope performs an observation. The torques and forces from reaction wheel imbalances are the primary disturbance source.

7.2 Model Preparation and Conditioning

The Finite Element Method (FEM) model of SIM Classic is utilized in the ensuing design example. The model was created as JPL using the Integrated Modeling of Optical Systems (IMOS) software toolbox. The model is a stick representation of SIM Classic, with trusses modeled with Bernoulli-Euler beam elements and optics modeled as lumped masses. Modal damping is specified to be 0.1%. The reaction wheel assembly (RWA) acts on the structure through a modeled 6-axis isolator with a 5 Hz corner frequency. Optical ray tracing is used to model the optical sensor and performance output matrices A detailed discussion of the model is found in [Gutierrez, 1999].

The raw model is particularly ill-conditioned. Initially the full-order FEM is truncated to a model preserving the first 113 modes with additional dynamics to capture actuator roll-off for the large bandwidth actuators (256 states total). In the current incarnation of the model the roll-off modes for the piezo stacks and the fast-steering mirrors are far too high in frequency and too lightly damped. Future versions of the model should realistically model high-frequency actuators. The six states corresponding to rigid-body translation modes are removed since they are neither observable nor controllable by any sensor/performance or actuator/disturbance. Further preparation of the model for application of the sensor/actuator indexing technique and for the application of the tuning algorithm is seen in the block diagram of Table 7.2.

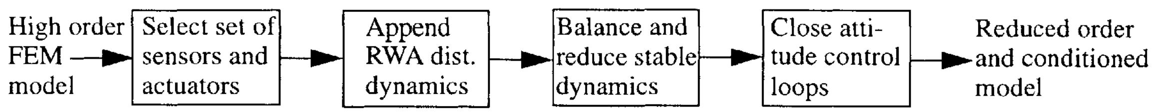

Figure 7.2 Preparing the SIM model for control examples

Sensors and actuator selection

The raw SIM model has a total of 24 actuators and 39 sensors. For demonstration purposes a reduced subset of the full sensor and actuator suite will be used in the ensuing examples. The optical control problem will be considered on the model with the attitude control loops are closed. At this stage we can remove some attitude control sensors (three rate gyroscope channels) from the problem. The remaining attitude control sensors and actuators are removed by closing the attitude control loop. Six disturbance inputs (three reaction wheel forces and three reaction disturbance torques) will be linked together and fed with a single noise spectrum driven by white noise.

The SIM model has a complete sensor/actuator suite for three interferometer channels: guide star 1 interferometer, guide star 2 interferometer and the science interferometer. The function of the guide interferometers are to lock onto bright guide stars with a high bandwidth and feed forward control action to the lower-bandwidth science interferometer. The SIM classic model baseline control does not capture this feedforward control and thus the science interferometer will not be considered in out examples. From the model we remove the actuators (a mirror mounted on a voice coil, a mirror mounted on a piezo stack, and four axes of fast-steering mirror wavefront tilt) and sensors (an external differential pathlength measure, an internal interferometer channel and four wavefront sensors) particular to the science interferometer channel.

Our final simplification is to difference the absolute wavefront sensors from each arm to produce differential wavefront tilt. For each interferometer channel we reduce four absolute sensors to two relative (x and y direction) sensors. Similarly, for each interferometer channel, we reduce four absolute fast-steering mirror actuators to two relative (tip/tilt) actuators.

Table 7.1 is a list of the remaining suite of actuators and sensors for the examples in this chapter. Also included is the disturbance channel and the six performance variables. An abbreviated name is presented for each input and output. Where available, resolutions are included for use with the sensor/actuator indexing algorithm.

TABLE 7.1 Signal definitions for the four-block control problem for the SIM observation control. Resolutions are included for the sensors and actuators, intensities for the disturbances and requirements for the performances.

Signal Type	Abbrev-iation	Description	Resol-ution[a]
Disturbance w	RWA d	Reaction wheel imbalance disturbance	1
Actuators u	VC G1	Mirror mounted on voice coil. Guide interferometer 1	N/A[b]
	PZT G1	Mirror mounted on a piezo stack. Guide interferometer 1	N/A
	VC G2	Mirror mounted on voice coil. Guide interferometer 2	N/A
	PZT G2	Mirror mounted on a piezo stack. Guide interferometer 2	N/A
	Tip G1	Fast-steering mirror tip axis.Guide interferometer 1	N/A
	Tilt G1	Fast-steering mirror tilt axis.Guide interferometer 1	N/A
	Tip G2	Fast-steering mirror tip axis.Guide interferometer 2	N/A
	Tilt G2	Fast-steering mirror tilt axis.Guide interferometer 2	N/A
Performance z	T DPL G1	Total differential pathlength. Guide interferometer 1	4.4 nm
	T DPL G2	Total differential pathlength. Guide interferometer 2	4.4 nm
	DWFTx G1	Differential wavefront tilt, x axis. Guide interferometer 1	0.33 asec
	DWFTy G1	Differential wavefront tilt, y axis. Guide interferometer 1	0.33 asec
	DWFTx G2	Differential wavefront tilt, x axis. Guide interferometer 2	0.33 asec
	DWFTy G2	Differential wavefront tilt, y axis. Guide interferometer 2	0.33 asec
Sensors y	T DPL G1	Total diff. pathlength. Guide interferometer 1 (fringe tracker)	5 nm
	I DPL G1	Internal differential pathlength. Guide interferometer 1	5 nm
	T DPL G2	Total diff. pathlength. Guide interferometer 2 (fringe tracker)	5 nm
	I DPL G2	Internal differential pathlength. Guide interferometer 2	5 nm
	WT X G1	Wavefront tilt sensor, X axis. Guide interferometer 1	0.1 asec
	WT YG1	Wavefront tilt sensor, Y axis. Guide interferometer 1	0.1 asec
	WT X G2	Wavefront tilt sensor, X axis. Guide interferometer 2	0.1 asec
	WT Y G2	Wavefront tilt sensor, Y axis. Guide interferometer 2	0.1 asec

a. The term 'resolution' applies for the actuators and the sensors. For the disturbance, 'intensity' is more appropriate and for the performance, 'requirement' is more appropriate. The resolutions listed here are estimates, the true resolutions for SIM are classified and unavailable in the open literature.

b. Actuator resolutions for SIM are unavailable.

It is essential to strip away unused sensors and actuators from a model for two reasons: (1) unnecessary sensors and actuators slow further computation, occupy additional memory and increase the modeler's bookkeeping burden (2) further model-conditioning steps may take advantage of knowledge of the sensor and actuator suite to scale or balance the system, resulting in a system erroneously scaled with unused sensor/actuator characteristics.

Disturbance modeling

The primary disturbance source is the reaction wheel assembly whose harmonic disturbances are averaged over their frequency range with a low-order pre-whitening filter, represented with four states [Gutierrez, 1999]. The six disturbance inputs, (reaction wheel forces and torques in each direction) are then driven by the pre-whitening filter which is driven by a unit intensity white noise.

In [Gutierrez, 1999] a RWA pre-whitening filter is given as

$$G_d(s) = \frac{As^2}{(s+\omega_o)^4} \tag{7.1}$$

where $\omega_o = 2\pi \cdot 100$ (compare with Equation D.1). This four repeated real poles cause the filter to be numerically ill-conditioned. Real poles and pole repetition create difficulty for eigensolvers and for matrix inversion algorithms, and should be avoided if possible. An improved filter is designed with four complex poles; for example with four poles placed in a stable Butterworth configuration. In the redesigned filter the roll-off characteristics are sharper, and more closely represent the physical wheel disturbance.

Model reduction

The order of the model is typically larger than required. For example the optics controllers of this chapter are examples of active output isolation. The relevant actuator-to-sensor channels tend to be simple which implies that a low-order model can be used for stability-preserving control design. Additional modes in the model can be used to design the controller to emphasize noise rejection in specific frequency bands. In this case model reduction represents an engineering trade between model fidelity and model accuracy.

The removal of unnecessary sensors and actuators from the model may leave uncontrollable actuator dynamics and unobservable sensor dynamics. It is essential that these states be removed since (1) they burden the model (computationally and memory intensively) and (2) they can result in numerical ill-conditioning (possible singularity in some algorithms, *e.g.* standard model balancing).

The rotational rigid body modes are critically stable and are essential to the model. Thus we consider only reduction of the stable modes. To extract the stable modes we transform the model to a 2×2 block real-modal form. After checking to ensure that the transformation does not affect the model transfer matrix we apply a truncation transformation (Equation 3.49) to extract the stable dynamics.

Balanced reduction can be used to reduce the order of the model. However for numeric conditioning reasons the SIM model cannot be balanced with conventional (MATLAB) balancing tools. The developed balanced truncation technique of Section 3.1.2 allows us to balance and reduce the SIM model with little loss in accuracy. The model is reduced from 256 states to 138 states. The result of applying the technique to the SIM model is seen in Figure 3.2.

Attitude control

The model is provided with JPL-designed attitude controllers. The attitude controller is made up of a lead near crossover followed by a double-pole lag to ensure appropriate roll-off. A 3×3 constant matrix multiplies the controller to account for the off-axis principal axes of the SIM spacecraft. The attitude control loop has a bandwidth of 0.1 Hz and damps and stiffens the three rotational modes to 0.1 Hz.

The system can be transformed to a modal form. Further balancing on the now-stable system may be erroneous since there is a large frequency separation between the lowest frequency modes (stabilized attitude modes at 0.1 Hz) and the highest frequency modes (fast-steering mirror roll-off modes at ~ 5 kHz).

We now have a stable open-loop (optical control) system with 148 states. In the sequel we will refer to this model as the open-loop SIM model.

7.3 SIM Dynamic Coupling

In this section we apply the sensor/actuator indexing technique to the open-loop SIM model. First we briefly analyze the dynamics of one of the guide interferometer channels. Figure 7.3 plots the magnitudes of a subset of the transfer functions for the guide 1 interferometer channel. The outputs are plotted in appropriate units (nm phasing and arcseconds pointing) while the inputs are scaled for display purposes.

We see the disturbance input channels display a high modal density. The disturbance has no energy at DC and rolls-up with frequency. For DPL measures the transfer functions peak around 20 Hz, while wavefront tilt measures peak around 30 Hz. The disturbance input channels roll-off with the wheel pre-whitening dynamics at around 100 Hz. We note that the y-direction disturbance to wavefront tilt is an order in magnitude lower than its x-direction counterpart. The voice coil input transfer function display strong coupling to the DPL measures. A lightly damped voice coil mode is apparent ~ 4 Hz which limits the bandwidth of the voice coil actuator. The voice coil is only lightly coupled to the wavefront tilt measures, likely through the motion of a small mass. If we compare to the voice coil transfer functions for the Origins Testbed (Figure 6.7) we see the SIM model voice coil damping may be underestimated. In the plotted bandwidth the piezo mirror actuators

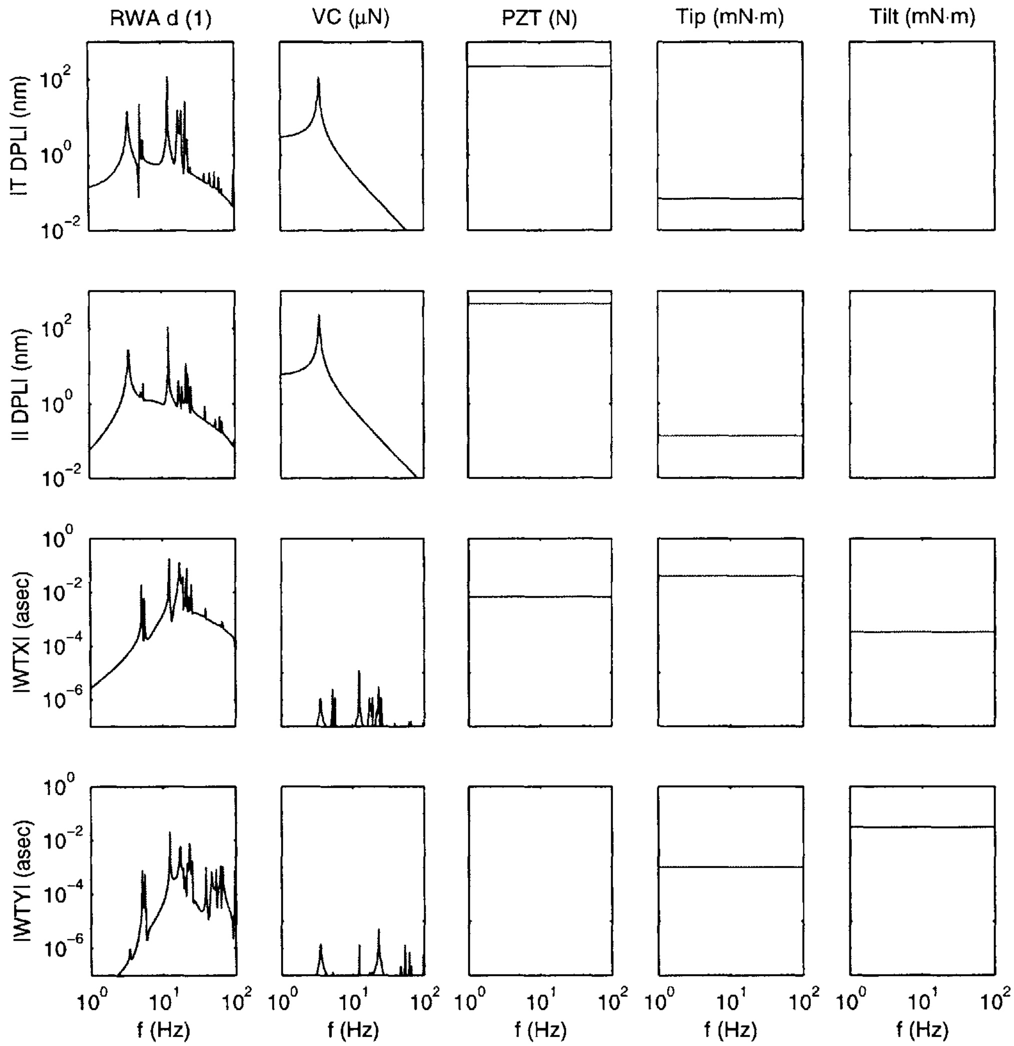

Figure 7.3 Subset of the magnitude of the transfer matrix for guide interferometer 1 of the SIM model. Attitude control loops are closed but the optics loops are open.

resembles a feedthrough term to the DPL measures. The piezo mirror (as scaled for the plot) also appears to couple to the x-direction wavefront tilt. The sensor/actuator indexing algorithm will quantify this coupling with proper scaling. Lastly, the tip and tilt actuators appear as feedthrough terms to the wavefront measures. Tip actuation couples to the x-direction while tilt couples to the y-direction with cross terms down two orders of magnitude. Reciprocally to the piezo/y-direction wavefront tilt coupling, the tip actuator shows some scaled coupling to the interferometer channels. We note that all of the feedthrough terms are modeled as lightly damped second order channels with a frequency much greater than the band of interest. Compared with the OT we see that the feedthrough channels of SIM are modeled with a roll-off higher in frequency and with less damping.

We now apply the actuator/sensor indexing algorithm of Chapter 3 the SIM model. The resulting sensor/actuator indexing matrix, S_t, shows which sets of sensors and actuators are most effective for control.

The SIM model is cast into the four-block control problem with the disturbance, actuator, performance and sensor variables outlined in Table 7.1. The algorithm of Chapter 3 can now be applied. The user must supply four sets of information as shown in Table 3.1. For the open-loop SIM example:

1. The plant model is delivered in a four-block state-space form, (A, B_w, B_u, C_z, C_y) (Section 7.2).
2. The scaling gains, R_y, R_w, R_z are set using the resolutions (for u and y variables), intensities (for w variables), and performance requirements (for z variables) which are listed in Table 7.1. The actuator resolutions are not available and must be estimated. Approximate actuator resolutions are calculated by scaling the actuator until a unit-DC signal provides a unit-resolution response in the appropriate sensor. The voice coil resolution is gained by an additional factor of 100 to allow coarse/fine handoff with the piezo actuator. The scaling factors weight the relative importance of the sensors and actuators by capturing the anticipated signal-to-noise.
3. The standard value of $\gamma = 1$ is used for the output isolation mixing parameter (Equation 3.114).
4. The relative importance of the rigid body modes must be assigned by setting the ω_{RM} parameter (Section 3.2.3). In the SIM model the rigid body modes are stabilized by the attitude control system so ω_{RM} is unused.

To determine the suitability of particular sensor/actuator combinations for control the S_t index is used. Table 7.2 displays the S_t matrix for the open-loop SIM model.

The largest indices couple into blocks indicated with the shading, suggesting a control topology. S_t indicates that both guide interferometers can be decoupled. Further, phasing

TABLE 7.2 Sensor and Actuator indexing matrix for the SIM model. Light shading corresponds to phasing control channels. Dark shading corresponds to fine-pointing control channels.

	T DPL G1	I DPL G1	T DPL G2	I DPL G2	WT X G1	WT Y G1	WT X G2	WT Y G2
VC G1	3.7	4.9	0.9	2.1	-13.4	-14.7	-12.9	-15.6
PZT G1	6.7	6.4	3.2	3.4	-3.6	-23.3	-7.5	-23.9
VC G2	0.9	2.1	3.6	4.8	-15.0	-15.5	-14.0	-16.4
PZT G2	3.2	2.9	6.7	6.9	-7.1	-22.7	-4.0	-23.4
Tip G1	4.2	4.5	-0.1	0.1	6.3	0.5	0.5	-1.4
Tilt G1	-1.8	-1.4	-1.5	-1.7	-0.6	3.1	-1.5	-2.9
Tip G2	0.3	0.4	3.8	4.4	-0.3	-2.2	5.8	1.2
Tilt G2	-3.1	-2.1	-0.2	0.5	-3.4	-3.6	1.4	3.2

control (T DPL and I DPL to VC and PZT) and fine-pointing control (WT X and WT Y to Tip and Tilt FSM's) are decoupled and indicated with light and dark shading respectively. The highest value in the matrix corresponds to the use of the high-bandwidth PZT with the low-noise DPL channels. We note the x-direction wavefront tilt to tip actuation blocks are much greater than the y-direction wavefront tilt to tilt actuation blocks. This is consistent with the appropriate transfer functions of Figure 7.3 considering the performances of differential wavefront jitter in x and y directions are weighted equally. Some cross-coupling of the two interferometers is observed for the phasing control, far less for fine-pointing control. The effect of this will be exposed in the presentation of the tuned SIM controllers. S_t also indicates that the DPL sensors couple with the tip actuators. This is consistent with feedthrough terms that we see in the transfer matrix of Figure 7.3.

The shaded blocks in the S_t matrix indicate the topology of the SIM baseline controller.

7.4 Baseline Controller

The baseline controller is classically designed with the topology of the shaded boxes in the S_t matrix of Table 7.2. The phasing control is designed by JPL and is included with the SIM Classic model. The fine-pointing controller is designed at MIT.

Phasing control

The structure of the phasing controller is diagrammed in Figure 6.16. A similar phasing controller is designed for each guide interferometer channel. The controller is made up of three blocks:

1. $K_{ph,v}$. Control from the internal differential pathlength measure to the voice coil actuator. Five-state SISO controller intended for mid-frequency (0.1 to 5 Hz) pathlength control.
2. $K_{ph,p}$. Control from the internal differential pathlength measure to the piezo stack actuator. Five-state SISO controller intended for high-frequency (greater than 4 Hz) pathlength control. Avoids stroke limitation with zero DC gain.
3. $K_{ph,f}$. Control from the fringe tracker (measures total differential pathlength) to the voice coil and piezo controllers. Five-state SISO controller intended for low-frequency (below 0.1 Hz) pathlength control.

Additional detail can be found in [Gutierrez, 1999]. Though the individual controllers are designed as SISO, the formulation of the final controller is a fifteen-state 2×2 MIMO controller. Balanced model reduction allows the controller to be reduced to twelve states. The bandwidth of the baseline phasing controller is approximately 60 Hz.

Fine-pointing control

For each guide interferometer and for each direction (x,y) a fourth-order SISO controller is designed for controlling the x-direction (y-direction) wavefront tilt sensor to tip (tilt) actuator. The control design consists of:

- a complex second-order lag filter with a break frequency two orders of magnitude below the desired crossover frequency,
- a zero at a frequency a factor of three below the desired crossover frequency, and
- a complex second-order lag filter for roll-off with a break frequency a factor of five a above the desired crossover frequency.

The controller is an improvement on the design by [Gutierrez, 1999] since it (1) achieves a similar performance with similar stability margins with one less state, and (2) numerical conditioning is improved by replacing real poles with a complex pole pair to achieve the desired roll-off.

Baseline control performance

The baseline controller can be applied to the SIM model and the performance and stability robustness can be measured. The performance is computed through a Lyapunov technique. For guide channel 1 the open-loop jitter on the external DPL is 60 nm RMS. The baseline controller reduces it to 3.8 nm RMS, a 24.0 dB improvement. The open-loop jitter on the x-direction differential wavefront title is reduced from 0.343 arcsec RMS (open loop) to 0.047 arcsec RMS, a 17.3 dB improvement. Similar improvements are computed for the other performance measures. Figure 7.4 is a plot of the performance autospectra and Sensitivity singular values of the SIM model with the baseline controller.

Considerable improvement in the phasing plot is observed up to approximately 60 Hz, while the fine-pointing controller bandwidth is seen to be 30 Hz. The phasing control rejects all of the highest-energy autospectrum peaks in the differential pathlength (2 to 20 Hz). Alternately the high-energy peak at 46 Hz in the differential wavefront tilt is beyond the bandwidth of the fine-pointing control. The maximum singular values of the Sensitivity demonstrate smooth behavior not much exceeding 12 dB. A small spike at 500 Hz corresponds to the roll-off of the fine-pointing loops marginally exciting the lightly-damped 500 Hz FSM mode.

7.5 Tuned Controller

The tuning cost function is introduced in Chapter 4 and repeated here for convenience:

$$J_A(p) = J(p) + S_R(p) + d(p) + M(p) . \tag{7.2}$$

The settings of the terms of the tuning cost for the SIM control tuning are tabulated in Table 7.3.

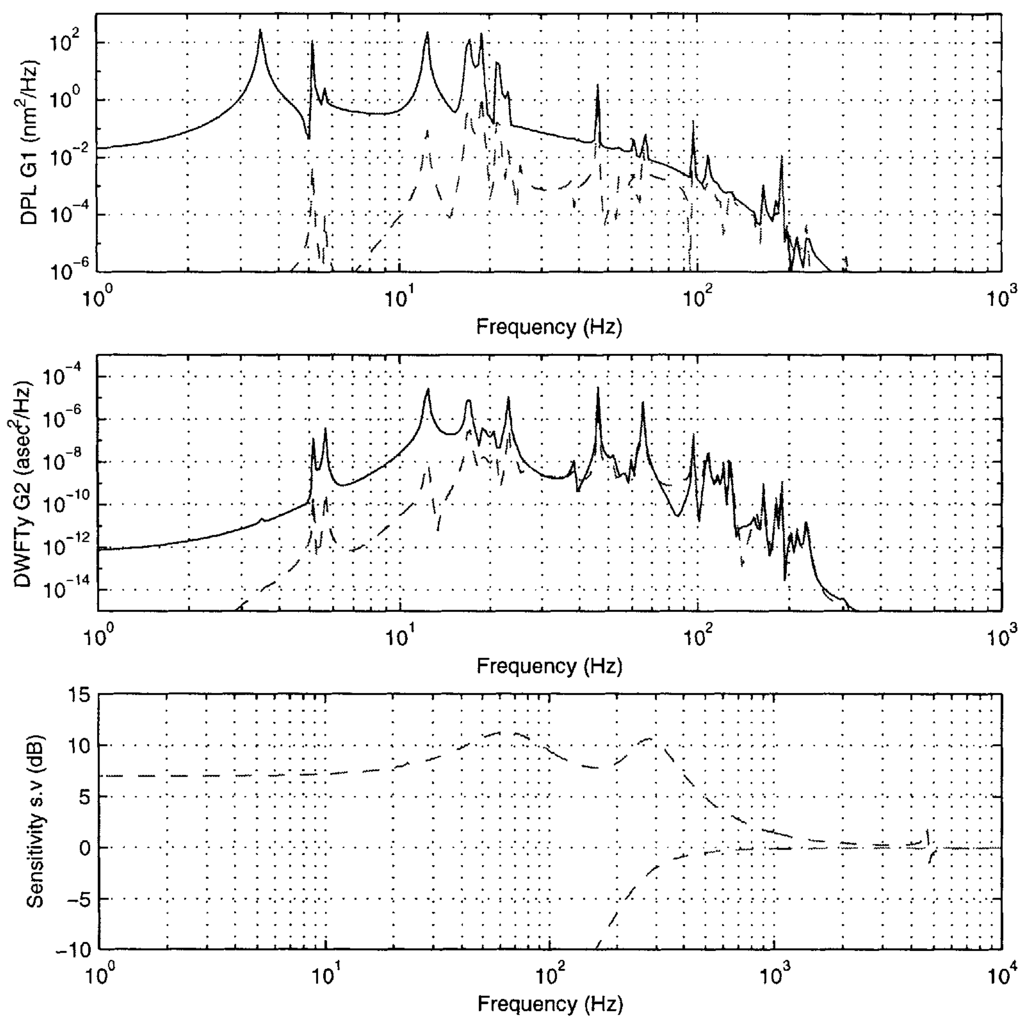

Figure 7.4 Performance and stability of tuned fine-pointing controller. The top plot is the autospectrum of the external DPL of guide interferometer 1, the middle plot is the autospectrum of the differential wavefront tilt of guide interferometer 2, and the lower plot are the maximum and minimum singular values of the Sensitivity transfer matrix. The open loop is plotted in dark solid and the baseline controller is dashed.

Figure 7.5 is a block diagram of the family of tuned controllers that are designed for the SIM model. From the baseline controller the phasing blocks are tuned (maintaining the block separation of guide channels 1 and 2) to form controller S1. The phasing control poles are fixed and the relevant input and output matrix elements are tuned. Numerical

TABLE 7.3 Tuning terms (from Equation 7.2) for SIM tuned controller family

Term		Setting
RMS Performance	$J(p)$	Weighted RMS of the phasing six performance metrics, z of Table 7.1
Stability Robustness	$S_R(p)$	No penalty for low-frequency deviations, $f < 120$ Hz. Penalize all maximum s.v. of sensitivity deviations > 10 dB threshold in the band $120 < f < 2000$ Hz. Decrease threshold to 5 db for $f > 2000$ Hz. Increase penalty at $f > 2$ kHz to provide margin near roll-off. Critical point distance metric is not used, *i.e.* $\gamma_{cr} = 0$.
Controller Deviation	$d(p)$	Not used in the SIM examples
Controller Magnitude	$M(p)$	Not used in the SIM examples

conditioning issues caused by (1) large frequency separation in the poles of the phasing controller and (2) the large dynamic range of the phasing controller do not allow tuning of the controller poles. From the S1 controller, the fine-pointing controller is tuned to form controller S2. We keep the cross-channel (guide channel 1 and guide channel 2) separation but allow the controller cross terms from the x-direction (y-direction) wavefront sensor. From controller S2, all previously tuned blocks are tuned to results in the final controller, S3.

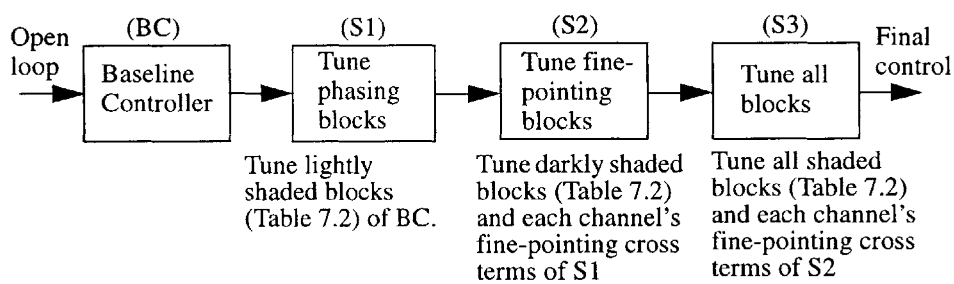

Figure 7.5 SIM tuned controller family: controllers are synthesized by tuning the previous controller in the block diagram.

The performances of the tuned controllers are tabulated in Table 7.4.

TABLE 7.4 Performance variables for the family of tuned SIM controllers. All absolute measures are RMS quantities. Decibel quantities are improvements of the controlled performance relative to the appropriate open-loop performance variable.

Controller	num. states	Performance Variable											
		T DPL G1		T DPL G2		DWFTx G1		DWFTy G1		DWFTx G2		DWFTy G2	
	n_c	(nm)	(dB)	(nm)	(dB)	(asec)	(dB)	(asec)	(dB)	(asec)	(dB)	(asec)	(dB)
None		60.0	0	41.1	0	0.343	0	0.0209	0	0.282	0	0.0184	0
BC	40	3.8	24.0	3.1	22.4	0.047	17.3	0.0047	13.0	0.037	17.6	0.0047	11.9
S1 (Tuned phasing)	40	1.4	32.6	1.8	27.2	0.047	17.3	0.0046	13.1	0.037	17.6	0.0047	11.9
S2 (Tuned pointing)	40	1.5	32.0	1.8	27.2	0.034	20.1	0.0021	20.0	0.028	20.1	0.0019	19.7
S3 (Tune all blocks)	40	1.2	34.0	1.6	28.2	0.034	20.1	0.0018	21.3	0.028	20.1	0.0014	22.4

In Figure 7.6 two performance channels and the Sensitivity singular values are plotted for the S1 case. The tuned controller achieves greater phasing performance without much affecting the fine-pointing performance. Small changes in the fine-pointing performance result from coupling in the plant. In the phasing autospectra plot we see that the tuned controller sacrifices low frequency performance to improve the performance in the critical 20 Hz range. The tuned controller increases the performance without extending the baseline phasing control's 60 Hz bandwidth. The maximum singular value of the Sensitivity transfer matrix remains unchanged indicating that the additional performance has been achieved without sacrificing stability robustness.

The corresponding performance and stability robustness plots for the S2 case are plotted in Figure 7.7. In this case the fine-pointing control is tuned from the S1 design. The phasing performance is made marginally worse from fine-pointing/phasing cross-coupling. The fine-pointing performance is improved particularly at higher frequency. The tuning algorithm recognizes the large bandwidth of the fine-pointing actuators and extends the control bandwidth. The bandwidth is extended until the high-frequency FSM mode at 500 Hz pops up in the Sensitivity singular value plot. The 5 dB threshold in the maximum sin-

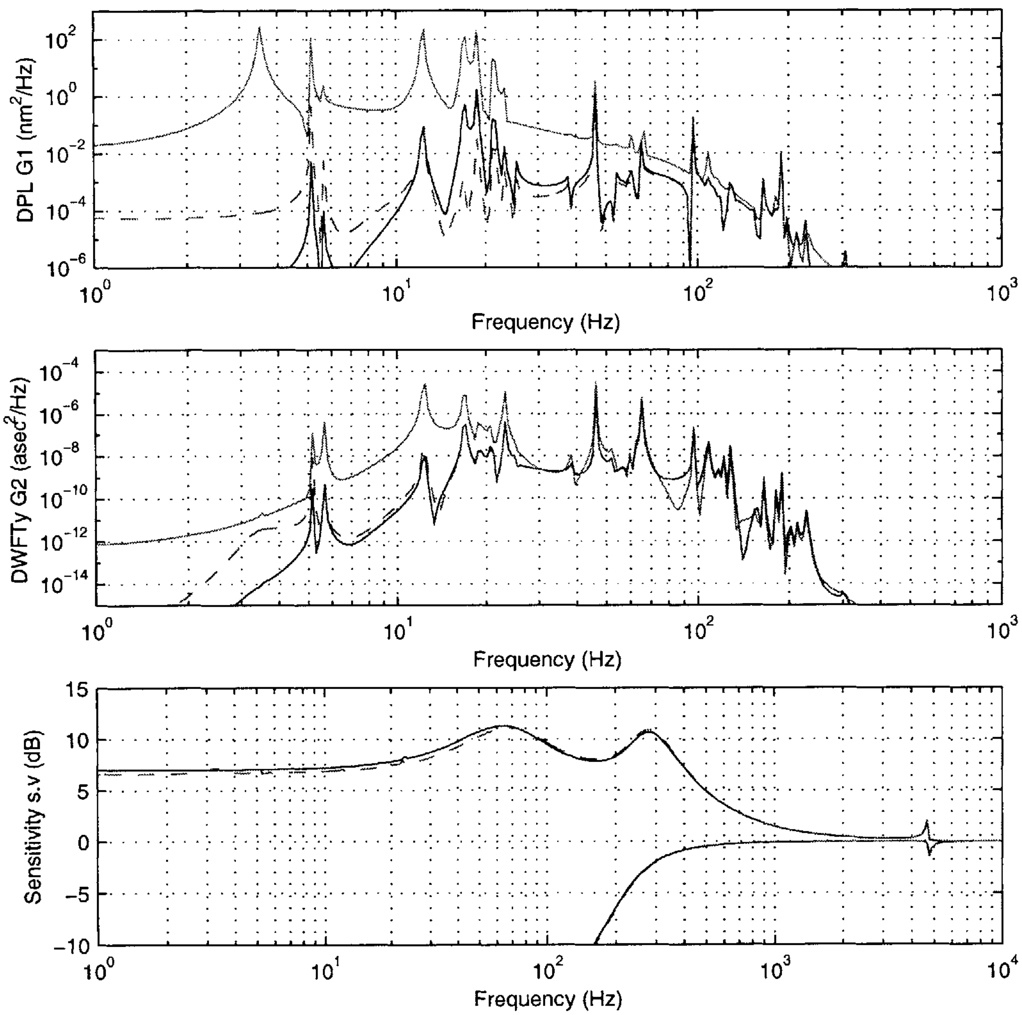

Figure 7.6 Performance and stability of tuned phasing controller S1. The top plot is the autospectrum of the external DPL of guide interferometer 1, the middle plot is the autospectrum of the differential wavefront tilt of guide interferometer 2, and the lower plot are the maximum and minimum singular values of the Sensitivity transfer matrix. The open loop is plotted in light solid, the baseline control case in dark solid and the tuned controller is dashed.

gular value for frequencies greater than 2 kHz limits the bandwidth of the tuned fine-pointing controller to approximately 150 Hz.

The performance and stability plots for the final design, S3, are plotted and compared with the baseline controller in Figure 7.8. In this final design the stability penalty was

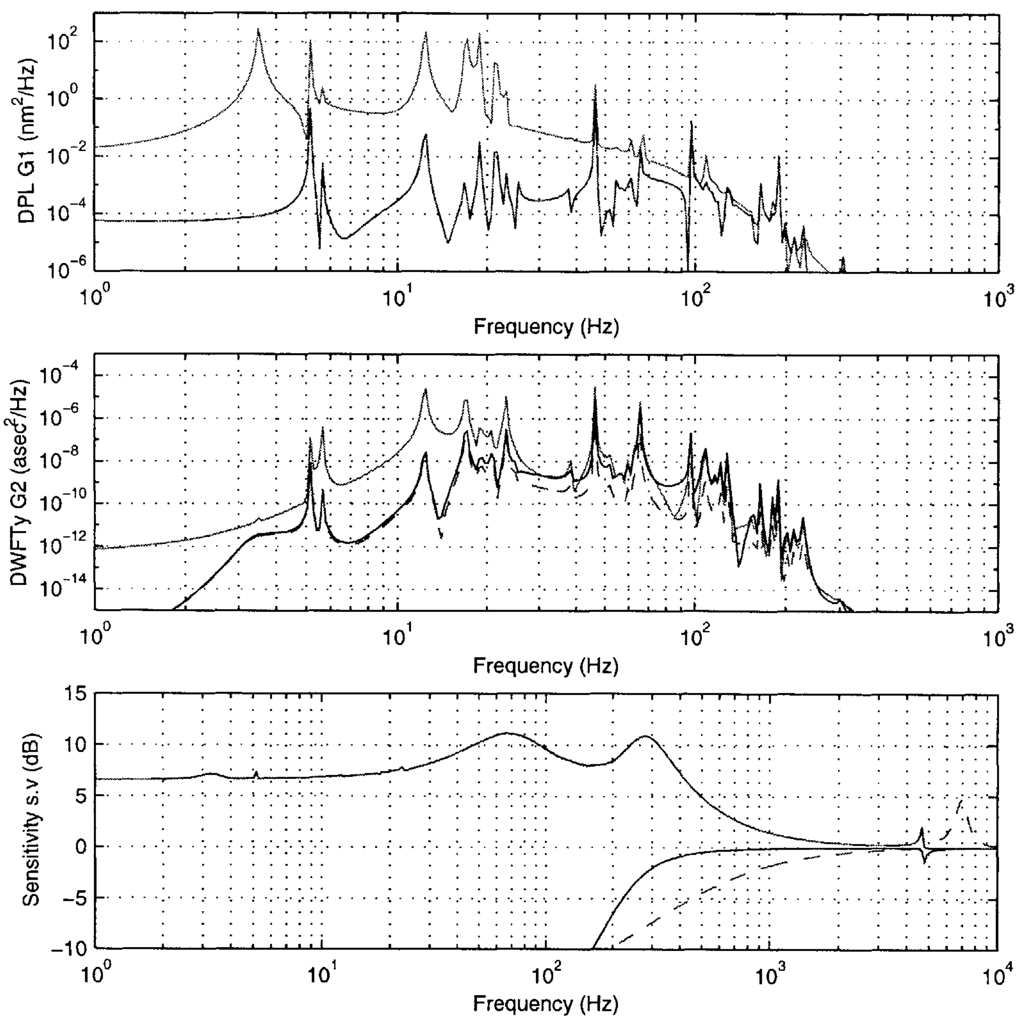

Figure 7.7 Performance and stability of tuned fine-pointing controller S2. The top plot is the autospectrum of the external DPL of guide interferometer 1, the middle plot is the autospectrum of the differential wavefront tilt of guide interferometer 2, and the lower plot are the maximum and minimum singular values of the Sensitivity transfer matrix. The open loop is plotted in light solid, the tuned phasing control case is dark solid and the tuned controller is dashed.

decreased allowing an improved performance at the expense of an increase in the Sensitivity maximum singular value at a frequency of 30 Hz. The phasing gives up performance at 5 Hz to increase the control gain in the 20 Hz band. The phasing bandwidth is increased to approximately 90 Hz. The tuned fine-pointing control improves the performance in the 20 to 150 Hz band with only a slight low-frequency performance degradation. The 1.2 nm phasing achieved in guide channel 1 is roughly the requirement for star nulling.

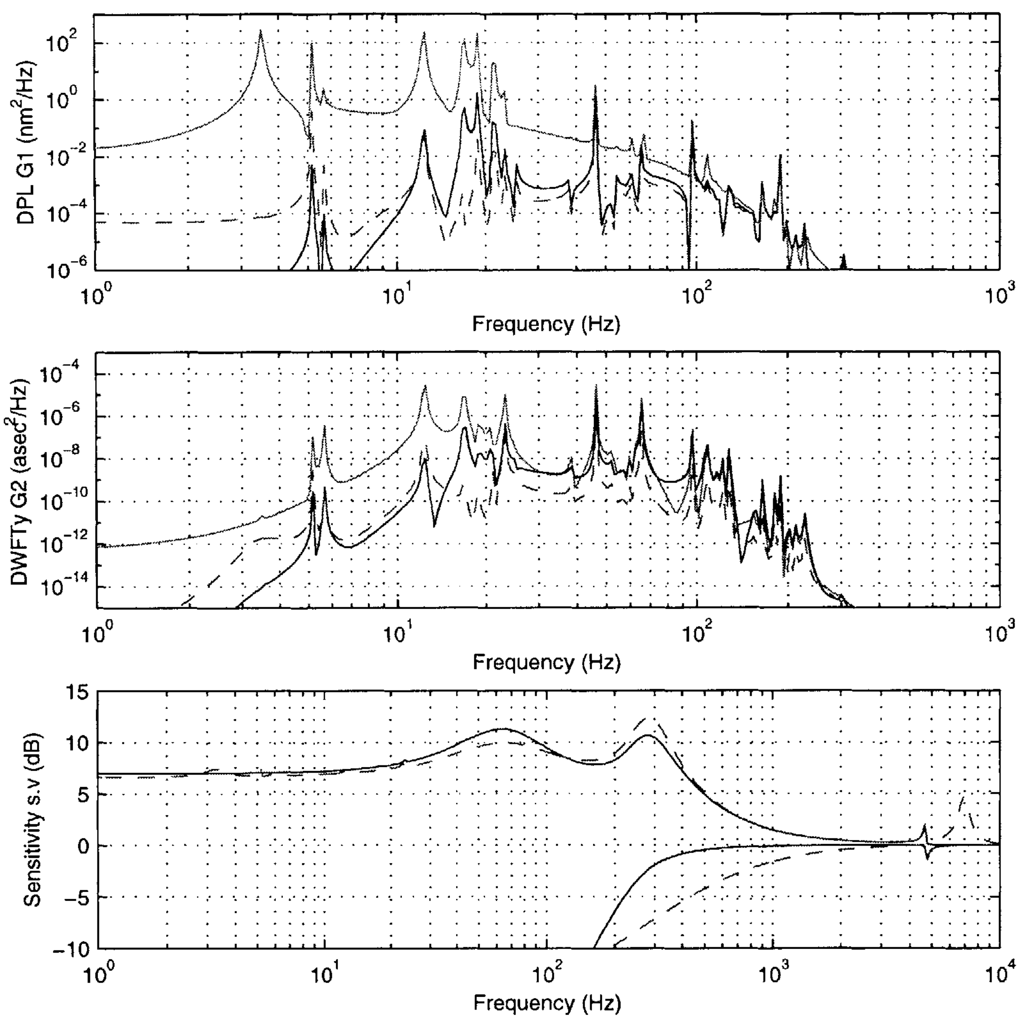

Figure 7.8 Performance and stability of final tuned controller S3. The top plot is the autospectrum of the external DPL of guide interferometer 1, the middle plot is the autospectrum of the differential wavefront tilt of guide interferometer 2, and the lower plot are the maximum and minimum singular values of the Sensitivity transfer matrix. The open loop is plotted in light solid, the baseline control case in dark solid and the tuned controller is dashed.

The performance and stability of the family of tuned controllers for the SIM model is summarized in Figure 7.9. The final design, S3 achieves the greatest performance by allowing an increase in the maximum singular value of the Sensitivity transfer matrix.

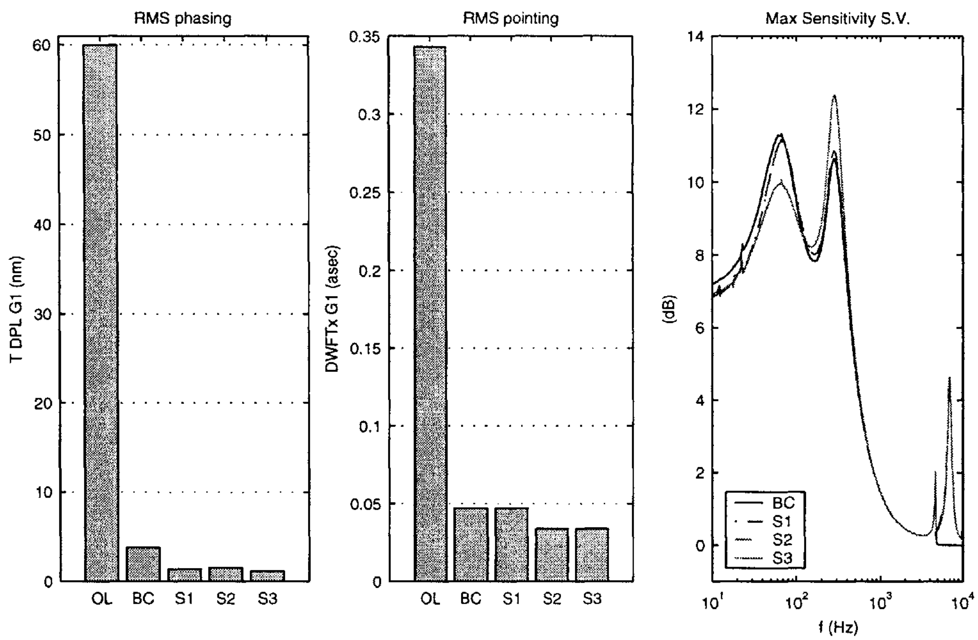

Figure 7.9 Plots of performance and maximum Sensitivity s.v. for the incremental tuned controller designs from the controller family of Figure 7.5 (following arrows on the figure). RMS phasing and pointing performance are listed.

The deviation of the tuned controller from the baseline is plotted. In Figure 7.10 the magnitudes of the baseline and S3 phasing controller transfer functions are plotted. The total DPL sensor channels are only marginally tuned while the channels that use the internal DPL are greatly modified, particularly with more low-frequency gain. Physically, the low-frequency gain of the baseline controller results from the fringe tracker control, $K_{ph,f}$, which uses only sensor measurement from the total DPL. The tuned controller improves performance without extending the bandwidth by taking greater advantage of the internal DPL measure at low frequency. Figure 7.11 plots the magnitudes of the baseline and S3 fine-pointing controller transfer functions. Aside from the addition of slight cross terms, the tuned controller improves the performance by increasing the bandwidth without increasing the low frequency gain. Taking advantage of the natural bandwidth of the actuators is essential to meeting the tight SIM control requirements.

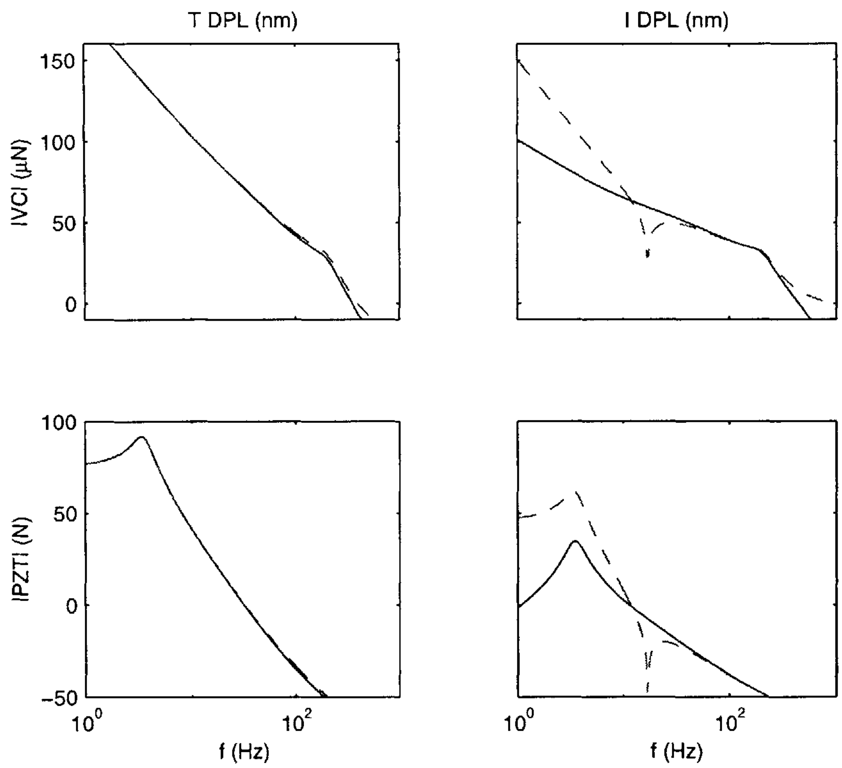

Figure 7.10 Tuned and baseline phasing controller for guide interferometer 1. The baseline controller is light solid and the tuned controller is dashed

7.6 Summary

The tuning methodology is applied to the FEM model of the SIM Classic spacecraft. The Space Interferometry Mission is introduced. The JPL-designed model is numerically conditioned and reduced with the balanced truncation algorithm of Chapter 3. The sensor/ actuator indexing algorithm of Chapter 3 is applied to the model and suggests a block structure for the baseline controller. The baseline controller is composed from a JPL-designed phasing controller and a classical fine-pointing controller designed for the thesis. The tuning methodology of Chapter 4 is applied to the baseline controller. Substantial

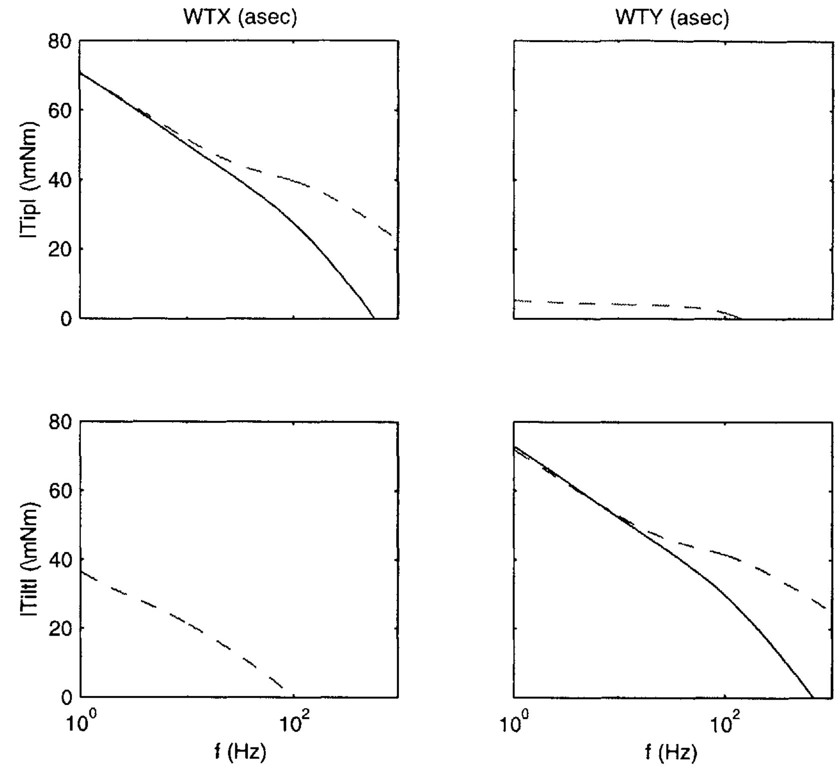

Figure 7.11 Tuned and baseline fine-pointing controller for guide interferometer 1. The baseline controller is light solid and the tuned controller is dashed

closed-loop improvements are achieved with the phasing and fine-pointing performance with little degradation in stability robustness. The phasing performance of one channel is reduced to 1.2 nm, near the requirement for parent star nulling. Insight from the tuned controller indicates the usefulness of using the internal interferometer as a low-frequency phasing sensor, and of extending the fine-pointing bandwidth. With the successful application of the tools developed in this thesis to the SIM model we demonstrate their applicability to large-order systems and to future spaceborne telescopes.

Chapter 8

CONCLUSIONS AND CONTRIBUTIONS

The concluding chapter summarizes the sensor/actuator effectiveness assessment algorithm and the tuning methodology that has been developed and experimentally validated in the preceding chapters. Special attention is given to the application of the developed techniques to future spaceborne telescopes. Major research contributions and recommendations for further work are highlighted.

8.1 Thesis Summary and Conclusions

Future spaceborne telescopes have optical performance requirements that will extend control capabilities beyond the current state-of-the-art. Non-updated FEM models and high mission cost drive the space telescope controller to be conservative and robust while the performance requirements drive the space telescope controller to have high performance. Further, conservatism constrains the controller topology and synthesis technique to have heritage to predecessor missions. There is a need for a control design technique which tunes a heritage-rich baseline controller for improved performance. The developed tuning satisfies this need. An optimization-based tuning strategy represents a compromise between a low-performance, classically-designed controller with a constrained sensor/actuator topology and a high-performance modern controller with a fully connected input/output structure. The thesis develops and experimentally applies such a control design strategy and sets it within the framework of the dynamics, modeling and control of future spaceborne telescopes.

In Chapter 2 a framework is developed for the design of controllers. Initially some notations are introduced. The use of (1) the maximum singular value of the Sensitivity transfer matrix as a conservative measure of stability robustness an (2) the inverse of the distance from the MIMO Nyquist locus to the critical point as a necessary but not sufficient measure of stability robustness are discussed. The use of both metrics are supported by previous experimental results in the Literature. The control design framework captures and organizes the design and synthesis strategy for controllers that is practiced with the experimental programs of the MIT Space Systems Laboratory. The framework structures the critical steps of control design: problem specification, plant modeling and analysis, control strategy selection and synthesis, and controller evaluation and implementation. Hardware dependent issues are highlighted. Tuning is introduced as a design iteration in the framework. Lastly, the controller tuning problem is rigorously specified.

In Chapter 3 an algorithm is presented which characterizes the effectiveness of sensor/actuator pairs for control of the open-loop plant model. The work follows some decentralized state estimation work that is included as Appendix A and some sensor/actuator placement work from the Literature. By combining metrics of modal observability and controllability with metrics of modal disturbance and performance contributions, an index can be computed for each sensor and actuator that quantifies how well an actuator can control modes that are important in the performance and how well a sensor can observe modes that are disturbed. A correction is added to account for actuators that are designed for active output isolation. These actuators are decoupled from the structure and have little controllability to important modes but have actuation bandwidth in the important frequency range. The correction uses an artificial controllability for the actuator based on its gain. It is important to capture the special case of active output isolation actuators since the optical control actuators of space telescopes tend to be of this type. The sensor/actuator effectiveness matrix is tested on a sample structure and shown to suggest a control topology with LQG performance similar to one found by a complete enumeration of all possible topologies. In future chapters the sensor/actuator index is used a a guide for selecting the topology of baseline controllers and for applying the tuning methodology.

In Chapter 4 a methodology for tuning a baseline controller is developed. The tuning strategy is a direct nonlinear optimization that iteratively computes controller parameters to improve a cost. The cost is made up of four terms: a performance penalty, a stability robustness penalty, a deviation of the baseline and tuned controller penalty, and a controller channel gain penalty. Each of the penalty terms is quantified by an expression for controller tuning with a plant design model and for tuning directly with measured plant data. Appropriate gradients with respect to the controller parameters are derived. The stability robustness penalty is captured through the proximity of the MIMO Nyquist locus to the critical point and the maximum singular value of the Sensitivity transfer matrix. A general, real, controller parameterization is developed which allows the addition of controller states and constraints on the controller sensor/actuator topology. A nonlinear minimization algorithm is described which reduces the augmented cost while maintaining a stable closed loop. Examples of applying the tuning methodology to modify the controller architecture are provided. The tuning methodology is general and need not be restricted in application to spaceborne telescopes. Limitations of a nonlinear descent approach include a dependence on the feasible space of tuned controllers parameterized from the baseline controller. With the tuning algorithm developed, the remainder of the thesis is devoted to validation.

A one-dimensional interferometer sample problem is developed in Chapter 5. The sample problem, with twelve states, a rigid-body mode, modeled optical sensors and actuators, and a modeled reaction-wheel-like disturbance is a non-trivial analogue to a future spaceborne interferometer. The effectiveness of the sensors and actuators for control was determined with the algorithm of Chapter 3 and used to guide control design. A baseline controller was classically designed and then the tuning methodology of Chapter 4 was applied to improved the closed-loop performance and stability robustness. The tuning methodology was used to add states and open sensor/actuator control channels. Additionally a second baseline controller was designed with LQG synthesis. The resulting controller was tuned to remove sensor/actuator control channels. Comparing the two tuned controllers, we find that despite a similar structure (order and sensor/actuator topology) the LQG-tuned controller achieves the same performance and stability robustness with less bandwidth. We conclude that it may be advantageous to design a global modern controller for SIM and then apply the tuning methodology to design a controller with the desired sensor/actuator topology.

The development and construction of the Origins Testbed, the first spacecraft-like test article with: (1) large-angle slew capability, (2) high-resolution optical phasing metrology with coarse and fine actuators, (3) arcsecond optical pointing, and (4) realistic spacecraft-like disturbance sources (reaction wheels), is detailed in Chapter 6. The OT is designed to capture the three elements of space telescopes operation: (1) target acquisition (slew), (2) optical alignment, and (3) observation. The sensor and actuator suite of the Origins Testbed is detailed. The sensor/actuator indexing algorithm is applied to identify sensor and actuator combinations that are effective for control. The effective sensors and actuators are grouped and a baseline controller is classically designed and experimentally implemented. The baseline slew controller provides integral control of the OT's rigid-body dynamics while the baseline optical controller achieves a 9.4 dB phasing performance improvement and a 11.8 dB pointing improvement to jitter induced by a reaction wheel windup disturbance during an observation. By applying the tuning methodology to add states and open control channels the performance could be improved to 15.8 dB in the phasing channel and 17.1 dB in the pointing channel with little degradation in stability robustness. Experimentally, the developed techniques are demonstrated to perform with physical real-world system.

With the confidence generated by the successful application of the tuning methodology to a physical spacecraft-like system, we demonstrate its applicability to a large-scale model of a future spaceborne telescope in Chapter 7. The SIM model is introduced and its numerical conditioning is improved through the removal of unnecessary states and remodeling of the disturbance source. The sensor/actuator indexing algorithm is applied to evaluate sensors and actuators for control and a classically-designed baseline controller is formed from JPL-designed attitude and phasing control and a MIT-designed fine-pointing controller. The performance of the baseline controller is analyzed and shown to achieve 24.0 dB phasing performance improvement. The baseline controller is tuned and without adding states or adversely affecting stability robustness 34.0 dB of phasing performance improvement is achieved. Similar results are achieved with the fine pointing control. The additional phasing performance results from increasing the low-frequency control gain on the internal interferometer channels. With 1.2 nm RMS phasing, the tuned controller is close to meeting the 1 nm requirement for SIM's nulling mode. With a demonstration of the developed techniques on a SIM model we hope that the techniques and insight from this thesis will practically help the engineering of future spaceborne telescopes.

All of the thesis objectives were achieved and are abridged and repeated here:

- Outline a framework for the design of controllers for lightweight flexible spacecraft.
- Develop a technique to quantify the suitability of a plant for local control, and to quantify the advantages of global control. In particular we wish to
  - Quantify the effectiveness of sensors and actuators for control,
  - Determine the incremental effect of adding sensors and actuators.
- Develop a control design technique which takes advantage of modern optimal control theory while preserving the critical mission heritage of conventional, classical control designs. The desirable features of the methodology include:
  - improvements in performance and/or stability robustness over the baseline controller,
  - an ability to control the deviation of the tuned controller from the baseline controller,
  - an ability to tune control designs using design models *and* experimentally determined measurement models,
  - an ability to quantify and take advantage of the addition of extra states to the baseline controller,

- an ability to quantify and take advantage of the enhancement of coupling in the baseline controller.

- Develop a laboratory test article which captures the relevant dynamics and control issues anticipated for future space-based lightweight, flexible spacecraft.
- Experimentally validate the control design methodology on the laboratory test article.
- Demonstrate the application of the control design methodology to an existing integrated model of the Space Interferometry Mission.

8.2 Contributions

The following unique contributions were made by meeting the thesis research objectives.

- A framework for the design of controllers for spaceborne telescopes is developed. The framework follows from experience gained from previous research and includes the steps of: defining the problem, modeling for control, determining plant couplings, selecting a control strategy, synthesizing a controller, reducing the controller order, evaluating the controller, and implementing the controller. Controller tuning is included in the framework as an iteration loop.
- An improvement to the numerical robustness of the common balanced reduction method is developed. The method is termed balanced truncation and involves truncating modes whose controllability and/or observability are below a threshold, before computing the balancing transformation matrix. An optional pre-balance improves accuracy by balancing the 2×2 modal blocks of the system individually. While conventional balancing fails, the balanced truncation algorithm is demonstrated to accurately reduce the SIM FEM model.
- An algorithm is developed for determining the effectiveness of particular actuators and sensors for the regulator control problem. A measure of modal observability (controllability) is weighted by a measure of the modal disturbance (performance) cost for each sensor (actuator). The resulting vectors are combined to compute an index for each sensor/actuator pair. The index is adjusted to account for active output isolation actuators with poor structural mode controllability but high gain in the control bandwidth. A control topology suggested by the algorithm compares favorably on a sample structure to the optimal topology found with a complete enumeration.
- A methodology is developed for tuning baseline controllers to allow trades of four control features: (1) performance, (2) stability robustness, (3) devia-

tion of the tuned controller from the baseline controller, and (4) control channel magnitudes. The baseline controller is parameterized in a general form that enables the addition of states, and the enforcement of a controller sensor/actuator topology. The tuning algorithm uses a nonlinear program to select control parameters to decrease an augmented cost with terms corresponding to a penalty for each of the four control features listed above. Each penalty term is described by a function and the corresponding gradients with respect to control parameters are derived. Penalty term expressions are developed in parallel for tuning plants characterized by a design model *or* without a model, directly on measured data. Two stability robustness metrics are developed, one which penalizes the deviation of the maximum singular value of the Sensitivity transfer matrix over a threshold, and the other which penalizes the closeness of a pass of the MIMO Nyquist locus to the critical point.

- An automated algorithm for determining closed-loop system stability directly on model data is developed. The technique automates the rules of MIMO Nyquist stability determination as plotted on a Nichols plot. If discrete frequency points are sparse near a critical point pass then a linear interpolation is used to increase the density of points and the automated stability-determination algorithm is called recursively.
- The sensor/actuator effectiveness matrix is validated as a guideline for determining effective channels for control, and linked with the tuning methodology on a one-dimensional interferometer sample problem.
- The first spacecraft-like test article with a large-angle slew capability, a 50 nm phasing metrology system, and arcsecond pointing optics in the presence of reaction-wheel induced disturbances is designed, developed and experimental tested. The test article has utility beyond validating of the techniques developed in the thesis, including: optimal slewing experiments, modeling and model updating, characterizing the interaction of the structure and reaction wheels, operating telescopes remotely and autonomously, automating optical alignment, and validating alternate control methodologies.
- The tuning methodology is experimentally validated on the Origins Testbed. Following a procedure anticipated for control design for future spaceborne telescopes a classical baseline controller is designed and then tuned. The sensor/actuator effectiveness matrix for the OT provides a guideline for tuning control channels. The tuning methodology was experimentally shown to improve closed-loop performance without affecting the stability robustness.
- The tuning methodology is applied to a large-order model of the SIM spacecraft. The SIM model is numerically conditioned. By following the guidance of the sensor/actuator effectiveness matrix the SIM baseline controller is tuned to improve the performance without affecting the stability robustness.

Successful application of the developed techniques to the large-order SIM model highlights their practical usefulness for control design.

- An optimal decentralized state estimation framework was developed. Given a plant model, a technique is suggested that, based on balanced model reduction theory, computes a local model corresponding to each sensor. The reduced models are selected to satisfy a dynamics exactness relation which allow the local models' state estimates to be combined into an optimal global model state estimate with the developed decentralized state estimator. A tool is developed that quantifies the suitability of each sensor for global state estimation through an analysis of the estimate error of the local models' global state estimates.
- Necessary conditions are derived for arbitrary-topology H_2 optimal controllers. The developed conditions extend the necessary conditions for a controller constrained to be block diagonal by augmenting the cost function with a Lagrange multiplier term that constrain particular controller input/output channels. The controller's Markov parameters are used for the topology constraint.

8.3 Recommendations for Future Work

The work of this thesis can be extended and complemented with research in a number of areas:

- A connection between the developed stability robustness metrics and model uncertainty for future spaceborne telescopes [Bourgault, 2000] should be made. With an uncertainty model for space telescopes, the inherent conservatism of the use of the MIMO Nyquist locus as a measure of stability robustness could be countered. Perform trades of computational complexity (ease of use within the tuning framework) and quality of stability robustness measure for the developed metric and conventional robustness metrics (μ, Popov) given a space telescope uncertainty model.
- The feasible set of available tuned controllers should be expanded. The nonlinear program computes controller parameters to minimize the augmented cost. The standard BFGS algorithm is modified to ensure the stepsize is chosen small enough to ensure the tuned controller maintains stability. The implication of this constrains the feasible set of available tuned controllers to be only those which stabilize the plant which are connected (through the controller parameters) to the baseline controller. Expanding the feasible set to include all stability-preserving controllers, or to allow some searching through the space of non-stability-preserving controllers would allow improved tuned designs.

- The numerical conditioning of the reduced near-modal controller parameterization could be improved by allowing alternate (*e.g.* balanced) forms. A technique which allows improved conditioning while maintaining the reduced parameter set of the near-modal form would be ideal.
- The application of the tuning methodology to an LQG-designed baseline controller for SIM should be compared to the designs tuned from SIM's classically-designed baseline controller. The one-dimensional interferometer design example demonstrated that a controller tuned from an LQG-designed baseline controller could exhibit identical performance and stability robustness but with much less bandwidth than an controller tuned from a classically-designed baseline controller with the same order and input/output structure.
- The tuning methodology should be developed directly in the discrete-time domain. Most control applications, including those anticipated for future spaceborne telescopes, implement control laws on an inherently digital real-time computer. The development in this thesis is in the continuos-time domain, and using a nonlinear least-square identification routine, the tuned continuous controllers are converted to discrete-time controllers. This final step and the loss of accuracy associated with it, can be eliminated by directly designing in the discrete domain. The conversion to the discrete domain should be straightforward since many of the tuning costs are computed as summation over discrete frequency samples.
- The controller tuning methodology should be tested for the design of controller for additional plants. The MACE reflight provides a near-term opportunity where the tuning methodology can receive its first spaceflight tests. Experimental heritage of the technique should be built.
- The dynamics of the Origins Testbed should be scaled and compared to the anticipated dynamics of future spaceborne telescopes. This scaling analysis would allows us to quantify traceability of the OT to SIM and NGST.
- The tuning methodology should be extended to allow on-line or adaptive tuning. SIM and NGST may require controller tuning while on-orbit. Two steps are suggested for extending the developed tuning technique to allow on-orbit controller updates: (1) develop a capability to stop operation of the telescope, perform identification experiments, and tune the controller directly with the measured data, off-line, and (2) develop a capability to tune on-line directly with measured data that results from normal telescope operation.
- The sensor/actuator effectiveness algorithm should be extended for determining the optimal placement of disturbances and sensors for the system identification problem. A comparison of the developed technique to conventional strain-energy techniques is warranted.

REFERENCES

[Anderson, 1993] Anderson, E. H., *Robust Placement of Actuators and Dampers for Structural Control*, Ph.D. thesis, Massachusetts Institute of Technology, SERC Report #14-93, October 1993.

[Åström et al., 1998] Åström, K. J., H Panagopoulos, and T. Hagglund, "Design of PI Controllers based on Non-Convex Optimization", *Automatica*, Vol. 34, No. 5, pp. 585-601, 1998.

[Åström and Hagglund, 1995] Åström, K. J., and T. Hagglund, *PID Controllers: Theory, Design and Tuning, 2nd Ed.*, North Carolina: Instrument Society of America, 1995.

[Åström and Wittenmark, 1990] Åström, K. J., and B. Wittenmark, *Computer Controlled Systems Theory and Design*, 2nd Ed., Prentice-Hall Inc., 1990.

[Athans and Schweppe, 1965] Athans, M., and F. C. Schweppe, *Gradient Matrices and Matrix Calculations*, MIT Lincoln Laboratory, Technical Note 1965-53, 1965.

[Balas and Packard, 1996] Balas, G. J., and A. Packard, "The structured Singular Value (μ) Framework", In *The Control Handbook,* CRC Press, 1996.

[Bazaraa et al., 1993] Bazaraa, M. S., H. D. Sherali, and C. M. Shetty, *Nonlinear Programming Theory and Algorithms, 2nd Ed.*, John Wiley & Sons, 1993.

[Bernstein, 1999] Bernstein D. S., "On Bridging the Theory/Practice Gap", *IEEE Control System*, Vol. 19, No. 6, pp. 64-70, 1999.

[Bierman, 1972] G. J. Bierman, "A Comparison of Discrete Linear Filtering Algorithms", *IEEE Transactions on Aerospace and Electronic Systems*, Vol. 9, No. 1, pp. 28-37, January 1972

[Blackwood et al., 1991] Blackwood, G. H., R. N. Jacques, and D. W. Miller, "The MIT multipoint alignment testbed: technology development for optical interferometry", SPIE Vol. 1542, *Active and Adaptive Optical Systems,* pp. 371-391, 1991.

[Bourgault, 2000] Bourgault, F., *Model Uncertainty and Performance Analysis for Precision Controlled Space Structures,* Master's thesis, Massachusetts Institute of Technology, Space Systems Laboratory, May 2000.

[Boyd and Barratt, 1991] Boyd, S. P., and C. H. Barratt, *Linear Control Design, Limits of Performance*, New Jersey: Prentice-Hall Inc., 1991.

[Boyd et al., 1988] Boyd, S. P., V. Balakrishnan, C. H. Barratt, N. M. Khraishi, X. Li, D. G. Meyer, and S. T. Norman, "A New CAD Method and Associated Architectures for Linear Controllers", *IEEE Transactions on Automatic Control,* Vol. 33, No. 3, pp. 268-283, 1988.

[Campbell et al., 1999] Campbell, M. E., J. P. How, S. C. O. Grocott, and D. W. Miller, "On-Orbit Closed-Loop Control Results for the Middeck Active Control Experiment", *Journal of Guidance, Control, and Dynamics*, Vol. 22, No. 2, pp. 267-277, 1999.

[Chao and Athans, 1996] Chao, A., and M. Athans, "Stability Robustness to Unstructured Uncertainty for Linear Time Invariant Systems", In *The Control Handbook,* CRC Press, 1996.

[Collins and Sadhukhan, 1998] Collins E. G., and D. Sadhukhan, "A comparison of descent and continuation algorithms for H_2 optimal, reduced-order control designs", *International Journal of Control*, Vol. 69, No. 5, pp 647-663, 1998.

[Colavita et al., 1999] Colavita, M. M. *et al.*, "The Palomar Testbed Interferometer", *The Astrophysical Journal*, No. 510, pp. 505-521, 1999.

[Crawley et al., 2001] Crawley, E. F., M. Campbell, S. R. Hall, *The Dynamics of Controlled Structures*, Cambridge University Press, to be published 2001.

[Davis et al., 1999] Davis, L. D., J. A. King, S. W. Greeley, D. C Hyland, "Autonomous System Identification and Control of MACE II Using the Frequency Domain Expert Algorithm", *AIAA Space Technology Conference*, Albuquerque, NM, September 1999.

[deBlonk et al., 1996] deBlonk B., H. Gutierrez, M. Ingham, S. Kenny, Y. Kim, G. Mallory, "Origins Technology Testbed: Experiment Requirements Document", MIT Space Systems Laboratory Internal Document, 1996.

[de Weck et al., 2000] de Weck, O. L., D. W. Miller, G. J. W. Mallory, and G. E. Moshier, "Integrated modeling and dynamics simulation for the Next Generation Space Telescope (NGST)", SPIE Astronomical Telescopes and Instrumentation Conference, Munich, March 2000.

[Finney and Heck, 1995] Finney, J. D. and B. S. Heck, "Matrix Scaling for Large-Scale System Decomposition", *Proc. American Control Conference*, Seattle WA, June 1995.

[Freudenberg et al., 1982] Freudenberg, J. S., D. P. Looze, and J. B. Cruz, "Robustness analysis using singular value sensitivities", *International Journal of Control,* Vol. 35, No. 1, 1982.

[Freudenberg and Looze, 1985] Freudenberg, J. S., and D. P. Looze, "Right Half Plane Poles and Zeros and Design Tradeoffs in Feedback Systems", *IEEE Transactions on Automatic Control,* Vol. 30, No. 6, pp. 555-565, 1985.

[Gawronski and Lim, 1996] Gawronski, W., and K. B. Lim, "Balanced Actuator and Sensor Placement for Flexible Structures", *International Journal of Control*, Vol. 65, No. 1, pp. 131-125, 1996.

[Gelb, 1974] Gelb, A., Ed., *Applied Optimal Estimation*, MIT Press, 1974.

[Giesy and Lim, 1993] Giesy, D. P., and K. B. Lim, "H_∞ Norm Sensitivity Formula with Control System Design Applications", *Journal of Guidance, Control, and Dynamics*, Vol. 16, No. 6, pp. 1138-1145, 1993.

[Glaese, 1994] Glaese, R. M., *Development of Zero-Gravity Structural Control Models from Analysis and Ground Experimentation*, Master's thesis, Massachusetts Institute of Technology, January 1994. SERC Report #3-97.

[Grocott et al., 1997] Grocott, S. C. O., J. P. How, and D. W. Miller, "Experimental Comparison of Robust H_2 Control Techniques for Uncertain Structural Systems", *Journal of Guidance, Control and Dynamics*, Vol. 20, No. 3, pp. 611-614, 1997.

[Grocott, 1994] Grocott, S. C. O., *Comparison of Control Techniques for Robust Performance on Uncertain Sructural Systems*, S.M. thesis, Massachusetts Institute of Technology, January 1994, SERC Report #2-94.

[Gupta, 1980] Gupta, N. K., "Frequency-Shaped Cost Functionals: Extension of Linear-Quadratic-Gaussian Design Methods", *Journal of Guidance and Control*, Vol. 3, No. 6, pp. 529-535, 1980.

[Gutierrez, 1999] Gutierrez, H. L., *Performance Assessment and Enhancement of Precision Controlled Structures During Conceptual Design,* Ph.D. thesis, Massachusetts Institute of Technology, February 1999, SERC Report #1-99.

[Hamdan and Nayfeh, 1989] Hamdan, A. M. A., and A. H. Nayfeh, "Measures of Modal Controlability and Observability for First- and Second-Order Linear Systems", *Journal of Guidance and Control*, Vol. 12, No. 3, pp. 421-428, 1989; and *Journal of Guidance and Control*, Vol. 12, No. 5, pp. 768, 1989.

[Hassibi et al., 1999] Hassibi A., J. P. How, and S. P. Boyd, "Low-Authority Controller Design by Means of Convex Optimization" *Journal of Guidance and Control*, Vol. 22, No. 6, pp. 862-872, 1999.

[Hillier and Lieberman, 1995] Hillier, F. S., and G. J. Lieberman, *Introduction to Operations Research*, Sixth Edition, McGraw Hill, 1995.

[Hjalmarsson et al., 1998] Hjalmarsson, H., M. Gevers, S. Gunnarsson, and O. Lequin, "Iterative Feedback Tuning: Theory and Applications", IEEE Control Systems, Vol. 18, No. 4, pp. 26-41, 1998.

[Henderson et al., 1998] Henderson, T. C., M. D. Piedmonte, L. K. McGovern, J.-W. Jang, B. V. Lintereur, *Structural Control Toolbox*, Draper Laboratory Report, CSDL-R-2804, November 1998.

[Ho et al., 1998] Ho, W. K., K. W. Lim, and W. Xu, "Optimal Gain and Phase Margin Tuning for PID Controllers", *Automatica*, Vol. 34, No. 8, pp. 1009-1014, 1998.

[Horn and Johnson, 1985] Horn R. A., and C. R. Johnson, *Matrix Analysis*, Cambridge University Press, 1985.

[How, 1993] How, J. P., *Robust Control Design with Real Parameter Uncertainty using Absolute Stability Theory*, Ph.D. thesis, Massachusetts Institute of Technology, SERC Report #1-93, January 1993.

[Hyland and Bernstein, 1984] Hyland, D. C., and D. S. Bernstein, "The optimal projection equations for fixed-order dynamic compensation", *IEEE Transactions on Automatic Control,* Vol. 29, No. 11, pp. 1034-1037, 1984.

[Jacques, 1995] Jacques, R. N., *On-line System Identification and Control Design for Flexible Structures*, Ph.D. thesis, Massachusetts Institute of Technology, SERC Report #3-95, May 1995.

[Johansson et al., 1998] Johansson, K. H., B. James, G. F. Bryant, and K. J. Åström, "Multivariable Controller Tuning", *Proceedings of the American Control Conference*, Philadelphia, PA, pp. 3514-3518, June 1998.

[Joshi, 1999] Joshi. S. S., "The Need for a Systems Perspective in Control Theory and Practice", *IEEE Control System*, Vol. 19, No. 6, pp. 56-63, 1999.

[Kim and Junkins, 1991] Y. Kim and J. L. Junkins, "Measure of Controllability for Actuator Placement", *Journal of Guidance and Control*, Vol. 14, No. 5, pp. 895-902, 1991.

[Kwakernaak and Sivan, 1972] Kwakernaak, H., and R. Sivan, *Linear Optimal Control Systems*, John Wiley & Sons, Inc., 1972

[Lehtomaki et al., 1981] Lehtomaki N. A., N. R. Sandell, and M. Athans, "Robustness Results in Linear-Quadratic Gaussian Based Multivariable Control Designs", *IEEE Transactions on Automatic Control,* Vol. 26, No. 1, pp. 75-93, 1981.

[Lim, 1992] Lim, K. B., "Method for Optimal Actuator and Sensor Placement for Large Flexible Structures", *Journal of Guidance and Control*, Vol. 15, No. 1, pp. 49-57,

1992.

[Lin, 1996] Lin, C. Y., *Towards Optimal Strain Actuated Aeroelastic Control*, Ph.D. thesis, Massachusetts Institute of Technology, February 1996.

[Lintereur, 1998] Lintereur, B. V., *Constrained H_2 Design via Convex Optimization with Application*, S.M. thesis, Massachusetts Institute of Technology, May 1998.

[Looze and Freudenberg, 1996] Looze, D. P., and J. S. Freudenberg, "Tradeoffs and Limitations in Feedback Systems", In *The Control Handbook,* CRC Press, 1996.

[Lublin 1992] Lublin, L., *Multivariable Stability Robustness for Control of Flexible Beams and Trusses*, S.M. thesis, Massachusetts Institute of Technology, SERC Report #6-92, May 1992.

[Lublin and Athans, 1995] Lublin, L. and M. Athans, "An Experimental Comparison of H_2 and H_∞ Designs for an Interferometer Testbed", in *Lecture Notes in Control and Information Sciences: Feedback Control, Nonlinear Systems, and Complexity* (B. Francis, and A. Tannedaum, eds.), Springer-Verlag, 1995.

[Lublin et al., 1996] Lublin L., S. Grocott, and M. Athans, "H_2 and H_∞ Control", In *The Control Handbook,* CRC Press, 1996.

[Ly et al., 1985] Ly, U.-L., A. E. Bryson, and R. H. Cannon, "Design of Low-order Compensators using Parameter Optimization", *Automatica*, Vol. 21, No. 3, pp. 315-318, 1985.

[Ly, 1998] Ly, U.-L., *Multivariable Control System Design Using Nonlinear Programming*, Department of Aeronautics and Astronautics Report, University of Washington, Seattle WA, 1998.

[Maghami and Joshi, 1993] Maghami, P. G. and S. M. Joshi, "Sensor-Actuator Placement for Flexible Structures with Actuator Dynamics", *Journal of Guidance and Control*, Vol. 16, No. 2, pp. 301-307, 1993.

[Mallory and Miller, 1999] Mallory, G. J. W., and D. W. Miller, "Control Design for Future Space Based Telescopes: A Classical / Modern Approach", *18th IASTED Conference on Modeling, Identification and Control*, Innsbruck, Austria, February 1999.

[Mallory et al., 2000] Mallory, G. J. W., A. Saenz-Otero, and D. W. Miller, "The Origins Testbed: capturing the dynamics and control of future space-based telescopes", accepted for publication in *Optical Engineering*, June 2000.

[Mallory and Miller, 2000] Mallory, G. J. W., and D. W. Miller, "Decentralized State Estimation for Flexible Space Structures", accepted for publication in *Journal of*

Guidance and Control, 2000.

[Mallory et al., 1998] Mallory, G. J. W., H. L. Gutierrez, and D. W. Miller, "MIT Origins Testbed: Initial Control Results", *21st AAS Guidance and Control Conference*, Breckenridge, CO, February 1998.

[Masters, 1997] Masters, B., *Evolutionary Design of Controlled Structures*, Ph.D. thesis, Massachusetts Institute of Technology, April 1997. SERC Report #1-97.

[Masterson, 1999] Masterson, R. A., *Development and Validation of Empirical and Analytical Reaction Wheel Disturbance Models*, Master's thesis, Massachusetts Institute of Technology, June 1999. SERC Report #4-99.

[MacMartin et al., 1991] MacMartin, D. G., S. R. Hall, and D. S. Bernstein, "Fixed Order Multi-Model Estimation and Control", *Proceedings of the American Control Conference*, Boston, MA, June 1991.

[McCasland, 1989] W. N. McCasland, *Sensor and Actuator Selection for Fault-Tolerant Control of Flexible Structures*, Ph.D. thesis, Massachusetts Institute of Technology, February 1989.

[McGovern, 1996] McGovern, L. K., *A Constrained Optimization Approach to Control with Application to Flexible Structures*, Ph.D. thesis, Massachusetts Institute of Technology, May 1996.

[Melody and Neat, 1999] Melody, J. W., and G. W. Neat, "Validation of an Integrated Modeling Methodology's Closed-Loop Performance Prediction Capability" *Journal of Guidance, Control, and Dynamics*, Vol. 22, No. 4, pp. 566-572, 1999.

[Mercadal, 1991] Mercadal, M., "Homotopy Approach to Optimal, Linear Quadratic Fixed Architecture Compensation" *Journal of Guidance, Control, and Dynamics*, Vol. 14, No. 6, pp. 1224-1233, 1991.

[Miller and Mallory, 1998] Miller, D. W., and G. J. W. Mallory, "Control Testbeds and Flight Demonstration: Transitioning Theory to Application", *Proceedings of the American Control Conference*, Philadelphia, PA, pp. 873-878, June 1998.

[Miller et al., 1996] Miller D. W., E. F. Crawley, J. P. How, K. Liu, M. E. Campbell, S. C. O. Grocott, R. M. Glaese, T. D. Tuttle, G. Stover, J. A. Woods-Vedeler, J. deLuis, E. Bokhour, R. Grimes, K. Scholle, C. Krebs, and R. Renshaw, "The Middeck Active Control Experiment (MACE): Summary Report", June 1996, SERC Report #7-96.

[Miotto, 1997] Miotto, P., *Fixed Structure Methods for Flight Control Analysis and Automated Gain Scheduling*, Ph.D. thesis, Massachusetts Institute of Technology,

June 1997.

[Moore, 1981] Moore, B. C., "Principal Component Analysis in Linear Systems: Controllability, Observability, and Model Reduction", *IEEE Transactions on Automatic Control*, Vol. AC-26, No. 1, pp. 17-32, 1981.

[Mutambara, 1998] Mutambara, A. G. O., *Decentralized Estimation and Control for Multisensor Systems*, CRC Press, 1998.

[Narendra and Annaswamy, 1989] Narendra, K. S., and A. M. Annaswamy, *Stable Adaptive Systems*, Prentice-Hall Inc., 1989.

[Neat and O'Brien, 1996] Neat, G. W., and J. F. O'Brien, "Micro-Precision Interferometer Testbed: Fringe Tracker Control System", *19th AAS Guidance and Control Conference*, Breckenridge, CO., February 1996.

[Neat et al., 1997] Neat, G. W., A. Abramovici, J. W. Melody, R. J. Calvet, N. M. Nerheim, J. F. O'Brien, "Control Technology Readiness for Spaceborne Optical Interferometer Missions", *The Space Microdynamics and Accurate Control Symposium*, Toulouse, France, May 1997.

[O'Brien and Neat, 1995] O'Brien, J. F., and G. W. Neat, "Micro-Precision Interferometer: Pointing Control System", *4th IEEE Conference on Control Applications*, Albany, NY, September 1995.

[Ogata, 1990] Ogata, K., *Modern Control Engineering*, Prentice Hall Inc., 1990

[Okada and Skelton, 1990] Okada, K., and R. E. Skelton, "Sensitivity Controller for Uncertain Systems", *Journal of Guidance, Control, and Dynamics*, Vol. 13, No. 2, pp. 321-329, 1990.

[O'Neal and Spanos, 1991] O'Neal M., and J. T. Spanos, "Optical pathlength control in the nanometer regime on the JPL phase B interferometer testbed", SPIE Vol. 1542, *Active and Adaptive Optical Systems*, pp. 359-370, 1991.

[Peebles, 1987] Peebles, P. Z., Jr., *Probability, Random Variables, and Random Signal Principles*, 2nd Ed., McGraw-Hill, 1987.

[Polak and Salcudean, 1989] Polak E., and S. E. Salcudean, "On the Design of Linear Multivariable Feedback Systems Via Constrained Nondifferentiable Optimization in H^{∞} Spaces", *IEEE Transactions on Automatic Control*, Vol. 34, No. 3, pp. 268-276, 1989.

[Press et al., 1992] Press, W. H., S. A. Teukolsky, W. T. Vetterling, and B. P. Flannery, *Numerical Recipes in C*, 2nd Edition, Cambridge University Press, 1992.

[Richter and Collins, 1989] Richter, S., and E. G. Collins, "Square Root Parallel Kalman

Filtering Using Reduced-Order Local Filters" *IEEE Conference on Decision and Control*, Vol. 1, pp. 506-511, 1989.

[Roy et al., 1991] Roy, S., R. H. Hashemi, and A. J. Laub, "Square Root Parallel Kalman Filtering Using Reduced-Order Local Filters", *IEEE Transactions on Aerospace and Electronic Systems*, Vol. 27, No. 2, pp. 276-289, March 1991.

[Safanov and Tsao, 1997] Safanov, M. G., and T.-C. Tsao, "The Unfalsified Control Concept and Learning", *IEEE Transactions on Automatic Control,* Vol. 42, No. 6, pp. 843-847, June 1997.

[Sandell et al., 1978] Sandell Jr., N. R., P. Varaiya, M. Athans, and M. G. Safanov, "Survey of Decentralized Control Methods for Large Scale Systems", *IEEE Transactions on Automatic Control*, Vol. AC-23, No. 2, pp. 108-128, April 1978.

[Skelton and Chiu, 1983] Skelton R. E. and D. Chiu, "Optimal Selection of Inputs and Outputs in Linear Stochastic Systems", *Journal of Astronautical Sciences*, Vol. XXXI, pp. 399-414, 1983.

[Skelton and DeLorenzo, 1983] Skelton, R. E. and M. L. DeLorenzo, "Selection of Noisy Actuators and Sensors in Linear Stochastic Systems", *Large Scale Systems Theory and Applications*, Vol. 4, pp. 109-136, 1983.

[Skelton and Hughes, 1980] Skelton, R. E. and P. C. Hughes, "Modal Cost Analysis for Linear Matrix-Second-Order Systems", *Journal of Dynamics, Measurement and Control*, Vol. 102, pp. 151-158, 1980.

[Slotine and Li, 1991] Slotine, J.-J., and W. Li, *Applied Nonlinear Control*, Prentice Hall Inc., 1991.

[Sparks and Juang, 1992] Sparks, D. W., and J. Juang, "Survey of Experiments and Experimental Facilities for Control of Flexible Structures", *Journal of Guidance, Control, and Dynamics*, Vol. 15, No. 4, pp. 801-816, 1992.

[Stewart and Sun, 1990] Stewart, G. W., and J.-G. Sun, *Matrix Perturbation Theory*, Academic Press, Inc., 1990.

[Sun, 1988] Sun, J.-G., "A Note on Simple Non-Zero Singular Values", *Journal of Computational Mathematics*, Vol. 6, No. 3, pp. 258-266, July 1988.

[Unwin et al., 1999] Unwin, S. C., R. Danner, S. G. Turyshev. M. Shao, "Science with the Space Interferometry Mission", *SIM Taking the Measure of the Universe*, JPL Report, NASA, 1999.

[Vadali et al., 1995] Vadali S.R., M. T. Carter, T. Singh, and N. S. Abhyankar, "Near-Minimum-Time Maneuvers of Large Structures: Theory and Experiments", *Jour-*

nal of Guidance, Control and Dynamics, Vol. 18, No. 6, pp. 1380-1385, 1995.

[Van de Vegte, 1990] Van de Vegte, J., *Feedback Control Systems*, Prentice Hall Inc., 1990.

[Woodley et al., 1999] Woodley, B. R., J. P. How and R. L. Kosut, "Direct Unfalsified Controller Design - Solution Via Convex Optimization", *Proceedings of the American Control Conference*, San Diego, CA, pp. 3302-3306, June 1999.

[Youla et al., 1976] Youla, D. C., H. A. Jabr, and J. J. Bongiorno, "Modern Wiener-Hopf design of optimal controllers: part II", *IEEE Transactions on Automatic Control*, Vol. AC-21, No. 3, pp. 319-338, June 1976.

[Zhou et al., 1996] Zhou, K., J. C. Doyle, and K. Glover, *Robust and Optimal Control*, Prentice Hall Inc., 1996.

Appendix A

DECENTRALIZED STATE ESTIMATION

In Chapter 3 techniques for breaking a system up into a set of reduced-order local models is presented. This allows the global control problem to be broken up into a set of simpler local control problems. Despite the decentralized control, certain high-level monitoring tasks such a fault detection and isolation may require a global estimate of the system's state. The development in this appendix allows the state estimates of reduced-order local models to be fused into the optimal global state estimate. A slight restriction on the form of the reduced-order models is required and is satisfied by the reduced-order model determination technique of Section 3.1.2. The development of the decentralized state estimator is a condensed version of that presented in [Mallory and Miller, 2000].

Given a linear system and the correct system model, a Kalman filter provides the state estimate which minimizes the root-mean-squared error. This global Kalman filter must use the full-state system model, and it must have access to the noisy measurements from all sensors. In certain large-scale systems, the high order of the system and the large number of sensors can make the traditional global estimator intractable. Complete communication of all sensor information can be expensive. The problem is further compounded by geographically separated sensors, as in, for example, a power network, or multiple scanning sensors in a multiple target radar tracking problem. The high system order and strict requirement on sensor communication favor a decentralized estimation approach.

Decentralized estimation involves the estimation of the state at each sensor node. Each node is assumed to have an associated local model and a processor. The i-th node estimate is updated from only measurements generated at the i-th node in the completely decentralized case, but more generally some internodal communication may be allowed.

A.1 Global Estimators

Consider the state estimation problem posed for the continuous system given by Equation 2.3,

$$\begin{aligned} \dot{x}(t) &= A(t)x(t) + B_w(t)w(t) \\ y(t) &= C_y(t)x(t) + D_{yw}(t)w(t) \end{aligned} \tag{A.1}$$

where, without loss of generality, we continue our development without the control input, u. Further, we allow the system to be linear time-varying. Since decentralized estimation is performed on a real-time computer, and further to preserve the decoupling of the traditional predict and update cycles, we develop the decentralized estimator for a discrete-time system. Thus we transform Equation A.1 to discrete-time [Åström and Wittenmark, 1990] to arrive at,

$$\begin{aligned} x(k) &= A(k)x(k) + B_w(k)w(k) \\ y(k) &= C_y(k)x(k) + n(k) \end{aligned}, \tag{A.2}$$

where the state-space matrices are the discrete-time equivalent of those introduced in Equation A.1. The state initial condition, $x_0 \sim N(\overline{x_0}, P_0)$, is a normal white noise process of mean $\overline{x_0}$ and symmetric, positive-definite covariance, P_0. Similarly, $w(k) \sim N(0, \Xi(k))$ is the process noise and $n(k) \sim N(0, \Theta(k))$ is the sensor noise. $w(k)$ and $n(k)$ are assumed independent from each other, and from the initial condition, x_0.

A.1.1 Kalman Filter

The Kalman filter is a global state estimator which provides the RMS optimal estimate of the state. Given the system model of Equation A.2, the discrete Kalman filter [Gelb, 1974] is generated by,

$$\hat{x}(k+1|k) = A(k)\hat{x}(k) \tag{A.3}$$

$$P_m(k+1) = A(k)P(k)A^T(k) + B_w(k)\Xi(k)B_w^T(k) \tag{A.4}$$

forming the predict cycle, and,

$$\hat{x}(k+1) = \hat{x}(k+1|k) + K(k+1)[y(k+1) - C_y(k+1)\hat{x}(k+1|k)] \tag{A.5}$$

$$\begin{aligned} P(k+1) &= [I - K(k+1)C_y(k+1)]P_m \\ &= P_m - P_mC_y(k+1)[C_y(k+1)P_mC_y{}^T(k+1) + \Theta(k+1)]^{-1}C_y(k+1)P_m \end{aligned} \tag{A.6}$$

$$\begin{aligned} K(k+1) &= P(k+1)C_y^T(k+1)\Theta^{-1}(k+1) \\ &= P_mC_y^T(k+1)[C_y(k+1)P_mC_y^T(k+1) + \theta(k+1)]^{-1} \end{aligned} \tag{A.7}$$

forming the measurement update cycle. In Equation A.6, we drop the index of the $k + 1$ predict cycle state estimate error covariance $P_m = P(k+1|k)$.

A.1.2 Information Filter

The information filter is an alternate form of the Kalman filter [Mutambara, 1998]. It is algebraically equivalent to the Kalman filter, producing the optimal state estimate and covariance matrix at each time step. More accurately, an information matrix is generated at each step, and is defined by the relation,

$$L(i|j) \equiv P^{-1}(i|j) \tag{A.8}$$

where $P(i|j)$ is the i-th error covariance, given the j-th measurement. This information matrix has the property that when it is large then we have much information about the state, and that the state estimate is good. The information state is defined from the system state with the transformation:

$$l(i|j) \equiv L(i|j)x(i|j). \tag{A.9}$$

We begin the derivation of the information filter by defining the invertible term,

$$S(k) = C_y(k)P_m(k)C_y^T(k) + \Theta(k) \tag{A.10}$$

and rewriting a term of Equation A.6 as

$$\begin{aligned} I - KC_y &= (I - KC_y)P_mP_m^{-1} \\ &= (P_m - KSS^{-1}C_yP_m)P_m^{-1} \end{aligned} \tag{A.11}$$

where, for simplicity, the index dependence has been suppressed. Now, we substitute Equation A.7 for K to write

$$\begin{aligned} I - KC_y &= (P_m - P_mC_y^TS^{-1}C_yP_m)P_m^{-1} \\ &= PP_m^{-1} \end{aligned}. \tag{A.12}$$

Rewriting Equation A.5 and substituting Equation A.7 results in,

$$\begin{aligned} \hat{x}(k+1) &= (I - KC_y)\hat{x}(k+1|k) + Ky(k+1) \\ &= PP_m^{-1}\hat{x}(k+1|k) + Ky(k+1) \end{aligned} \tag{A.13}$$

by multiplying by P^{-1}, and substituting Equation A.7 for K, we can rewrite in terms of information variables as,

$$\hat{l}(k+1) = \hat{l}(k+1|k) + C_y^T\Theta^{-1}y(k+1) \tag{A.14}$$

By applying the Matrix Inversion Lemma to Equation A.6 we can write,

$$P^{-1}(k+1) = P_m^{-1} + C_y^T\Theta^{-1}C_y \tag{A.15}$$

By substituting the information definitions into Equation A.3 and Equation A.4, we can write for the predict cycle of the information filter

$$\hat{l}(k+1|k) = L_m A(k) L(k) \hat{l}(k), \tag{A.16}$$

$$L_m = [A(k)L(k)^{-1}A^T(k) + B_w(k)\Xi(k)B_w^T(k)]^{-1} \tag{A.17}$$

and for the update cycle,

$$\hat{l}(k+1) = \hat{l}(k+1|k) + C_y^T(k+1)\Theta^{-1}(k+1)y(k+1), \tag{A.18}$$

$$L(k+1) = L_m + C_y^T(k+1)\Theta(k+1)C_y(k+1). \tag{A.19}$$

The information filter has a simpler (from a computational point of view) update cycle than the traditional Kalman filter, but suffers from a more complex predict cycle.

A.2 Decentralized State Estimator

We develop a decentralized filter which is a hybrid of the Kalman and information filter, derived from combining two filters presented in [Roy et al., 1991]. Consider the measurement vector, $y = \begin{bmatrix} y_1 & y_2 & \dots & y_q \end{bmatrix}^T$, where we have partitioned the vector into a column of single sensor measurements. The development holds equally for multiple sensor partitions. The output equation is thus partitioned as $C_y = \begin{bmatrix} C_{y1}^T & C_{y2}^T & \dots & C_{yq}^T \end{bmatrix}^T$ and the sensor noise as $n = \begin{bmatrix} n_1 & n_2 & \dots & n_q \end{bmatrix}^T$. We make the assumption that each sensor has an independent noise process, and thus, the sensor noise covariance can be decoupled as $\Theta = \text{diag}\{\Theta_1, \Theta_2, \dots, \Theta_q\}$.

The assumption of independent sensor noises allows us to decentralize the update (measurement) cycle of the Kalman filter while maintaining local estimates which can be globally recombined into the optimal state estimates. The assumption of independent sensor noise is valid if the sensors indeed generate their own noise, in the form of quantization error for example, but does not hold if the sensor noise is generated by some underlying process.

Assume we have the i-th local model, corresponding to the y_i measurement. The local model of order m_i is given by,

$$\begin{aligned} x_i(k+1) &= A_i(k)x_i(k) + B_{wi}(k)v(k) \\ y_i(k) &= c_i(k)x_i(k) + n_i(k) \end{aligned} . \tag{A.20}$$

The local models may be formed using the balanced reduction techniques of Chapter 3. For the measurement equation to hold we must have

$$C_{yi}(k)x(k) = c_i(k)x_i(k) \tag{A.21}$$

which is a type of *dynamics exactness relation* [Sandell et al., 1978].

A.2.1 Local Model State Estimation

At the i-th local node, we implement an optimal local filter, combining elements of the Kalman and information filter, resulting in a predict cycle given by,

$$\hat{x}_i(k+1|k) = A_i(k)\hat{x}_i(k), \tag{A.22}$$

$$P_{mi}(k+1) = A_i(k)P_i(k)A_i^T(k) + B_{w_i}(k)\Xi(k)B_{w_i}^T(k), \tag{A.23}$$

and a local measurement update cycle given by,

$$\hat{l}_i(k+1) = \hat{l}_i(k+1|k) + c_i^T(k+1)\Theta_i^{-1}(k+1)y_i(k+1) \tag{A.24}$$

$$F_i(k+1) = F_{mi} + c_i^T(k+1)\Theta_i(k+1)c_i(k+1) \tag{A.25}$$

where we have substituted our appropriate i-th local model parameters into the global optimal filter. The information matrices and covariance matrices are related by $Y_i(k) = P_i^{-1}(k)$ and $Y_{mi}(k) = P_{mi}^{-1}(k)$.

A.2.2 Decentralized Global State Estimator

With the partition of measurements, we can rewrite Equation A.18 for the global information update as

$$\begin{aligned}\hat{l}(k+1) &= \hat{l}(k+1|k) + \left[C_{y1}^T \ \dots \ C_{yq}^T\right] \mathrm{diag}\{\Theta_1^{-1}, \dots, \Theta_q^{-1}\} \left[y_1 \ \dots \ y_q\right]^T \\ &= \hat{l}(k+1|k) + \sum_{i=1}^{q} C_{yi}^T(k+1)\Theta_i^{-1}(k+1)y_i(k+1)\end{aligned} \tag{A.26}$$

We assume the following relation holds between the i-th global output vector, C_i, and the i-th local output vector, c_i:

$$C_{yi}(k) = c_i(k)T_{ci}(k). \tag{A.27}$$

If the local and global state are related through the transformation $x_i(k) = T_i(k)x(k)$, and the transformation has a unique pseudo-inverse, $T_i^{\dagger}$, then by using Equation A.21, we have $T_{ci}(k) = T_i(k)$. If the state transformation does not have a unique pseudo-inverse, then we can often use $T_{ci}(k) = c_i^{\dagger}(k)C_{yi}(k)$, where the right pseudo-inverse of c_i has been used. Since we have decoupled single sensors, such that C_{yi} has full row rank, then we can find a relation, T_{ci}, such that Equation A.27 holds.

Substituting Equation A.27 into Equation A.26 we have

$$\hat{l}(k+1) = \hat{l}(k+1|k) + \sum_{i=1}^{q} T_{ci}^T(k+1)c_i^T(k+1)\Theta_i^{-1}(k+1)y_i(k+1). \tag{A.28}$$

Substituting Equation A.24 results in

$$\hat{l}(k+1) = \hat{l}(k+1|k) + \sum_{i=1}^{q} T_{ci}^T(k+1)[\hat{l}_i(k+1) - \hat{l}_i(k+1|k)], \tag{A.29}$$

a decentralized version of Equation A.18.

Using a similar approach we write Equation A.19 as,

$$\begin{aligned} L(k+1) &= L_m + \sum_{i=1}^{q} C_{yi}^T(k+1)\Theta_i(k+1)C_{yi}(k+1) \\ &= L_m + \sum_{i=1}^{q} T_{ci}^T(k+1)c_i^T(k+1)\Theta_i(k+1)c_i(k+1)T_{ci}(k+1) \end{aligned} \tag{A.30}$$

which, when we substitute Equation A.25 results in

$$L(k+1) = L_m(k+1) + \sum_{i=1}^{q} T_{ci}^T(k+1)[L_i(k+1) - L_{mi}(k+1)]T_{ci}(k+1) \tag{A.31}$$

Equation A.29 and Equation A.31 are decentralized measurement update equations in information form. This filter preserves the optimality of the global estimator. To recover the decentralized measurement update equations in conventional notation, it is a matter of substituting conventional states and covariance matrices for the information state and the information matrices respectively. It should be noted that compared with other techniques, this decentralized filter sacrifices local estimate performance, to allow the recovery of the optimal global estimate.

We note that each local Kalman filter must pass two information state variables, $\hat{l}_i(k+1)$ and $\hat{l}_i(k+1|k)$, both of size, $m_i \times 1$, as well as two information matrices, $L_i(k+1)$ and $L_i(k+1|k)$, both of size $m_i \times m_i$. Of course symmetry of the information matrix requires that only a triangular partition be passed. If the filter is implemented with conventional variables, we must pass the corresponding system state and covariance matrices. This filter is advantageous since it passes data one-way, from the local estimators to the fusion center.

The filter is only partially decentralized. The local estimates are recombined in the measurement update cycle, but the predict cycle still requires the use of Equation A.3 and Equation A.4. In the special case where the process noise decouples in analogous way to our assumption of measurement noise decoupling, i.e., $\Xi = \text{diag}\{\Xi_1, \Xi_2, \ldots\Xi_m\}$, and further we have

$$x_i(k+1) = A_i(k)x_i(k) + B_{w,i}(k)w_i(k) \tag{A.32}$$

with independent local process noises, w_i, then further decentralization of the time update equation can be achieved [Roy et al., 1991]. However, decoupling the process noise is not a valid assumption in flexible space-structure applications. For example, the reaction wheels of a space telescope are the primary disturbance source, and their effect can be observed by all system sensors. Thus, when local models are formed, the individual process noises are strongly correlated.

To summarize, as long as we choose local models such that Equation A.27 is satisfied, then through Equation A.29 and Equation A.31 we maintain a way to combine the local estimates into an optimal global estimate. Figure A.1 is a schematic of the recombination of local estimates into the global estimate.

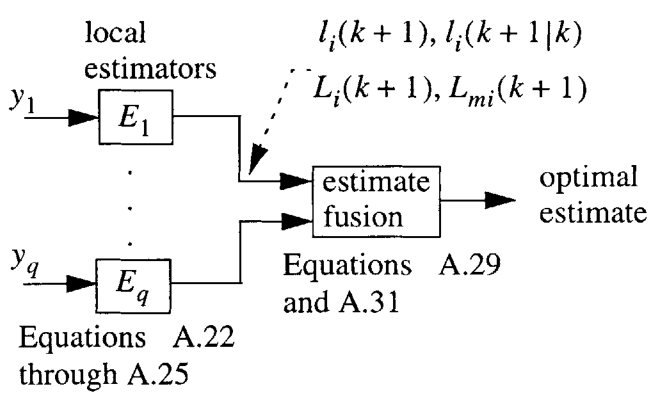

Figure A.1 Recovering optimal estimates from local estimates

The developed estimator allows us to obtain a local estimate of the state at each sensor node which could be used by a local controller. If the global estimate is required, one-way communication from the sensor nodes to the central estimator allows recovery of the optimal global estimate. By computing the number of multiplications at each time-step, the traditional Kalman filter and the developed decentralized filter can be compared in terms of computational complexity. Following the development of [Bierman, 1972] the number of computations per-cycle for both methods can be compared. The decentralized filter requires more total computations since local estimates must be computed along with the global estimate. If we assume the local estimates are computed on parallel processors, then most multiplications take place at the estimation fusion processor. For a standard implementation, the decentralized central processor requires marginally more computations than the global optimal filter. Other computation algorithms exist (e.g. square-root methods), and thus numerical complexity is more a function of implementation than of method.

A.3 Local Model Selection

We now develop a technique for selecting local models. The technique is founded on model-reduction. The local models are not optimal, but are selected using a sound engineering method which we will later demonstrate applies to large-scale physical systems and in particular to flexible space structures. One technique uses physical coordinates for selecting reduced-order models for decentralized estimation [Mutambara, 1998]. A problem with this method is that large-scale systems are rarely described by physical models. They are typically described with a reduced-order FEM. Other techniques, such as ε-decomposition to extract local dynamics based on the size of elements of the A matrix, are plagued with similar difficulties [Finney and Heck, 1995]. We present an alternate technique.

A.3.1 Local Balanced Truncation

By examining the dynamics of Equation A.2, we conclude that coupling can be achieved through four mechanisms: (1) mechanical coupling through the structure (non block-diagonal A), (2) measurement coupling through sensors (C_y), (3) disturbance input matrix coupling, (B_w), and (4) sensor noise coupling through non-diagonal sensor noise covariance (Θ). We need not consider coupling through the positive semidefinite process noise covariance since it may be transformed as $\Xi = U\Lambda U^T$ with diagonal Λ so that we can write $\underline{B}_w = B_w U\Lambda^{1/2}$ with a transformed uncorrelated process noise covariance, $\underline{\Xi} = I$. Thus process noise correlation has an analogous effect as B_w matrix coupling. We make the assumptions that the first three sources of coupling are dominant and that sensors have independent sensor noise.

Consider a full-order model at the i-th sensor node. This model has the state equation from Equation A.2 and

$$z_i(k) = C_{y,i}x(k) + n_i(k) \tag{A.33}$$

as the measurement equation. For stable, LTI discrete systems, the controllability Gramian satisfies the following discrete-time Lyapunov equation

$$W_c = AW_cA^T + B_wB_w^T \tag{A.34}$$

which provides a relative measure of the controllability of the states from the process noise. The larger the j-th diagonal of W_c, (relative to other diagonals) the more controllable the j-th state will be (relative to other states). In a dual sense, the observability Gramian for our full-order model satisfies,

$$W_o = A^TW_oA + C_{y,i}^TC_{y,i} \tag{A.35}$$

where the diagonals of W_o correspond to measures of relative observability for the i-th sensor.

Consider a general state transformation of the form, $\underline{x} = Tx$. By substituting into Equation A.2, a transformed state-space system can be obtained,

$$\underline{x}(k+1) = \underline{A}\underline{x}(k) + \underline{L}w(k) \tag{A.36}$$

$$z(k) = \underline{C}\underline{x}(k) + n(k) \tag{A.37}$$

with $\underline{A} = TAT^{\dagger}$, $\underline{L} = TL$, and $\underline{C} = CT^{\dagger}$. We note the use of the pseudo-inverse for cases were T is not necessarily invertible. For example, to truncate modes we can use a non-square T matrix.

For stable LTI systems, there exists an invertible state transformation matrix, T_{bi}, such that the resulting transformed system has equal and diagonal controllability and observability Hankel singular values,

$$\underline{W}_c = \underline{W}_o = \mathrm{diag}\{\sigma_1, \sigma_2, \ldots, \sigma_n\} \tag{A.38}$$

with Hankel singular values, $\sigma_l \geq \sigma_j$ for $l < j$. The large σ values correspond to states which are well disturbed and observed. Small values of σ correspond to states which are not disturbed, and/or not observed. Following model reduction arguments, these states can be removed from the model, since their effect will not be seen in the measurement. Balancing ensures a proper input/output scaling. System balancing and model reduction is presented in Section 3.1.2 where a balancing algorithm for continuous systems with improved numerical robustness is developed. A second state transformation matrix, T_{ki}, (in this case state truncation) can be formed such that $x_{bi} = T_i x = T_{ki} T_{bi} x$ where $T_{ki} = \begin{bmatrix} I & 0 \end{bmatrix}$ is a $n_i \times n$ matrix formed with a $n_i \times n_i$ identity matrix and conformable zero matrix. This transformation extracts the first n_i states, corresponding to the n_i largest Hankel singular values.

If this model-reduction is applied to the i-th full-order system, we obtain $A_i = T_i A T_i^{\dagger}$, $B_{w,i} = T_i B_w$, and $c_{y,i} = C_{y,i} T_i^{\dagger}$ (See Equation A.21). Balanced reduction of the full-order local models provides a method to reduce the local models such that the disturbance to input characteristics are approximately preserved. What remains to be outlined is a tool to determine the order of the reduced-order local models.

Assuming the local models are formed using the balanced truncation, we are interested in recovering the best global state estimate from each local estimator. The local Kalman filter at each sensor node produces an estimate of the reduced and balanced state. To recover the i-th estimate of the global state, we use the properties of the pseudo-inverse to 'invert' the state transformation, resulting in $x_g = T_i^\dagger x_{bi}$, with system matrices $A_g = T_i^\dagger A_i T_i$, $B_g = T_i^\dagger B_{w,i}$, $C_g = c_{y,i} T_i$, and $K_g = T_i^\dagger K_i$. We note that since information has been lost in the state truncation, we do not recover the global state uniquely.

A.3.2 Performance Evaluation

We develop a method to quantify the performance of the global state estimates from using the reduced order models. The true steady state discrete time Kalman filter follows from combining Equation A.3 and Equation A.5, resulting in

$$\hat{x}(k+1) = A\hat{x}(k) + K[z(k+1) - CA\hat{x}(k)] \tag{A.39}$$

which, upon substitution of Equation A.2 results in,

$$\hat{x}(k+1) = [A - KCA]\hat{x}(k) + KCAx(k) + KCB_w w(k) + Kv(k+1) \tag{A.40}$$

The filter gain is obtained through solving the familiar algebraic discrete Riccati equation for the steady-state predict error covariance.

Similarly, the non-optimal, decentralized filter can be written as,

$$\hat{x}_g(k+1) = A_g\hat{x}_g(k) + K_g[z(k+1) - C_g A_g \hat{x}_g(k)] \tag{A.41}$$

where decentralized dynamics are written with a g subscript. The gain, K_g, is again computed by obtaining the solution of an algebraic discrete Riccati equation, where care is taken to ensure the decentralized (from the local estimator) noise covariance is used. Substitution of the true measurement equation from, Equation A.2, and the dynamics leads to

$$\begin{aligned} \hat{x}_g(k+1) &= A_g\hat{x}_g(k) + K_g[Cx(k+1) + n(k+1) - C_g\hat{x}_g(k+1)] \\ &= [A_g - K_g C_g A_g]\hat{x}_g(k) + K_g CAx(k) + K_g CB_w w(k) + K_g v(k+1) \end{aligned} \tag{A.42}$$

Generalizing the approach of [Gelb, 1974] to discrete systems, we can determine the state estimate error for filtering with the incorrect decentralized model. Subtracting the state equation from Equation A.2 from Equation A.42 results in an estimation error, given as

$$\begin{aligned} \tilde{x}(k+1) &= \hat{x}_g(k+1) - x(k+1) \\ &= [A_g - K_g C_g A_g]\tilde{x}(k) + [(A_g - A) + K_g(CA - C_g A_g)]x(k) \\ &\quad + (K_g C - I)B_w w(k) + K_g v(k+1) \end{aligned} \tag{A.43}$$

The state equation of Equation A.2 and Equation A.43 can be combined to form the state-space system given by

$$\begin{aligned} \begin{bmatrix} \tilde{x}(k+1) \\ x(k+1) \end{bmatrix} &= \begin{bmatrix} A_g - K_g C_g A_g & (A_g - A) + K_g(CA - C_g A_g) \\ 0 & A \end{bmatrix} \begin{bmatrix} \tilde{x}(k) \\ x(k) \end{bmatrix} \\ &\quad + \begin{bmatrix} (K_g C - I)U\Lambda^{1/2} & K_g \Theta^{1/2} \\ KU\Lambda^{1/2} & 0 \end{bmatrix} \begin{bmatrix} \underline{w}(k) \\ \underline{v}(k+1) \end{bmatrix} \end{aligned} \tag{A.44}$$

where the process noise and sensor noise processes have been transformed into unit-intensity white noise processes through diagonalization of their respective covariance matrices. Equation A.44 is in the form

$$q(k+1) = A_a q(k) + B_a \xi(k) \tag{A.45}$$

where $\xi(k)$ is a unit-intensity, white noise process. The steady-state covariance can be found by solving the discrete-time Lyapunov equation,

$$P_a = A_a P_a A_a^T + B_a B_a^T \tag{A.46}$$

In this case the solution is partitioned as

$$P_a = \begin{bmatrix} P_g & V^T \\ V & P_x \end{bmatrix}, \tag{A.47}$$

where P_g corresponds to the state estimate variances of the Kalman filter with incorrect dynamics, P_x corresponds to the variance of the system state, and V corresponds to their correlation. We note that the block triangular form of A_a allows solution of the $2n \times 2n$ Lyapunov Equation A.46, to be computed by successively solving three $n \times n$ Lyapunov equations. However, this method requires the solution of a generalized Lyapunov equation of the form $X = AXB + C$, where $B \neq A^T$. The generalized Lyapunov equation is numerically more difficult to solve than the standard form, and thus we elect to solve Equation A.46 directly.

We can evaluate the performance of the local estimators by comparing the local state estimate error variances, $\mathrm{diag}(P_g)$, with the global, optimal, state estimate error variances.

A.4 Example

A simple example will be conducted, to demonstrate and explain the technique. The sample system is shown in Figure A.2. The dynamics for the system are obtained. We first write the continuous-time matrix, A_c, such that the homogenous dynamics are $\dot{x} = A_c x$ where $x = \begin{bmatrix} x_1 & x_2 & x_3 & x_4 & \dot{x}_1 & \dot{x}_2 & \dot{x}_3 & \dot{x}_4 \end{bmatrix}^T$. A zero-order-hold discretization of A_c is performed, resulting in a discrete A matrix. The other model elements for the example include $B_w = \begin{bmatrix} 0 & I \end{bmatrix}^T$ and $C = \begin{bmatrix} I & 0 \end{bmatrix}$, where 0 is a 4×4 zero matrix and I is a 4×4 identity matrix. Thus, the four sensors directly measure the positions of the four masses respectively. The model parameters are $\{m_1, m_2, m_3, m_4\} = \{50, 20, 6, 1\}$, $\{k_1, k_2, k_3, k_4\} = \{1, 3, 7, 10\}$, and the noise covariance is given by $\Xi = I$, and $\Theta = \mu I$.

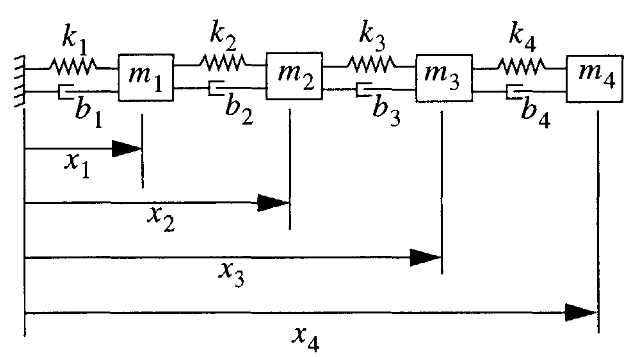

Figure A.2 Four spring design example to demonstrate a technique for selecting reduced-order local models

The system is transformed into a real-modal form, with the block-diagonal dynamics matrix made up of 2×2 blocks of the form

$$A_{bl} = \begin{bmatrix} -\omega\zeta & \omega\sqrt{1-\zeta^2} \\ -\omega\sqrt{1-\zeta^2} & -\omega\zeta \end{bmatrix}. \tag{A.48}$$

Proportional damping is chosen by assigning ζ. The modes are ordered with frequency, *e.g.* states 1 and 2 correspond to the first mode's states.

Figure A.3 is a plot of the Hankel singular values corresponding to each full-order local model of the example of Figure A.2. We see that sensor 1 has four large singular values which implies that four states are necessary to preserve reasonable local state estimates in the reduced-order local model. Likewise, sensor 2 requires six states, sensor 3 requires 6 states, and sensor 4 requires all eight states.

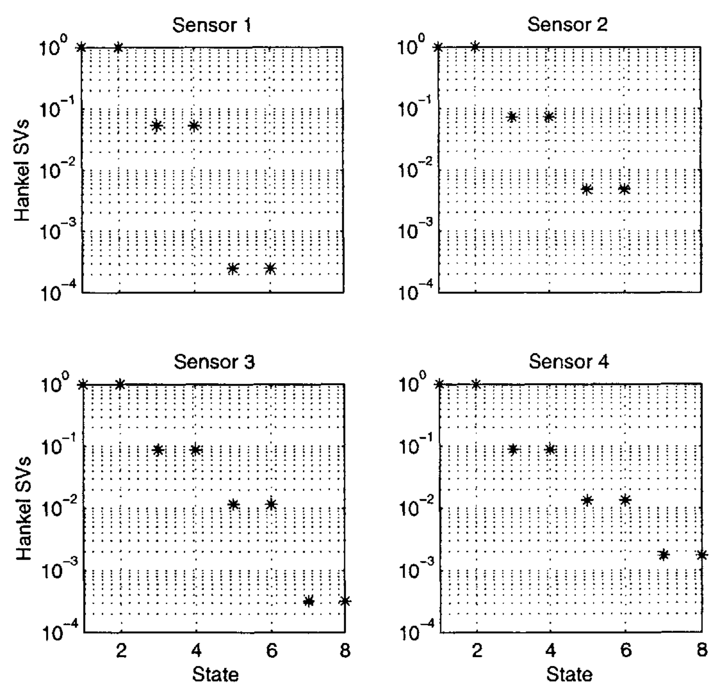

Figure A.3 Hankel singular values for balanced full-order local models corresponding to each sensor

In Figure A.4, for the system with $\zeta = 0.001$ proportional damping, we plot the j-th state's normalized accuracy,

$$A_{i,j} = \frac{P(j,j)}{P_{g,i}(j,j)} \tag{A.49}$$

formed by the error covariance of each state's local estimator global estimate $P_{g,i}(j,j)$, normalized by the estimate error covariance of each of the states from the fully centralized, optimal Kalman filter, $P(j,j)$. A value of 1 corresponds to an optimal estimate of the state. The partitions of the bar chart correspond to increasing the order of the local estimators from 2,4,6 to 8. The peak value of each state's estimate correspond to the full-order local model estimate of the global state estimates corresponding to a particular sensor, and provides an upper-bound on the achievable performance for a local state estimator of the form required by the development of Section A.2. For example, looking at the Sensor 1 chart, we see that a full-order local model can achieve an estimate for state 2, 38% as well as the centralized Kalman filter. That is, the variance of the optimal error for state 1 is 62% better than our best estimate variance from the sensor 1 local filter. (We emphasize that we are now examining local estimates of the global state, and not the optimal global estimate). When compared with the optimal filter, the high-order local filters can only capture the states directly measured. We also note that the high-order local estimates do not achieve the performance obtained by the global estimator. The global estimator does indeed use some information from Sensors 2,3 and 4 to estimate the position and velocity of m_1.

Figure A.4 provides an engineering design tool to determine the order of the reduced-order models. A trade-off of order and global state estimate accuracy is presented. The global estimator performs the best with an optimal normalized accuracy of 1. The derivation of Section A.2 shows that a decentralized filter can be designed with one-way communication from the local nodes to recapture the optimal state estimates. In Figure A.4 the bars correspond to the cumulative accuracy of the local estimators as the local model order increases. The maximum value of the bars correspond to the accuracy of the best possible

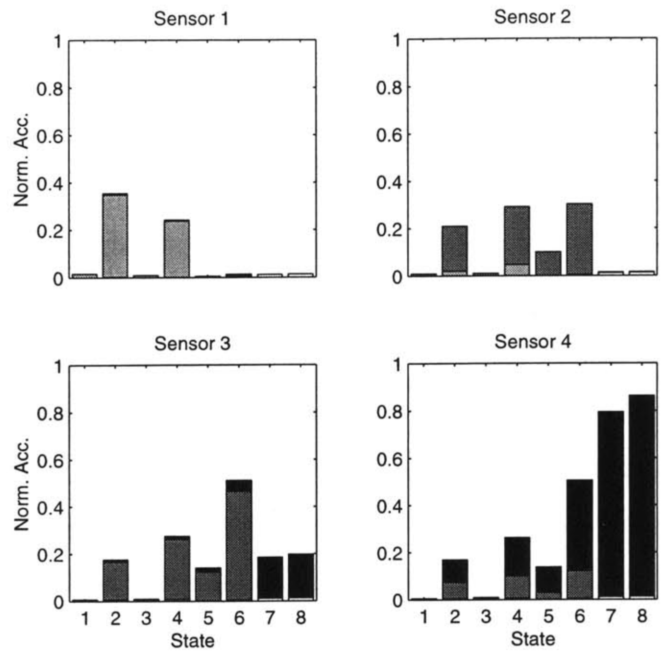

Figure A.4 Plot of normalized local estimator's global state estimate accuracies as the order of the local models is increased for proportional damping of ζ=0.001. 1 corresponds to global fully coupled estimation. The order (2,4,6,8) of the local models increases as we ascend from light to dark.

estimates given single sensors. The loss in performance compared with the global estimators corresponds to the effect of limiting the local estimator to the use of a single sensor. The reduced-order balanced decoupled models show further performance degradation. We note that the effect of model reduction varies from state to state. Time series simulations validate the computed variances to within 2%.

In the case of Sensor 1, we see that a point of diminishing returns is reached with a fourth-order local model such that marginal benefit is achieved by using an sixth order model. This conclusion verifies the claim of four important singular values captured in Figure A.3. The figure also can show which states are not measured well by any sensor (*e.g.* state 1), and are thus estimated well only by the global filter. From examining eigenvectors, we see the first mode corresponds to a motion of all four masses which is measured equally well by all sensors, allowing the global filter to leverage averaging to minimize the effect of sensor noise. This explains the poor local estimates of states 1 and 2. As we increase in frequency the modeshapes become more local, until the fourth mode is mainly a motion of m_4, well measured by sensor 4. However, this mode is not a dominant mode which explains why a full eighth-order local model is required by sensor 4 to estimate states 7 and 8.

In Figure A.5 we plot the corresponding chart for the system as $\zeta \to 1$. In the case of higher damping we see local estimates approach the global estimates with low order local models. This is attributed to each mode having a less local (in frequency) effect which increases the correlation between states.

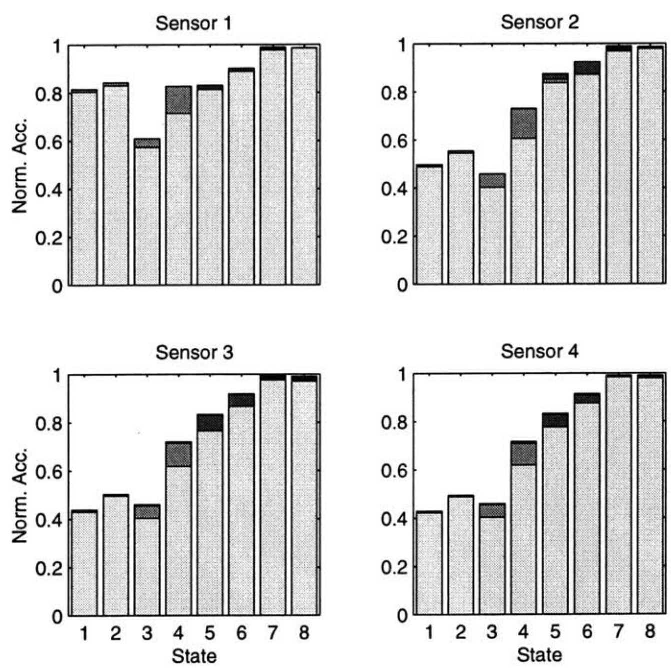

Figure A.5 Plot of normalized local estimator's global state estimate accuracies as the order of the local models is increased for proportional damping of $\zeta \to 1$. 1 corresponds to global fully coupled estimation. The order (2,4,6,8) of the local models increases as we ascend from light to dark.

A.5 Summary

A decentralized estimator which preserves the optimal global estimates has been detailed. The estimator combines local estimates made at each sensor node to recover the optimal estimates. A technique based on model reduction theory is introduced for determining the local models. In addition, a technique to determine the best global state estimates from linear combinations of a local mode is derived. Further, the technique suggests a tool to evaluate the suitability of particular sensors to estimate the system state. A dual development can determine the suitability for the system to decentralized control.

As an extension of the work in this appendix [Mallory and Miller, 2000] apply the decentralized estimation framework to the SIM spacecraft model and conclude that SIM is not a good candidate for local state estimation.

Appendix B

CONSTRAINED TOPOLOGY LQG CONTROL DESIGN

In Chapter 3 an algorithm for the assignment of a sensor/actuator topology is developed. Dynamic coupling in the design plant is exploited to assign sensors and actuators for effective control design. We assume local controllers for assigned sensor/actuator sets are designed set-at-a-time, and the global system controller is built from the local controllers. In this appendix, the synthesis of global H_2 controllers with a constrained topology is explored.

The optimal projection equations of [Hyland and Bernstein, 1984] derive first-order necessary conditions for the optimal H_2 compensator whose order is constrained to be less than the plant. The resulting controller is, in general, fully connected from sensors to actuators. Following a more general strategy, [Mercadal, 1991] derives first-order necessary conditions for the optimal H_2 controller for a controller constrained to be a given order and a given block diagonal sensor/actuator topology.

B.1 Controller Topology Constraints

The standard H_2 or Linear Quadratic Gaussian controller for the n-th order design plant given in Equation 2.3 has an order n and is fully connected. The controller $K(s)$ relates the n_y sensors to the n_u actuators and can be written with SISO transfer function as given by Equation 3.1 where K_{ij} represents the SISO transfer function relating the j-th sensor to the i-th actuator. We can write,

$$K_{ij} = \frac{\partial u_i}{\partial y_j} \tag{B.1}$$

In state-space form, we borrow from the notation of Equation 2.5 to write

$$K_{ij}(s) = C_{c,i}(sI - A_c)^{-1}B_{c,j} \ , \tag{B.2}$$

where $C_{c,i}$ is the i-th row of the controller output matrix, and $B_{c,j}$ is the j-th column of the controller input matrix and A_c is the n_c-th order controller dynamics matrix.

A control topology constraint on the i, j channel forces the controller to not use sensor j to influence actuator i. In transfer function notation we have

$$K_{ij}(s) = 0, \tag{B.3}$$

or

$$\frac{\partial u_i}{\partial y_j} = 0. \tag{B.4}$$

In terms of the state-space parameters we can constrain the first n_c Markov parameters for the i, j channel to be given by a sequence $\{k_{ij}\}$:

$$C_{c,i}A_c^m B_{c,j} = k_{ij}, \forall m = 0, 1, \ldots, n_c - 1 \, . \tag{B.5}$$

If Equation B.5 holds then $C_{c,i}A_c^k B_{c,j}$ for $k \geq n_c$ can be written as a weighted sum of the elements of $\{k_{ij}\}$ by the Cayley Hamilton Theorem. In this manner, a particular control channel can be pre-specified to an impulse response while the remaining control parameters are kept free. In the special case of constrained control topology we set $\{k_{ij}\} = 0$.

For each element of the controller that we wish to constrain to zero we have n_c Markov parameter constraint equations. We can reduce the number of constraint equations by noting that

$$\sum_{m=0}^{n_c-1} (C_{c,i} A_c^m B_{c,j})^2 = 0 \tag{B.6}$$

is uniquely satisfied by the $n_c - 1$ constraint equations of Equation B.5. Thus we have a single constraint equation for each controller channel that we constrain to be zero.

In the trivial case where a sensor or actuator is not to be used we can remove the particular sensor or actuator from the design model.

B.2 First Order Necessary Conditions

We expand upon a similar derivation in [Zhou et al., 1996] to derive the first-order necessary conditions for the constrained topology controller.

Given the design plant of Equation 2.3 with $D_{zu} = 0$ we close the loop with the controller of Equation 2.5, resulting in the close-loop system of Equation 2.7. The closed-loop H_2 cost can be written as

$$J = \mathrm{tr}[B_w^{(cl)} B_w^{(cl)} X^{(cl)}] \tag{B.7}$$

where $X^{(cl)}$ satisfies the Lyapunov Equation,

$$X^{(cl)} A^{(cl)} + A^{(cl)^T} X^{(cl)} + C_z^{(cl)^T} C_z^{(cl)} = 0. \tag{B.8}$$

We can partition $X^{(cl)}$ as

$$X^{(cl)} = \begin{bmatrix} X_{11} & X_{12} \\ X_{12}^T & X_{22} \end{bmatrix}, \tag{B.9}$$

where X_{11} is of dimension $n \times n$, X_{12} is of dimension $n \times n_c$ and X_{22} is of dimension $n_c \times n_c$.

We augment the cost by the Lyapunov Equation B.8 with the Lagrange multiplier matrix $Y^{(cl)}$, and by a constraint Equation B.6 with Lagrange multiplier λ_{ij} for each zero-constrained channel. The augmented cost is written as,

$$J_a = \operatorname{tr}[B_w^{(cl)} B_w^{(cl)} X^{(cl)} + [X^{(cl)} A^{(cl)} + A^{(cl)^T} X^{(cl)} + C_z^{(cl)^T} C_z^{(cl)}] Y^{(cl)}] + \sum_{\{i,j\} \in \Lambda} \lambda_{ij} \sum_{m=0}^{n_c-1} (C_{c,i} A_c^m B_{c,j})^2 \tag{B.10}$$

where Λ is the set of $\{i, j\}$ that are constrained to be zero channels.

We assume the controller is parameterized with respect to state-space parameters, and we define the matrix $E_{kl}^{A_c}$ as the matrix of similar dimension to A_c with a unity entry at the $k \times l$ location, while all other entries are zero. $E_{kl}^{B_c}$ and $E_{kl}^{C_c}$ are defined similarly for the B_c and C_c matrices respectively. Thus the $k \times l$ element of the controller dynamics matrix can be extracted using $a_{kl} = E_{kl}^{A_c} A_c$. $Y^{(cl)}$ is partitioned as is $X^{(cl)}$ in Equation B.9.

By taking derivatives of the augmented cost with respect to $Y^{(cl)}$ we recover the Lyapunov equation:

$$\frac{\partial J_a}{\partial Y^{(cl)}} = 0 \Rightarrow X^{(cl)} A^{(cl)} + A^{(cl)^T} X^{(cl)} + C_z^{(cl)^T} C_z^{(cl)} = 0 \tag{B.11}$$

By taking derivative with respect to $X^{(cl)}$ we recover the dual Lyapunov equation,

$$\frac{\partial J_a}{\partial X^{(cl)}} = 0 \Rightarrow A^{(cl)} X^{(cl)} + X^{(cl)} A^{(cl)^T} + B_w^{(cl)} B_w^{(cl)^T} = 0 . \tag{B.12}$$

By taking derivatives with respect to the Lagrange multipliers, λ_{ij} we recover the constraint Equations B.6.

We also must take derivatives with respect to the controller parameters. For the controller dynamics matrix parameters we have,

$$\frac{\partial J_a}{\partial a_{kl}} = 0 \Rightarrow$$

$$\mathrm{tr}[E_{kl}^{A_c}[X_{12}^T Y_{12} + X_{22} Y_{22}]] + \sum_{\{i,j\} \in \Lambda} \lambda_{ij} \sum_{m=1}^{n_c - 1} \mathrm{tr}[B_{c,j} C_{c,i} A_c^{m-1}] \mathrm{tr}[E_{kl}^{A_c} C_{c,i}^T B_{c,j}] = 0 \tag{B.13}$$

Similar expressions can be derived for $\frac{\partial J_a}{\partial b_{kl}} = 0$ and $\frac{\partial J_a}{\partial c_{kl}} = 0$, the input matrix and output matrix parameters of the controller, respectively.

The preceding set of conditions comprise the first-order necessary conditions for the constrained topology H_2 optimal controller. These conditions expand on those derived in [Mercadal, 1991] since the controller need not be pre-specified as block diagonal. The controller order is pre-specified.

B.3 Synthesis

Synthesizing a controller using the first order necessary conditions is difficult since (1) the optimization problem can be shown to be nonconvex, and (2) the necessary conditions do not guarantee a stable closed loop system.

Homotopy algorithms have been employed with limited success for solving the optimal projection equations for reduced-order H_2 design [Richter and Collins, 1989], and for the block diagonal constrained H_2 controller, [Mercadal, 1991]. Homotopy does not guarantee the solution is a global minimum. Further, successful application of the technique has been limited to small order problems. An alternate approach to determining solutions to the first-order conditions of Section B.2 is to include Equation B.6 as a constraint and to use a constrained optimization algorithm to minimize J. This approach suffers similar difficulties to the homotopy algorithm.

In practice, developing a practical method to synthesize an optimal controller which satisfies the necessary conditions of Section B.2 is an area of further research. As such there is no direct method to verify the topologies selected by the algorithm of Chapter 3

Appendix C

SENSITIVITY WEIGHTED LQG CONTROLLER TUNING

In this appendix a special case of tuning is developed for sensitivity weighted linear quadratic Gaussian (SWLQG) controllers. We begin with an introduction to the standard LQG methodology. With the design plant in a modal form we present a simple adjustment to the LQG state weighting which results in a SWLQG controller. Sensitivity weights are used to penalize deviations in states that are uncertain. To tune a SWLQG controller, we abandon our standard parameterization of Section 4.2, and parameterize with respect to the sensitivity weights. The tuning algorithm can then be developed for this special case. An example is presented whereby a SWLQG controller, designed for the MACE test article, is tuned.

C.1 Linear Quadratic Gaussian Control

Linear Quadratic Gaussian (LQG or H_2) synthesis provides a foundation for SWLQG, and will be introduced. We assume that the system is imperfectly modeled as,

$$\begin{aligned} \dot{x} &= A^{(d)}x + B_w^{(d)}w + B_u^{(d)}u \\ z &= C_z^{(d)}x + D_{zw}^{(d)}w + D_{zu}^{(d)}u \\ y &= C_y^{(d)}x + D_{yw}^{(d)}w + D_{yu}^{(d)}u \end{aligned} \tag{C.1}$$

where the superscript d notation, $(\cdot)^{(d)}$, indicates the non-necessarily perfect design model. Under standard assumptions of controllability and observability, we wish to find a compensator to minimize the quadratic cost,

$$J = \lim_{T \to \infty} \frac{1}{T} E\left\{ \int_0^T (x^T R_{xx} x + 2x^T R_{xu} u + u^T R_{uu} u) dt \right\}, \tag{C.2}$$

with,

$$D_{zw}^{(d)} = 0, \tag{C.3}$$

$$V = \begin{bmatrix} B_w^{(d)} \\ D_{yw}^{(d)} \end{bmatrix} \begin{bmatrix} (B_w^{(d)})^T & (D_{yw}^{(d)})^T \end{bmatrix} = \begin{bmatrix} V_{xx} & V_{xy} \\ V_{xy}^T & V_{yy} \end{bmatrix} \geq 0,\ V_{yy} > 0 \text{ , and} \tag{C.4}$$

$$R = \begin{bmatrix} (C_z^{(d)})^T \\ (D_{zu}^{(d)})^T \end{bmatrix} \begin{bmatrix} C_z^{(d)} & D_{zu}^{(d)} \end{bmatrix} = \begin{bmatrix} R_{xx} & R_{xu} \\ R_{xu}^T & R_{uu} \end{bmatrix} \geq 0,\ R_{uu} > 0 , \tag{C.5}$$

The cost can also written as,

$$J = \lim_{T \to \infty} \frac{1}{T} E\left\{ \int_0^T z^T z dt \right\}. \tag{C.6}$$

The solution compensator is in the form of Equation 2.5, with the matrices,

$$\begin{aligned} A_c &= A^{(d)} + B_u^{(d)} F + L C_y^{(d)} + L D_{yu}^{(d)} F \\ B_c &= -L \\ C_c &= F \end{aligned} \tag{C.7}$$

where

$$F = -R_{uu}^{-1}[R_{xu}^T + (B_u^{(d)})^T X] \tag{C.8}$$

$$L = -[Y(C_y^{(d)})^T + V_{xy}]V_{yy}^{-1} \tag{C.9}$$

with, X and Y, the unique positive-definite solutions to the following Riccati equations,

$$0 = XA_r + A_r X + R_{xx} - R_{xu}R_{uu}^{-1}R_{xu}^T - XB_u^{(d)}R_{uu}^{-1}(B_u^{(d)})^T X \tag{C.10}$$

$$0 = A_e Y + YA_e^T + V_{xx} - V_{xy}V_{yy}^{-1}V_{xy}^T - Y(C_y^{(d)})^T V_{yy}^{-1}C_y^{(d)}Y \tag{C.11}$$

where,

$$A_r = A^{(d)} - B_u^{(d)}R_{uu}^{-1}R_{xu}^T \tag{C.12}$$

$$A_e = A^{(d)} - V_{xy}V_{yy}^{-1}C_y^{(d)} . \tag{C.13}$$

The LQG controller provides a closed loop system with optimal H_2 performance, but has no guaranteed stability margin. LQG synthesis will provide the designer with valuable insight into the potential stability problems. For example, if the LQG closed loop has a high sensitivity near the frequency of a flexible mode then we may wish to modify the design to sacrifice some H_2 performance for improved robustness against uncertainty in that flexible mode.

C.2 Sensitivity Weighted LQG

To derive the sensitivity weighted LQG (SWLQG), we follow [Grocott, 1994]. First we define a quadratic cost which will penalize state sensitivities, $\frac{\partial x}{\partial \alpha_i}$. We add an additional term to the cost functional of Equation C.2 to arrive at:

$$J = \lim_{T \to \infty} \frac{1}{T} E\left\{ \int_0^T \left(x^T R_{xx} x + \sum_{i=1}^{n_\alpha} \frac{\partial x}{\partial \alpha_i}^T R_{\alpha_i} \frac{\partial x}{\partial \alpha_i} + 2x^T R_{xu} u + u^T R_{uu} u \right) dt \right\} \tag{C.14}$$

We can take derivatives of the state equation of Equation C.1, to arrive at:

$$\frac{\partial \dot{x}}{\partial \alpha_i} = A^{(d)}\frac{\partial x}{\partial \alpha_i} + \frac{\partial A^{(d)}}{\partial \alpha_i}x + B_u^{(d)}\frac{\partial u}{\partial \alpha_i} + \frac{\partial B_u^{(d)}}{\partial \alpha_i}u. \tag{C.15}$$

To avoid the cost of augmenting with the sensitivity states, we make two simplifying assumptions: (1) we assume the contribution of $\frac{\partial u}{\partial \alpha_i}$ is small, and (2) that $\frac{\partial \dot{x}}{\partial \alpha_i} \approx 0$ (a similar assumption to the neglect of high frequency dynamics). C.15 simplifies to,

$$0 = A^{(d)}\frac{\partial x}{\partial \alpha_i} + \frac{\partial A^{(d)}}{\partial \alpha_i}x + \frac{\partial B_u^{(d)}}{\partial \alpha_i}u, \tag{C.16}$$

and if $(A^{(d)})^{-1}$ exists,

$$\frac{\partial x}{\partial \alpha_i} = -(A^{(d)})^{-1}\left(\frac{\partial A^{(d)}}{\partial \alpha_i}x + \frac{\partial B_u^{(d)}}{\partial \alpha_i}u\right). \tag{C.17}$$

Substituting Equation C.17 into Equation C.14 we arrive at

$$\begin{aligned} J = \lim_{T\to\infty}\frac{1}{T}E\Bigg\{\int_0^T [x^T&\left(R_{xx} + \sum_{i=1}^{n_\alpha}\frac{\partial (A^{(d)})^T}{\partial \alpha_i}(A^{(d)})^{-T}R_{\alpha_i}(A^{(d)})^{-1}\frac{\partial A^{(d)}}{\partial \alpha_i}\right)x \\ &+ 2x^T\left(R_{xu} + \sum_{i=1}^{n_\alpha}\frac{\partial (A^{(d)})^T}{\partial \alpha_i}(A^{(d)})^{-T}R_{\alpha_i}(A^{(d)})^{-1}\frac{\partial B_u^{(d)}}{\partial \alpha_i}\right)u \\ &+ u^T\left(R_{uu} + \sum_{i=1}^{n_\alpha}\frac{\partial (B_u^{(d)})^T}{\partial \alpha_i}(A^{(d)})^{-T}R_{\alpha_i}(A^{(d)})^{-1}\frac{\partial B_u^{(d)}}{\partial \alpha_i}\right)u]dt\Bigg\} \end{aligned} \tag{C.18}$$

By examining the cost function of Equation C.18 and that of Equation C.2, we see that the SWLQG problem is reduced to the LQG problem with weighting matrices modified as,

$$R_{xx}^{SW} = R_{xx} + \sum_{i=1}^{n_\alpha}\frac{\partial (A^{(d)})^T}{\partial \alpha_i}(A^{(d)})^{-T}R_{\alpha_i}(A^{(d)})^{-1}\frac{\partial A^{(d)}}{\partial \alpha_i} \tag{C.19}$$

$$R_{xu}^{SW} = R_{xu} + \sum_{i=1}^{n_\alpha} \frac{\partial (A^{(d)})^T}{\partial \alpha_i} (A^{(d)})^{-T} R_{\alpha_i} (A^{(d)})^{-1} \frac{\partial B_u^{(d)}}{\partial \alpha_i} \tag{C.20}$$

$$R_{uu}^{SW} = R_{uu} + \sum_{i=1}^{n_\alpha} \frac{\partial (B_u^{(d)})^T}{\partial \alpha_i} (A^{(d)})^{-T} R_{\alpha_i} (A^{(d)})^{-1} \frac{\partial B_u^{(d)}}{\partial \alpha_i} \tag{C.21}$$

In a dual sense, we modify the Kalman filter weighting matrices to be,

$$V_{xx}^{SW} = V_{xx} + \sum_{i=1}^{n_\alpha} \frac{\partial (A^{(d)})^T}{\partial \alpha_i} (A^{(d)})^{-1} V_{\alpha_i} (A^{(d)})^{-T} \frac{\partial A^{(d)}}{\partial \alpha_i} \tag{C.22}$$

$$V_{xu}^{SW} = V_{xy} + \sum_{i=1}^{n_\alpha} \frac{\partial (A^{(d)})^T}{\partial \alpha_i} (A^{(d)})^{-1} V_{\alpha_i} (A^{(d)})^{-T} \frac{\partial (C_y^{(d)})^T}{\partial \alpha_i} \tag{C.23}$$

$$V_{yy}^{SW} = V_{yy} + \sum_{i=1}^{n_\alpha} \frac{\partial C_y^{(d)}}{\partial \alpha_i} (A^{(d)})^{-1} V_{\alpha_i} (A^{(d)})^{-T} \frac{\partial (C_y^{(d)})^T}{\partial \alpha_i} \tag{C.24}$$

With the modified weighting matrices, the LQG framework is used to determine a compensator. The closed-loop system is no longer H_2 optimal, but if the sensitivity weighting matrices, R_{α_i} and V_{α_i} are chosen appropriately, considerable improvements in stability margin can be achieved with only a slight degradation of H_2 performance.

Special Case: Frequency Uncertainty in Flexible Structure

In the special case of frequency uncertainty in the complex modes of a flexible system, considerable simplifications result. If we put the system in real modal form we have

$$A^{(d)} = \mathrm{diag}\left\{ \dots \begin{bmatrix} -\zeta_i\omega_i & \omega_i\sqrt{1-\zeta_i^2} \\ -\omega_i\sqrt{1-\zeta_i^2} & -\zeta_i\omega_i \end{bmatrix} \dots \right\}. \tag{C.25}$$

If we consider the modal frequencies unknown, we have $\alpha_i = \omega_i$. We find the necessary sensitivity derivatives reduce to

$$\frac{\partial A^{(d)}}{\partial \alpha_i} = \mathrm{diag}\left\{ 0 \dots \begin{bmatrix} -\zeta_i & \sqrt{1-\zeta_i^2} \\ -\sqrt{1-\zeta_i^2} & -\zeta_i \end{bmatrix} \dots 0 \right\}, \tag{C.26}$$

$$\frac{\partial B_u^{(d)}}{\partial \alpha_i} = 0, \text{ and } \frac{\partial C_y^{(d)}}{\partial \alpha_i} = 0$$

With this assumption, $R_{xu}^{SW} = R_{xu}$, $R_{uu}^{SW} = R_{uu}$, $V_{xy}^{SW} = V_{xy}$, and $V_{yy}^{SW} = V_{yy}$. Further, we find,

$$(A^{(d)})^{-1}\frac{\partial A^{(d)}}{\partial \alpha_i} = \frac{1}{\omega_i}\mathrm{diag}\left\{ 0 \dots I \dots 0 \right\}. \tag{C.27}$$

By substituting into Equation C.19 and Equation C.22, we have for the i-th uncertain mode,

$$R_{xx}^{SW} = R_{xx} + \frac{1}{\omega_i^2}\mathrm{diag}\left\{ 0 \dots R_{\alpha_i}^j \dots 0 \right\} \tag{C.28}$$

$$V_{xx}^{SW} = V_{xx} + \frac{1}{\omega_i^2}\mathrm{diag}\left\{ 0 \dots V_{\alpha_i}^j \dots 0 \right\} \tag{C.29}$$

where $(\cdot)^j$ is the j-th 2×2 sub-block. To preserve the relative weighting of modes we make the final simplification, $R_{\alpha_i}^j = \beta_i\omega_i^2 R_{xx}^j$, and $V_{\alpha_i}^j = \beta_i\omega_i^2 V_{xx}^j$, where β_i is a sensitivity weighting factor. As β_i is increased, the penalty on the uncertainty of the i-th mode is increased, improving robustness to variations in the frequency of that mode.

We have reduced the SWLQG problem to the traditional LQG problem with the additional selection of a set of sensitivity weights, $\{\beta_i\}$ which penalize uncertainty in the flexible modes. The selection of these weights is the topic of research and will be further detailed.

C.3 SWLQG Tuning Gradients

With the SQLQG controller specified in the previous section, we are now in a position to compute the gradients for the tuning cost expressions as in Section 4.1. The cost expressions are defined in an identical manner where the baseline SWLQG controller (Equation C.7) is substituted for the controller and the sensitivity weights, $\{\beta_i\}$ are substituted for the controller parameters p.

In the tuning cost expressions, it is only the controller that explicitly depends on p ($\{\beta_i\}$ is the current case). Thus, computing the gradients of the tuning costs for the special SWLQG case reduces to computing $\frac{\partial A_c}{\partial \beta_i}, \frac{\partial B_c}{\partial \beta_i}, \frac{\partial C_c}{\partial \beta_i}$ and substituting into expressions such as Equation 4.31.

We make the simplifying assumption that there is no state-control cross weighting ($R_{xu} = 0$), and that the sensor and process noise are uncorrelated, ($V_{xy} = 0$). We write the gradient of the SWLQG controller as

$$\begin{aligned} \frac{\partial A_c}{\partial \beta_i} &= B_u^{(d)} \frac{\partial F}{\partial \beta_i} + \frac{\partial L}{\partial \beta_i} C_y^{(d)} + \frac{\partial L}{\partial \beta_i} D_{yu}^{(d)} F + L D_{yu}^{(d)} \frac{\partial F}{\partial \beta_i} \\ B_c &= -\frac{\partial L}{\partial \beta_i} \\ C_c &= \frac{\partial F}{\partial \beta_i} \end{aligned} \tag{C.30}$$

Now, we apply the chain rule. The derivatives of the LQ gain and the filter gain becomes,

$$\frac{\partial F}{\partial \beta_i} = -R_{uu}^{-1}(B_u^{(d)})^T \frac{\partial X}{\partial \beta_i} \tag{C.31}$$

and

$$\frac{\partial L}{\partial \beta_i} = -\frac{\partial Y}{\partial \beta_i}(C_y^{(d)})^T V_{yy}^{-1}. \tag{C.32}$$

To continue our development, we take derivatives of the Riccati equation (when $R_{xu} = 0$), Equation C.10, and arrive at,

$$0 = \frac{\partial X}{\partial \beta_i}A^{(d)} + (A^{(d)})^T\frac{\partial X}{\partial \beta_i} + \frac{\partial R_{xx}^{SW}}{\partial \beta_i} - \frac{\partial X}{\partial \beta_i}B_u^{(d)}R_{uu}^{-1}(B_u^{(d)})^T X - XB_u^{(d)}R_{uu}^{-1}(B_u^{(d)})^T\frac{\partial X}{\partial \beta_i}. \tag{C.33}$$

By substituting Equation C.8, we have,

$$0 = \frac{\partial X}{\partial \beta_i}(A^{(d)} + B_u^{(d)}F) + (A^{(d)} + B_u^{(d)}F)^T\frac{\partial X}{\partial \beta_i} + \frac{\partial R_{xx}^{SW}}{\partial \beta_i}. \tag{C.34}$$

This is a Lyapunov equation. Further, in the case of uncertain modal frequencies, we have from Equation C.28,

$$\frac{\partial R_{xx}^{SW}}{\partial \beta_i} = \mathrm{diag}\left\{ 0 \ \dots \ R_{xx}^j \ \dots \ 0 \right\}. \tag{C.35}$$

which will be positive semidefinite if $R_{xx} = (C_y^{(d)})^T C_y^{(d)}$. Also, by the properties of the Riccati equation, under standard assumptions of controllability and observability, the matrix $A^{(d)} + B_u^{(d)}F$ will be guaranteed stable. Thus, the Lyapunov equation, Equation C.34, is guaranteed to have a unique positive semidefinite solution. The dual Lyapunov equation for the observer is given by

$$0 = (A^{(d)} + LC_y^{(d)})\frac{\partial X}{\partial \beta_i} + \frac{\partial X}{\partial \beta_i}(A^{(d)} + LC_y^{(d)})^T + \frac{\partial V_{xx}^{SW}}{\partial \beta_i} \tag{C.36}$$

where again the term $A^{(d)} + LC_y^{(d)}$ is guaranteed to be stable. From Equation C.29, the driving term can be written as,

$$\frac{\partial V_{xx}^{SW}}{\partial \beta_i} = \mathrm{diag}\left\{ 0 \; \ldots \; V_{xx}^{j} \; \ldots \; 0 \right\} \tag{C.37}$$

which is positive semidefinite ensuring a unique solution for Equation C.36.

With these gradients, the tuning methodology of Chapter 4 can be applied to compute the sensitivity weights. The sensitivity can be used to directly compute the SWLQG controller by applying the relations of Section C.2.

C.4 Example: MACE

SWLQG was demonstrated to be an effective robust control synthesis technique during the MACE experiment [Grocott, 1994]. A critical design issue remains choosing the sensitivity weights, $\{\beta_i\}$, A special case of the tuning algorithm of Chapter 4 provides a method for determining the weights.

We consider a state-space model and measured data for the MACE test article and set up a control problem as specified in Table C.1. Additional detail on the MACE test article is found in [Miller et al., 1996] and [Grocott et al., 1997].

TABLE C.1 Input and output signals for the MACE example

Signal Type	Abbreviation	Description
Disturbance, w	SGZ	White noise in the secondary gimbal
Actuators, u	PGZ	Primary gimbal, z direction
Performance, z	$\int$PRZ	Integral of the primary rate gyro, z direction
Sensors, y	PRZ	Primary rate gyro, z direction

An LQG controller can be designed. The performance, maximum singular value of Sensitivity (magnitude in this SISO case) and Nichols stability plot are shown in Figure C.1.

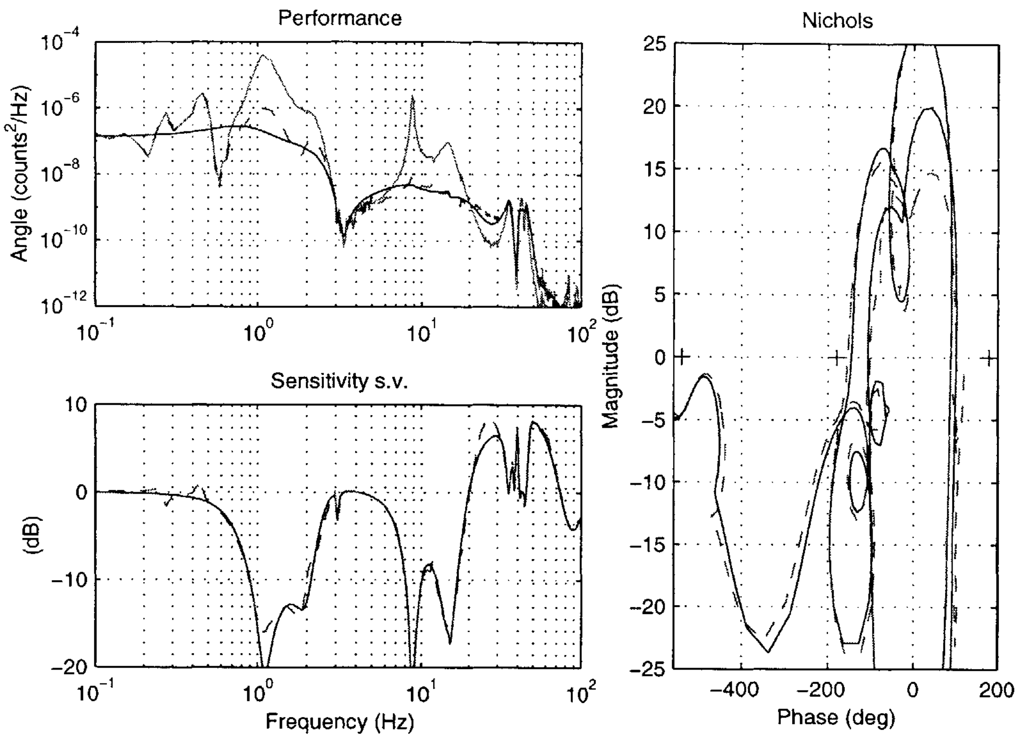

Figure C.1 Performance (top left), maximum singular value of the Sensitivity (bottom left) and Nichols plot (right) for the baseline LQG controller on the design model (solid) and measured data (dashed). The open loop is plotted with the light line in the performance plot.

The controller achieves a performance of 0.00139 counts RMS which is a 11.6 dB improvement. The spikes in the Sensitivity singular value indicate a lack of robustness, particularly near roll-off, in the 20 to 50 Hz range. Deviations between the model plot and the measured data plot also signify a potential lack of robustness. To improve the robustness we design a SWLQG controller.

After some design effort we choose sensitivity weights such that the 20 - 50 Hz spikes in the Sensitivity are greatly reduced, however, we find that the performance has crept up to 0.00161 counts RMS. To refine our weights and improve the performance to that of the baseline LQG controller, we apply the tuning methodology to improve the performance while we enforce a penalty on any increase of the maximum Sensitivity singular value. We form a hybrid tuning strategy where the state-space design model is used for performance metric and the measured data is used for the stability robustness metric. We note that a design model is necessary to form the SWLQG controllers. The performance and stability robustness of the initial and tuned SWLQG controllers are plotted in Figure C.2.

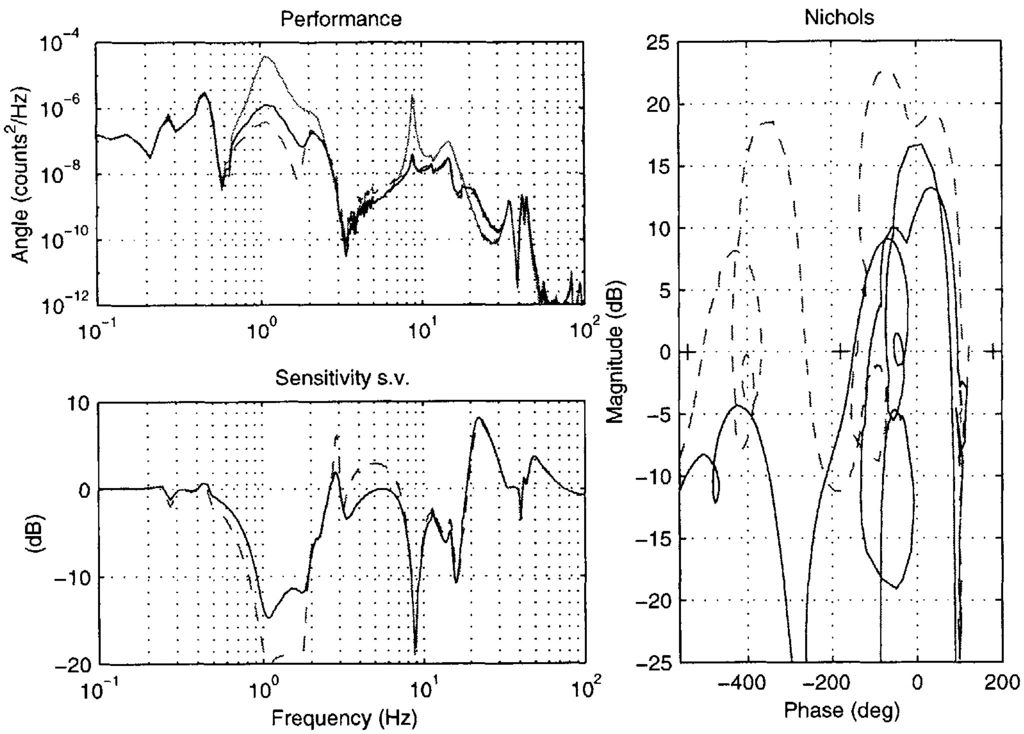

Figure C.2 Performance (top left), maximum singular value of the Sensitivity (bottom left) and Nichols plot (right) for the initial SWLQG controller (solid) and for the tuned SWLQG controller (dashed). Plots are generated with the measured plant data. The open loop is plotted with the light line in the performance plot.

As desired the SWLQG controllers both push down the Sensitivity s.v. in the critical 20-50 Hz range. The tuned controller exhibits improved performance over the initial SWLQG design. The resulting 0.00130 counts RMS is a 0.6 dB improvement over the baseline LQG design, a 1.8 dB improvement over the baseline SWLQG design, and a 12.2 dB improvement over the open-loop system. To achieve this increased performance, the tuned SWLQG controller sacrifices a pop-up of the Sensitivity spike at 3 Hz, a low frequency where we assume we have a good measure of the MACE structure. The three MACE controllers are summarized in Table C.2.

TABLE C.2 Performance and stability robustness summary of the MACE controllers: Baseline LQG, Initial SWLQG and tuned SWLQG.

Controller	Performance		Stability Robustness Comment
	Counts (RMS)	Imp. (dB)	
Baseline LQG	0.00139	11.6	Large spikes in the critical 20-50 Hz region correspond to poor robustness, particularly a sharp spike at 40 Hz.
Initial SWLQG	0.00160	10.4	Push down Sensitivity s.v. in the 20-50 Hz
Tuned SWLQG	0.00130	12.2	Keep Sensitivity down in the 20-50 Hz range but, pop-up at 3 Hz.

One special consideration is that the stability weights must be positive (or slightly negative) to maintain the positive semidefinite requirement of the R_{xx} matrix. Our unconstrained optimization does not guarantee this, which limits the application of the SWLQG tuning methodology.

C.5 Summary

The tuning of SWLQG controllers provides a special case of the tuning methodology. Rather than using the standard controller parameterization, we parametrize with the sensitivity weights. The tuning cost gradients with respect to the sensitivity weights are computed and found to result from the solution of well-behaved Lyapunov equations. An LQG controller is designed for a MACE control design example. The desired performance is obtained but with poor stability robustness. With SWLQG synthesis, a controller is designed with better stability behavior but without maintaining the desired performance. By applying the tuning methodology, the SWLQG controller is tuned to obtain the desired performance with good stability behavior.

Appendix D

IDENTIFYING WITH A PHYSICAL DISTURBANCE MODEL

In general it is impossible to characterize the effect of the disturbance on the plant. Two measurement limitations are responsible:

1. It is impossible to directly measure the disturbance states.
2. It is impossible to measure the transfer function from the disturbance to the sensors or performance (G_{yw} and G_{zw}).

We can, however usually measure the disturbance-to-performance and disturbance-to-sensor autospectra. The limitation is that a measured autospectra contains no phase information. We can, also, physically model the disturbance such as the broadband reaction wheel model of [Masterson, 1999]. In this appendix, the use of a BGFS nonlinear programming method similar to that employed by the tuning of Chapter 4, will be demonstrated for identifying the state-space representation of the G_{yw} and G_{zw} dynamics.

Actuator to Sensor Identification and Underlying Assumptions

The measurement model can be computed by fitting frequency response data using the Frequency Domain Observability Range Space Extraction (FORSE) algorithm coupled with logarithmic least squares tuning as detailed in [Jacques, 1995]. Using this nonlinear system identification routine a state-space model can be fit to the measured $G_{yu}(\omega_k)$ and $G_{zu}(\omega_k)$ data resulting in $\{A, B_u, C_z, C_y\}$ matrices. We now make two assumptions (in addition to a insisting on a stable system)

1. The set of actuators controls all plant modes (with the exception of the disturbance uncontrollable pre-whitening filter dynamics).
2. The system has no feedthrough term ($D = 0$).

The first assumption ensures that all of the plant dynamics are captured in the determined A matrix, and ensures that $\{B_u, C_z, C_y\}$ need not be modified with the addition of the disturbance channel. The second assumption is for simplification. Based on the two assumptions, the problem of system identification is reduced to determining pre-whitening dynamics and to determining the B_w matrix.

Broadband RWA Disturbance Model

During an observation, the wheels spin from 0 to 1100 revolutions per minute. Following the physical argument that the fundamental harmonic of the reaction wheel disturbance increases as wheel frequency squared [Masterson, 1999], a low-order state-space prefilter for the wheel disturbance can be formed as in [Gutierrez, 1999]. The transfer function for the prefilter is given by,

$$H_p(s) = \frac{K_p s^2}{(s+\omega_p)^4} \tag{D.1}$$

where $\omega_p = 2\pi\frac{1100}{60}$ is the cut-off frequency of the disturbance spectrum and K_p is approximately set (it will later be tuned). The state-space representation of the pre-whitening filter is given by $\{A_p, B_p, C_p\}$. The state-space reaction wheel disturbance is plotted in Figure D.1.

Appending the plant with the disturbance mode we obtain an augmented system given by the state-space matrices:

$$A_a = \begin{bmatrix} A & B_w C_p \\ 0 & A_d \end{bmatrix}, B_a = \begin{bmatrix} 0 \\ B_d \end{bmatrix}, C_a = \begin{bmatrix} C_z & 0 \\ C_y & 0 \end{bmatrix}. \tag{D.2}$$

In Equation D.2, the remaining unknown is B_w.

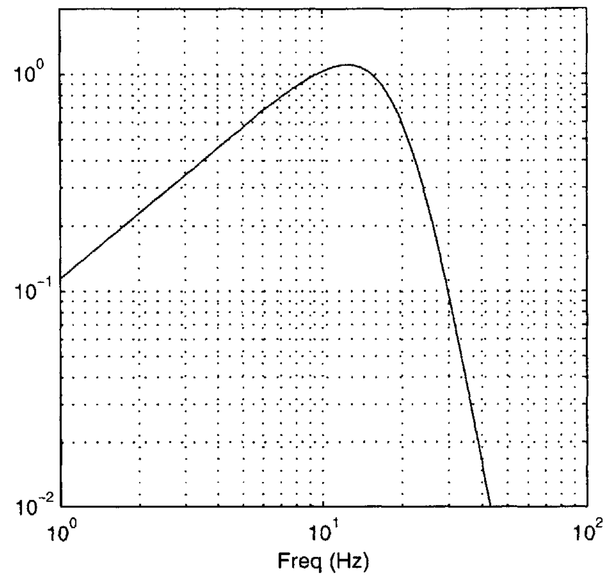

Figure D.1 Reaction wheel disturbance prefilter autospectrum. The disturbance increases as wheel speed squared and cuts off sharply at the highest wheel speed frequency.

Estimating the Disturbance Input Matrix

To compute B_w we develop a nonlinear optimization strategy similar to that developed in Chapter 4 for controller tuning. The model transfer matrix can be computed as,

$$\begin{bmatrix} G_{zw}^{(m)}(\omega_k) \\ G_{yw}^{(m)}(\omega_k) \end{bmatrix} = C_a(j\omega_k I - A_a)^{-1} B_a \tag{D.3}$$

where the $(\cdot)^{(m)}$ superscript indicates the model.

For the i-th sensor and j-th actuator, the model autospectra is determined as in Equation 6.1,

$$A_{y_i w_j}^{(m)}(\omega_k) = G_{y_i w_j}^{(m)}(\omega) G_{y_i w_j}^{(m)}(\omega)^* . \tag{D.4}$$

We define a cost function as

$$J_{ID} = \sum_{i=1}^{\{y,z\}} \sum_{j=1}^{\{w\}} \sum_{k=1}^{n_k} \Gamma_{ij}(A_{ij}^{(m)}(\omega_k) - A_{ij}(\omega_k))^2, \tag{D.5}$$

where the summation is performed over each output (sensor and performance), and a summation is performed over each input (disturbance). The weighting elements, Γ_{ij} are tuned to capture the relative importance of specific channels.

If we define the elements of the B_w as optimization parameters p we can compute the gradient of the cost with respect to the l-th parameter as:

$$\frac{\partial J_{ID}}{\partial p_l} = -4 \sum_{i=1}^{\{y,z\}} \sum_{j=1}^{\{w\}} \sum_{k=1}^{n_k} \Gamma_{ij}(A_{ij}^{(m)}(\omega_k) - A_{ij}(\omega_k)) \mathrm{Re}\left[(G_{ij}^{(m)}(\omega_k))^H \frac{\partial}{\partial p_l} G_{ij}^{(m)}(\omega_k)\right], \tag{D.6}$$

where $\frac{\partial}{\partial p_l} G_{ij}^{(m)}$ is computed using Equation 4.31 with Equation D.3's expression for $G_{ij}^{(m)}$ substituted for K. Since the parameters are the elements of B_w we have,

$$\frac{\partial A_a}{\partial p_l} = \begin{bmatrix} 0 & \frac{\partial B_w}{\partial p_l} C_p \\ 0 & 0 \end{bmatrix}, \frac{\partial B_a}{\partial p_l} = 0, \frac{\partial C_a}{\partial p_l} = 0. \tag{D.7}$$

Now we have a well-defined cost and analytic expressions for the gradient so we may apply the BFGS algorithm of Section 4.3.1 to estimate B_w. In this case, there is no need to check for stability preservation since the block-diagonal formation of stable dynamics preserves stability.

Example: Application to the OT

Figure D.2 is a plot of the measured DPL and QC autospecta during an observation. The autospectra resulting from the identified state-space model is overlaid.

The modeled spectra is seen to have significant differences from the measured data, but has the same general shape. The maxima of the autospectra at 10 and 20 Hz strongly dom-

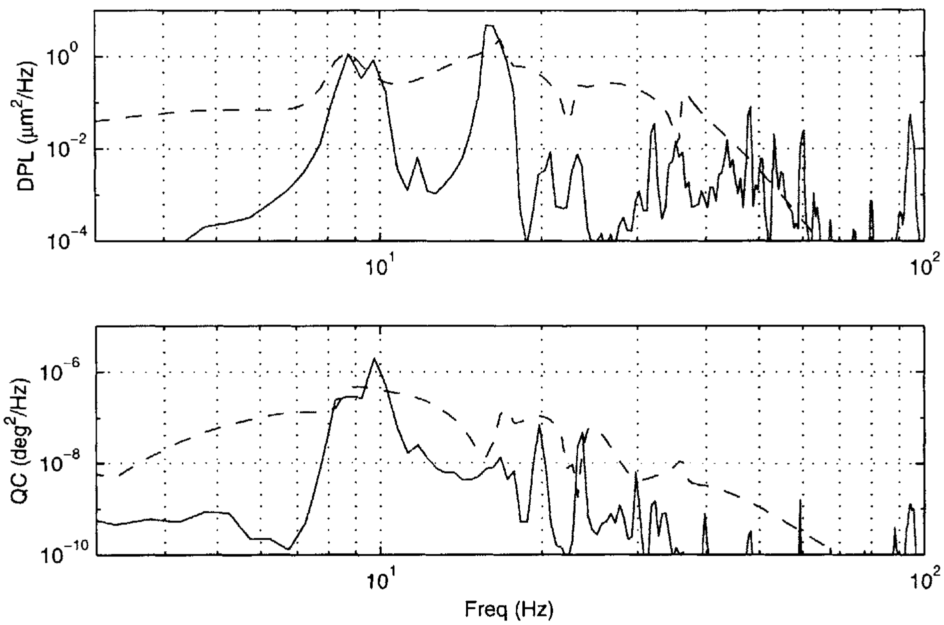

Figure D.2 Autospectra of the DPL and QC performance variables as the wheel winds-up during an observation. Measured data is indicated with the solid line, and the estimated state-space model is indicated with the dashed line. The modeled spectra has the rough shape of the measured spectra.

inate the measured performance and we see that both spectra have maxima over the same frequency bands. The magnitudes are inaccurate for three principal reasons: (1) the model of the broadband wheel spectrum is inaccurate: the sharp roll-off is impossible to captured with a low order state-space model and the spectrum is built on the assumption that the wheel spends the same amount of time at each speed during the observation, (2) the non-wheel disturbance sources have been neglected, and (3) the B_w is under-parameterized to trade optimization convergence with accuracy. The complete parameterization of B_w would require 6 non-independent wheel spectra PSD's [Gutierrez, 1999].

In our case, the roll-off limitations of the broadband wheel model force us to not use this wheel physics-based determination of the G_{yw} and G_{zw} dynamics for the sensor / actuator ranking algorithm in Chapter 6.

Appendix E

ORIGINS TESTBED: TUNED CONTROLLER FAMILY

The experimentally measured results of the application of the family of tuned controllers to the Origins Testbed are presented in this appendix. The controllers are related as depicted in Figure 6.22 and annotated in Table 6.10. A description of the controllers is found in Section 6.5.

Three plots are presented for each of the 11 tuned controllers:

1. **Controller magnitudes**: The magnitudes of the controller gains are presented and compared with the magnitudes of the previous controller in the family of Figure 6.22.
2. **Performance autospectra**: The autospectra of the DPL and QC performance variables are plotted for the tuned controller, the previous controller in the family of Figure 6.22, and compared with the open-loop case.
3. **Stability plots**: The absolute stability (Nichols) plot and the stability robustness (singular values of the sensitivity) plot are presented for the tuned controller as determined by simulation (applying the controller to the design data), and as experimentally measured.

For each controller a table presents the predicted performance (predicted by applying the controller to the design data) and the measured performance. Also the decibel change in the performance as compared to the previous controller in the family of Figure 6.22 is recorded.

Controller T1

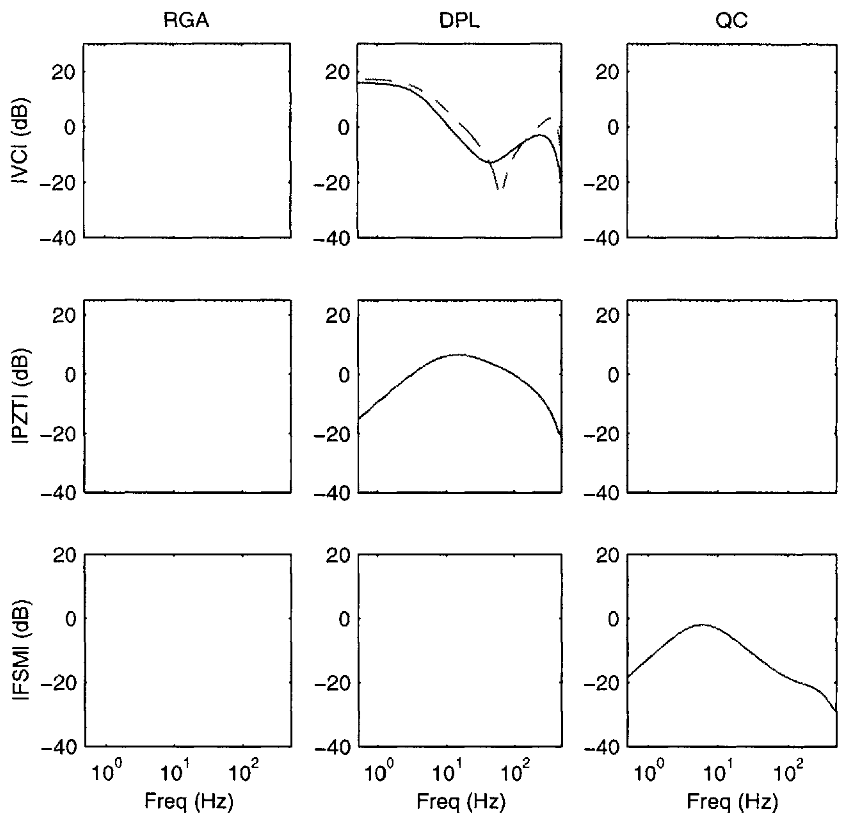

Figure E.1 T1 controller magnitudes (dashed), and baseline controller magnitudes (solid)

The DPL-to-VC channel is tuned to increase the bandwidth and provide additional authority over the bandwidth of interest and without adversely affecting stability robustness.

TABLE E.1 Measured and predicted performance of controller T1

	RMS Performance		Meas. imp.	Meas. imp.
Perf Variable	**Predict**	**Meas**	**over OL**	**over BC**
DPL	1.47 μm	1.29 μm	11.4 dB	2.0 dB
QC	1.59 arcsec	1.63 arcsec	12.7 dB	0.9 dB

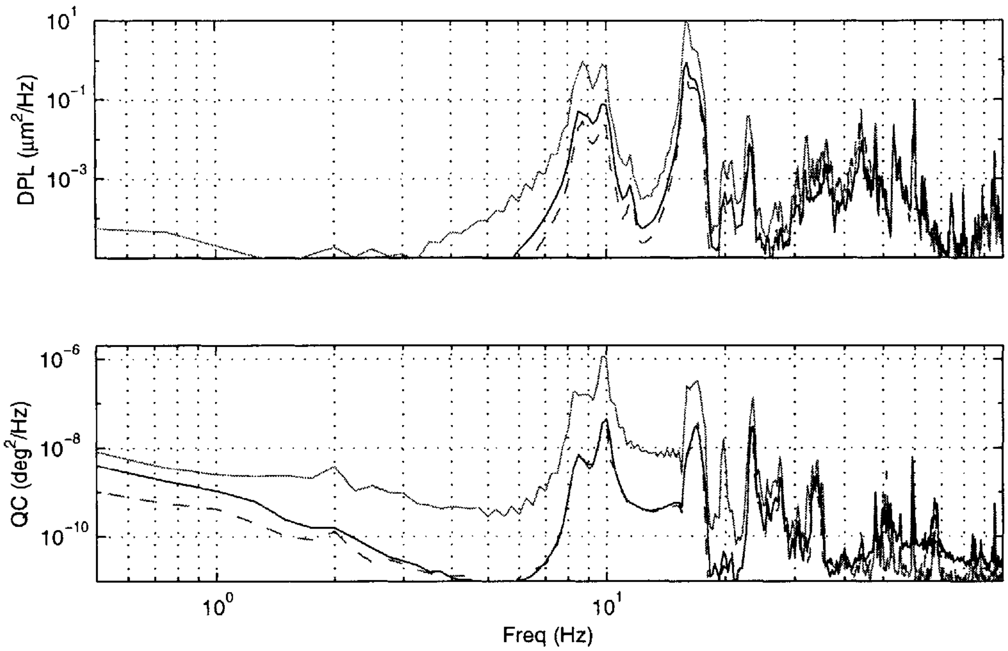

Figure E.2 Experimental performance autospectra: open-loop (light), baseline controller (solid), T1 controller (dashed)

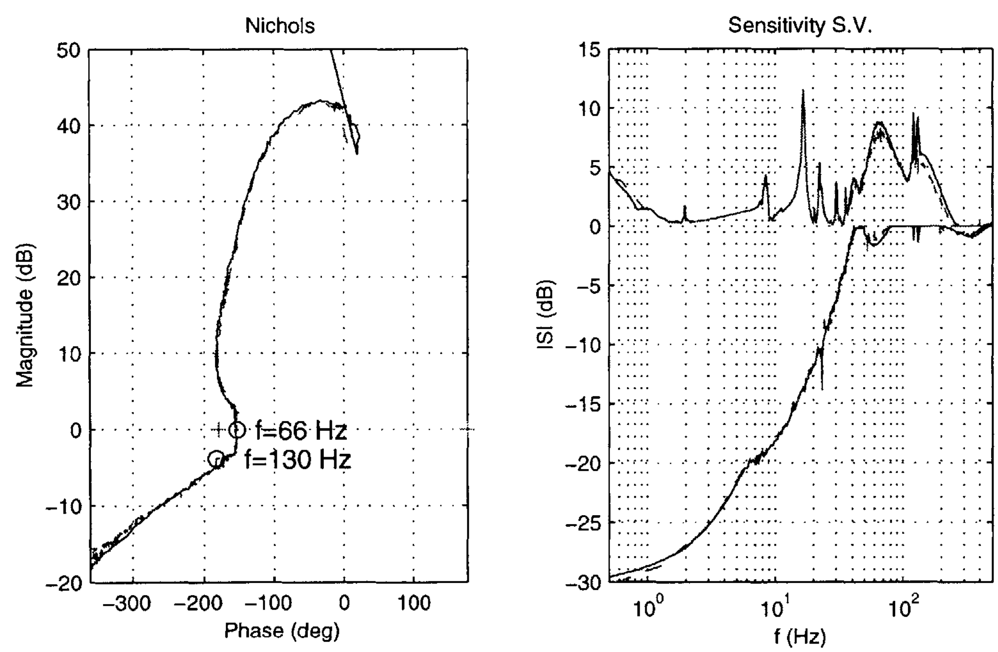

Figure E.3 Stability plots for T1 controller: simulated control on design data (solid), and measured (dashed)

Controller T2

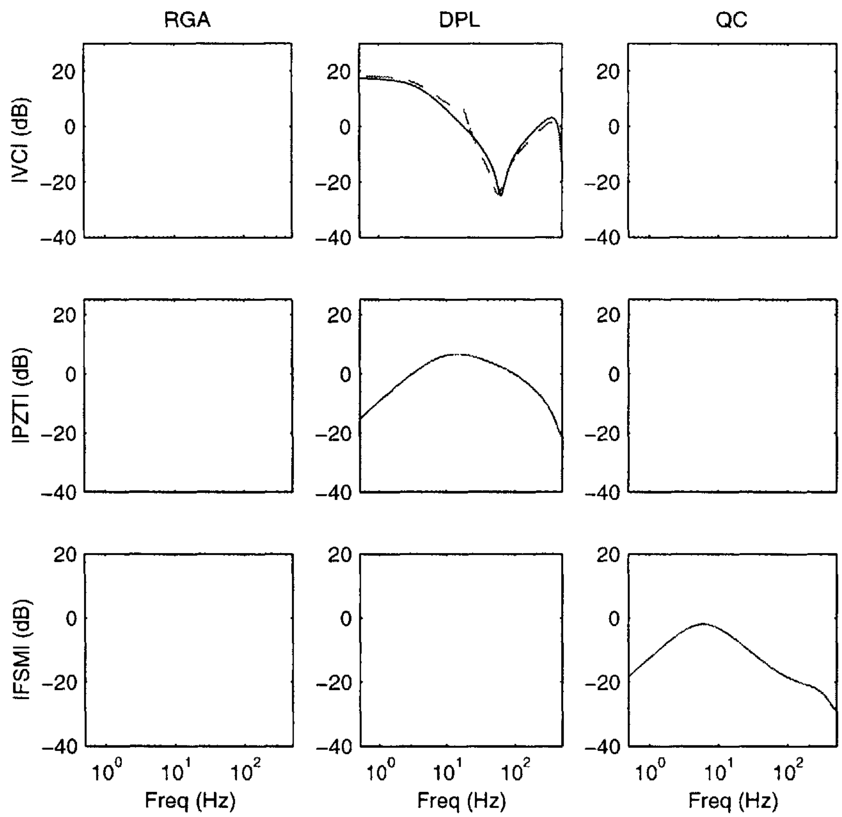

Figure E.4 T2 controller magnitudes (dashed), and T1 controller magnitudes (solid)

The DPL (phasing) performance is improved with a slight sacrifice of performance in the QC (fine pointing). The extra state provides gain in the performance-critical 10 Hz band.

TABLE E.2 Measured and predicted performance of controller T2

	RMS Performance			
Perf Variable	**Predict**	**Meas**	**Meas. imp. over OL**	**Meas. imp. over T1**
DPL	1.09 μm	0.97 μm	13.8 dB	2.4 dB
QC	1.60 arcsec	1.68 arcsec	12.4 dB	-0.3 dB

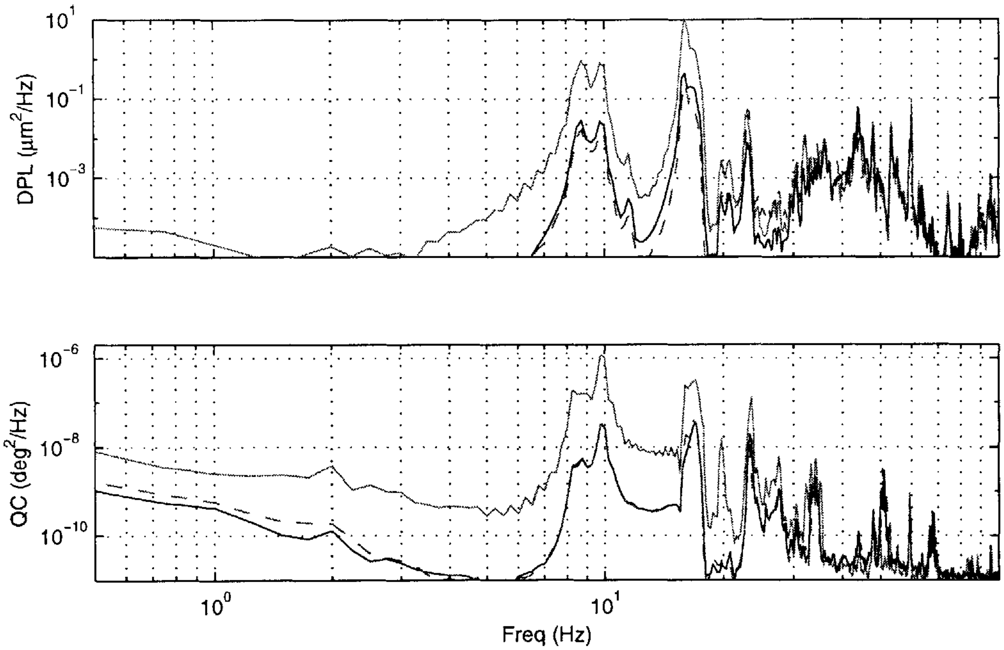

Figure E.5 Experimental performance autospectra: open-loop (light), T1 (solid), T2 controller (dashed)

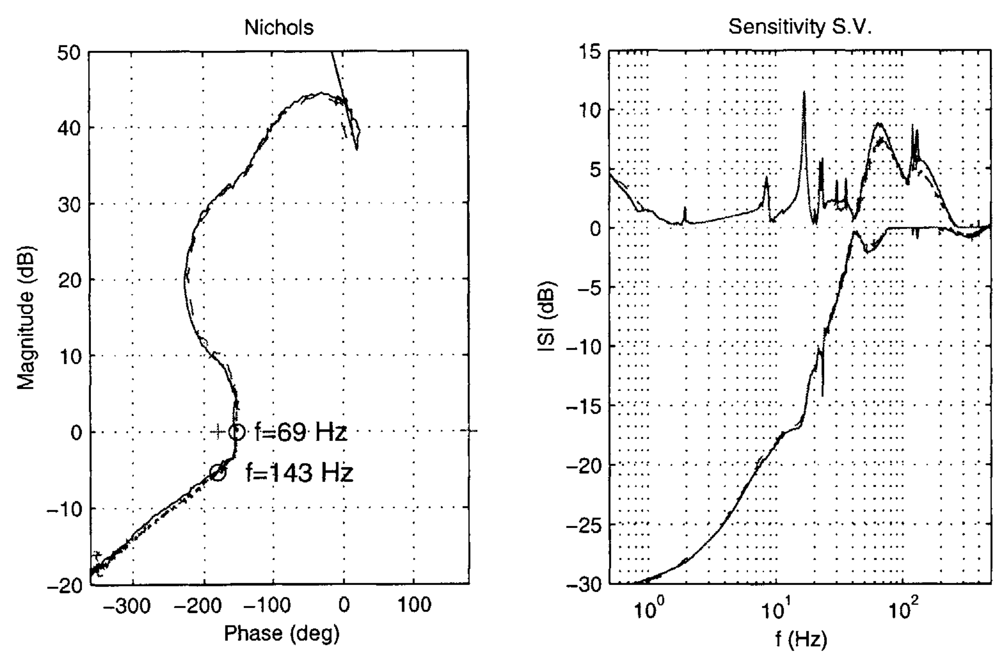

Figure E.6 Stability plots for T2 controller: simulated control on design data (solid), and measured (dashed)

Controller T3

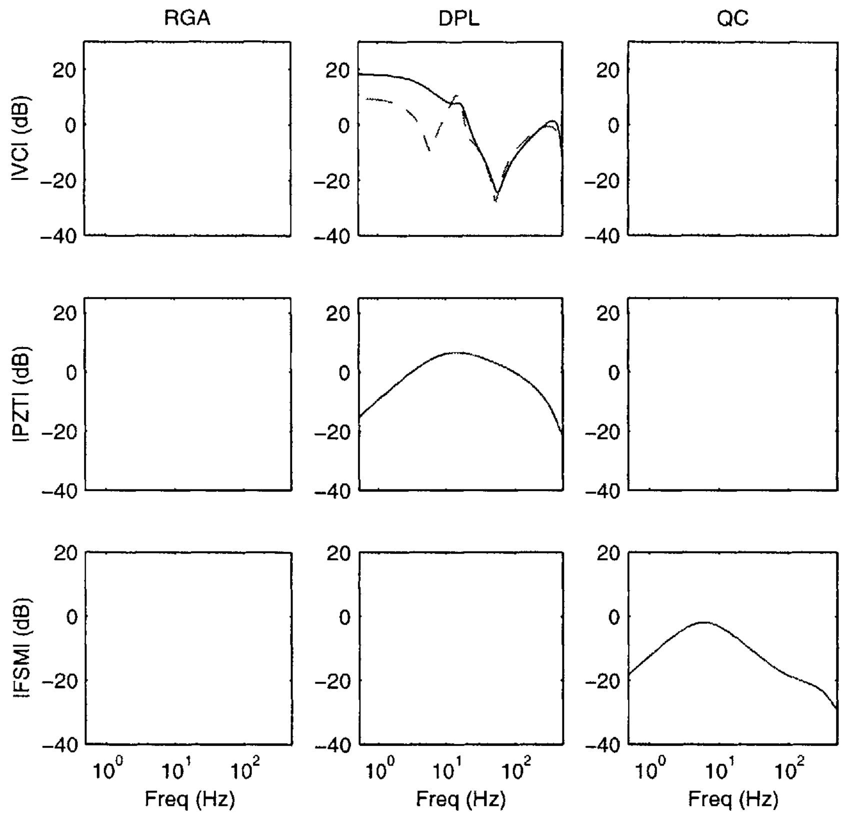

Figure E.7 T3 controller magnitudes (dashed), and T2 magnitudes (solid)

Additional tuning of the DPL-to-VC channel sacrifices low frequency control to achieved greater authority in the performance-critical 10 Hz frequency band.

TABLE E.3 Measured and predicted performance of controller T3

Perf Variable	RMS Performance Predict	RMS Performance Meas	Meas. imp. over OL	Meas. imp. over T2
DPL	0.98 μm	0.89 μm	14.6 dB	0.8 dB
QC	1.56 arcsec	1.62 arcsec	12.8 dB	0.3 dB

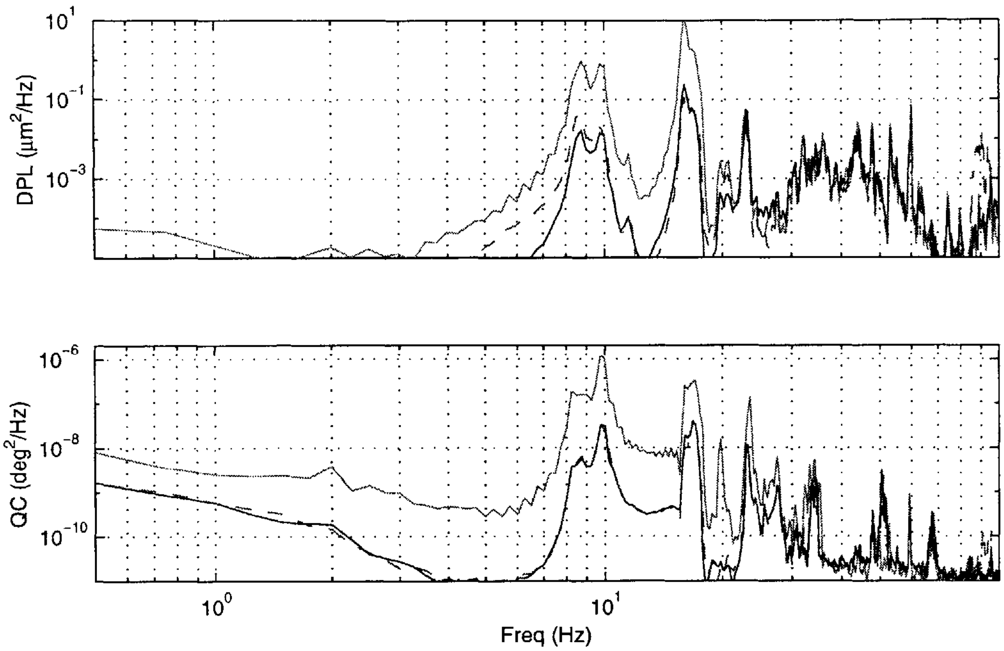

Figure E.8 Experimental performance autospectra: open-loop (light), T2 (solid), T3 controller (dashed)

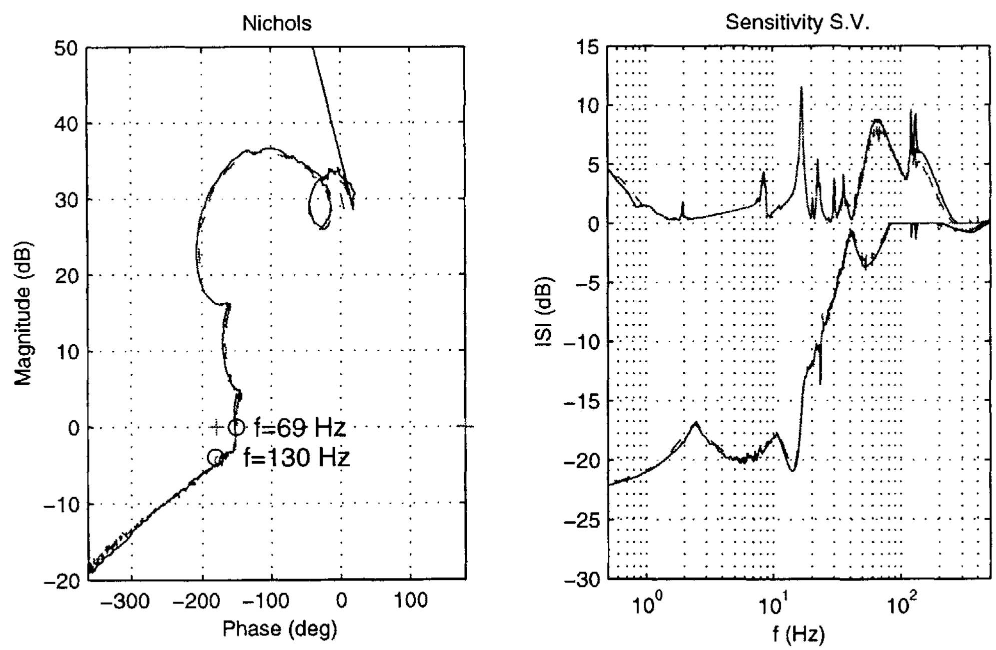

Figure E.9 Stability plots for T3 controller: simulated control on design data (solid), and measured (dashed)

Controller T4

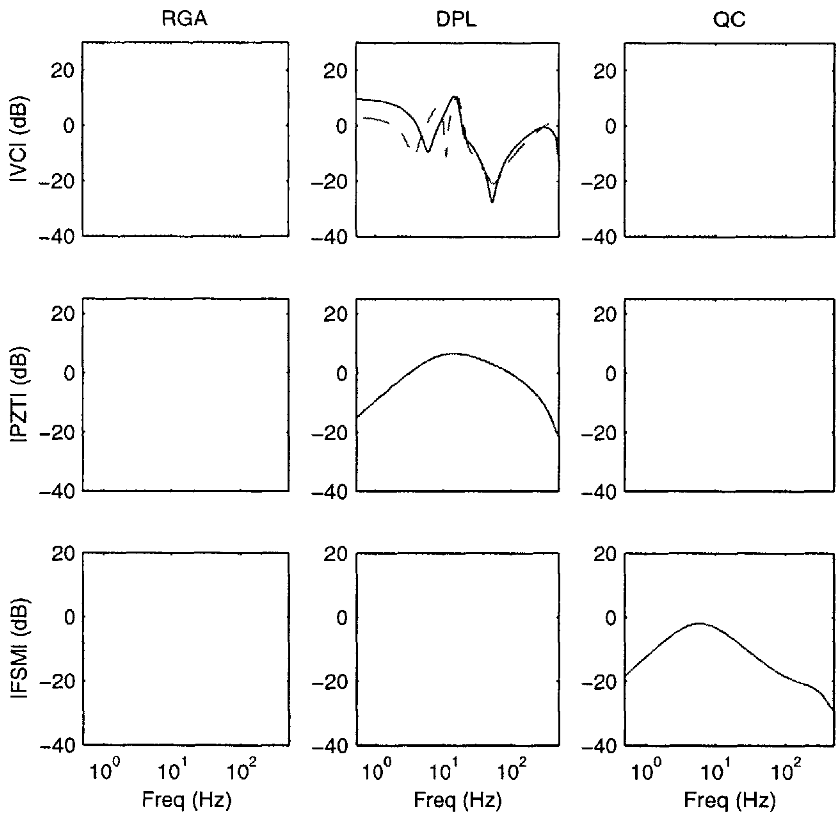

Figure E.10 T4 controller magnitudes (dashed), and T3 controller magnitudes (solid)

Further low-frequency performance is sacrificed to increase the gain slightly in the performance-critical 10 Hz band. A marginal DPL performance improvement is recorded. The QC performance decrease is likely measurement error.

TABLE E.4 Measured and predicted performance of controller T4

	RMS Performance			
Perf Variable	**Predict**	**Meas**	**Meas. imp. over OL**	**Meas. imp. over T3**
DPL	0.90 μm	0.87 μm	14.8 dB	0.2 dB
QC	1.56 arcsec	1.70 arcsec	12.3 dB	-0.3 dB

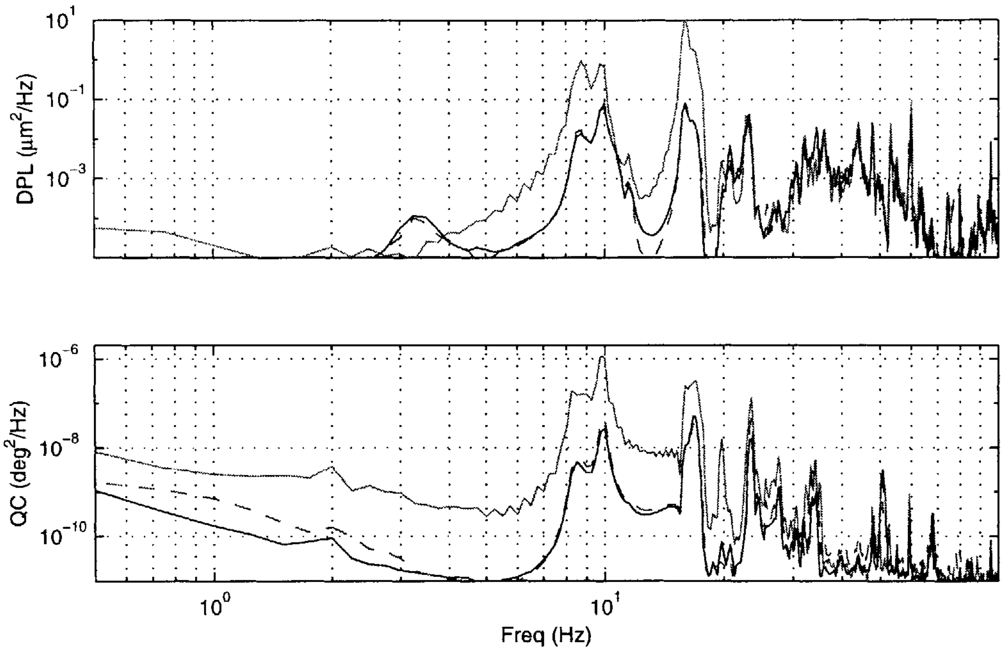

Figure E.11 Experimental performance autospectra: open-loop (light), T3 controller (solid), T4 controller (dashed)

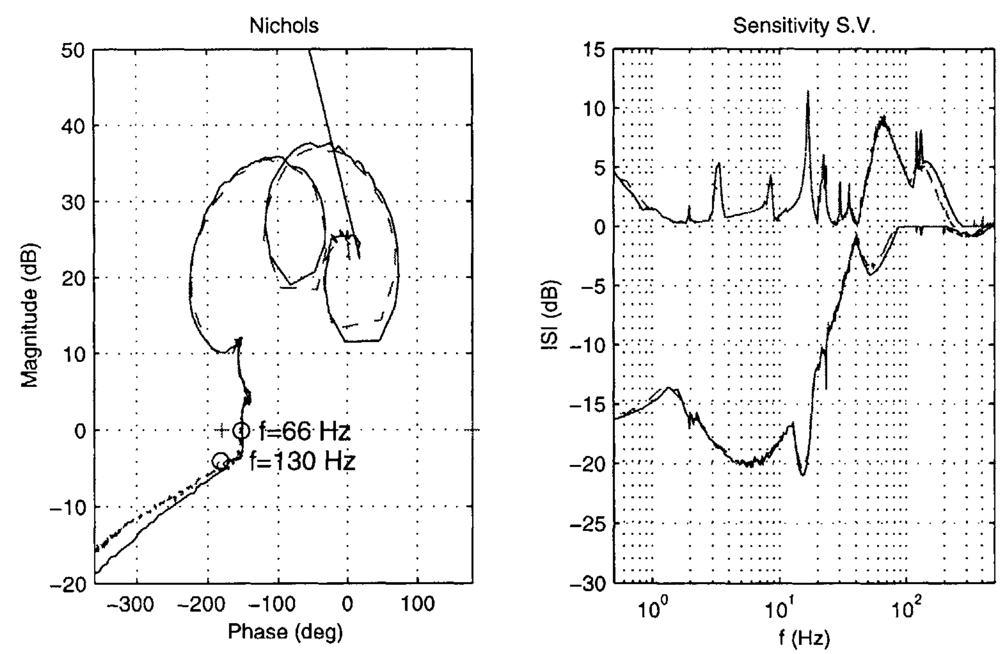

Figure E.12 Stability plots for T4 controller: simulated control on design data (solid), and measured (dashed)

Controller T5

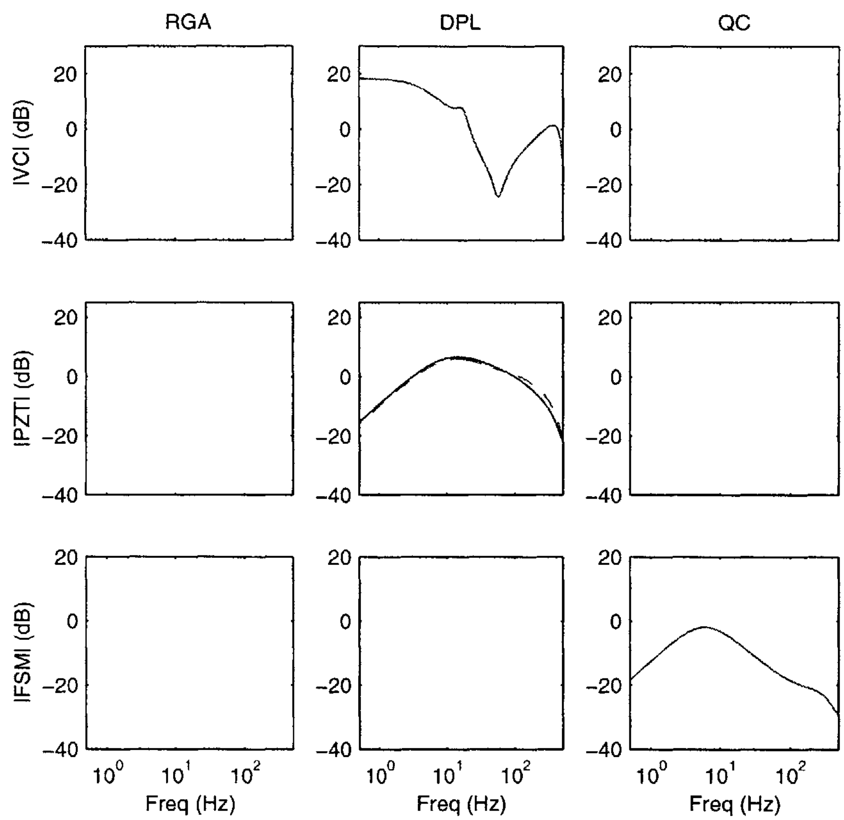

Figure E.13 T5 controller magnitudes (dashed), and T2 controller magnitudes (solid)

The DPL-to-PZT channel is tuned slightly to increase the gain near the performance-critical 20 Hz band. A slight (0.1 dB) DPL performance improvement was predicted. The measurement recorded a 0.1 dB performance decrease in the DPL.

TABLE E.5 Measured and predicted performance of controller T5

	RMS Performance			
Perf Variable	Predict	Meas	Meas. imp. over OL	Meas. imp. over T2
DPL	1.06 μm	0.98 μm	13.7 dB	-0.1 dB
QC	1.59 arcsec	1.68 arcsec	12.4 dB	0.0 dB

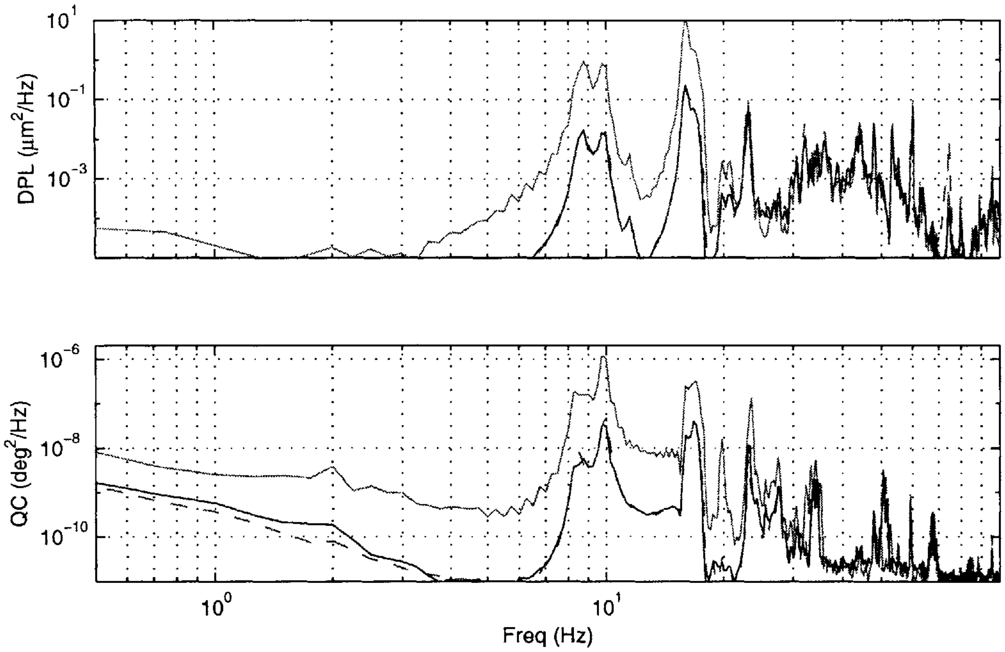

Figure E.14 Experimental performance autospectra: open-loop (light), T2 controller (solid), T5 controller (dashed)

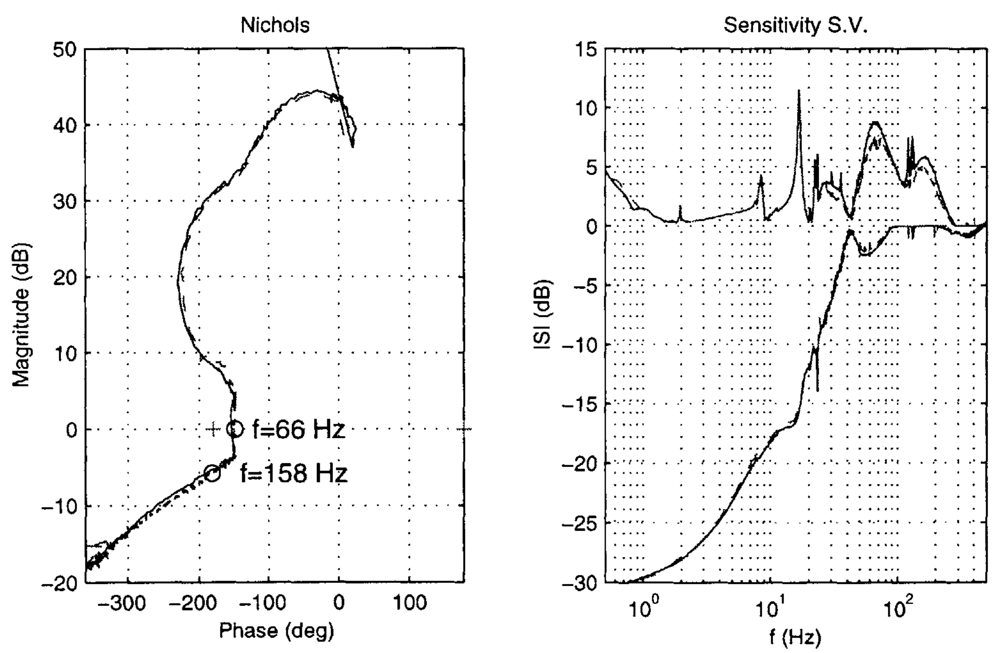

Figure E.15 Stability plots for T5 controller: simulated control on design data (solid), and measured (dashed)

Controller T6

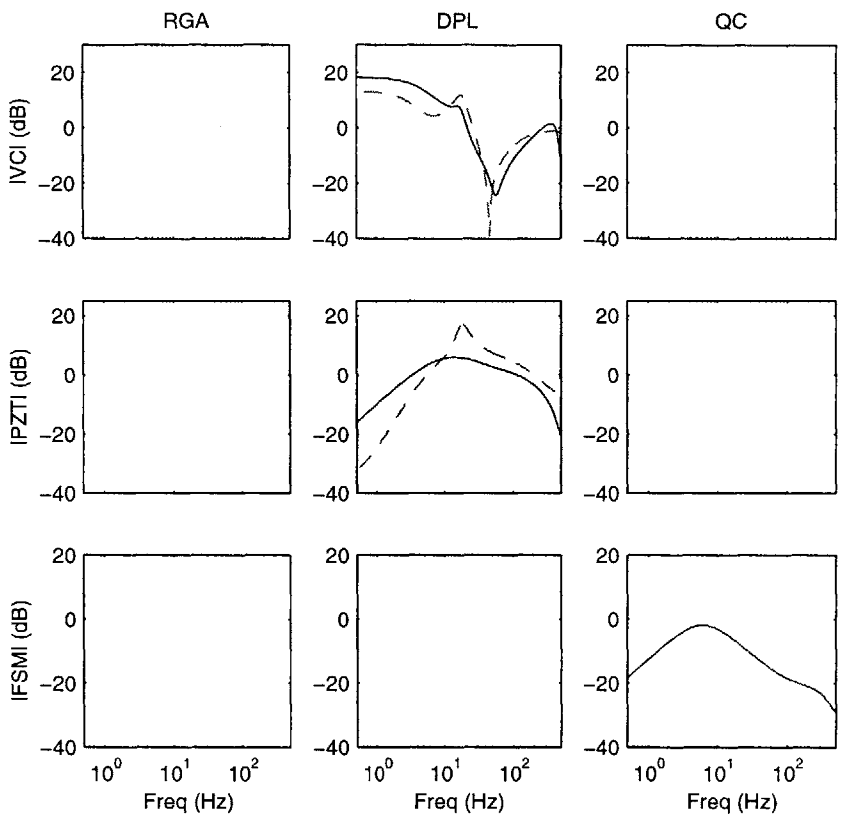

Figure E.16 T6 controller magnitudes (dashed), and T5 controller magnitudes (solid)

The entire phasing block is tuned simultaneously. Low-frequency PZT use is penalized heavily in the design. A considerable improvement in DPL performance is obtained by allowing the PZT increased authority in the performance-critical 18 Hz band.

TABLE E.6 Measured and predicted performance of controller T6

	RMS Performance			
Perf Variable	**Predict**	**Meas**	**Meas. imp. over OL**	**Meas. imp. over T5**
DPL	0.81 μm	0.66 μm	17.1 dB	3.4 dB
QC	1.58 arcsec	1.85 arcsec	11.6 dB	-0.8 dB

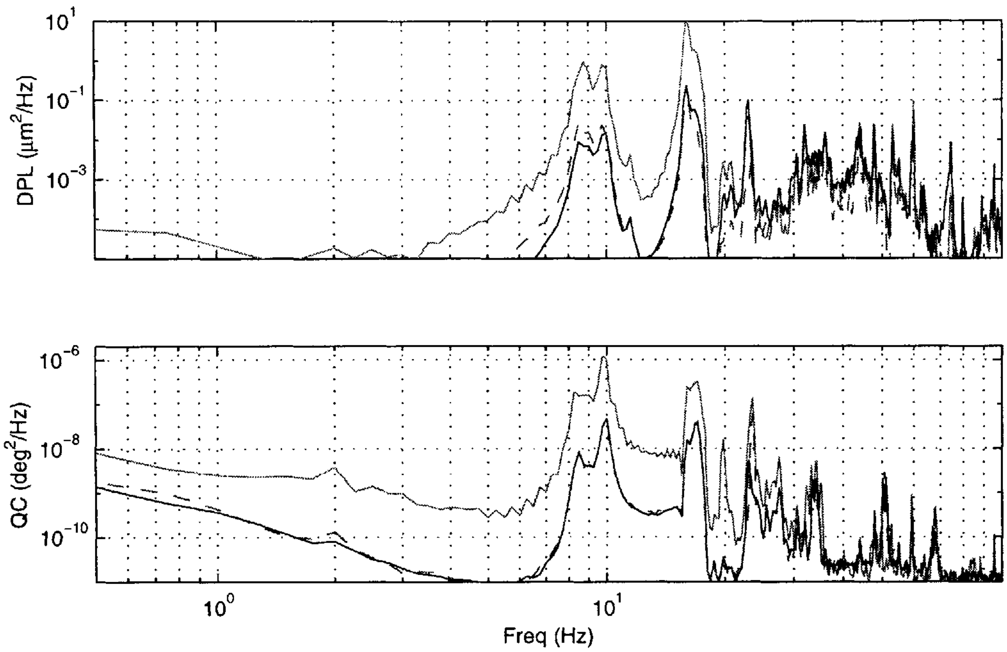

Figure E.17 Experimental performance autospectra: open-loop (light), T5 controller (solid), T6 controller (dashed)

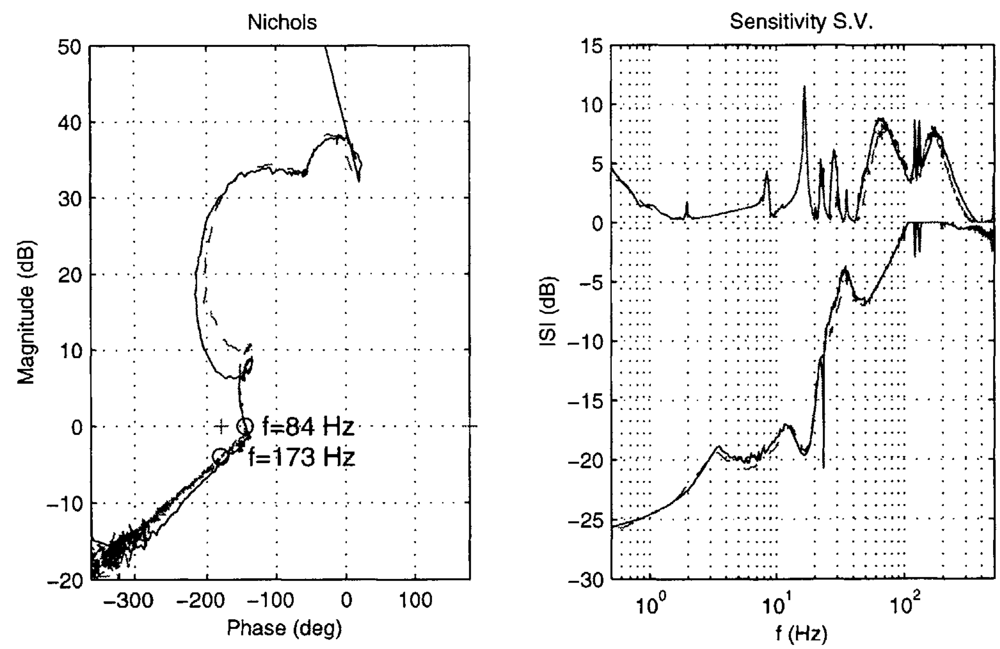

Figure E.18 Stability plots for T6 controller: simulated control on design data (solid), and measured (dashed)

Controller T7

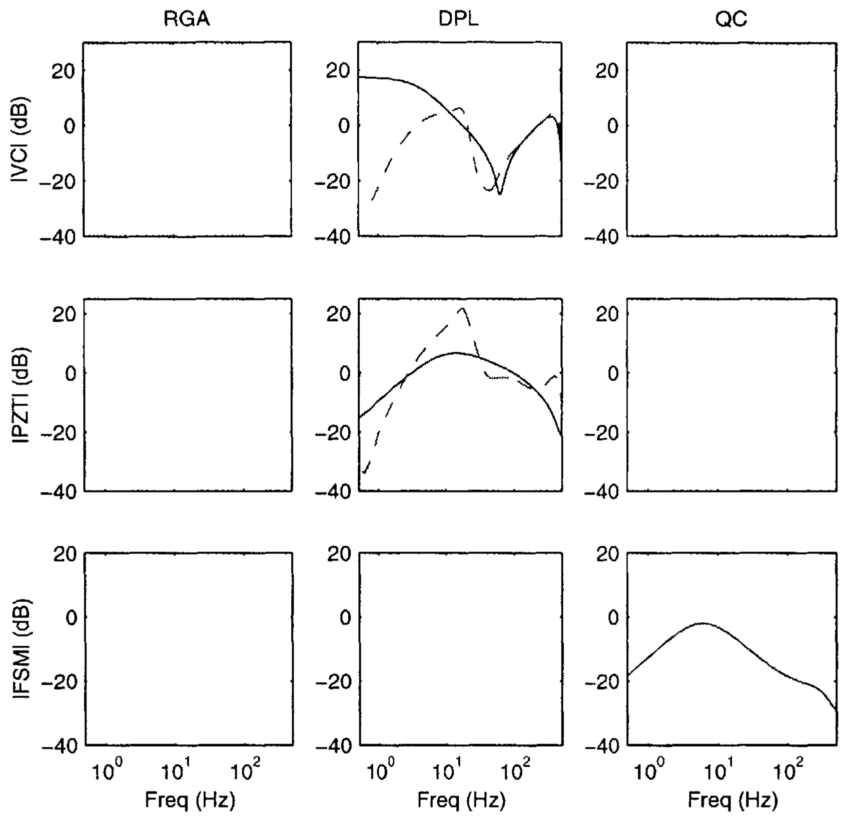

Figure E.19 T7 controller magnitudes (dashed), and T1 controller magnitudes (solid)

Low frequency phasing control is sacrificed to increase the gain in the performance-critical 10-20 Hz band. The performance improvement comes with little change in the stability robustness of the baseline controller.

TABLE E.7 Measured and predicted performance of controller T7

	RMS Performance			
Perf Variable	**Predict**	**Meas**	**Meas. imp. over OL**	**Meas. imp. over T1**
DPL	0.86 μm	0.76 μm	16.0 dB	4.6 dB
QC	1.55 arcsec	1.86 arcsec	11.6 dB	0.3 dB

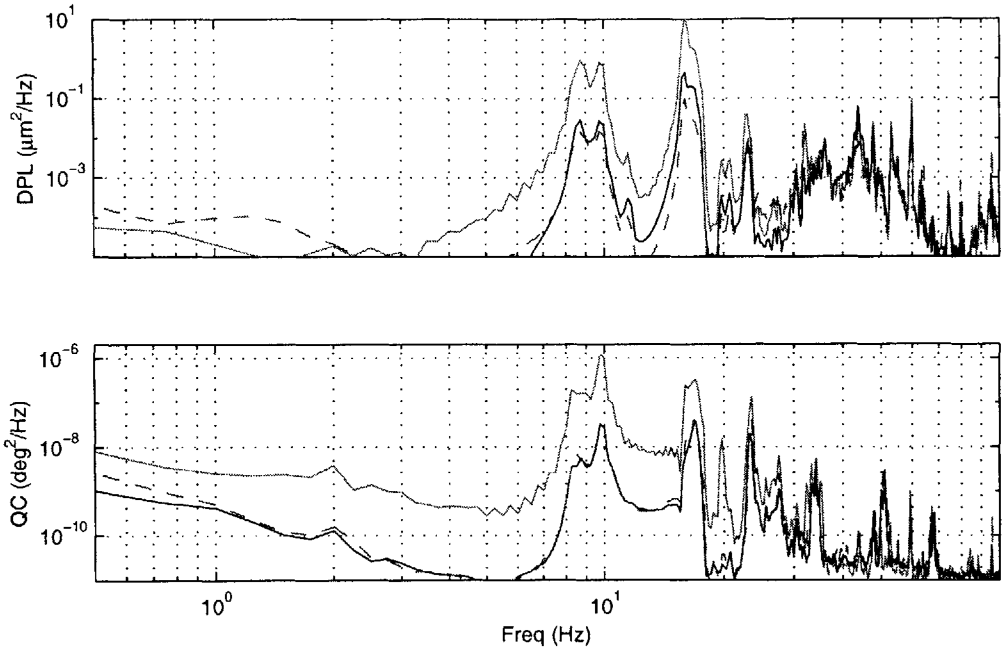

Figure E.20 Experimental performance autospectra: open-loop (light), T1 controller (solid), T7 controller (dashed)

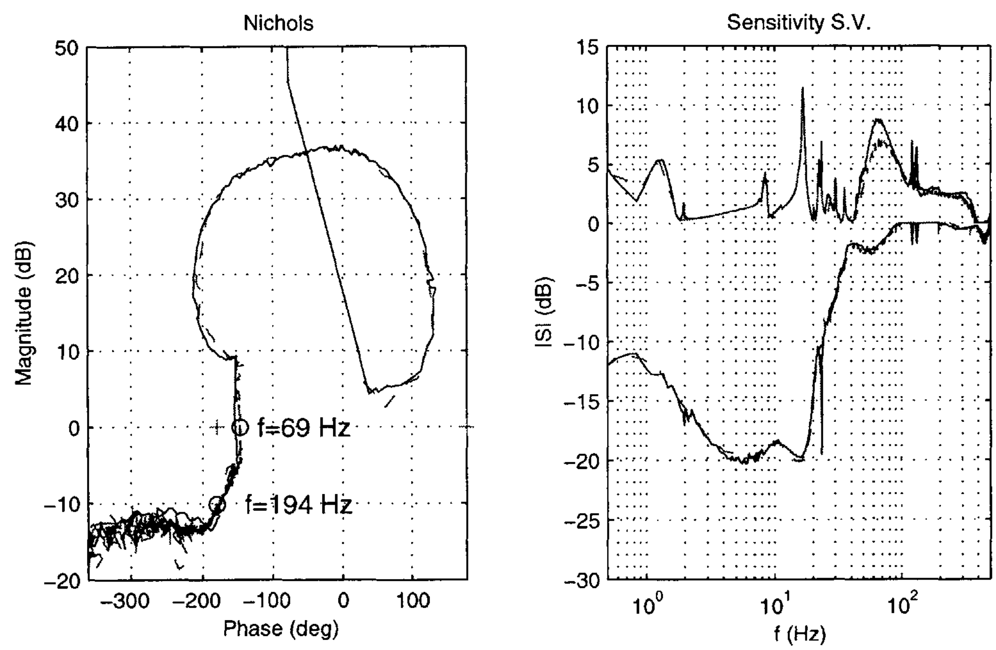

Figure E.21 Stability plots for T7 controller: simulated control on design data (solid), and measured (dashed)

Controller T8

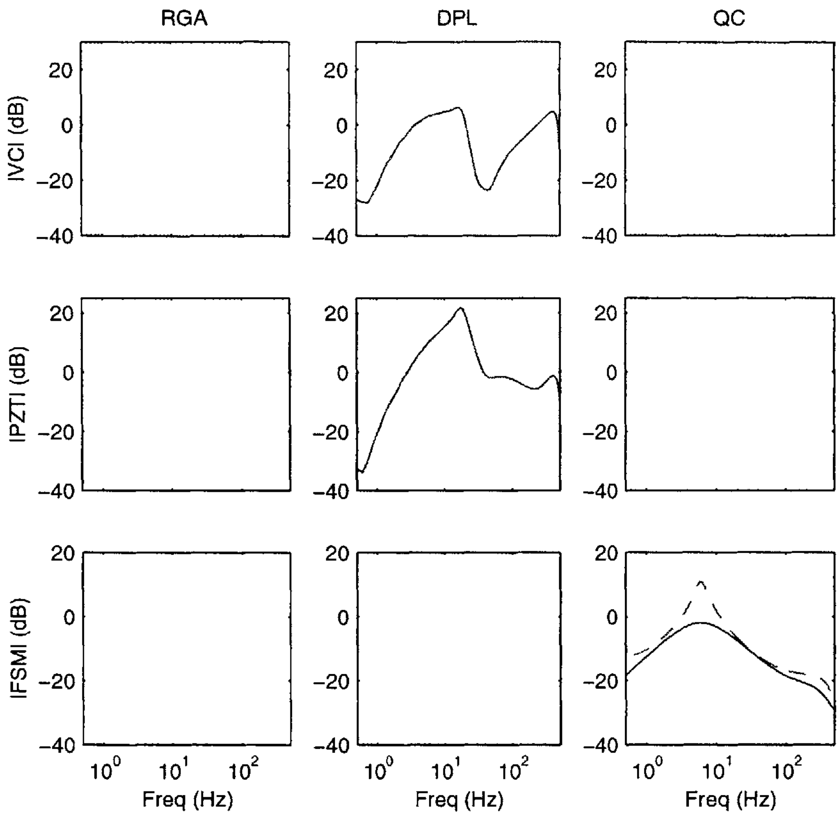

Figure E.22 T8 controller magnitudes (dashed), and T7 controller magnitudes (solid)

The gain of the QC-to-FSM channel is increased in the performance-critical 10 Hz band. The performance is obtained with no sacrifice in measured stability robustness. Low frequency use of the FSM piezo is penalized in the design.

TABLE E.8 Measured and predicted performance of controller T7

	RMS Performance			
Perf Variable	**Predict**	**Meas**	**Meas. imp. over OL**	**Meas. imp. over BC**
DPL	0.86 μm	0.71 μm	16.5 dB	0.5 dB
QC	1.19 arcsec	1.34 arcsec	14.4 dB	2.9 dB

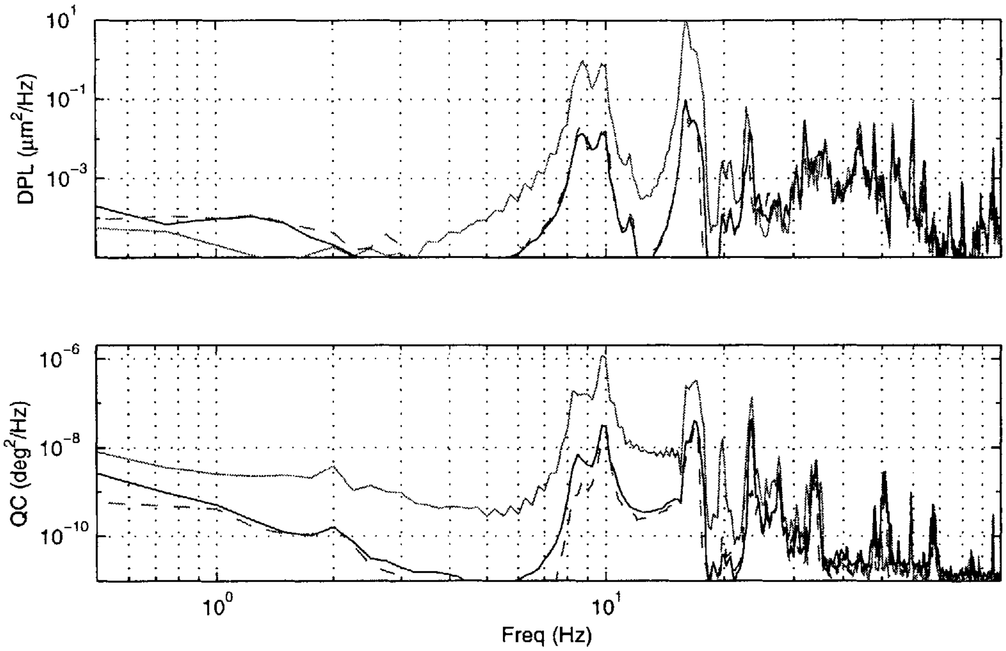

Figure E.23 Experimental performance autospectra: open-loop (light), T7 controller (solid), T8 controller (dashed)

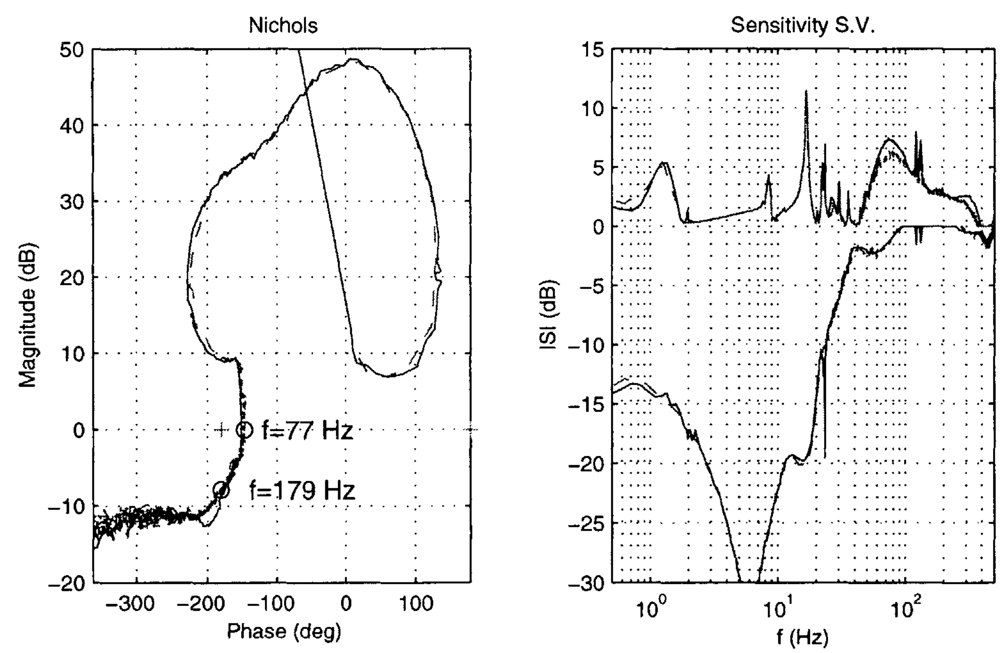

Figure E.24 Stability plots for T8 controller: simulated control on design data (solid), and measured (dashed)

Controller T9

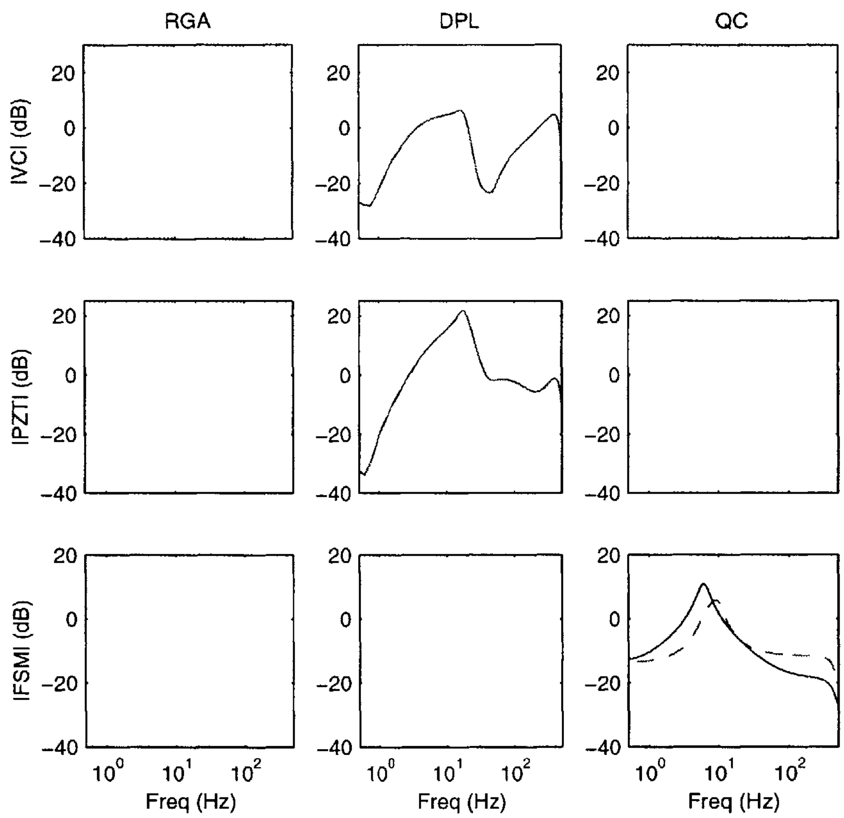

Figure E.25 T9 controller magnitudes (dashed), and baseline controller magnitudes (solid)

The addition of two states allows the peak control channel gain to closer approach the performance-critical 10 Hz band, while only slightly affecting the stability robustness. Further the bandwidth of the QC-to-FSM channel is increased.

TABLE E.9 Measured and predicted performance of controller T9

Perf Variable	RMS Performance Predict	RMS Performance Meas	Meas. imp. over OL	Meas. imp. over T8
DPL	0.86 μm	0.69 μm	16.7 dB	0.2 dB
QC	1.02 arcsec	1.18 arcsec	15.5 dB	1.1 dB

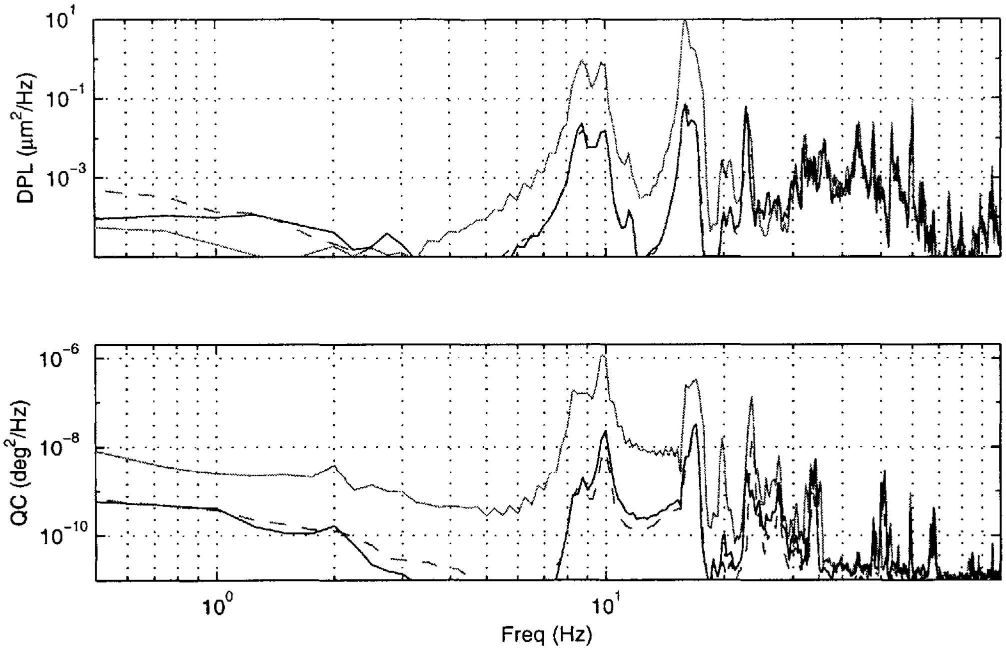

Figure E.26 Experimental performance autospectra: open-loop (light), T8 controller (solid), T9 controller (dashed)

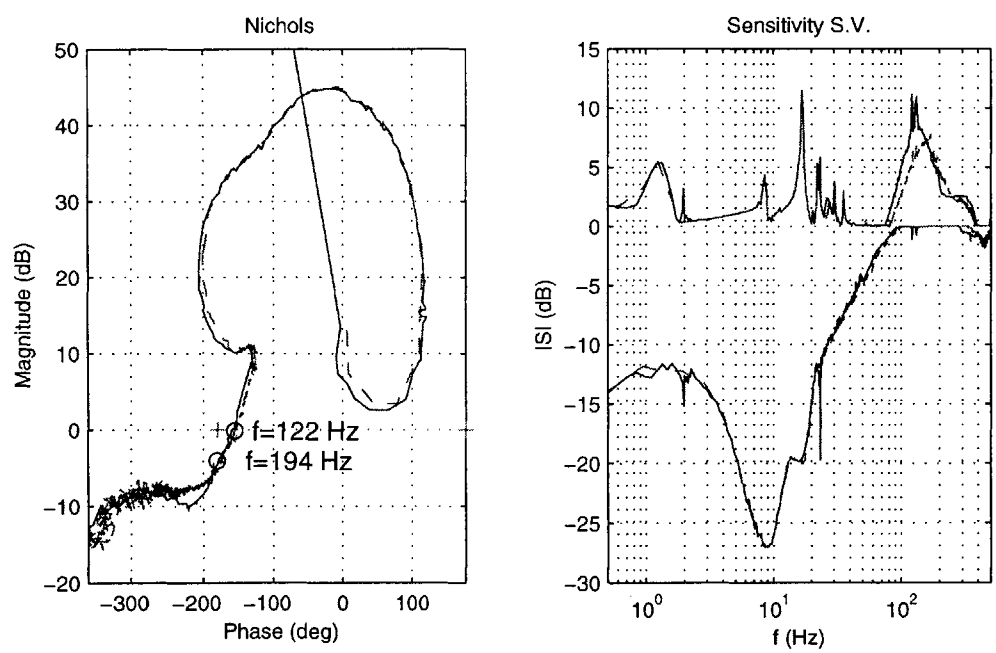

Figure E.27 Stability plots for T9 controller: simulated control on design data (solid), and measured (dashed)

Controller T10

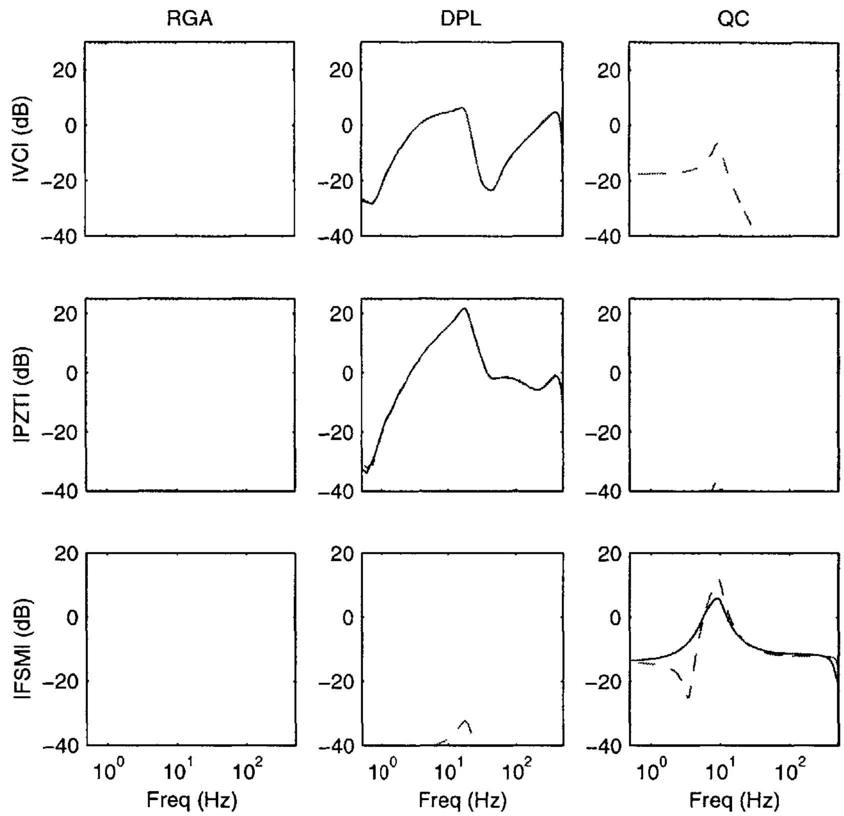

Figure E.28 T10 controller magnitudes (dashed), and T9 controller magnitudes (solid)

Tuning the entire optical phasing block allows the phasing control and the fine pointing control to share states to achieve greater performance. Some phasing (DPL) performance is sacrificed for an improvement in pointing (QC) performance.

TABLE E.10 Measured and predicted performance of controller T10

Perf Variable	RMS Performance Predict	RMS Performance Meas	Meas. imp. over OL	Meas. imp. over T9
DPL	0.86 μm	0.76 μm	15.9 dB	-0.8 dB
QC	0.98 arcsec	1.00 arcsec	16.9 dB	1.4 dB

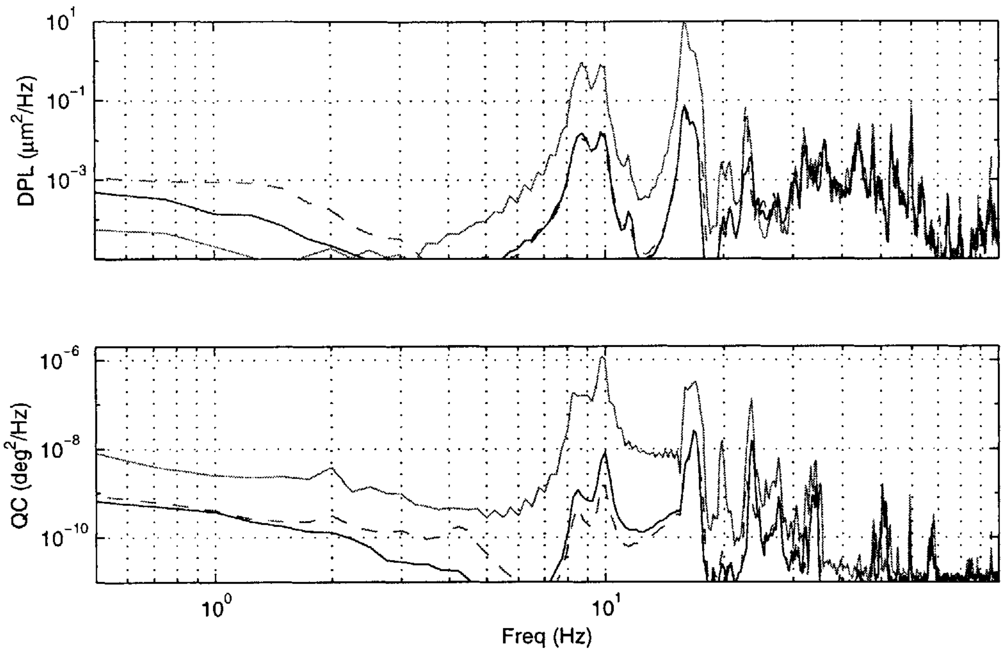

Figure E.29 Experimental performance autospectra: open-loop (light), T9 controller (solid), T10 controller (dashed)

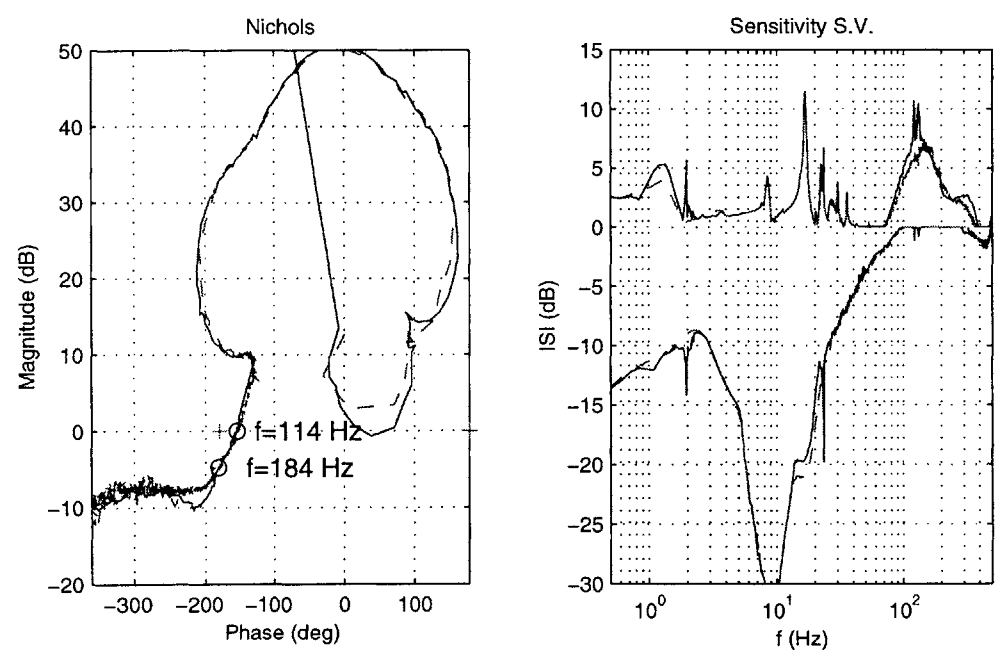

Figure E.30 Stability plots for T10 controller: simulated control on design data (solid), and measured (dashed)

Controller T11

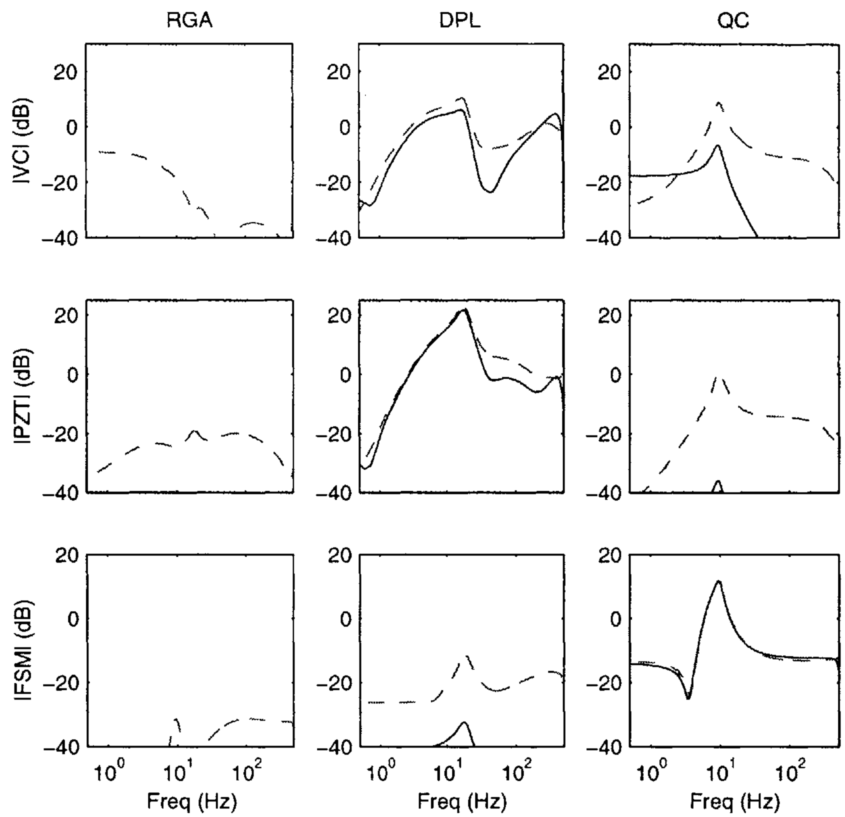

Figure E.31 T11 controller magnitudes (dashed), and T10 controller magnitudes (solid)

The RGA sensor is incorporated. Low frequency use of the PZT and FSM are penalized in the design. The predicted performance improvement is greater than that experimentally achieved. Further a measured sensitivity spike at 22 Hz indicated a model/measurement mismatch which may lead to problems should the design be further tuned.

TABLE E.11 Measured and predicted performance of controller T1

	RMS Performance			
Perf Variable	**Predict**	**Meas**	**Meas. imp. over OL**	**Meas. imp. over BC**
DPL	0.66 μm	0.77 μm	15.9 dB	0.1 dB
QC	0.86 arcsec	0.98 arcsec	17.2 dB	0.3 dB

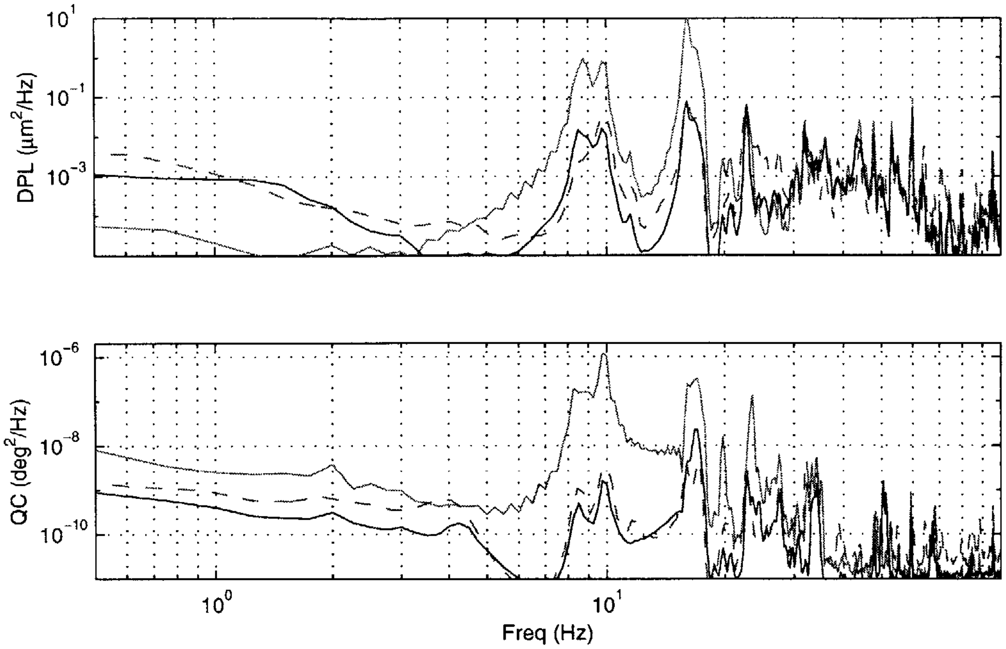

Figure E.32 Experimental performance autospectra: open-loop (light), T10 controller (solid), T11 controller (dashed)

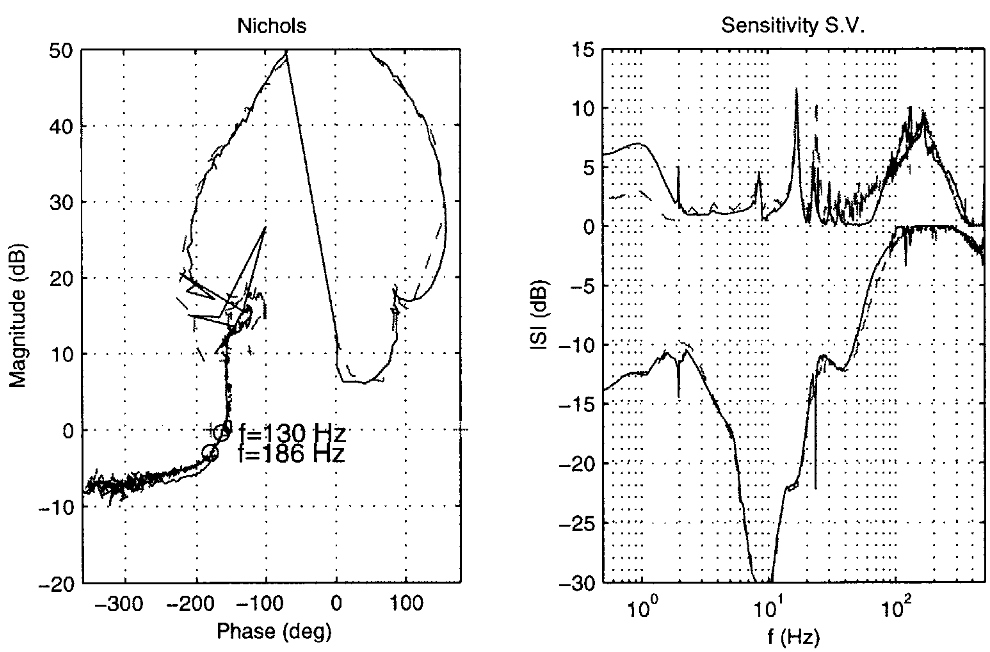

Figure E.33 Stability plots for T11 controller: simulated control on design data (solid), and measured (dashed)